The University of Hull

A Matrix Isolation Study
of
Transition Metal Halides
and their Structure.

being a Thesis submitted for the Degree of
Doctor of Philosophy
in the University of Hull

by
Antony Wilson, B.Sc.

June 09

This thesis is the result of my own work, except where due reference is given. No part of this work has been, or is currently being, submitted for a degree, diploma or other qualification at this or any other university or higher education establishment. This thesis does not exceed the 100,000 word limit, including tables, footnoted, bibliography and appendices.

Antony Wilson

Abstract

The work within this thesis has concentrated on the formation and isolation of titanium, vanadium, palladium, and mercury halides, with emphasis on the fluorides.

TiF, TiF_2, TiF_3, and TiF_4 have all been isolated within an argon matrix and infrared spectra obtained. From the titanium isotope splitting pattern a bond angle has been determined for TiF_2 for the first time of 165^o, or effectively linear. This work is also the first time that TiF has been isolated within an argon matrix. Work has also been conducted with vanadium which has lead to the isolation of VF_5, VF_4, VF_3, and VF_2, with VF_4 undergoing Fermi Resonance. This is the first time that VF_4 and VF_2, consistent with a linear structure, have been isolated within a matrix.

Work conducted upon palladium led to the isolation of numerous palladium fluorides, identified by the palladium isotope patterns in their IR spectra. Due to the similarity of the calculated stretching frequencies of PdF_2, PdF_3, PdF_4, and PdF_6 the assignment was challenging and so identification of these bands was conducted based photolysis and annealing behaviour in conjunction with computational calculations. This has allowed for the assignment of the bands present to PdF_6, PdF_4, PdF_3, PdF_2, and PdF.

The bond length of molecular HgF_2 has also been determined for the first time at 1.94(2) Å using the Hg L_3-edge with EXAFS. Although the initial aim of this work was to isolate HgF_4, using IR, UV/Vis, and XANES, no evidence could be found for oxidation states of mercury higher that Hg^{II}. The work also developed a new clean way of making HgF_2 in a matrix. The identification of a new Hg…X_2 complex was also discovered which when photolysed forms the HgX_2 compound, this has only been proven for HgF_2. This was achieved by isolating mercury atoms in an argon matrix doped matrices, photolysis of this matrix the led to the formation of HgF_2 in significant amounts.

Acknowledgements.

I would like to extend my deepest gratitude to my supervisor, Dr. Nigel Young, for offering me this opportunity and for his continued patience and guidance throughout the course of this work. I would also like to thank Dr. Adam Bridgeman for granting this studentship to me initially and his supervision in the initial year of my work, plus his computational contributions.

Special thanks must go to project students over the years for their contributions to this work, and because I made a promise a mention also for Helen. I would also like to thank my parents for their unwavering support of my university studies and their continual emotional and financial support throughout my university life, without them this thesis would have never been produced and so this thesis is dedicated to them.

I would like to thank the E.P.S.R.C. for a research studentship and to the University of Hull for funding, and all members of the Inorganic Chemistry department past and present for their input and support over the years. The mechanical workshop and the glass blowers must also get a thank you, without them this work would have stalled on many occasions.

Contents

Chapter 1 Introduction

Chapter 2 Matrix Isolation and Spectroscopic Techniques

Chapter 3 Theory

Chapter 4 Experimental

Chapter 5 First Row Transition Metal Halides

Chapter 6 Second Row Transition Metal Halides

Chapter 7 Third Row Transition Metal Halides

Chapter 1

Introduction

1.1 Introduction.

Chemists are often concerned with the structure and various other properties of individual molecules, but matter is rarely found in the form of isolated molecules. Intermolecular interactions dominate the physical nature of matter in the solid and liquid phases, and are experimentally observed even in the gas phase. Intermolecular interactions are strongest between chemically reactive species such as most atoms, free radicals and high temperature monomers, all of which can be studied in the gas phase only at low concentrations and high effective temperatures. Even under such extreme conditions some species are so reactive that they only exist for a few micro- or milliseconds after they are formed making their study difficult.

One possible way of overcoming these short lifetimes is the use of matrix isolation, which enables these species to be trapped and studied over a time frame of hours rather than seconds often with the use of solid noble gases as inert matrices. These matrices can exert a small influence on species, similar to that of a solution but with reduced level of interaction. Further details of the effects of a matrix are presented later. Stable high temperature vapour species can successfully be studied with matrix isolation due to the fact that sample density can be increased significantly and with reactive/unstable species it can act to stabilise them.

Overall one of the most important advantages of matrix isolation is that it allows the species to be trapped in a state analogous to the gas phase and this means that comparison of these highly reactive species to computational calculations, which are most accurate in the gas phase, is relatively easy. Further advantages of matrix isolation arise from the low temperatures which can reduce the excited state population and trap molecules in their ground state, thus reducing the complexity of spectroscopic data. In matrix isolation rotational transitions are almost totally removed, although this can be a disadvantage as it can reduce information about the moment of inertia, it does mean that only single levels are observed in IR spectra for each vibrational mode, which aides speciation.

1.2 Matrix Isolation.

1.2.1 The History of Low Temperature Experiments.

Low temperature scientific study began to develop at the end of the nineteenth century due to the discovery of methods of liquefying gases. One of the first experiments that was carried out was done in 1924 by the Kamerlingh Onnes Laboratory in Leiden, Netherlands. They studied the emission spectrum of oxygen and nitrogen atoms produced by electron, photon or x-ray bombardment of impure solid nitrogen and rare gases. Liquid helium and hydrogen were used as the refrigerants but because these liquefied gases were unavailable elsewhere at the time the technique did not become widely used.[1]

The poor optical quality of frozen solutions at 77 K prevented the use of absorption studies more widely and led to G.N. Lewis *et al.* studying which solvents formed a clear glass when frozen. This led to the use of EPA (ether, isopentane and alcohol mixed together), which formed a clear glass at 77 K[2] (provided an excess of ethanol was not present), and this enabled ultraviolet-visible (UV/Vis) spectra to be obtained. This development of clear glasses led to the generation of reactive species by photolysis of the frozen glass and an absorption spectrum taken. Reactive species were also obtained without the use of photolysis, for example the reduction of triarylmethyl halides with silver mercury amalgam producing triarylmethyl radicals.[3]

The low temperature glasses formed from this mixture of ether, isopentane and alcohol has several disadvantages. They are not chemically inert to reactive species and they also absorb strongly in the infrared region of the spectrum, thus preventing the use of any infrared (IR) spectra.

1.2.2 Development of Matrix Isolation.

The origin of the modern technique of matrix isolation developed later than these early experiments with organic glasses. In 1954 G. Porter and G.C. Pimentel simultaneously and independently proposed that argon and nitrogen could be used as supports for the stabilisation of molecules and for the photo-production of free radicals.[4, 5] Pimentel *et al.* developed the technique in the late 1950s, pioneering the method which basically involved cooling a matrix support such as a spectroscopically transparent window to low temperatures. On this support, which was under a vacuum, a matrix could form by bleeding inert gas into the vacuum chamber along with a reactive species, which was generated from a number of deposition methods. Using matrix isolation Pimentel *et al.* were able to positively identify the transient species HNO in 1958,[6] and HCO in 1960,[7] both of these radicals were isolated in solid xenon. A biography of Pimentel can be found in a Festschrift edition of The Journal of Physical Chemistry.[8]

After this pioneering early work the field of matrix isolation began to flourish. The early 1960s saw the identification of thirty previously unknown transient species. An example of these include the work by Linevsky, who showed that the technique was suitable for studying high temperature vapours,[9] he managed to isolate $(LiF)_n$ from a molecular beam effusing from a Knudsen cell. With the technique shown to be capable of isolating a range of species, the use of matrix isolation continues to this day. A bibliography[10, 11] of all publications up to 1997 is available which includes the vast number of experiments undertaken in this field. There are also reviews available in the Molecular Spectroscopy series of books,[12-14] RSC annual reports,[15-19] and some specialist books.[20-24]

References.

1. S. Craddock and A. J. Hinchcliffe, *Matrix isolation, A technique for the study of reactive inorganic species,* Cambridge University Press, Cambridge, 1975.
2. G. N. Lewis and D. Lipkin, *J. Am. Chem. Soc.*, 1942, **64**, 2801.
3. G. N. Lewis, D. Lipkin and T. T. Magel, *J. Am. Chem. Soc.*, 1944, **66**, 1579.
4. I. Norman and G. Porter, *Nature*, 1954, **174**, 508.
5. E. Whittle, D. A. Dows and G. C. Pimentel, *J. Chem. Phys.*, 1954, **22**, 1943.
6. H. Brown and G. C. Pimentel, *J. Chem. Phys.*, 1958, **29**, 883.
7. G. E. Ewing, W. E. Thompson and G. C. Pimentel, *J. Chem. Phys.*, 1960, **32**, 927.
8. W. L. S. Andrews, B. S. Ault, M. J. Berry and C. B. Moore, *J. Phys. Chem.*, 1991, **95**, 2607.
9. M. J. Linevsky, *J. Chem. Phys.*, 1961, **34**, 587.
10. D. W. Ball, Z. H. Kafafi, L. Fredin, R. H. Hauge and J. L. Margrave, *Bibliography of Matrix Isolation Spectroscopy: 1954 - 1985*, Rice University Press, Houston, 1988.
11. D. W. Ochsner, D. W. Ball and Z. H. Kafafi, *A Bibliography of Matrix Isolation Spectroscopy: 1985-1997*, Naval Research Laboratory, Washington, DC, 1998.
12. A. J. Downs and S. C. Peake, *Mol. Spec.*, 1971, **1**, 523.
13. B. M. Chadwick, *Mol. Spec.*, 1975, **3**, 281.
14. B. M. Chadwick, *Mol. Spec.*, 1979, **6**, 72.
15. M. J. Almond and N. Goldberg, *Annu. Rep. Prog. Chem., Sect. C, Phys. Chem.*, 2007, **103**, 79.
16. M. J. Almond and K. S. Wiltshire, *Annu. Rep. Prog. Chem., Sect. C, Phys. Chem.*, 2001, **97**, 3.
17. M. J. Almond, *Annu. Rep. Prog. Chem., Sect. C, Phys. Chem.*, 1997, **93**, 3.
18. M. J. Almond and R. H. Orrin, *Annu. Rep. Prog. Chem., Sect. C, Phys. Chem.*, 1991, **88**, 3.
19. R. N. Perutz, *Annu. Rep. Prog. Chem., Sect. C, Phys. Chem.*, 1985, **82**, 157.
20. H. E. Hallam, *Vibrational Specroscopy of Trapped Species*, Wiley, London, 1973.
21. L. Andrews and M. Moskovits, *Chemistry and Physics of Matrix-Isolated Species*, North-Holland, Amsterdam, 1989.
22. M. J. Almond, *Short-Lived Molecules*, Ellis Horwood, Chichester, 1990.

23. M. Moskovits and G. A. Ozin, eds., *Cryochemistry*, Wiley-Interscience, New York, 1976.
24. M. J. Almond and A. J. Downs, *Spectroscopy of Matrix Isolated Species*, Wiley, Chichester, 1989.

Chapter 2

Matrix Isolation and Spectroscopic Techniques

2.1 Introduction.

Before the development of matrix isolation gas phase spectroscopy was the dominant form of spectroscopy for highly reactive species, especially when conducting IR studies. For stable species such as carbon dioxide IR gas phase studies are simple and can provide a large amount of structural information. The information that can be derived from a gas phase IR spectra include the molecule's fundamental vibrational and their rotational energy levels. This rotational fine structure can be very complicated but can also be used to determine rotational constants which allow the accurate determination of bond lengths and angles for molecules. But they can also provide many problems; the busy spectrum and the broadening of fundamental bands can make it very difficult to determine exact positions of fundamental bands. This is more pronounced for large molecules which have more fundamental frequencies which may be close together.

Other problems that can occur in gas phase studies result when the molecules to be studied are not volatile and so must be heated to get into the gas phase. This can lead to problems as some compounds may decompose upon heating and produce various vapour species which can complicate the spectrum, and on some occasions the species you desire may not even be produced. Further problems which can arise with this technique are 'hot bands'. This problem relates to that fact that in the vaporisation of the compound energy can be absorbed and a transition from the first to the second excited vibrational state of the molecule may be observed which serves to further complicate the spectrum. These hot bands can be very problematic as the energy of separation between the first and second excited state is less than that of the ground and first excited state so a separate band or a shoulder will be observed.

Despite these problems with gas phase spectroscopy it is a very useful technique that can be used to study stable compounds effectively. However, for unstable species gas phase studies are difficult and offer no way to prevent decomposition of these species. Matrix isolation offers a solution to the study of these types of species. Matrix isolation experiments involve the preparation of a rigid lattice that acts as a host for preserving and immobilising the reactive species of interest indefinitely. This occurs due to the nature of the high dilution and low temperature conditions of the experiments and thus prevents any unimolecular decomposition or bimolecular collisions that occur under normal conditions. Other techniques used to study highly reactive species include Supersonic Molecular Beams,[1-3] and the use of helium nanodroplets,[4, 5] both of which are extremely complicated techniques in comparison to matrix isolation.

The modern use of matrix isolation centres on five main areas of research, which are:

- Vapour species studies - samples are heated under vacuum, the vapour produced is then co-condensed with a matrix gas preserving all the species within it. These are then characterised spectroscopically by a number of methods.
- Characterisation of radical and novel species - techniques such as laser ablation (focusing of a high power laser on a sample) are ideal for the formation of radical species. These can then be captured in a matrix and characterised. Sputtering (ions focused on a sample) is another technique less frequently used but can produce metal atoms.
- Reactions in matrices - matrix reactions can be induced between two or more trapped species through the use of photolysis (light energy) and/or annealing (thermal energy), the products can then be studied.
- Matrix interactions - the matrix interacts with isolated species. These interactions are studied in order to gain a fuller understanding of the matrix environment.
- Pyrolysis – involves the co-condensation of the products of pyrolysis (thermal decomposition) of an organic molecule with the matrix material, this is often used to stabilise free radicals.

2.2 Spectroscopic Methods.

Spectroscopy involves the absorption or emission of electromagnetic radiation in resonance with a transition between two discrete states of a molecule or atom. The most common spectroscopic method used with matrix isolation is IR, but electronic spectroscopy is also often used, but with the vast array of modern day spectroscopic techniques the scope of potential uses with matrix isolation is huge.

IR spectroscopy is often used as it allows for speciation of molecules due to the loss of rotational structure in the matrix which is often exactly what is desired and spectroscopic bands in the IR spectrum are sharpened by matrix isolation, as discussed later. Electronic spectroscopy involves electronic transitions which in principle can occur in any part of the electromagnetic spectrum, but most commercially available UV/Visible spectrometers cover a range of about 190-850 nm wavelength, corresponding to 52000 to 12000 cm^{-1}. Some of the problems experienced with matrix isolated UV spectra include a broadening of the peaks, sometimes by 100-500 cm^{-1}, and also when compared to gas phase data the peaks can be shifted by as much as 1000 cm^{-1} mainly to higher energies. This can make it difficult, especially in complex spectra, to assign peaks correctly to transitions observed in gas phase data.

2.3 Matrix Materials.

What is a matrix material and what makes a good one? A matrix material is simply the gas that is used to form the solid matrix upon the spectroscopic window. The question of what makes a good matrix material really depends on what is being studied. As mentioned earlier many matrix experiments are conducted in order to characterise a vapour or transient species. In these experiments, the required matrix needs to interact with the species as little as possible. Therefore, an inert gas would be most suitable. In contrast to this however, are experiments conducted using a reactive matrix. These experiments are conducted in order to induce a reaction of a species with the matrix material itself. An example being the co-condensation of $CrCl_2$ with CO to form $CrCl_2(CO)_4$.[6] In these experiments interaction is obviously desirable. Despite these differences there are a number of universal properties desired if a gas is to be good a matrix material.

1. The first property of a matrix gas should be inertness with the exception of the type of experiment just specified. The noble gases fulfil this criterion best, as they are the most inert of all the possible matrix materials. Nitrogen is also relatively inert however when studying free radicals it may sometimes be deemed reactive and therefore its use should be appropriate to the experiment.
2. Purity of the gas is another property deemed necessary to a matrix isolation experiment. Without purity, non-reproducible spectra are taken and the matrix formed has a high degree of lattice distortions which encourages movement of species through the matrix. Purity can be controlled by using good quality gases and by eliminating leaks from vacuum equipment.
3. The matrix material should ideally be fully transparent in the spectroscopic region of interest. Fundamental bands of a species could be missed if the matrix has absorptions in the spectral region. For IR experiments, the noble gases and nitrogen have no absorptions and are therefore commonly used. The issue of transparency is however more complex than just whether or not the gas used has absorption bands. The thickness of the matrix and its crystallinity can all affect light scattering. For example if xenon is deposited below 50 K a highly scattering film will result which will mean a large reduction in radiation reaching the detector.[7] Therefore, factors need to be considered such as deposition rate and temperature when carrying out a matrix experiment. A good rule of thumb is to have slow deposition rate, which will keep the thickness down and the crystallinity high.
4. Rigidity is another important property. There would be no point in isolating species in the matrix if the support was not rigid enough to keep them that way. Lack of rigidity allows species to move through the matrix meaning the spectrum obtained for an experiment would simply be of multimer products. In accessing the suitability of matrix materials for their rigidity, temperature is the most important factor. Pimentel investigated[8] this property and as a guide came up with the rule that for a matrix material to be rigid enough the melting point (T_m) of the material must

be at least double that of the temperature for which the material is to be used. The point where diffusion of species through the matrix does become appreciable is termed T_d. With modern cryostats being able to achieve temperatures of around 12 K, making argon and heavier noble gases all suitable for use along with nitrogen. Convenient closed cycle systems can also achieve 4.2 K where neon matrices would be suitable.

5. Two thermodynamic properties are also important for matrix gases. These are the latent heat of fusion (L_f) of the gas and the lattice energy (U_0). The latent heat of fusion is important as it is a measure of how much energy needs to be removed from the molecules as they form on the matrix support. Obviously, if the energy cannot be removed quickly enough the matrix temperature will rise causing diffusion of the species. Usually however, if the deposition rate of the matrix is kept slow, this factor can be kept under control. The lattice energy is also important as this relates to the amount of energy required to remove a molecule from its place in the lattice once the matrix has formed. Too high a lattice energy would mean that when diffusion studies are desired they would only be possible at high temperatures, which is not desirable.
6. The final property required by a good matrix material is a high thermal conductivity (γ). As a matrix forms it grows in thickness. This puts the responsibility for removing the thermal energy of the atoms at the newly forming surface onto the bulk matrix material instead of the deposition window, as the heat has to be conducted through the matrix to the cryostat. The better the thermal conductivity of the matrix gas the easier this heat will be removed.

With all these properties in mind it is easy to see why the best choices for a matrix material are the noble gases and nitrogen. They are chemically inert, transparent to IR radiation and in the case of nitrogen and argon, the most common used, they are relatively cheap. These are by no means the only gases used in matrix isolation experiments. A number of reactive matrices are often investigated these include carbon monoxide, methane and oxygen. Table 2.1 displays the thermal properties of these and other commonly used matrix materials.

Material	**T_d (K)**	**Melting Point (K)**	**Boiling Point (K)**	**Vapour pressure of 10^{-3} mm at ... (K)**	**L_f (J mol^{-1})**	**$-U_0$ (J mol^{-1})**
Ne	10	24.6	27.1	11	335	1874
Ar	35	83.3	87.3	39	1190	7724
Kr	50	115.8	119.8	54	1640	11155
Xe	65	161.4	165.0	74	2295	16075
N_2	30	63.2	77.4	34	721	6904
CH_4	45	90.7	111.7	48	971	-
O_2	26	54.4	90.2	40	444	-
CO	35	68.1	81.6	38	836	7950
NO	-	109.6	121.4	66	2310	-

Table 2.1 Thermal properties of commonly used matrix materials.[8]

2.4 The Structure of the Matrix.

The exact morphology of solid matrices i.e. whether the matrices are glassy, polycrystalline or single crystal is unknown. Due to the matrices being formed on a single crystal of either alkali halide or sapphire, a degree of epitaxy is expected. The structure of the matrix has not been deduced unambiguously, though through experiments performed by Young[9] and co-workers using Extended X-ray Absorption Fine Structure (EXAFS) and Knözinger's neutron experiments[10] on deposited krypton the structure is more closely understood and these experiments have gone someway to deduce the structure of the matrix. It is important that, especially when cage effects are considered, basic packing principles are considered.

2.4.1 Close Packed Structure Under 'Matrix Conditions'.

When considering cage effects, the closed-packed structure and the size of the sites available to accommodate the guest molecule need to be considered. All noble gases, except for helium, crystallise with a face-centred cubic (fcc) structure.[11] Argon has been shown to form a hexagonal close-packed structure (hcp) occasionally and the tendency for this structure to form is increased in the presence of impurities such as nitrogen, oxygen and carbon monoxide. These two simple regular lattice structures are shown in Figure 2.1. In both fcc and hcp structures there are two tetrahedral holes per atom and one octahedral hole per atom. These hole types are shown in more detail in Figure 2.2 for an fcc lattice, as can be seen from Figure 2.2 octahedral holes provide more space for occupation than tetrahedral holes. The topic of solid state rare gases is extensively review by Pollack.[12]

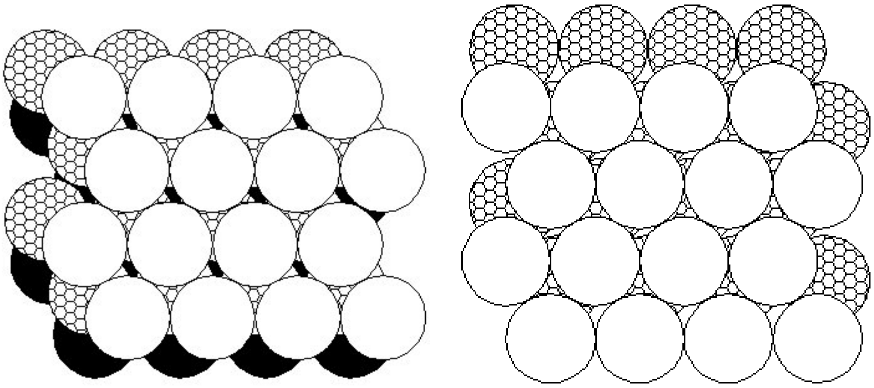
a) b)

Figure 2.1 Representation of the packing observed in a) fcc and b) hcp structures. The fcc structure has layers of ABC and the hcp structure has layers of ABA. For the ABA packing the third layer is not shown as this overlays exactly over the first layer.[13]

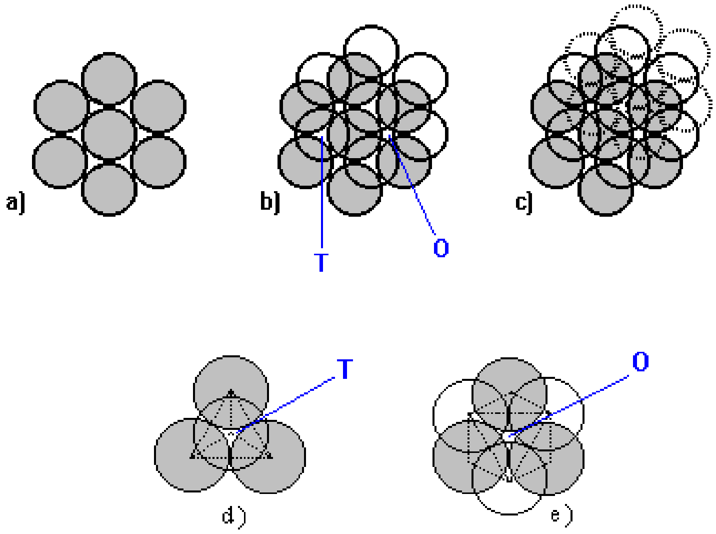

Figure 2.2 Close packing of spheres in fcc lattice, showing three layers, (a), (b), (c), and the tetrahedral and octahedral holes,[8] and tetrahedral and octahedral holes shown between the layers, (d) and (e).

2.5 Matrix Effects.

Now that the best materials have been identified for the use as matrix gases and the method with which the matrix can arrange itself, it is appropriate to discuss how the matrix environment can accommodate a species and how it can affect the results of experiments. There are six known, common effects, which can all contribute to the modification of vibrational band shapes, their intensity and their frequency. The following effects could be deemed the disadvantages of matrix isolation spectroscopy.

While some of these effects, such as the elimination from absorption spectra of bands due to absorption by molecules in excited states, are easy to understand, other effects though are not so easy. It becomes necessary to consider how the interaction of a matrix with a trapped species comes to change its spectroscopic properties.

2.5.1 Multiple Trapping Sites.

The first such effect is the phenomena of multiple trapping sites. When a molecule is matrix isolated it is often trapped within a substitutional site in the matrix gas lattice. This means the trapped molecule takes the place of one of the atoms or molecules of the crystal lattice. This however, is not the only possibility, and as molecules become larger this type of trapping become less likely as other sites also exist. Crystal lattices have interstitial sites where small solute molecules may be isolated. Another possibility is that a species may lie in a lattice imperfection, such as a dislocation site. The significance of these differing sites is profound, as in each site the intermolecular forces between the matrix and the solute vary, which results in differing perturbations of the species' energy levels. This can result in a different vibrational frequency for each site, which complicates the spectrum.

Crystal data on matrices shows that different sites are possible. The most common matrix materials, such as the noble gases are spherical and therefore arrange in close packed structures. They do this to maximise the van der Waals forces between the atoms and as a consequence they maximise the number of neighbours around each atom. For larger molecules the various sites adopted will involve more or less perfect packing in the immediate cage and the surrounding layers, and the presence of impurities in or near the cage. All these may affect the effective matrix potential and hence the vibration frequency or the electronic transition energy of the molecule, giving rise to a variety of bands in the spectra. Table 2.2 details the site diameters for all the available sites within some common matrix gases. Obviously as atomic radii increase the size of both the substitutional and interstitial sites increases.

	Substitutional hole	**Octahedral hole**	**Tetrahedral hole**
Solid (4 K)	**(Å)**	**(Å)**	**(Å)**
Ne	3.16	1.31	0.71
Ar	3.75	1.56	0.85
Kr	3.99	1.65	0.90
Xe	4.34	1.80	0.97
CH_4	4.15	1.73	0.94
N_2 (4 K)	3.991		
N_2 (20 K)	4.004		
CO (23 K)	3.999		

Table 2.2 Site diameter of common matrix gases at 4 K.[14-18]

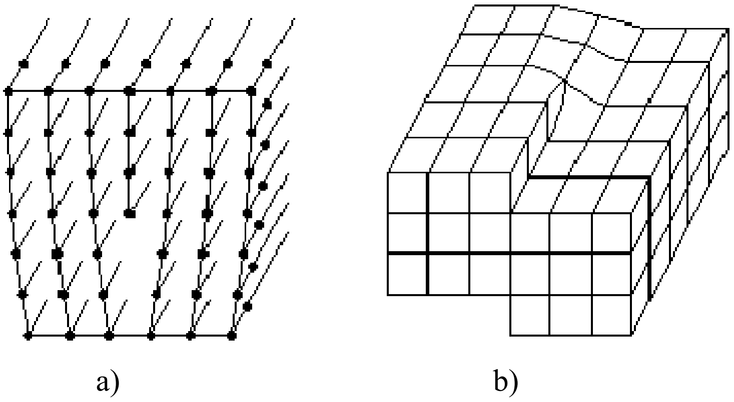

Figure 2.3 Trapping sites generated by imperfections in the crystal caused by a) pure edge dislocation and b) screw dislocation.[8]

As shown, in a perfect crystal there are three trapping sites available, with the substitutional hole being most readily occupiable, multiple substitutional holes can also occur, i.e. the removal of two or more argon atoms. To complicate things further, in matrix isolation experiments the lattice formed is unlikely to be perfect and therefore lattice imperfections will be prevalent within the matrix. These imperfections, termed dislocations, commonly occur in two forms, an edge dislocation and a screw dislocation and are shown in Figure 2.3. Molecules with larger dimensions than the trapping site can be accommodated by either introducing strain into the host crystal, the formation of multiple vicinal vacancies or by forcing the matrix to adopt a glassy structure.

These dislocations occur due to the nature of the deposition process, well ordered crystals take time to arrange. Matrix experiments however, rapidly cool gas from room temperature to 12 K not allowing time for exact ordering. These additional trapping sites are therefore created and have the ability to perturb solute atoms to differing degrees. Site effects are therefore one of the drawbacks of the matrix isolation technique. In many experiments single sharp bands that are reproducible are observed with no perceivable problems related to trapping sites. Occasionally band splitting is observed as will be demonstrated by some of the results in this work, given later. The range of trapping sites discussed here justifies the splitting observed. With nitrogen matrices lifting of degeneracy is often observed which results in more bands being observed than expected, this is due to the structure of the nitrogen lattice.

2.5.2 Molecular Rotation.

In the gas phase molecules rotate, in matrices however most molecules are held tightly within the crystal lattice and therefore no rotation is observed. Consequentially no rotational fine structure is observed; instead sharp, reproducible bands assigned to the fundamental frequencies are seen. This lack of rotation is one of the advantages of matrix isolation spectroscopy, but also a disadvantage. This is due to the fact that as the rotational fine structure of the spectra is lost, sharp peaks can be observed along with other peaks that would normally be obscured by the rotational fine structure. But this also results in a loss of detail and information which the rotational fine structure presents, i.e. the loss of the ability to calculate interatomic distances from moments of inertia. It is well established though that for very small molecules, such as H_2O, quantised rotation may be possible in some matrices.[19-21] The spectra observed are however not as complicated as those seen in the gas phase due to the low temperatures involved. This manifests itself in the appearance of separate R(0), Q(1) and P(1) lines in each vibrational and electronic transition, corresponding to changes in the rotation quantum number J of $0 \rightarrow 1$, $1 \rightarrow 1$ and $1 \rightarrow 0$, respectively. In some instances transitions starting from higher rotational levels than $J = 1$ are observed if the circumstances of the experiment allow such levels to be continuously populated by absorption of energy followed by re-emission. A characteristic of multiplets due to rotation is that marked changes occur reversibly in their relative intensities as the temperature of the matrix changes because the thermal energy appropriate to the temperature (4-10 K) is similar to that needed to populate the $J = 1$ level from the $J = 0$ level. Thus these features are complicating to the spectrum but are often fairly easy to assign due to this temperature dependence.

2.5.3 Matrix Shift.

In the gas phase, molecules have vibrational frequencies that are relatively independent from interactions with other molecules. However, in the matrix environment the isolated species are subject to solute-matrix interactions. These interactions which vary with matrix site, hence the trapping effects are known as matrix shifts. They also vary with matrix material and the shift is described by the following expression.

$$\Delta\nu = \nu_{gas} - \nu_{matrix}$$

The interactions disturb the solute's vibrational energy levels and usually shift bands to lower frequency. These shifts are usually small and can give information about molecular interactions within the matrix, these shifts are most often 'red' shifted, but 'blue' shifts are known.[22] The magnitude of the matrix shift is observed for matrix gases in the following order $Ne < Ar < Kr < Xe < N_2$.

2.5.4 Aggregation.

Unless the solute to matrix gas ratio is in the region of 1:1000 some form of aggregation is likely to occur.[8] The effect of aggregation upon a vibration frequency will, of course, depend on the strength of the interaction between the species concerned. In the limit of a weak interaction with a neighbour outside the immediate matrix cage only slight shifts in the vibration frequencies may be expected; a variety of such shifts in the interactions could readily give rise to a multiplet. The effect of allowing diffusion to occur would be to diminish the intensity of the peaks due to such weakly interacting pairs, which would move closer together to form definite dimers.

Dimers may behave as two loosely linked monomer molecules, if only weak forces exist between the portions; in this case only small changes in frequency are expected. Stronger interactions, such as chemical bond formation, will result in the spectrum of the monomer being replaced by that of the dimer. In most cases dimer spectra may be distinguished from spectra due to monomers and loose aggregates because the proportion of dimers is likely to increase as diffusion proceeds, at the expense of monomers and loose aggregates. Also by varying the concentration the bands should be identifiable.

2.5.5 Coupling with Lattice Vibrations.

These are rare and unlikely to be applicable to the work undertaken here but nevertheless they do occur in some ionic matrices. The vibrational modes of a solute molecule may couple with modes of the lattice causing a perturbation of the frequencies.

2.5.6 Phonon Bands.

The final matrix environment effect is the phenomena known as phonon bands. These occur when a matrix impurity or solute disturbs the matrix lattice symmetry and activates normally unseen lattice vibrational modes and are seen at the low energy part of a spectrum.

2.6 Species Generation.

There are numerous ways of generating a species for matrix isolation study; these methods are usually determined by the nature of the material that is desired to be isolated and studied. Control of the vapour pressure is an important aspect of species generation in matrix isolation and sometimes it is required to reduce vapour pressure using low temperature baths. One of the first suggestions of a method for the isolation of a solid compound was by Pimentel[23] who suggested the use of a Knudsen cell in 1960, and it was first successfully used in 1961 by Linevsky in 1961.[24] Since these early experiments various other techniques have been suggested and successfully used, the most common of which will now be outlined and explained.

2.6.1 Direct Vaporisation.

Metal atoms and molecular compounds can be produced by the direct heating of a bulk metal, such as a ribbon, rod or filament by applying a low-voltage and high current. This method has difficulty with metals such as manganese and chromium which cannot be machined into filaments and with gold, silver and copper due to their high conductivities. In the case of gold, silver and copper their high conductivities means that their melting point is below the temperature required to attain a high enough vapour pressure. This is usually countered by mounting them on a support filament, such as molybdenum, tantalum or tungsten.

2.6.2 Induction Heating and Pyrolysis.

Knudsen cells can be heated indirectly by an external heating coil or *via* induction heating. A high power radio frequency field is produced to induce eddy currents in the cell material. This then heats the cell as a result of dissipative processes within it. This is generally used in the heating of impure materials, which act as precursors, to sublimation temperature in the Knudsen cell.

2.6.3 Sputtering.

This method uses the bombardment of a solid metal target with ions, such as Ar^+. A hollow cathode sputtering source involves a low pressure inert gas discharge being used to 'sputter' metal atoms from inside the cathode. These discharged ions posses a lot of kinetic energy, typically around 1 keV, which is enough to cause the ejection of atoms from the target. These atoms can then be matrix isolated or reacted with molecules to form novel species. Although this technique appears attractive previous work in the laboratory by N. Harris has shown that atoms that are produced are far too dilute to observe any reactions.[25]

2.6.4 Electron Bombardment.

High energy electrons are thermionically produced from a hot tungsten filament and electrostatically accelerated towards the target material held in a water-cooled crucible. The electron beam is magnetically deflected and focused onto the target by a permanent magnet.

2.6.5 Laser Ablation.

This involves the use of a laser beam which is focused on a solid target. The laser is used to eject a high energy induced plasma of atoms and electrons which can go on to react with molecules seeded in the matrix. This technique has been extensively used by Andrews *et al.* in over 250 papers.

References.

1. S. H. Ashworth, F. J. Grieman, J. M. Brown, P. J. Jones and I. R. Beattie, *J. Am. Chem. Soc.*, 1993, **115**, 2978.
2. F. J. Grieman, S. H. Ashworth, J. M. Brown and I. R. Beattie, *J. Chem. Phys.*, 1990, **92**, 6365.
3. S. H. Ashworth, F. J. Grieman, J. M. Brown and I. R. Beattie, *Chem. Phys. Lett.*, 1990, **175**, 660.
4. F. Stienkemeier and K. K. Lehmann, *J. Phys. B. -At. Mol. Opt.*, 2006, **39**, R127.
5. M. Y. Choi, G. E. Douberly, T. M. Falconer, W. K. Lewis, C. M. Lindsay, J. M. Merritt, P. L. Stiles and R. E. Miller, *International Reviews In Physical Chemistry*, 2006, **25**, 15.
6. I. R. Beattie, P. J. Jones and N. A. Young, *J. Am. Chem. Soc.*, 1992, **114**, 6146.
7. E. D. Becker and G. C. Pimentel, *J. Chem. Phys.*, 1956, **25**, 224.
8. H. E. Hallam, *Vibrational Specroscopy of Trapped Species*, Wiley, London, 1973.
9. I. R. Beattie, N. Binsted, W. Levason, J. S. Ogden, M. D. Spicer and N. A. Young, *High Temp. Sci.*, 1989, **26**, 71.
10. W. Langel, W. Schuller, E. Knözinger, H. W. Fleger and H. J. Lauter, *J. Chem. Phys.*, 1988, **89**, 1741.
11. E. R. Dobbs and G. O. Jones, *Rep. Prog. Phys.*, 1957, **20**, 516.
12. G. L. Pollack, *Rev. Mod. Phys.*, 1964, **36**, 748.
13. G. L. Miessler and D. A. Torr, *Inorganic Chemistry*, 2nd Edn., Prentice Hall, 1988.
14. D. N. Batchhelder, D. L. Losee and R. O. Simmons, *Phys. Rev.*, 1967, **162**, 767.
15. O. G. Peterson, D. N. Batchelder and R. O. Simmons, *Phys. Rev.*, 1966, **150**, 703.
16. D. L. Losee and R. O. Simmons, *Phys. Rev.*, 1968, **172**, 944.
17. D. R. Sears and H. P. Klug, *J. Chem. Phys.*, 1962, **37**, 3002.
18. S. C. Greer and L. Meyer, *Z. Angew. Phys.*, 1969, **27**, 198.
19. K. S. Seshadri, L. Nimon and D. White, *J. Mol. Spectrosc.*, 1969, **30**, 128.
20. A. Buchler and J. B. Berkowitz-Mattuck, *J. Chem. Phys.*, 1963, **30**, 128.
21. P. A. Akishin, L. N. Gorokhov and Y. S. Khodeev, *Zh. Strukt. Khim.*, 1961, **2**, 209.
22. M. E. Jacox, *J. Mol. Spectrosc.*, 1985, **113**, 286.

23. G. C. Pimentel, *Forming and Trapping Free Radicals*, Academic Press, New York, 1960.
24. M. J. Linevsky, *J. Chem. Phys.*, 1961, **34**, 587.
25. N. Harris, PhD Thesis, Univeristy of Hull, 2001.

Chapter 3

Theory

3.1 Introduction.

The origin of molecular spectra is based around the fact that when molecules are placed in an electromagnetic field a transfer of energy can occur. This, however, will only occur when Bohr's frequency condition is satisfied:

$$\Delta E = h\nu \tag{3.1}$$

Where ΔE is the energy between two quantized states, h is Planck's constant, and ν is the frequency of the photon. A molecule can therefore absorb and emit energy according to this law.

The energy of a molecule can be split into three different components; these being the rotational energy of the molecule, the vibrational energy of the molecule and the energy associated with the motion of its electrons. Figure 3.1 illustrates the energy levels of a diatomic molecule. The rotational energy levels are closely spaced and therefore absorb energy in the microwave region of the spectrum. The vibrational energy levels, which are discussed in depth in this chapter, are spaced less closely and absorb energy in the IR region of the spectrum. The electronic energy levels are spaced far apart and require energy in the visible or UV part of the spectrum in order to induce a transition, as shown in Figure 3.2.

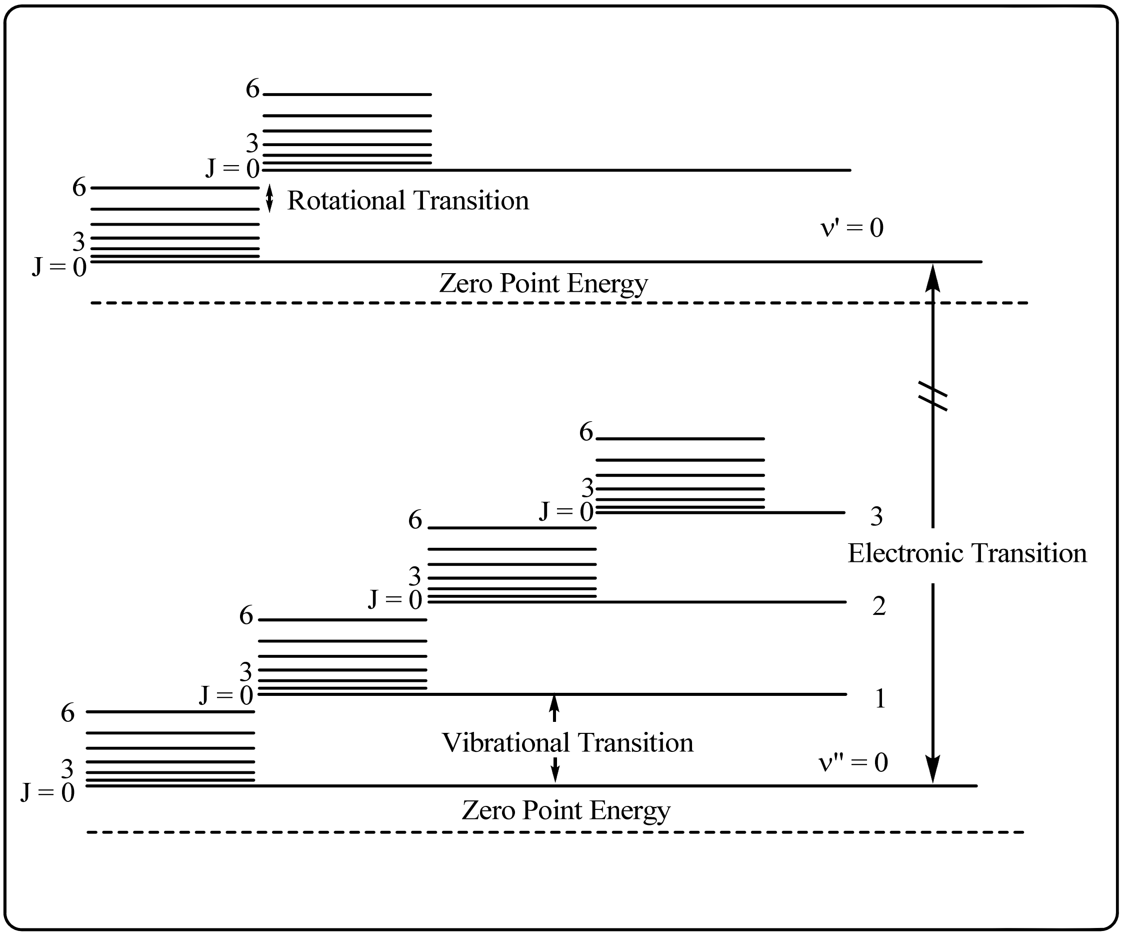

Figure 3.1 Possible energy levels for a diatomic molecule.

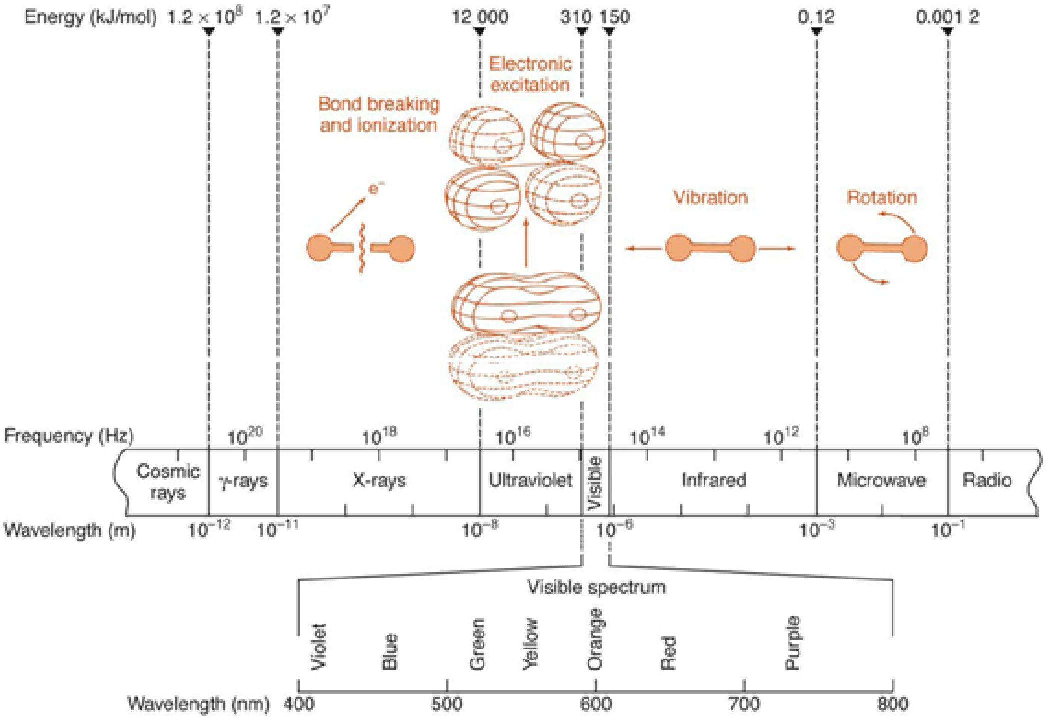

Figure 3.2 Representation of the electrmagnetic spectrum and its effect of diatomic molecules.[1]

3.2 Vibrational Theory.

Atoms and molecules can posses electronic, vibrational and rotational energy, these energy states can only have specific values, as shown in Figure 3.1. The energy that these quantized levels possess forms the basis of spectroscopy. As shown in Figure 3.2 electromagnetic radiation in the X-ray area (10^{18} Hz) has the ability to break bonds and ionise molecules, it can also be used for a technique known as x-ray diffraction. UV radiation can be used to excite electrons into higher energy levels. IR radiation can be absorbed by molecules and subsequently increase their vibrational energy and microwave radiation is used for rotational spectroscopy as the radiation interacts with the oscillating component of the rotating molecules. All of these types of spectroscopy are based on the absorption of electromagnetic radiation. Specific reference will now be given to the most commonly used technique within this work.

3.2.1 Diatomic Molecules.

If we consider vibrational theory from a basic point of view initially, then a diatomic molecule can be represented as two balls, atoms, connected by a spring. This 'molecule' will obey Hooke's law ($F = -kx$) and from Hooke's law Equation 3.2 can be derived for the potential energy of the molecule.

$$E = \frac{1}{2}kx^2 \tag{3.2}$$

$$\text{where } x = r - r_e$$

Where E is the potential energy, x is the distance the atom has moved from the equilibrium position, and k is the bond force constant. Figure 3.3 shows Equation 3.2 as a parabola which is referred to as the 'harmonic' potential.

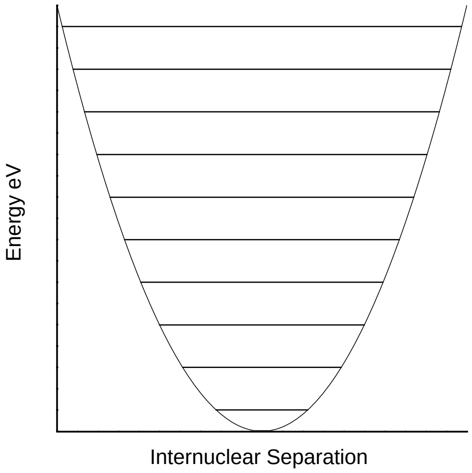

Figure 3.3 Harmonic potential energy curve.

From this classical view of a molecule, mechanics predicts that harmonic motion will occur with a frequency of ν.

$$\nu = \frac{1}{2\pi}\sqrt{\frac{k}{\mu}}$$

$$\text{where } \frac{1}{\mu} = \frac{1}{m_x} + \frac{1}{m_y}$$

where μ is the reduced mass and m_x and m_y are the masses of the two atoms.

The problem with the use of a classical view of a molecule is that according to classical mechanics, a harmonic oscillator may vibrate with any amplitude, which means that it can posses any amount of energy, which does not represent a molecule very well. Quantum mechanics, however, shows that molecules can only exist in definite energy states. In the case of harmonic potentials, these states are equidistant and are given by

$$E = \left(n_i + \frac{1}{2} \right) h\nu$$

where $n_i = 0,\ 1,\ 2\ldots$. The vibrational quantum number represents the lines on Figure 3.3, and h is Plank's constant. At $n_i = 0$, the potential energy has its lowest value, which is not the energy of the potential minimum. The former exceeds the latter by $\frac{1}{2} h\nu_i$, this is the so-called *zero point energy*. This energy cannot be removed from the molecule even at temperatures approaching absolute zero and represents the energy associated with the ground state and also implies that the atoms are never stationary, even at absolute zero.

The use of harmonic potentials to determine the vibrational spectra of molecules is inaccurate though as the use of selection rules, discussed later, with this theory predicts that:

Selection rule:

$\Delta n = \pm 1$

So,

$n = 0 \rightarrow n = 1$, possible

$\varepsilon_{final} = \left(1\frac{1}{2}\right) nh\nu$

$\varepsilon_{initial} = \frac{1}{2} nh\nu$, therefore $\Delta\varepsilon = nh\nu$

So, from this selection rules it follows that a spectrum would contain a single peak at ν. Unfortunately by looking at actual spectra this does not always occur and so the harmonic solution must not be the full story. In particular the observation of peaks at approximately twice, three times the fundamental, are called overtones. These result from a modification of the $\Delta n = \pm 1$ selection rule to $\Delta n = \pm 1, \pm 2, \pm 3$, and this produces small bands higher in the spectrum.

This is because the bonds in a molecule do not obey Hooke's law exactly. The force needed to compress a bond by definite distance is larger than the force required to stretch this bond. For a real diatomic molecule the potential curve is not a parabola; it rises more steeply than the parabola for $r \langle r_e$, and levels off at the dissociation energy as $r \rightarrow \infty$. This is shown by the anharmonic curve, Figure 3.4. Aside from the clear difference of the inclusion of the possibility of bond dissociation another key difference is also that the anharmonic potential has the distance between the energy levels decreasing as energy increases. The anharmonic potentials may be represented by approximate functions, the most common is known as the Morse function:[2-6]

$$E = D_e \left[1 - \exp^{-\sqrt{\frac{f_e}{2D_e x}}} \right]^2$$

f_e is the force constant near the potential minimum, D_e is the dissociation energy. The latter equation allows the determination of the energy at any point on the anharmonic curve.

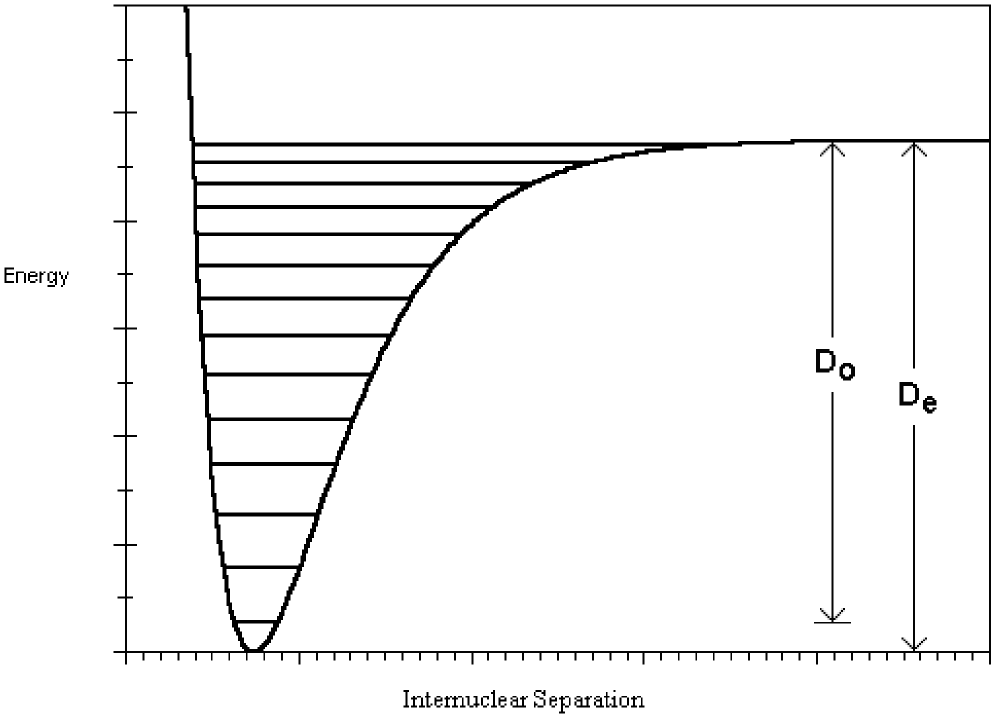

Figure 3.4 Anharmonic potential energy curve.

In real systems we must take account of the anharmonic nature of the oscillations. Such a curve, Figure 3.4, cannot be readily expressed by a formula despite the attempts by Morse's function, and others, the calculation of exact expressions for all the allowed energy levels from such a formula is impossible, in the Morse functional case it cannot express large energies very accurately. It is therefore customary to treat the anharmonic oscillator as a perturbed harmonic oscillator, and to express the perturbed set of permitted energy levels by:

$$G_v = \omega_e\left(n+\frac{1}{2}\right) - \omega_e x_e\left(n+\frac{1}{2}\right)^2 + \omega_e y_e\left(n+\frac{1}{2}\right)^3 ....$$

Only the first two terms are usually retained; ω_e is then the so-called harmonic vibration frequency of the system, and $\omega_e x_e$ the anharmonicity. It should, however, be apparent that neither has any physical significance on its own; together they may be used to generate the set of vibrational energy levels, or the set of observed vibrational transitions between these levels.

3.2.2 Polyatomic Molecules.

For polyatomic molecules the case becomes more complicated as multiple nuclei are now present, each with their own harmonic oscillations. This can be resolved as a superposition of normal vibrations. Each atom has three *degrees of freedom*: it can move independently along each of the axes of a Cartesian coordinate system. If n atoms constitute a molecule, there are $3n$ degrees of motional freedom. Three of these degrees – the translational ones – involve moving all of the atoms simultaneously in the same direction parallel to the axes of a Cartesian coordinate system. Another three degrees of freedom also do not change the distance between the atoms, they describe rotations, e.g. about the principal axes of the inertial ellipsoid of the molecule. The remaining $3n - 6$ degrees are motions which change the distances between the atoms: the length of the chemical bonds and the angles between them. Since these bonds are elastic, periodic motions can occur. All vibrations of an idealized molecule result from superposition of $3n - 6$ non-interacting normal vibrations. These $3n - 6$ degrees of freedom only represents non-linear molecules, $3n - 5$ is used for linear molecules as no rotational freedom exists around the molecular axis.

Figure 3.5 shows the three normal vibrations of the water molecule, the symmetric (a) and the antisymmetric stretching vibration of the OH bonds (b), v_s and v_a, and the deformation vibration δ (c). In a symmetric molecule, the motion of symmetrically equivalent atoms is either symmetric or antisymmetric with respect to the symmetry operations. Since in the case of normal vibrations the centre of gravity and the orientation of the molecular axes remain stationary, equivalent atoms move with the same amplitude.

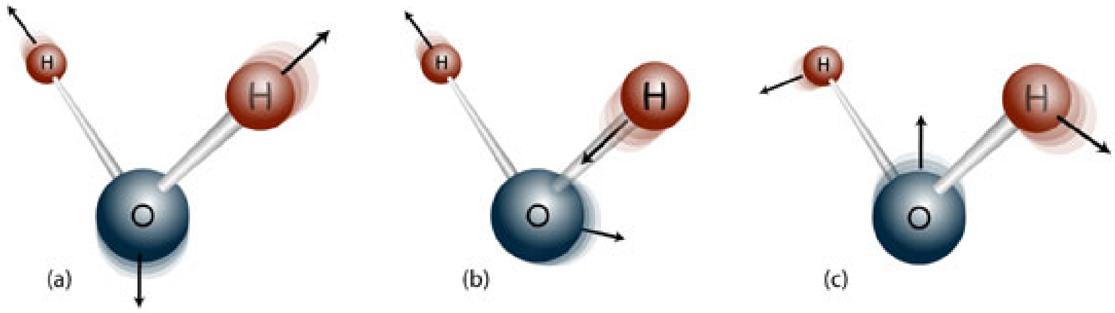

Figure 3.5 Vibrational modes of water.[7]

3.3 Group Theory.

The symmetry of many molecules is often immediately obvious. Benzene has a six-fold symmetry axis and is planar. Fullerene, C_{60}, contains 60 carbons atoms, regularly arranged in six- and five-membered rings with the same symmetry as that of the Platonic bodied pentagon dodecahedron and icosahedron.

To be able to treat symmetry properties of molecules, symmetry operators are defined, which when applied bring a molecule into coincidence with itself. For all molecules there are five types of symmetry operators:

E – the *identity operator*
i – the *inversion operator*
σ – the *reflection operator*
C_n^k - n-fold *rotation operator*
S_n^k - n-fold *rotation-reflection operator*

Below are the names of the symmetry elements introduced by Schoenflies**,** followed by the 'international' notation, introduced by Hermann (1928) and Mauguin (1931)

Notation by:	**Schoenflies**	**Hermann/Mauguin**
Identity	E	1
Centre of symmetry	i	$\overline{1}$
Symmetry plane	σ	m
Proper axis	C_n	2,3,4
Improper axis	S_n	$\overline{2},\overline{3},\overline{4}$

Table 3.1 Table showing the representations used by Hermann/Mauguin[8] and Schoenflies to describe symmetry.

Each molecule has several different symmetry operators and these collectively are known as a point group. The name point group indicates that at least one point, the centre of mass, remains unmoved when symmetry operations are carried out. Point groups are usually characterized by symbols, introduced by Schoenflies in 1891. The first application of group theory to molecular vibrations was by Brester[9] and Wigner.[10]

During all normal vibrations the moving atom deforms a molecule such that the deformed object is either symmetric or antisymmetric with respect to the different symmetry operations belonging to its point group. 'Symmetric' means that the symmetry operator transforms one atom to an equivalent atom which is moving in the same direction. 'Antisymmetric' means that the equivalent atom is moving in the opposite direction.

Objects which have C_n or S_n axes with $n \geq 3$ have 'degenerate' vibrations, i.e. two (or more, for cubic or icosahedral point groups or linear molecules) vibrations have the same frequency. Carrying out a symmetry operation leads to a linear combination of degenerate vibrations.

A symmetry operator causes a symmetry operation. It moves a molecule into a new orientation, equivalent to its original one. Symmetry operations may be represented by algebraic equations. The position of a point (an atom of a molecule) in a Cartesian coordinate system is described by the vector *r* with the components *x, y, z*. A symmetry operation produces a new vector *r'* with the components x', y', and z'. The algebraic expression representing a symmetry operation is a matrix.

A general rotation of a Cartesian coordinate system is described by:

$$\begin{bmatrix} C_{xx} & C_{xy} & C_{xz} \\ C_{yx} & C_{yy} & C_{yz} \\ C_{zx} & C_{zy} & C_{zz} \end{bmatrix} \begin{bmatrix} x \\ y \\ z \end{bmatrix} = \begin{bmatrix} x' \\ y' \\ z' \end{bmatrix}$$

Every atom in the molecule has three degrees of freedom, i.e. it can move independently along each of the axes of a Cartesian coordinate system. A molecule with n atoms therefore has $3n$ motional degrees of freedom. In order to classify these symmetry operators of the point group of the molecule have to be applied to them.

Thus if a symmetry operator is applied to a molecule it results in a representation by a group of square matrices, each having the dimension $3n \cdot 3n$. Thus if we consider a simple molecule with 3 atoms, such as H_2O, the matrix produced will be a $9 \cdot 9$ matrix. The following matrix is for the *E* operation.

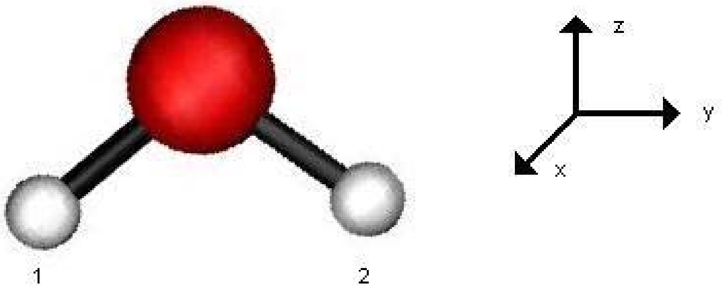

Figure 3.6 Representation of H_2O molecule.

$$\begin{bmatrix} 1 & 0 & 0 & 0 & 0 & 0 & 0 & 0 & 0 \\ 0 & 1 & 0 & 0 & 0 & 0 & 0 & 0 & 0 \\ 0 & 0 & 1 & 0 & 0 & 0 & 0 & 0 & 0 \\ 0 & 0 & 0 & 1 & 0 & 0 & 0 & 0 & 0 \\ 0 & 0 & 0 & 0 & 1 & 0 & 0 & 0 & 0 \\ 0 & 0 & 0 & 0 & 0 & 1 & 0 & 0 & 0 \\ 0 & 0 & 0 & 0 & 0 & 0 & 1 & 0 & 0 \\ 0 & 0 & 0 & 0 & 0 & 0 & 0 & 1 & 0 \\ 0 & 0 & 0 & 0 & 0 & 0 & 0 & 0 & 1 \end{bmatrix} \begin{bmatrix} O_x \\ O_y \\ O_z \\ H_x^1 \\ H_y^1 \\ H_z^1 \\ H_x^2 \\ H_y^2 \\ H_z^2 \end{bmatrix} = \begin{bmatrix} O_x \\ O_y \\ O_z \\ H_x^1 \\ H_y^1 \\ H_z^1 \\ H_x^2 \\ H_y^2 \\ H_z^2 \end{bmatrix}$$

The trace, i.e. the sum of the diagonal elements of the matrix and is symbolised by χ. Equivalent symmetry operators form a class. Symmetry operators of the same class have the same character, since the equivalent representation matrices have the same trace. For most applications of group theory it is sufficient to use the characters of the 'irreducible representations' instead of the original representations. This is because only the integers which lie on its diagonal, i.e. the ones that contribute to the character, are needed.

The sub matrices are also representations, i.e. so-called irreducible representations. The completely reduced representations can be regarded as the direct sum (represented by the symbol ω) of n_i multiples of irreducible representations Γ_i, where n_i is a positive number or zero:

$$\Gamma_{red} = n_1 \Gamma_1 \omega \cdot n_2 \Gamma_2 \omega ....$$

For an n-atomic molecule, the sum of the numbers of normal coordinates n_i equals the number of motional degrees of freedom $3n$:

$$\sum_i n_i = 3n$$

So Γ_{3N} is the shorthand for 'the representation of the point group based on the 3N vectors as basis sets' Γ_{3N} is made up of the rotational, translational and vibrational motions of the molecule. Γ_{3N} can be calculated by applying the symmetry operations to the molecule. This is done by firstly determining the number of vectors that are unshifted, but as this can become very cumbersome it is common practice to simply determine the number of unshifted atoms (N_I) by the symmetry operation multiplied by the contribution per unshifted atom (χ_I), also shown by the sum of characters associated with the x, y, and z component for each symmetry operation. Table 3.2 shows what the results of this would be for a C_{2v} triatomic molecule, such as H_2O.

C_{2v}	E	$C_2\ (z)$	$\sigma_v(xz)$	$\sigma_v(yz)$	Σ	Σ/h
N_I	3	1	3	1	(4)	
χ_I	+3	-1	+1	+1		
Γ_{3N}	+9	-1	+1	+3		
A_1	+1	+1	+1	+1	12	3
A_2	+1	+1	-1	-1	4	1
B_1	+1	-1	+1	-1	8	2
B_2	+1	-1	-1	+1	12	3

Table 3.2 Determination of Γ_{3N} for C_{2v}.

Then by either application of the reduction formula:

$$n_i = \frac{1}{h}\sum_c g'_c \chi_i \chi_r$$

where n_i is the number of times the irreducible representation i occurs in the reducible representation, h is the order of the group (total number of symmetry operations), g'_c is the number of symmetry operations in the symmetry class, χ_i is the character of the irreducible representation, the number in the character table, and χ_r is the character of the reducible representation, the value of Γ for the symmetry representation.

Or by eye, Γ_{3N} can be determined:

$$\Gamma_{3N} = 3A_1 + A_2 + 2B_1 + 3B_2$$

Then since

$$\Gamma_{3N} = \Gamma_{rot} + \Gamma_{trans} + \Gamma_{vib}$$

Γ_{vib} can be determined since Γ_{rot} and Γ_{trans} are simply obtained from the character table. Γ_{rot} irreducible representation is indicated by whichever row(s) in the character table contain either R_x, R_y, and R_z, while the Γ_{trans} irreducible representation is indicated by whichever contains x, y and z. For H_2O, which is C_{2v}, the character table is shown in Table 3.3.

C_{2v}	**E**	**C_2 (z)**	**$\sigma_v(xz)$**	**$\sigma_v(yz)$**	**Linear functions, rotations**	**Quadratic functions**	**Cubic functions**
A_1	+1	+1	+1	+1	z	x^2, y^2, z^2	z^3, x^2z, y^2z
A_2	+1	+1	-1	-1	R_z	xy	xyz
B_1	+1	-1	+1	-1	x, R_y	xz	xz^2, x^3, xy^2
B_2	+1	-1	-1	+1	y, R_x	yz	yz^2, y^3, x^2y

Table 3.3 Character table for C_{2v}.

So,

$$\Gamma_{rot} = A_2 + B_1 + B_2$$

$$\Gamma_{trans} = A_1 + B_1 + B_2$$

So by elimination

$$\Gamma_{vib} = 2A_1 + B_2$$

Γ_{vib} can then be separated into stretching and deformation representations

$$\Gamma_{vib} = \Gamma_{str} + \Gamma_{def}$$

Γ_{str} is easily determined in a similar way to Γ_{3N} above, by determining the number of unshifted stretching modes during the symmetry operations then again by using either the reduction formula or by eye, for the C_{2v} molecule this works out as

C_{2v}	E	C_2 (z)	$\sigma_v(xz)$	$\sigma_v(yz)$	Σ	Σ/h
Γ_{str}	2	0	0	2	(4)	
A_1	+1	+1	+1	+1	4	1
A_2	+1	+1	-1	-1	0	0
B_1	+1	-1	+1	-1	0	0
B_2	+1	-1	-1	+1	4	1

Table 3.4 Table showing Γ_{str} for C_{2v}.

Thus, $\Gamma_{str} = A_1 + B_2$.

It is therefore easy to determine Γ_{def} by subtraction which works out to be:

$\Gamma_{def} = A_1$.

Γ_{str} and Γ_{def} can be used to determine how many IR and Raman bands will be present in the spectra of the molecule. By looking at the C_{2v} character table there would be 3 Raman and 3 IR bands in the spectrum as both A_1 and B_2 are Raman and IR active (see below).

3.4 Selection Rules.

To determine the activity of the vibrations in the IR and Raman spectra, the selection rules must be applied to each normal vibration. From a quantum mechanical point of view, a vibration is active in the IR spectrum if the dipole moment of the molecule is changed during the vibration, and is active in the Raman spectrum if the polarisability of the molecule is changed during the vibration.

The reason for these selection rules relates to the interaction between the electromagnetic radiation and the molecule. Chemical bonds involve electrostatic attraction between positively charged atomic nuclei and negatively charged electrons. The displacement of atoms during molecular vibrations can lead to distortions in the distribution of this electric charge and these distortions can be resolved as a dipole change(s), also possible are a quadrupole, octapole contributions etc. An oscillating molecular dipole interacts directly with the oscillating electric vector of the electromagnetic radiation of the same frequency. This leads to a resonant absorption of radiation. The resonant absorption introduces enough energy to raise the oscillator from level *n* to level (*n* + 1) if the quantum energy of the radiation, expressed as *hv*, is equal to the energy of the oscillator, expressed as *hv*, if $v \equiv \omega$. This is the vibrational selection rule. It is because of this increase from a *n* level to a (*n* + 1) level that electric dipole interactions are responsible for the absorption of radiation in the IR region of the spectrum and hence the spectrum can be obtained.

As the selection rules have already shown not all molecular vibrations lead to oscillating dipoles and thus consideration of the symmetry of the molecule, group theory, is used as a guide to determine whether a molecular vibration is IR active or not.

The selection rule for IR spectra can be expressed as in integral by quantum mechanics:

$$[\mu]_{\upsilon''\upsilon'} = \int \psi_{\upsilon''}(Q_a)\mu\psi_{\upsilon'}(Q_a)dQ_a$$

Here μ is the dipole moment in the electronic ground state, ψ is the vibrational eigenfunction, and υ'' and υ' are the vibrational quantum numbers before and after the transition, respectively, and Q_a is the normal coordinate. The above integral can be resolved into three identical ones for each direction x, y and z. If one of these integrals is non zero the normal vibration associated with Q_a is IR active, but this only occurs if the triple product contains the totally symmetric representation.

As stated earlier, for a normal vibration to be Raman active there must be a change in the polarisability of the molecule during the vibration. By inspection of point group character tables this can be determined by binary combinations of x, y and z such as xy or xz. The selection rule can also be expressed quantum mechanically by the following integral:

$$[\alpha]_{\upsilon'\upsilon''} = \int \psi_{\upsilon'}(Q_a)\alpha\psi_{\upsilon''}(Q_n)dQ_a$$

Polarisability consists of nine components with six unique ones, α_{xx}, α_{yy}, α_{zz}, α_{xy}, α_{yz}, α_{xz}. The integral can therefore be resolved into six, one for each of the components. If one of these integrals is evaluated to be non zero the vibration is Raman active and contains the totally symmetric representation. It should be pointed out that the fact that a vibrational mode is shown to be active in either the Raman or IR does not mean a band will be observed in the spectrum. This is because this treatment does not give any indication of the intensity of the band. A band could in theory be predicted to be IR active or Raman active but is not seen because the band is weak.

Not all a molecule's vibrations have to be IR active. Likewise the same holds true for Raman activity. However, a molecule's vibrational modes are commonly either one or other and often they can be both Raman and IR active. This means Raman and IR spectroscopy are complementary, often only by the use of both techniques can a molecule's vibrational modes be fully characterised.

Another important rule is the mutual exclusion principle which states that, for a molecule with a centre of inversion, the fundamentals which are active in the Raman spectrum are inactive in the IR spectrum and vice versa, i.e. the two spectra are mutually exclusive. There are some vibrations which are forbidden in both spectra such as the torsional vibration of ethylene, as it contains neither a translation, *x*, *y*, or *z* Cartesian vector, nor a component of polarisability.

3.5 SOTONVIB.

3.5.1 Wilson's GF Method.

Within this work the SOTONVIB[11] program has been used extensively to help determine the structure of molecules based upon their isotope splitting patterns and so a brief explanation of the concepts behind the program is given here,

The SOTONVIB[11] program uses the Wilson GF method to determine the bond angles and splitting patterns of selected molecules. The Wilson GF method uses the kinetic (G) and potential (F) energies of a system to calculate various properties of a vibrating molecule. The kinetic energy of a vibrating system is related to the motion of the atoms within the molecule whilst the potential energy of a system is related to the interactions between atoms within the molecule which is described in terms of force constants.

An XY_2 molecule will be presented here as an example. If changes in the internal co-ordinates (r^1 and r^2 represent the two bond lengths, while θ represents the bond angle) of a molecule are represented by a column matrix R and its transpose $\widetilde{R}$

$$R = \begin{bmatrix} \Delta r^1 \\ \Delta r^2 \\ \Delta\theta \end{bmatrix} \qquad\qquad \widetilde{R} = \left[\Delta r^1 \Delta r^2 \Delta\theta\right]$$

the potential energy, V, can be written as:

$$2V = \widetilde{R}FR$$

where F is a matrix composed of force constants. This matrix contains information on the force constants of each of the vibrational stretching modes and the forces constants:

$$F = \begin{bmatrix} f_{11} & f_{12} & r_1 f_{13} \\ f_{21} & f_{22} & r_2 f_{23} \\ r_1 f_{31} & r_2 f_{32} & r_1 r_2 f_{33} \end{bmatrix} \equiv \begin{bmatrix} F_{11} & F_{12} & F_{13} \\ F_{21} & F_{22} & F_{23} \\ F_{31} & F_{32} & F_{33} \end{bmatrix}$$

where r_1 and r_2 are the equilibrium lengths of the X-Y_1 and X-Y_2 bonds, respectively, with f_{11} and f_{22} being the stretching force constant of the Y_1-X and X-Y_2 respectively, f_{33} is the bending force constant. The other symbols represent interaction force constants between the stretching and stretching, or between the stretching and bending vibrations. In order to make the dimensions of all the force constants the same (Nm^{-1}), f_{13} (or f_{31}), f_{23} (or f_{32}) and f_{33} are multiplied by r_1, r_2 and $r_1 r_2$, respectively.

The kinetic energy is not as easy to describe as the potential energy, Wilson showed[12] that it can be written as:

$$2T = \widetilde{\dot{R}} G^{-1} \dot{R}$$

Where $\dot{R}$ is the derivative of R with respect to time and the reduced mass and internal displacement co-ordinates are used to provide the G matrix, of which the reciprocal is taken (G^{-1}).[13]

Wilson showed that the vibrational frequency could then be determined by the use of the secular equation:

$$|GF - E\lambda| = 0$$

where G and F are the kinetic and potential energies, E is the identity matrix and λ is related to the wavenumber $\tilde{\nu}$ by the following relationship:

$$\lambda = 4\pi^2 c^2 \tilde{\nu}^2 \text{ and } \tilde{\nu} = 1302.83\sqrt{\lambda}$$

The order of the equation is equal to the number of internal co-ordinates used.

For a diatomic molecule this means that the potential energy of a system can be described simply by k, while the kinetic energy can be described by $1/\mu$. Within this work the calculation were performed by inputting the structure of the molecule with the use of Cartesian coordinates and then using force constants from previous work on similar molecules to produce a starting point, then by adjusting the force constants until a reasonable fit to the experiments work is obtained.

3.5.2 Determination of Bond Angles.

Within this work the main reason for using this program was to resolve IR bands with isotopic data and thus calculate the bond angles of the molecules from this. To show how this was achieved a simple example is again given, the stretching of a bent XY_2 molecule.

For the G element the symmetric stretch, ignoring coupling to the bending mode,

$$G_s = \mu_y + \mu_x(1 + \cos\alpha)$$

And for the asymmetric stretch

$$G_{as} = \mu_y + \mu_x(1 - \cos\alpha)$$

Where α is the full angle, i.e. 180° for a linear molecule. If the molecule is linear $\alpha = 180^o$, and thus $\cos \alpha = -1$ and the equations simplify to:

$$G_s = \mu_y$$

$$G_{as} = \mu_y + 2\mu_x$$

If we consider the F element now we use the following equation

$$v_s = 130.283\sqrt{F_s G_s}$$

$$v_{as} = 130.283\sqrt{F_{as} G_{as}}$$

Where F_{a+as} are the force constants for the stretching modes, usually between 100 and 2000 Nm^{-1}. The equation for the G and F elements can be used in combination with one another to obtain bond angles from isotopic separation:

$$\frac{v}{v^i} = \frac{\frac{1}{2\pi c}\sqrt{FG}}{\frac{1}{2\pi c}\sqrt{F^i G^i}} = \frac{\sqrt{FG}}{\sqrt{F^i G^i}} = \frac{\sqrt{G}}{\sqrt{G^i}}$$

This can be simplified to simply to G matrix elements as it is assumed that the F matrix elements remain constant. This allows the use of isotopic separation for XY_2 and XY_3 molecules to determine bond angles. The use of the following equation allows the direct determination of the bond angle in an XY_2 molecule.

$$cos\alpha = 1 - \left\{\frac{M_X M_X^i\left[M_Y(v_3)^2 - M_Y^i\left(v_3^i\right)^2\right]}{2M_Y M_Y^i\left[M_X^i\left(v_3^i\right)^2 - M_X(v_3)^2\right]}\right\}$$

Where α is the full angle, M_x is the mass of the relevant atom and the ^{i} represents the isotopically substituted atoms. This however, only applies to molecules with the C_{2v} symmetry point group and thus only XY_2, X^iY_2 and XY^i_2 but not XYY^i.

3.6 Electronic Spectroscopy (UV/Vis).

UV/Vis spectroscopy is the study of transitions between electronic states in an atom or molecule. Electronic transitions occur between two states of a molecule or atom, each of which has its own potential curve, Figure 3.4. If the curve has a minimum there will be quantised vibrational levels, and transitions to more than one of these may be observed. In such a case information about the vibrational energy levels may be derived from the electronic spectrum. An absorption spectrum will, for a matrix isolated sample, contain transitions from the vibrational ground state of the lower electronic state to various vibrational levels of the electronic excited state, and this gives information about the upper potential curve, while an emission spectrum will usually occur from the lowest vibrational level of the upper state to various vibrational levels of the lower curve.

Atoms have relatively simple electronic spectra as they only contain electronic degrees of freedom whereas molecules also contain vibrational and rotational degrees of freedom making their electronic spectra more complicated but this also makes them easier to observe. Within this work UV/Vis spectroscopy was used as a method to identify either atoms or small molecules that are IR silent. Selection rules play a large part in electronic spectroscopy and so will now be detailed. The first selection rule is called the orbital/dipole selection rule. This states that 'Transitions are only allowed if the orbital quantum number changes by + 1 or – 1, $\Delta l = \pm 1$. This means that transitions from s to p orbitals or p to d are allowed, but transitions from s to s are forbidden as are s to d, the origin of this is that a photon has angular momentum of 1.

The second selection rule states that transitions are only allowed if the spin of the system remains the same, $\Delta S = 0$. This means that the electromagnetic radiation cannot change the spin of the electrons, and so transitions may only occur between orbitals where no change of spin is required. The final selection rule is called the Laporte selection rule; this states that 'if a molecule possesses a centre of symmetry the only allowed electronic transitions are those between orbitals of differing parity, i.e. $g \leftrightarrow u$, but $g \leftrightarrow g$ and $u \leftrightarrow u$ are forbidden.

These electronic transitions can be classified into five categories:

- Ligand-ligand transitions.
- Metal-metal transitions.
- Metal-to-ligand transitions.
- Ligand-to-metal transitions.
- Intervalence transitions.

Ligand to ligand transitions occur when a ligand with low lying empty orbitals posses characteristic electronic absorption of their own. This usually is applicable to organic ligands which contain a π system. These transitions are affected by the metal centre as the metal often is involved in the low lying orbitals. Metal to metal transitions occur between orbitals which are localised on the metal centre, d-d transitions etc. These transitions can provide detailed information on the electronic structure of the compound but are usually weak due to the selection rules.

Metal to ligand, or ligand to metal, transitions are often called charge transfer bands because they involve transfer of an electron from the metal to the ligand (often called MLCT), or vice versa (LMCT). These types of transitions are important for transition metals and the bands are generally extremely intense, so much so that they can often mask d-d transitions and dominate the spectrum. Intervalence transitions occur in compounds which have more than one transition metal atom in different oxidation states. It is possible for an intervalence charge transfer (IVCT) to occur at an energy that corresponds to the energy barrier for thermal electron transfer. These bands occur in the near infrared and visible spectra and certain IVCT transitions are solvent dependent.

3.7 Effect of the Matrix on Spectroscopy.

As discussed earlier the matrix can affect the number, position, and shape of peaks observed in spectra. Due to some of these effects it becomes necessary to consider how the interaction of a matrix with a trapped species comes to change its spectroscopic properties.[14]

The effect of the matrix on the energy levels, and hence on the observed vibrational and electronic transition energies, of a diatomic molecule, discussed above, may similarly be treated as a perturbation of the harmonic potential by the interaction of the vibrating molecule with the cage that contains it. If the cage is treated as effectively a sphere, of diameter D, then adding the potential energy of the molecule, represented by $b(D-y)^{-n}$, this can express the repulsive force between the cage and the molecule as a function of y of the molecule. The exponent, n, will usually be in the range 6-12, as for other cases involving interatomic repulsion.

The modified potential energy, E', is now given by:

$$E' = \frac{1}{2}kx^2 + b(D-y)^{-n}$$

The third effect of added repulsive potential upon the vibration frequency is best seen by calculating the new effective force constant at the new potential minimum. Just as:

$$\frac{d^2E}{dx^2} = k$$

$$\text{so } \frac{d^2E'}{dx^2} = k + n(n+1)b(D+y)^{-(n+2)}$$

The effective force constant is thus increasing, and the vibration frequency will increase because it is directly proportional to the square root of the force constant. The effect of a repulsive potential on an anharmonic oscillator will, of course, be similar to the effect on a harmonic oscillator. In addition, since the additional repulsive potential makes the total potential energy curve more nearly parabolic we may expect the matrix to reduce the anharmonicity.[14]

Conversely, an attractive potential between the trapped species and the cage will have the effects of

1. increasing the equilibrium bond distance,
2. lowering the potential energy of the minimum,
3. decreasing the vibrational frequency, and
4. increasing the anharmonicity.

Examples of both types of potential have been found, in some cases the effects studied for different matrices. Where electronic transitions are involved it is often found that the effect of the matrix changes, being attractive for one state and repulsive for the other. Such changes can be correlated with the expected changes in equilibrium bond length between the two states.

The situation for polyatomic molecules is, of course, more complex than for diatomics, but it seems reasonable to retain the concepts of repulsive and attractive matrix potentials superimposed on the molecular potential. An increased vibration frequency is then said to be due to a repulsive matrix cage, a decreased frequency to an attractive matrix cage.

It has been found that even for the same molecule in the same matrix some bands in the vibrational spectrum may increase in energy while others decrease in energy. Where opposite shifts are found for different bands of the same molecule it is necessary to suppose that one vibration takes place in the presence of an effective attractive potential due to the matrix, while the other is subject to a repulsive potential. When the two vibrations involve motion in different spatial directions it is easy to visualise how this may arise, but it seems that even two vibrations involving motions in the same direction show opposite shifts. In such cases it may be supposed that the high energy vibration is somehow able to influence the shape and size of the cage so that the effective potential is attractive, whereas the low frequency vibration is subject to the normal repulsive effect of neighbouring matrix atoms. It may be noted that high energy vibrations contribute most to the zero point energy of the system, which is a property of the trapped molecules as such. Any reduction in the high energy vibrational frequency due to an attractive potential contributes directly to a lowering of the zero point energy and therefore a reduction of the total energy of the system even in its ground state.[14]

3.8 Ultraviolet Photolysis of Precursor in the Matrix.

The photolysis of a precursor in a matrix can only be efficiently carried out using radiation that is strongly absorbed by the molecule, and that has sufficient energy to break chemical bonds. In a few cases it may be possible to photolyse a coloured precursor using visible radiation, but in general UV radiation is required.[14]

A UV lamp depends on an electrical discharge through a vapour to excite the UV radiation. The characteristics of the radiation emitted are controlled by the nature of the vapour used and its pressure. Low pressure lamps tend to produce predominantly atomic emission lines, because the vapour is largely behaving as isolated atoms under the high pressure/low temperature conditions. Thus, if the lamp is filled with hydrogen at low pressure the emission is largely the atomic hydrogen line at 121.6 nm, while if it is filled with mercury vapour the emission lines at 154.9 nm and 253.7 nm are excited. High pressure lamps on the other hand give emission spectra consisting of broader bands, which may be continuous or maybe made up of many lines. In either case, the effect is to give a many line spectrum below 160 nm and 500 nm, as well as a true continuum between 160 nm and 500 nm. The high pressure mercury lamp gives broad bands over the range 230 nm to 470 nm.

The window through which the radiation passes between the discharge and the matrix (including the lamp envelope) is of great importance in governing the transmission of various wavelengths. Glass transmits only a little way into the UV and is generally useless for photolysis experiments. NaCl and KBr both transmit radiation down to 200 nm wavelength and make cheap windows for irradiation, but they fog easily in damp conditions and are too weak mechanically to be used for lamp envelopes.

Quartz is preferred for this purpose as it is high strength and its chemical and mechanical stability suits it for use in discharge tubes as well as for windows. The purest samples transmit down to about 160 nm. Below this wavelength only some crystalline fluorides, notably MgF_2 and LiF, form useful windows. LiF excels in this respect, the purest samples transmitting down to 100 nm. Unfortunately, it is subject to fogging and must be re-polished frequently to extremely high standard if it is to transmit efficiently. It is not sufficiently robust to withstand contact with a discharge plasma, and must therefore be used as a window in the end of a tube made of some other material.[14]

3.8.1 Results of Photolysis.

In general, absorption is only probable if the photon energy of the incident light is just sufficient to raise the molecule to some electronically excited state. This shall be called the ground state of the precursor P and the excited state reached after absorption of a single photon E. Such an absorption process corresponds to one of the electronic absorption bands of P; the probability of absorption will depend on the nature of the two states involved.

The excited electronic state E may behave in one or more different ways:

1. It may re-radiate, emitting a photon of the same energy as the incident photon, and returning to the ground state P. This is probably the most likely result in all cases where the transition $E \leftrightarrow P$ is allowed according to the selection rules for electronic excitation.
2. It may lose energy without radiating, usually by transferring the excess to the matrix. Such energy must be conducted away through the matrix to the

cooling system. Energy is usually accepted by the matrix in the form of 'lattice vibrations', low energy processes (of the order of 100 cm^{-1}) compared with electronic excitation (energies of the order of 50,000 cm^{-1} or more). The transfer is then by no means easy, and considerable local heating may occur before the energy is effectively dissipated.

3. It may radiate a photon of lower energy than the incident photon, so that the molecule ends up in a lower, but still excited state, L.
4. It may rearrange, giving a new molecule I (an isomer of P) of different total energy from the initial precursor. Even if the isomer I has a higher energy than P it is most likely that some excess energy will have to be removed. This may occur by radiation or by transfer to the matrix. The latter process is the more likely, and the resultant local heating will usually allow the matrix to 'accommodate' to the changed shape of the molecule.
5. It may dissociate, usually into two fragments, but occasionally into more. This may appear to be the desired end result, but two factors must be considered: (i) the fragments are essentially in contact, being trapped in the site once occupied by the precursor; and (ii) one or both fragments are almost certainly excited, that is to have a considerable amount of excess energy required to dissociate the precursor.

The net result, then, is the formation of two more-or-less reactive species in close proximity with considerable excess energy. They will almost inevitably react together, reversing the dissociation, to give the initial excited state E, a lower excited state L, or an isomer I. If it is possible for energy to be removed rapidly from the system by radiation or transfer to the matrix the ground state precursor P may also be formed. Only if these processes can be prevented can an appreciable number of fragments be stabilised. The various processes postulated here are set out in Figure 3.7.[14]

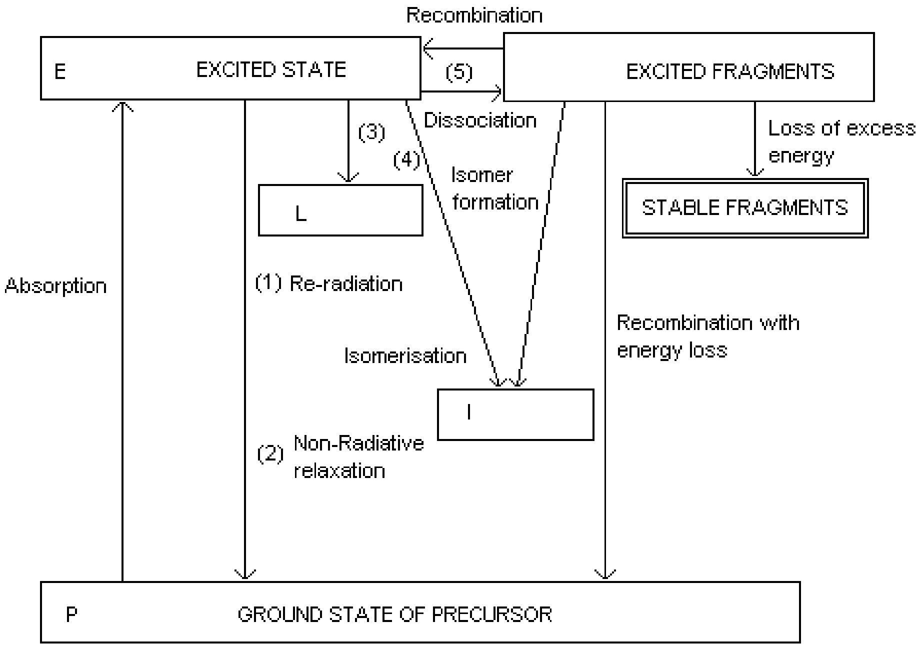

Figure 3.7 Showing the possible effects of photolysis and the routes of the possible effects.[14]

3.8.2 The Effects of Continued Photolysis.

New species can be produced from the precursor P if either process (4) or process (5) is a reasonably probable one, and if the products are not reconverted spontaneously to the precursor. Processes (1) and (3) lead back directly to the precursor, which is then available for a further excitation, while process (2) is essentially equivalent to the result of photolysis with a lower energy photon and may have results similar to (1), (3), (4) or (5). Prolonged irradiation should apparently result in complete conversion of the precursor to products, even if most individual precursor molecules have to be excited many times before forming the desired product.

Several factors prevent this ideal situation from being attained. Firstly, the desired fragmentation may be but one of several possible modes of decomposition of the excited state E, so that by-products are formed in some definite proportion of cases. It may be possible to influence this proportion by changing the energy of the excited photon. Often one may only be able to achieve the conversion of a few per cent of the precursor to the desired product because of competing reactions leading to by-products.

The second factor that must be considered is the possibility of absorption of the excited radiation by the desired product leading to its decomposition. If both the precursor and the product absorb the incident radiation, the rate of increase of concentration of product depends on the difference between the rates of production and decomposition. If the probability of decomposition equals or exceeds the probability of formation, no build-up of concentration can occur. In any case, only a proportion of the precursor can be converted to the desired product; in some circumstances a 'steady-state' concentration can be built up that will remain constant while the rate of decomposition equals the rate of formation of product. It is sometimes possible to find a wavelength of light absorbed by the precursor and not the product, which avoids the difficulty.

Further photolysis of an initial product can be turned to good account if the second product is also a species of interest. An example occurs in the photolysis of methyl azide; photolysis of the initially observed product, CH_2=NH, leads to loss of hydrogen and formation of HNC, an isomer of hydrogen cyanide.[15] In some cases the second step is achieved after prolonged irradiation at the original photon energy whereas in other cases irradiation at a different wavelength is required for the second step. Occasionally the effect of the second irradiation is to reverse the effect of the initial decomposition, or to transform an unstable isomer into the more stable form.[14]

3.9 X-ray Absorption Spectroscopy.

When X-rays pass through matter the transmitted intensity, I, is proportional to the incident intensity, I_o, and the exponent of the thickness of the material, X, and the total absorption coefficient, μ.

$$I = I_0 e^{-\mu X}$$

The total absorption coefficient is the sum of a true absorption coefficient, which relates to the photoelectric effect when a core electron is ejected and carries with it excess kinetic energy. Scattering process can occur when the electrons of the material interact with the X-ray photons. The majority of this scattering is Rayleigh scattering and so no energy loss is observed. This elastic process leaves the so-called coherently scattered radiation with the same wavelength and phase as the incident beam. But this Rayleigh scattering can produce interference effects when scattering occurs from various atoms combines. This gives rise to Bragg diffraction for highly crystalline materials, X-ray diffraction.

True absorption processes are different from these processes and generally have a higher cross-section than scattering processes, usually by orders of magnitude. In the absorption process of photo ionisation where a photoelectron is ejected from a core level, the absorption coefficient increases dramatically. This occurs at a specific energy called the binding energy and it is specific to the atom that is present and is referred to as the absorption edge, Figure 3.8.

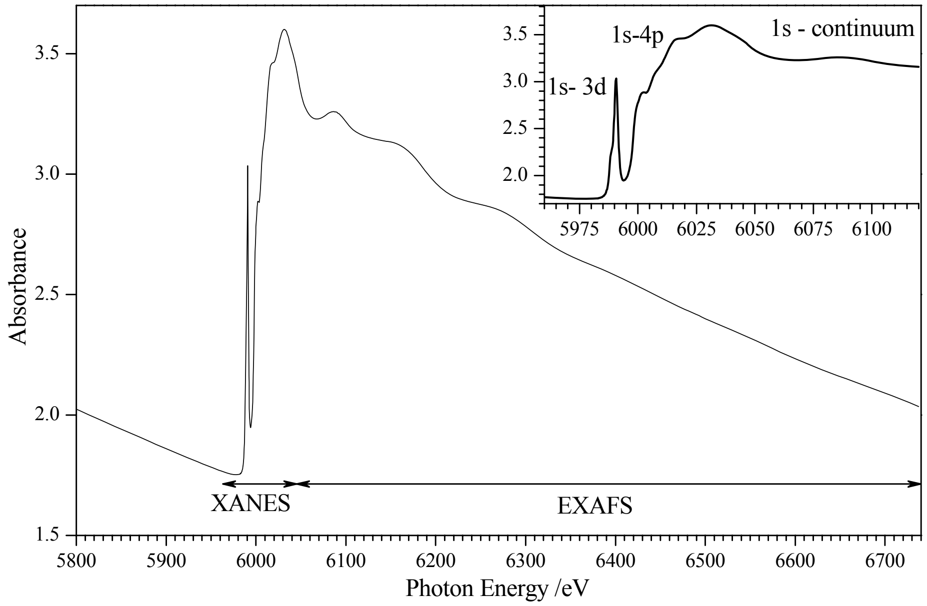

Figure 3.8 Cr K-edge XANES spectrum of CrO_2Cl_2 at 10 K.

From Figure 3.8 it can be seen that as the energy of the photon is increased the absorption coefficient, μ, gradually decreases due to the increased penetration of the X-rays at higher energy. Then there is a rapid increase at the absorption edge, there is also sometimes transitions in the pre-edge. In the absorption edge the X-ray photon is absorbed by the atom, which then results in photo-ionisation. As the photo electron is far lighter than the atom it is assumed that the electron carries away all of the excess kinetic energy.

Features in the pre-edge can often include transitions from the 1s shell to bound states such as the 3d and 4p shells for K-edges. These transitions can be useful in determining the electronic configuration and the geometry of the system studied. The precise position of the edge can also provide information on the oxidation state of these absorbing atoms. The strong oscillations directly after the edge are less well understood, they arise from many-body interactions and multiple scattering effects. The study of the area in the spectrum up to these oscillations is called X-ray Absorption Near Edge Spectroscopy (XANES). Oscillations are also produced after the absorption edge, that are well understood and they are studied within a technique called EXAFS.

3.9.1 EXAFS.

EXAFS is concerned with the path of the electron which is ejected by the absorption of X-rays by an atom. This ejected electron takes the form of a photoelectron wave that originates and propagates from the absorbing atom in a spherical fashion. This outgoing wave is back scattered by surrounding atoms causing constructive and destructive interference patterns as the photon energy is increased. This interference pattern, known as EXAFS oscillations, gives a great deal of information about the surrounding environment. This interference pattern means that EXAFS can provide very accurate structural information about atoms and the environment they are in. Distances between the absorber and back scattering atoms can be deduced as well and the types and number of back scattering atoms present.

EXAFS is a quantitative technique and is useful in conjunction with matrix isolation as the long range order is not necessary to determine parameters, meaning that the dilute matrix isolation samples can be analysed using EXAFS. In order to perform this analysis it is usually necessary to use synchrotron radiation as this provides a greater beam intensity than that which could be achieved within a laboratory. EXAFS studies for elements larger than calcium is straight forward. However for the lighter elements analysis requires special equipment. This is because for the lighter elements soft X-rays are used and so special vacuum chambers are required to remove absorptions by air. A major advantage to EXAFS is that in a MX_2 molecule the edge for the metal can be observed showing the position of X atoms, then the edge for X can be analysed showing the position of the metal. This analysis of multiple edges allows for greater accuracy in the structural information, and also presents ways of obtaining the bond angles.

3.9.1.1 Data Analysis.

Data analysis will be discussed in more detail later; the basis behind this analysis will be detailed here. Once various computer programs, PAXAS and Exspline, have been used to manipulate the data structural information can be extracted by fitting the theoretical and experimentally observed EXAFS spectra using the curve fitting program called EXCURV98.[16] The theoretical model can be produced by setting the types of atoms present and adjusting and refining the variables of atom distance (R) and coordination number (N). Direct comparison between the pure EXAFS oscillations and monitoring the values of the thermal and static disorder (A) and the ‘goodness of fit’ (R) shows the most likely structure of the molecule present. A Fourier Transform of the EXAFS curve then provides a distance for the interaction. The EXAFS equation[17, 18] used in this program is extremely complicated but a simplified version developed by Stern *et al.*[19] using the plane wave approximation is given below.

$$\chi(k) = -S_0^2 \sum_S \left[\left(\frac{N_S}{kR_{as}^2} \right) . \left| F_S(\pi, k) \right| . e^{(-2k^2\sigma^2 as)} . e^{\left(-\frac{2R_{as}}{\lambda(k)} \right)} . sin(2kR_{as} + 2\delta_a + \alpha_s) \right]$$

Terms:

N_s - Number of equivalent scatterers (i.e. the same atom types at the same distance).

k - photo-electron wavevector = $\sqrt{\left[\left(2m_e/\hbar^2\right)\left(E-E_0\right)\right]}$ where $\hbar^2 = \frac{h^2}{(2\pi)^2}$

R_{as} - Distance between the absorbing and backscattering atoms.

$2\delta_a$ - Phaseshift experienced by the photoelectron on leaving and re-entering the absorbing atom *a*.

α_s - Phaseshift experienced by the photoelectron when it is backscattered by the scattering atom *s*.

$|F_S(\pi, k)|$- Amplitude and phase of the backscattered photoelectron at given *k*.

$e^{(-2k^2\sigma^2 as)}$- Debye-Waller factor, which models the thermal and static disorder in the system.

$e^{\left(-\frac{2R_{as}}{\lambda(k)}\right)}$- Term reflecting the finite lifetime of the photoelectron, where $\lambda(k)$ is the electron mean free path.

S_0^2 - Shake up and shake off factor, which accounts for the fact that not all the photoelectrons participate in the EXAFS.

This equation gives information about what is there, how many atoms are present and how far apart they are. The section of the equation which gives details on what is present is highlighted in blue in the equation, the red part of the equation gives information on how many are present and the green part gives information on how far apart the various parts are.

References.

1. D. A. Skoog, D. M. West, F. J. Holler and S. R. Crouch, *Fundamentals of Analytical Chemistry*, 7th Edn., Brooks Cole, New York, 1996.
2. K. F. Lim and W. F. Coleman, *J. Chem. Educ.*, 2005, **82**, 1263.
3. J. M. Hollas, *Modern Spectroscopy*, 3rd Edn., Wiley, Chichester, 1996.
4. I. N. Levine, *Physical Chemistry*, 5th Edn., McGraw-Hill, New York, 2002.
5. C. N. Banwell, *Fundamentals of Molecular Spectroscopy*, 3rd Edn., McGraw-Hill, London, 1983.
6. P. F. Bernath, *Spectra of Atoms and Molecules*, Oxford University Press, New York, 1995.
7. R. Thomas, *Plus*, March 2003, 2003.
8. C. Mauguin, *Zeit. Kristallog.*, 1931, **76**, 542.
9. C. J. Brester, PhD Thesis, Utrecht University, 1923.
10. E. Wigner, *Group Theory And its Application To The Quantum Mechanics Of Atomic Spectra*, New York Academic Press New York, 1931.
11. I. R. Beattie, N. Cheetham, M. Gardner and D. E. Rogers, *J. Chem. Soc. A*, 1971, 2240.
12. E. B. Wilson, *J. Chem. Phys.*, 1941, **9**, 76.
13. E. B. Wilson, J. C. Decius and P. C. Cross, *Molecular Vibrations*, McGraw Hill, New York, 1955.
14. S. Cradock and A. J. Hinchcliffe, *Matrix Isolation*, 1st Edn., Cambridge University Press, 1975.
15. D. E. Milligan, *J. Chem. Phys.*, 1961, **35**, 1491.
16. N. Binsted, EXCURV98, A Program for Fitting Theoretical and Experimental EXAFS Curves., CCLRC, Daresbury Laboratory, U.K., 1998.
17. S. J. Gurman, N. Binsted and I. Ross, *J. Phys. C: Solid State Phys.*, 1984, **17**, 143.
18. S. J. Gurman, N. Binsted and I. Ross, *J. Phys. C: Solid State Phys.*, 1986, **19**, 1845.
19. D. E. Sayers, E. A. Stern and F. W. Lytle, *Phys. Rev. Lett.*, 1971, **27**, 1204.

Chapter 4

Experimental

4.1 Matrix Gases.

The requirements for a matrix gas are totally dependent on the system in question. Rare gases have no unpaired electrons so they give no E.S.R. spectrum, though the nuclear magnetic moment of some isotopes of krypton and xenon give rise to splittings in the E.S.R. spectra of some species isolated in these matrices. They are monatomic and have no molecular vibrations to give rise to IR and Raman bands. Their high ionisation potentials mean that the electronic absorption spectrum does not begin until rather high energies (short wavelengths). The first strong absorption corresponds to the first resonance transition $(n+1)s - np$. The wavelengths associated with these transitions are shown in Table 4.1.

Noble Gas	Resonance in nm	Resonance in eV
Ne	80	15.49
Ar	104	11.92
Kr	125	9.92
Xe	160	7.75

Table 4.1 Table showing the first resonance transition of noble gases.[1]

The solid matrix will have weaker absorptions at somewhat lower energy, and these matrix materials will therefore become effectively opaque at rather longer wavelengths than those listed here. The exact ‘cut-off’ point will depend on the sample thickness.

From these short wavelength limits, the rare gas matrices are free from interfering absorption bands throughout the UV, visible and IR regions. No emission will be excited unless the sample is irradiated with light of wavelength shorter than the cut-off point, and no Raman transitions are possible. Only in the far IR region, and the corresponding portion of the Raman spectrum, may there possibly be bands associated with the motions of the crystal lattice (lattice modes). Such modes are not normally observed in matrix isolated studies due to the energy being too low. For all practical purposes, then, the rare gas matrix may be considered free of bands in absorption, emission, Raman and E.S.R. spectra except for the short wavelength (vacuum UV) region.

Gas	Purity	Supplier
Ar	99.995%	Energas
F_2	99%	Prof E. Hope (Univ. of Leicester)
O_2	99.998%	Energas
H_2O	99%	Degassed, demineralised water
~10% F_2/Ar	9.62%	Air Liquid
N_2	99.995%	Energas
Cl_2	99.9%	Energas
Br_2	99.5%	Fisons

Table 4.2 Table showing matrix gases used in this study along with their purity and supplier.

The gases used within this work are displayed in Table 4.2 along with their purity and their supplier. The gases used were of two categories; the inert matrix gases, used in order to isolate the species of interest; and the reactive matrix gases which were used either neat or by dilution to see whether or not they would react with substances of interest to form novel compounds. The reactive matrix gases were diluted into the inert matrix gases using standard manometric techniques on a vacuum line, detailed later.

The gases were used as received from their supplier. The gases were introduced into the matrix isolation chamber by bleeding from a pre-made bulb or were introduced directly from a cylinder. Both methods employed the use of a needle valve to regulate the gas flow rate, which was estimated by the use of the bounce off pressure in the chamber.

4.2 Mass Spectrometry.

A VG SXP 1000 quadropole mass spectrometer was used in order to analyse any products formed with the experimental procedure devised. The same wires and equipment were used as in the IR and UV experiments and heated to their respective sublimation temperatures, as shown in Figure 4.01 and Figure 4.02.

The vapour generated entered into the chamber which was under vacuum generated by an Edwards diffstak 160 diffusion pump backed by an Edwards RV18 rotary vane pump. The vapour was then ionised by electron bombardment and the resulting ions were injected into the mass filter and detected by a wide bore channeltron multiplier. The resulting data was then analysed using the Postsoft package run on a PC.

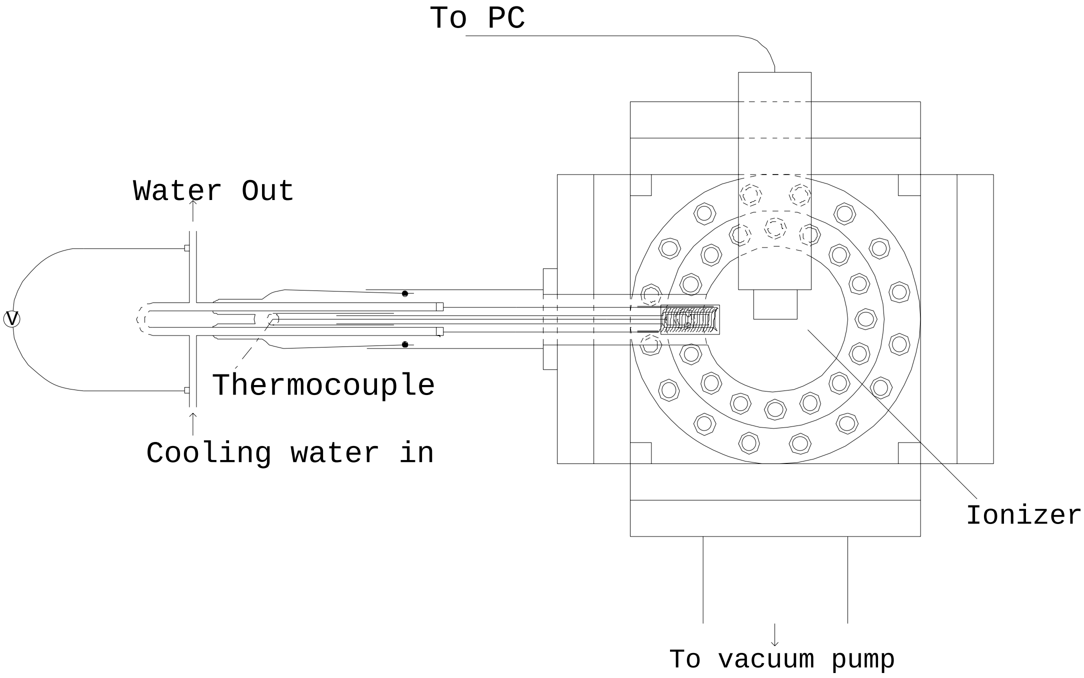

Figure 4.01 Mass spectrometer experimental set-up.

Photolysis was conducted within these experiments with the use of a 200 W LOT-Oriel Hg-Xe lamp with a fitted liquid light guide which is used for delivery. The use of selective photolysis involved either the use of filters or the use of a monochromator, often the full range of the lamp was used for experiments, referred to as broadband photolysis. The light reaches the chamber through the use of an optical cable which is connected to the end of the liquid light guide.

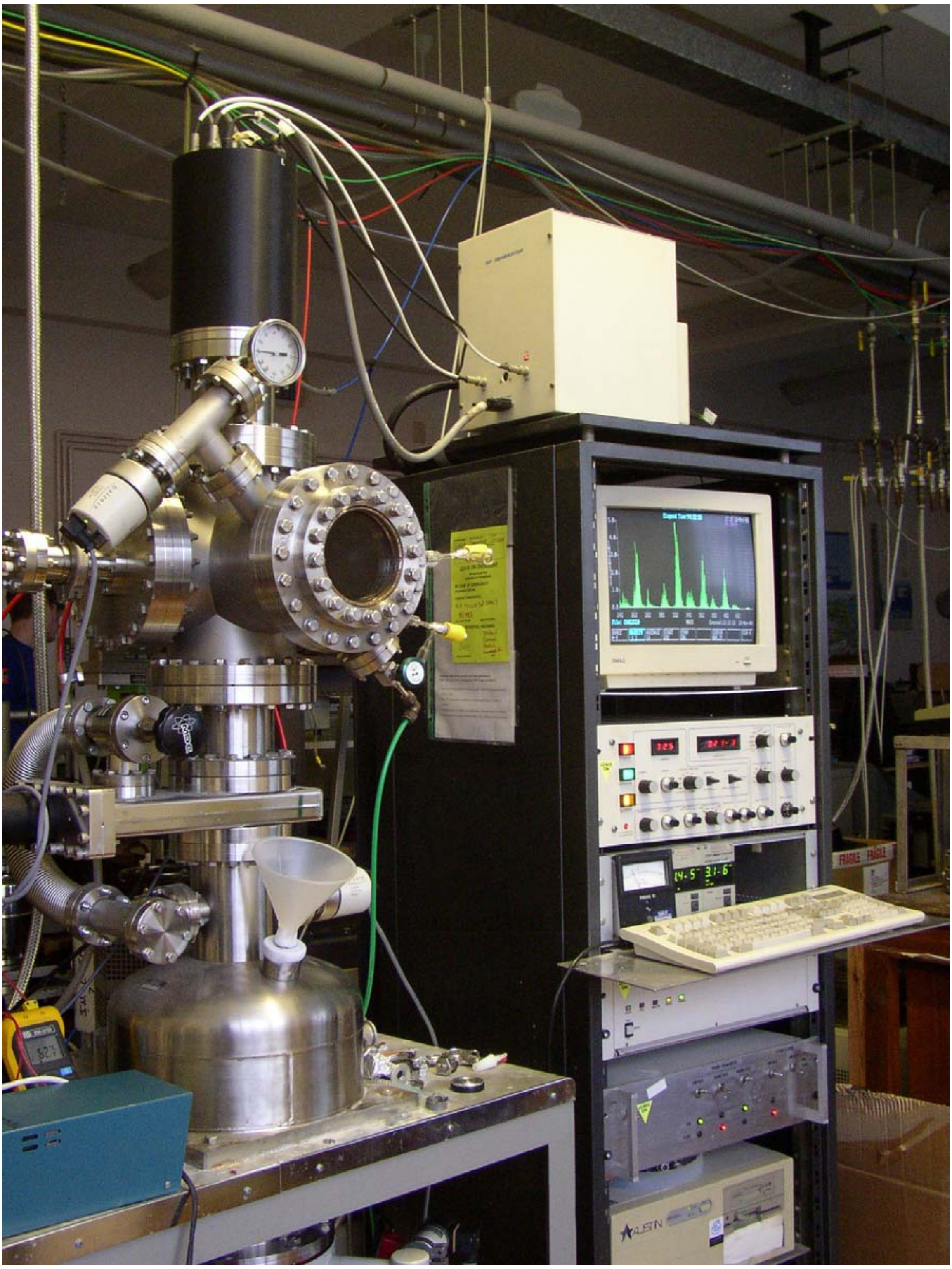

Figure 4.02 Mass Spectrometer connected to controlling computer.

The vapour diffusion pump is the basis of the whole vacuum system and so will be described in some more detail here. The vacuum diffusion pump is basically a stainless steel chamber containing vertically stacked cone shaped jet assemblies, Figure 4.03. Typically there are three jet assemblies of decreasing sizes, with the largest at the bottom. At the base of the chamber is 125 ml of a synthetic oil designed to have a low vapour pressure. The oil is heated to boiling by an electric heater at the bottom of the chamber. The vaporised oil moves upward and is expelled through the holes in the various assemblies. Water circulated through coils on the outside of the chamber cools the chamber to prevent thermal runaway and permit operation over long periods of time.

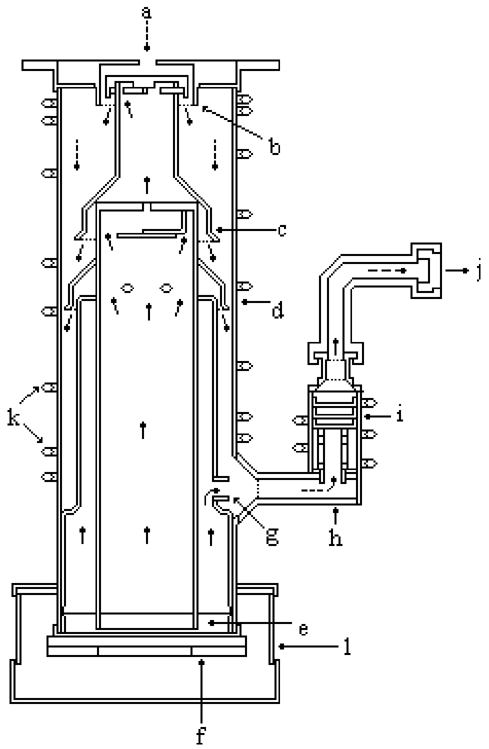

Figure 4.03 Vapour Diffusion Pump. (a) from apparatus, (b) top jet nozzle, (c) centre jet nozzle, (d) lower jet nozzle, (e) pump oil, (f) heating apparatus, (g) side ejector nozzle, (h) backing tube, (i) condenser, (j) to rotary pump, (k) water cooling, (l) radiation shielding.[2]

After exiting the jets, which have fairly large diameters, the high energy oil droplets travel downward in the space between the jet assemblies and the chamber walls at speeds up to 750 mph. The capture efficiency of the vapour jet depends on its density, velocity and molecular weight. The high velocity jet collides with gas molecules that enter it due to their thermal motion. This typically makes the molecules move in a downward motion and transports them towards the pump outlet, creating higher vacuum. At the base of the chamber, the condensed molecules of atmospheric gases are removed by the rotary pump, while the condensed oil begins another cycle.

The effect of removing molecules is to create a high vacuum in the upper portion of the chamber. It is this part of the chamber that communicates with the application where a high vacuum is needed. To prevent thermal runaway, water flows through cooling coils on the outside surface of the chamber. Since the chamber itself has no moving parts aside from the oil droplet, a vacuum diffusion pump can operate with stability over long periods. In all diffusion pumps, a small amount of back streaming occurs. By definition, back streaming is the migration of minute levels of oil that moves in the opposite direction - towards the inlet of the pump and into the process stream. The addition of a liquid nitrogen cryotrap is used to remove oil particles before they can reach the chamber.

4.3 Fourier Transform Infrared (FTIR) Matrix Isolation Spectroscopy.

The basic aim of the matrix isolation experiment is to create and subsequently trap reactive species of interest; this can lead to the need for a complicated array of equipment. The basic set-up used in these experiments is shown below in Figure 4.04; it consists of a vacuum chamber, which incorporates a cryostat, coupled to a pump with the chamber being held *in-situ* within a spectrometer.

In order to achieve the vacuum pressures required for the experiments conducted, in the order of 5×10^{-7} mbar at room temperature, an Edwards E04 vapour diffusion pump fitted with a liquid nitrogen trap was used. This was part of a two stage pumping system backed by an Edwards rotary pump. The rotary pump was used to achieve a vacuum of around

1×10^{-2} mbar before the Edwards vapour pump took over. The vacuum was monitored by multiple Edwards Penning gauges in various positions around the equipment.

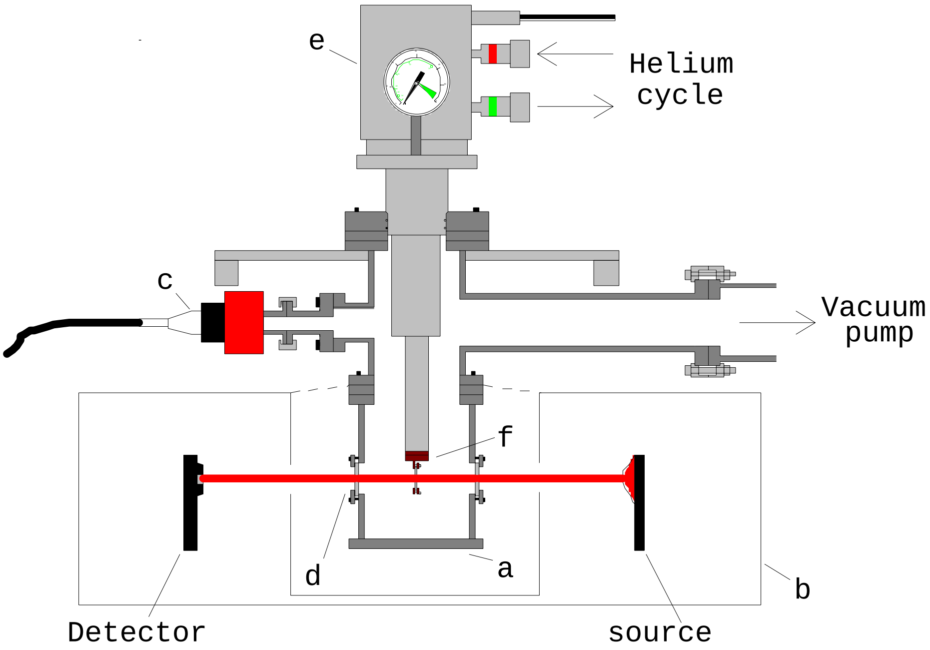

Figure 4.04 Illustrates the vacuum chamber (a), which sits inside the sample compartment of the spectrometer (b). The chamber is kept under high vacuum using a combination of a diffusion pump and a rotary pump, the vacuum is measured at (c). The KBr windows marked (d) allow the infrared radiation to pass into the chamber through the CsI window (f) and out again. The cryostat (e) cools the window to around 12 K.

The cryostat cools the spectroscopic window to around 12 K for experiments; this was achieved by using a cryostat coupled to a APD cryogenic Displex closed cycle helium refrigerator that achieved these temperatures at the window in around one hour. A closed cycle cryostat was used in this system as it can achieve the required temperature quickly and is extremely efficient and cheap to run. These cryostats use the Gifford-McMahon refrigeration cycle and consists of two heat transfer processes, the cooling is achieved through a series of complex actions which utilise Joule expansions to cool the tip of the cryostat, Figure 4.05 gives a diagram of the cryostat.

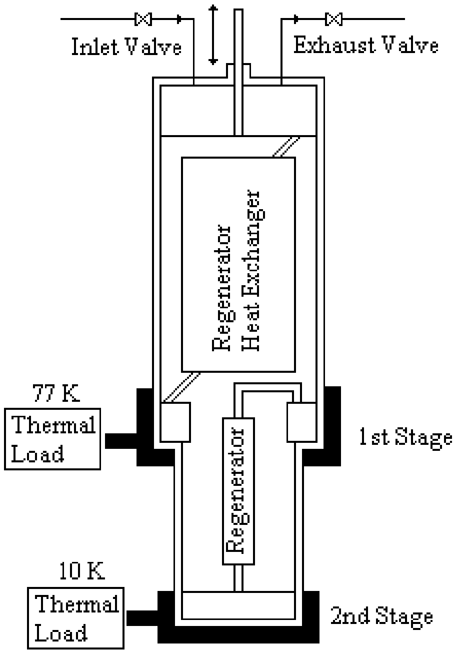

Figure 4.05 Schematic of the internal workings of the expander in a two stage closed cycle helium cryostat.[3]

This temperature was monitored using a thermocouple connected directly to a Scientific Instruments 9650 digital temperature controller. The window is specifically chosen depending on what spectroscopy is being undertaken. Table 4.4 shows the properties of various materials which can be used. The spectrometer has a working rage of 4000 – 400 cm^{-1} for mid – infrared (MIR) work using a KBr beam splitter and a CsI windowed DTGS detector. Far infrared (FIR) work required the use of a Mylar beam splitter and a polyethylene (PE) windowed detector to give a working range of 600 – 150 cm^{-1}, however the CsI deposition window cuts off radiation below 200 cm^{-1}. The CsI window used was mounted directly to the tip of the cryostat, Figure 4.06, a good thermal contact was achieved using an indium gasket with the window itself mounted in copper.

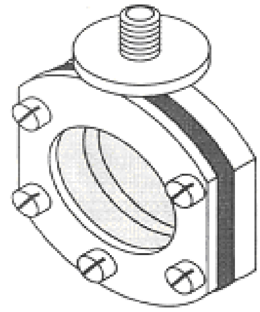

Figure 4.06 Cold window holders a) a brass clamp with a caesium iodide window inside.[4]

The cryostat was mounted to the octagonal shaped chamber using a rotatable seal which allowed the cryostat to be turned through greater than 90°. This was needed as the matrix was formed perpendicular to the path of the IR radiation used for spectra. The main reason this was done was due to the logistical reasons present if the gas entry points were in the limited space between the chamber and the spectrometer. It is much more convenient to have the gas entry points coming out of the front of the spectrometer where a much larger amount of space is available. Matrix gases were bled into the chamber by either 1/8 copper tubing or steel tubing, the flow rate was controlled with needle valves. The tubing was directly connected to the chamber with a vacuum seal achieved using viton ‘O’ rings. Figure 4.07 shows a typical experimental set up used. Photolysis was achieved on the deposition window by having a CaF_2 or silica window on the chamber through which UV light could be passed from an external UV source.

Material	**Useful transmission, cm^{-1}**	**Recommended application**
NaCl	40 000 – 625	
KCl	33 000 – 500	
KBr	43 000 – 400	External windows and economy cold window for IR and UV-visible
CsBr	40 000 – 300	Cold window for IR and UV-visible and external windows for extended IR range
CsI	40 000 – 200	Cold window for IR and UV-visible and external windows for extended IR range
LiF	83 000 – 1450	Vacuum UV
MgF_2	91 000 – 850	Vacuum UV
CaF_2	77 000 – 850	Cold window for UV-visible
BaF_2	66 000 – 800	
UV fused silica	59 000 – 4000	External windows for UV-visible
IR fused silica	43 000 – 2900	
Sapphire	33 000 – 1700	Cold window for UV-visible
Polyethylene	625 – 5	External windows for far IR. A silicon cold window is needed for FIR transmission

Table 4.4 Possible cold window substrates and their transmissions.

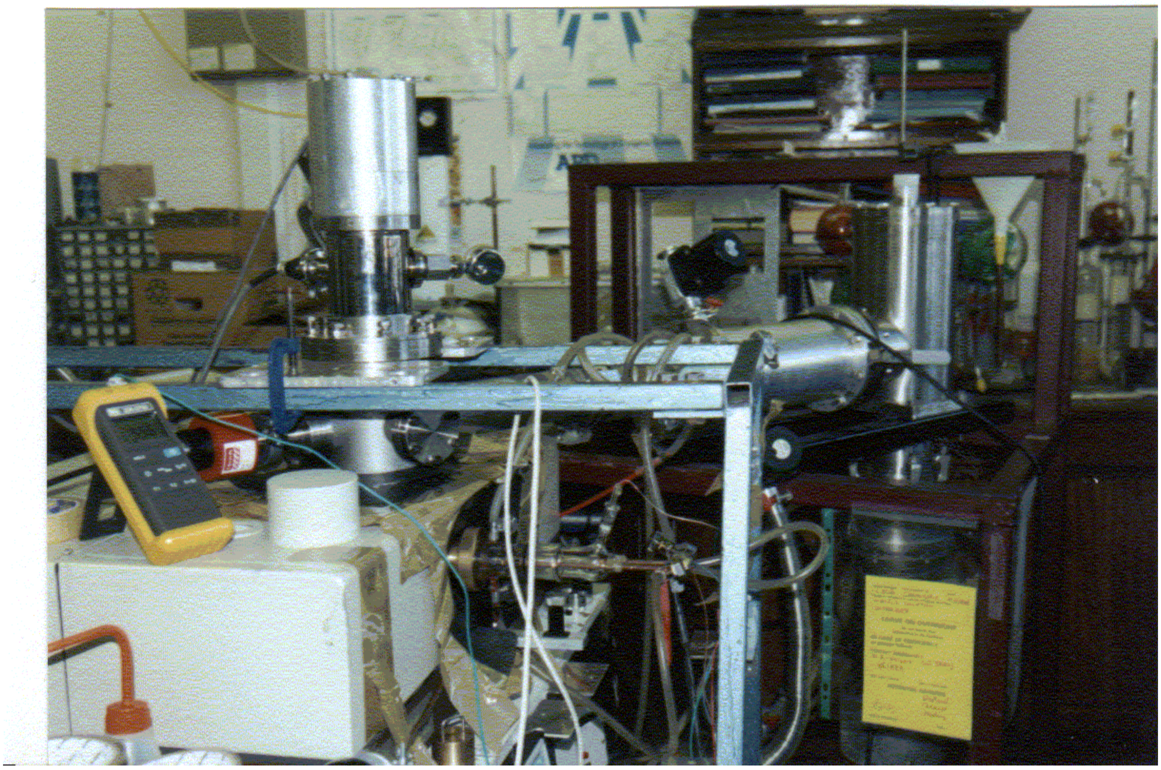

Figure 4.07 Matrix isolation IR spectroscopy equipment in situ.

The spectrometer used for FTIR spectra was a Bruker Equinox 55, this was connected to a PC which used Bruker Opus 3.0 software. Transmission spectra were recorded in the range 400-4000 cm^{-1} for the MIR using a KBr beam-splitter and a CsI windowed detector. The spectra were recorded with a resolution of 0.5 - 2 cm^{-1}. The majority of spectra were recorded with a 2 cm^{-1} resolution due to the time needed for more detailed spectra, but on occasion a 0.5 cm^{-1} resolution spectrum was taken so that the isotope patterns could be investigated.

The typical FTIR experiment consisted of the following procedure. Before the cryostat was turned on the equipment was degassed and the gas lines cleared. This involved heating the metal wires or samples close to their usage level to remove any traces of water and other containments. This also removes CO_2 which is often the largest unwanted compound present in the matrices. During this process the deposition window was turned away so that no contamination could occur. For a brief period the material was brought above its operating range to make sure all possible contaminants were removed. Next the chamber would be allowed to pump down to a typical pressure of around 1×10^{-7} mbar and cooling would begin. Upon cooling the typical temperature of 12 K would be achieved, monitored by the use of a silicon diode thermocouple connected to a Scientific Instruments 9650 (SI9650) digital temperature controller. Once this temperature was reached a background spectra would be taken, around 500 scans was usually used, and then deposition could begin. Deposition would usually proceed at a rate of 3-5 mmol hour^{-1} for the matrix gas, with the spectra monitored periodically. Once the desired matrix had been formed, usually after around 2 hours, photolysis and annealing could be applied depending on the needs of the specific experiment.

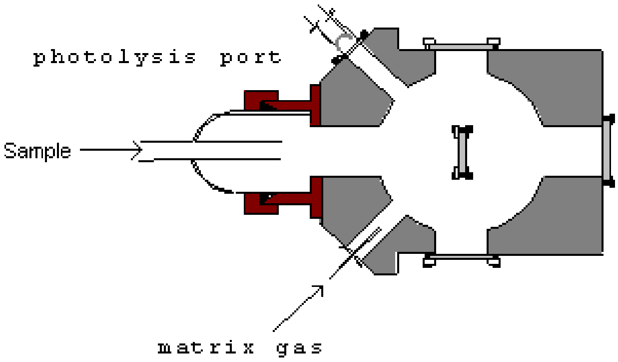

Figure 4.08 Showing a plan view of the sample chamber.

4.4 Matrix Isolation UV/Vis Spectroscopy.

The experimental procedure used for matrix isolation UV/Vis spectroscopy was not very different to that used for the FTIR spectroscopy. The equipment used was very similar with a few slight changes; the spectrometer used was a Cary 5E UV – Vis – NIR spectrometer with a range of 57,000 – 3,300 cm^{-1}. CaF_2 windows were used on the chamber and also for the cold deposition surface, as this material is transparent in the spectral range. The software used for data collection was Varian Cary 5 software package. The pumping system on this set up was also slightly different, through what was available; a Edwards Diffstak 100 vapour pump fitted with a liquid nitrogen trap was used. This was part of a two stage pumping system backed by an Edwards rotary pump. The rotary pump was used to achieve a vacuum of around 1×10^{-2} mbar before the Edwards vapour pump took over. The vacuum was monitored by multiple Edwards Penning gauge. Figure 4.09 shows the set up that was used.

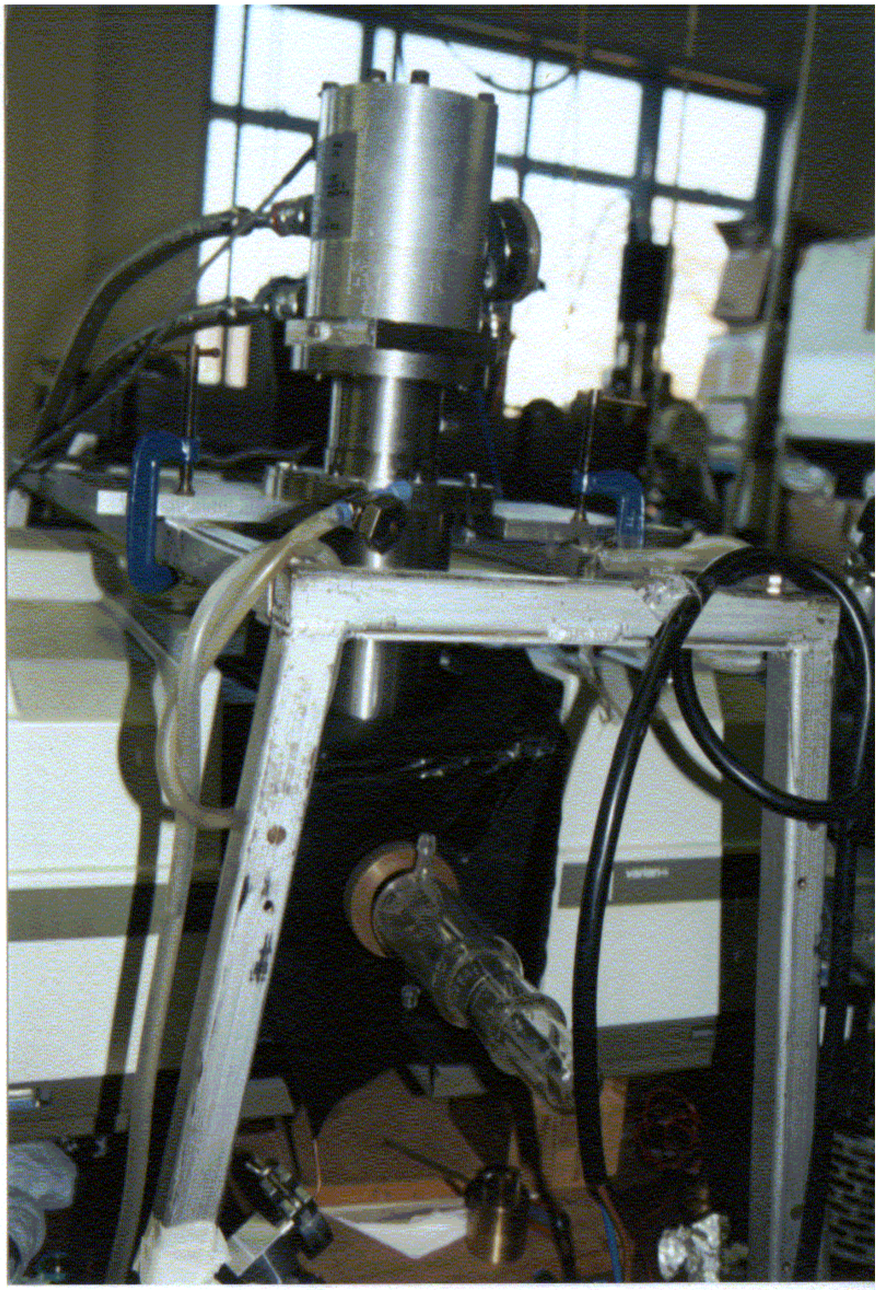

Figure 4.09 Matrix isolation UV spectroscopy equipment in situ, with RF water jacket attached.

As UV/Vis spectroscopy is a much more sensitive technique than IR spectroscopy, much less material is needed to be deposited in order to get a good spectrum. Thus deposition rates were much slower than for the IR experiments. Aside from this difference the experimental procedure is very similar, it should be noted that the spectral measurement time is much longer for UV/Vis as each individual frequency of light is measured separately.

4.5 Matrix Isolation EXAFS.

The matrix isolation EXAFS equipment was designed by N. A. Young[5] for use at the Daresbury laboratories in Cheshire, Figure 4.10 and Figure 4.11. The set-up is designed to monitor both FTIR and EXAFS simultaneously, this therefore allows for the characterisation of species in the matrix environment.

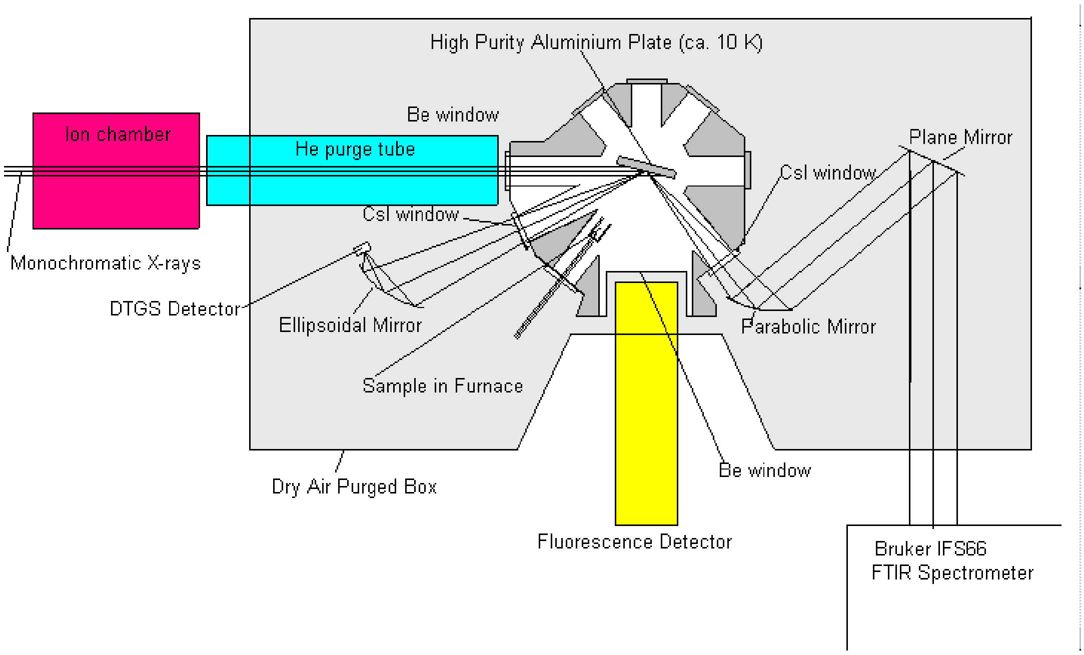

Figure 4.10 Diagram of the matrix isolation EXAFS equipment.[5]

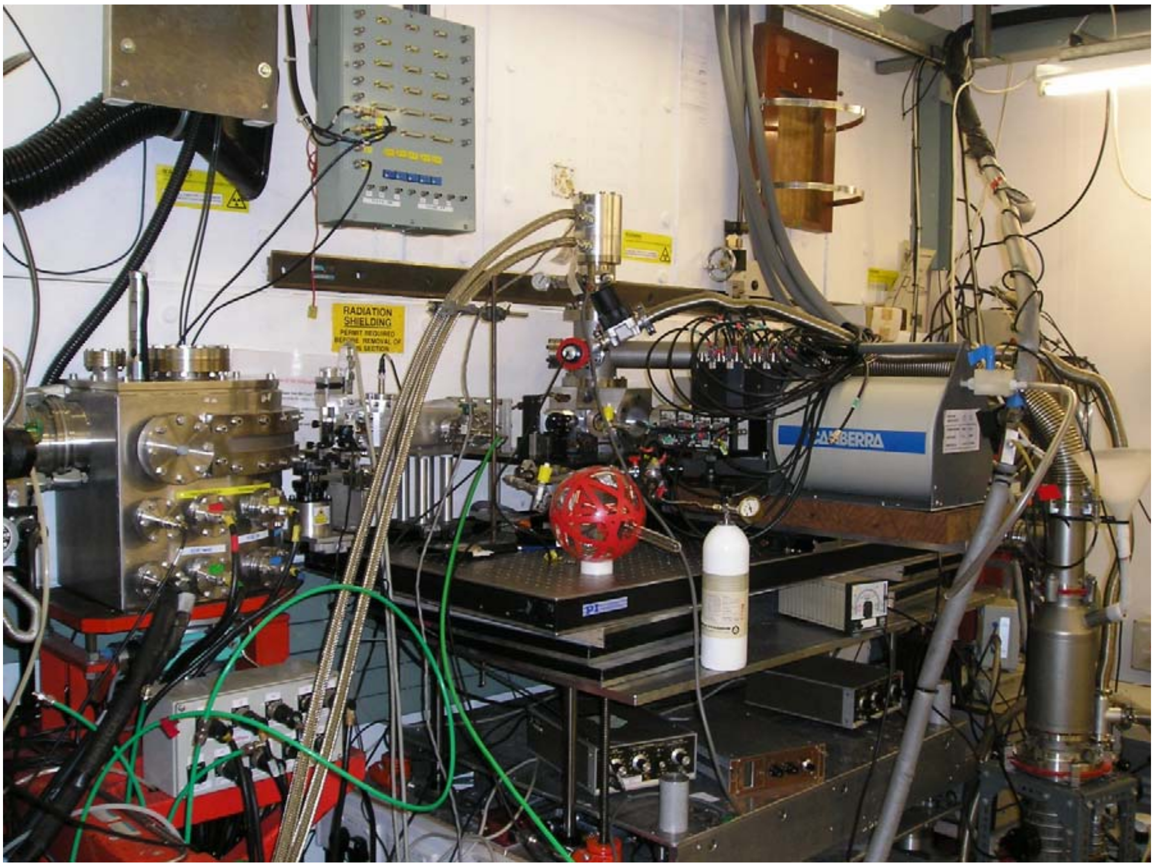

Figure 4.11 EXAFS equipment at station 9.3 Daresbury.

The deposition window in this experimental set up is a high purity aluminium plate which is connected to the cryostat. This means that the IR spectra are taken by means of reflectance from the aluminium plate rather than the usual method of transmission through the CsI window, which can also be used with the equipment but not in these experiments. To achieve the required temperature the same vacuum and cryostat equipment was used as previously described for IR experiments. The heart of the apparatus is a machined aluminium block that contains various ports for the passage of X-rays, IR, deposition equipment, and photolysis equipment. This equipment was used at the Daresbury Laboratory SRS (2 GeV, 100 – 200 mA) on Station 9.3, Figure 4.11. This station is equipped with a silicon (111) double crystal monochromator with harmonic rejection provided by a palladium coated mirror. The data were collected with a monolithic 9 element germanium solid state detector for fluorescence. Single XANES spectra and averages of twenty 20 minute EXAFS scans were used. The data were calibrated using tabulated values of metal foils.[6] All EXAFS data collected and reported within this thesis was collected by myself and N. A. Young, while all data analysis was conducted by N. A. Young.

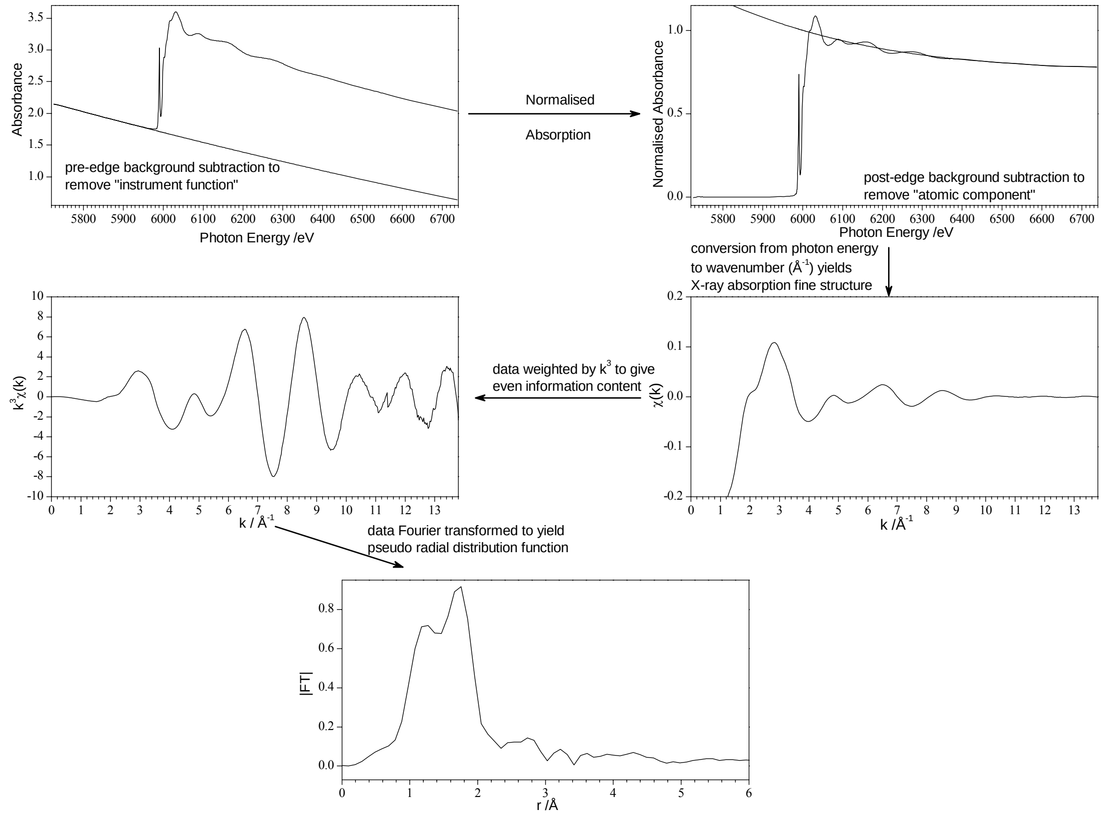

Figure 4.12 Diagram showing the use of various computer programs to analyse and manipulate EXAFS data.

When the data has been collected it must be converted from the raw absorption data into $\chi(k)$ in k space using a program called PAXAS.[7, 8] The monochromator position was first calibrated using the edge position obtained from a metal foil of a similar sample edge. Experimental spectra of the sample were then averaged together and adjusted as required by the calibration and converted from monochromator position to energy. The averaged spectrum was then background corrected in the pre and post-edge regions to leave only the pure EXAFS oscillations in *k* space using a program called Exspline.[8, 9] This process of using various programs is shown in Figure 4.12.

4.6 Experimental Considerations of Matrix Isolation.

There are several experimental considerations that need to be considered for matrix isolation studies and the main and most problematic of these is the deposition of the matrix gas and the species under investigation. For a species to be trapped in a matrix it must be in the gas phase so that it can be co-condensed with the matrix gas; there are two ways that this can be achieved. If the guest species has an appreciable vapour pressure at room temperature, it can simply be mixed with the host gas using standard vacuum line techniques. If the guest species does not have a measurable vapour pressure at room temperature it is then evaporated directly into the vacuum chamber, and combined with the matrix gas before co-condensing on the window. One constraint of this method is that the guest species must be volatile at temperatures below its decomposition point, with the exception to this being when the decomposition products of a particular sample are under investigation. The samples can be heated by a variety of methods with the most popular technique often used being a resistive heated furnace or a Knudsen cell. The concentrations of the guest species in relation to the host gas are difficult if not impossible to determine in these types of experiments. Some researchers have recommended the use of quartz crystal microbalances to monitor the flux from furnaces, but these were not used in any experiments outlined in this work.

The main spectroscopic technique used in conjunction with matrix isolation is IR spectroscopy due to the ease with which spectra can be obtained. Isotopomers are used to identify the bands and their dependence on certain elements in the molecule. The relative sensitivities of spectroscopic techniques differ over quite a wide range and though the analysis of a single matrix by different spectroscopic techniques is possible, it is often difficult. Potentially IR and UV can be interchanged and this is utilised by some matrix isolation groups. However, because UV is more sensitive than IR, the bands may be very intense in the UV spectrum and scattering of the UV radiation may also occur. Due to this sensitivity problem, matrices are deposited specifically for each spectroscopic technique and this leads to the question of whether the guest species is the same, especially when the samples are heated to produce the vapour species. To enable a matrix to be analysed by more the one spectrometer the matrix isolation equipment needs to be mounted onto a trolley that can be adjusted in both the vertical and horizontal direction.

Table 4.5 shows some of the temperatures required to reach vapour pressures of 10^{-3} Torr and some melting point of elements used in these experiments.

Element	**Temperature required for 10^{-3} Torr vapour pressure**	**Melting Point/ K**
Ti	1846	1940
V	1958	2190
Ta	3073	3270
Pd	1588	1825
Hg	289	234
Ir	2558	2727
Rh	2128	2233

Table 4.5 Vapour pressures and melting point of key elements from this work.[3]

4.7 Deposition Techniques.

In matrix isolation various deposition techniques are available for use. In this work thermal evaporation of solid samples has been predominantly used and therefore will be discussed in the most detail.

4.7.1 Thermal Evaporation.

In these experiments thermal evaporation was used by the heating of a metal wire. The main body of the furnace was made of two pieces of Pyrex, so that the length of the forward part can be exchanged to alter the length of the furnace. Inside the furnace are two copper electrodes that are held in position by Araldite. At the end of the copper electrodes the metal wire is connected with screws. The metal wire is placed on a tantalum support due to the high melting point and low vapour pressure of tantalum; also it provides a constant and unbroken source of heat. If the metal being studied was used alone as time passed more and more of the metal would evaporated and the resistance of the metal wire would increase and so with the same voltage being applied to it the rate of evaporation would increase drastically over time resulting in the filament burning out. This experimental set up is shown in Figure 4.13. In the majority of experiments undertaken the metal filament was made up of 3 strands of metal wire wrapped together, this was then combined with two tantalum wires to make the filament. The reason for this was related to the metal wires having a much smaller diameter of 0.25 mm and so multiple metal wires needed to be put together to equal the diameter of one tantalum wire. This filament was finished off by being wrapped with more metal wire to facilitate further metal evaporation. The main body of the furnace is water cooled to prevent the Pyrex from cracking with the temperatures involved, titanium melts at 1667 ^{o}C, for instance. The electrodes are also cooled to prevent them from overheating and expanding which would fracture the glassware. The electrical current needed was provided by a high power current supply which produced high currents (ca 40 A) and low voltages (ca 1-2 V). In later experiments a copper disc with a 5 mm hole in the centre was placed at the edge of the chamber, shown in Figure 4.13, to reduce the thermal load placed upon the window.

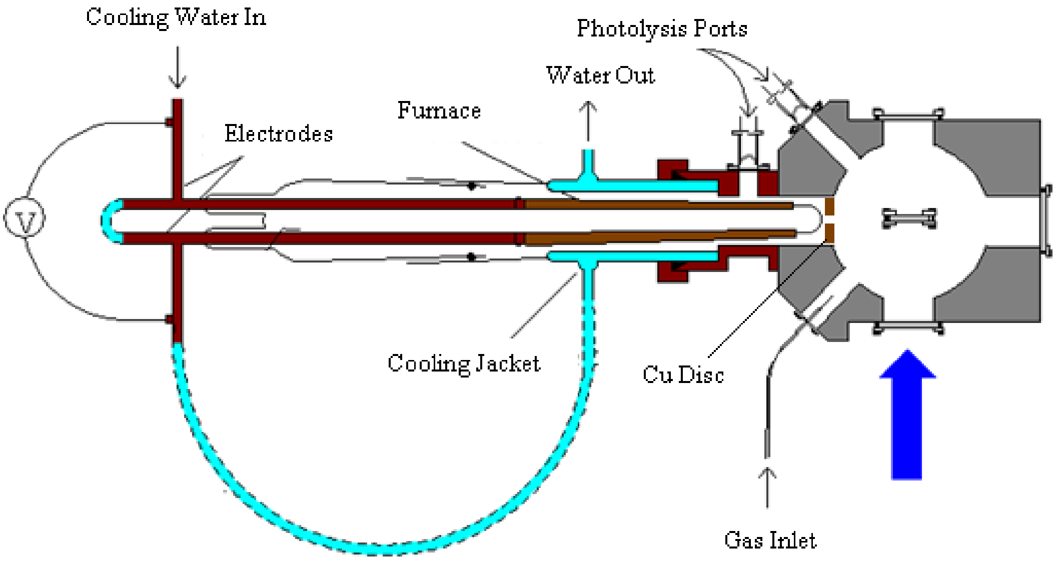

Figure 4.13 The 'furnace' used in the experiments.

4.7.2 Furnace Evaporation.

This is the one of the most commonly used of all matrix isolation deposition techniques. It is generally used for most solid compounds and some elemental substances that have low vapour pressures. This method involves resistively heating the substance until a sufficient vapour pressure is achieved. The vapour species is then isolated in the excess matrix gas. The furnace used in these experiments is displayed in Figure 4.14, with a close up of the sample region being displayed in Figure 4.15

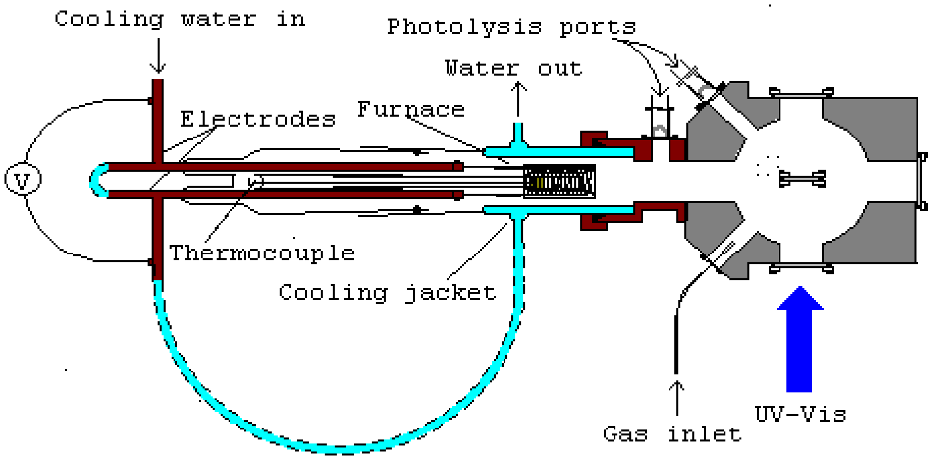

Figure 4.14 Diagram of furnace experimental set-up.

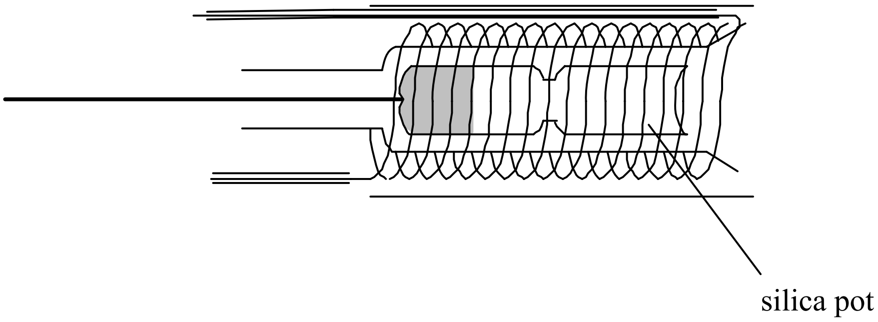

Figure 4.15 Close up diagram of silica sample pot inside the tantalum windings of the furnace.

The main body of the furnace, just like the thermal evaporation set up, is made from Pyrex, and it incorporated two copper electrodes that were held in position by Araldite. A silica tube extended from the rear of the glass body of the furnace between the copper electrodes. This tube held the sample in a specially designed wider region at the end of it. This main body of the apparatus sat inside a Pyrex water-jacket that was coupled to the matrix chamber *via* the use of the brass fitting. The seal was made with a viton 'O' ring, as was the seal between the water jacket and the glass furnace. The water jacket was connected to the mains water supply ensuring any excess heat was removed from the glassware preventing it from breaking. The electrodes were also water cooled in order to prevent them from overheating and expanding. This was the standard set up for a furnace with the only variable component being the water jacket where a range of sizes were available. This meant the sample could be held at variable distances from the matrix chamber.

In the close up region shown, Figure 4.16, the sample holder is displayed; this was made of silica and was 6 mm in diameter. These small pots were filled with material prior to the experiment and then placed inside the quartz tube. Around the quartz tube lay the windings of the furnace, which were made of platinum and tantalum wire. These metals were used because they posses extremely low vapour pressure and therefore do not contaminate the experiments. The wires were attached to the copper electrodes and were insulated where necessary by ceramic tubes. A thermocouple thermocoax type K monitored the temperature of the experiment with the tip lying just behind the sample pot.

The power source for the furnace was a transformer that delivered 20 V at 10 amps controlled by a variac. Using this set–up a temperature of around 1000°C was achievable. Before running an experiment the sample and the furnace had to be degassed to remove any molecules deposited on their surfaces such as CO_2. This was done by gently heating the sample up to its point of sublimation as indicated by a constant pressure rise on the Penning gauge.

4.7.3 RF Generator - Induction Heating.

This involved inductively heating a sample by using an RF generator. This inductive heating works on the basis of eddy currents (Foucault current). Basically the RF generator produces an alternating current which produces a changing magnetic field around the sample. As the sample is not a perfect conductor the eddy currents produced in the sample encounter resistance and thus heat the sample and only the sample. This allows the heating of the samples without the heating of any other parts of the equipment. The same equipment is used in this as for the furnace evaporations, as described above.

In these experiments this technique was used to inductively heat HgF_2 powder, Figure 4.16 shows the equipment set up.

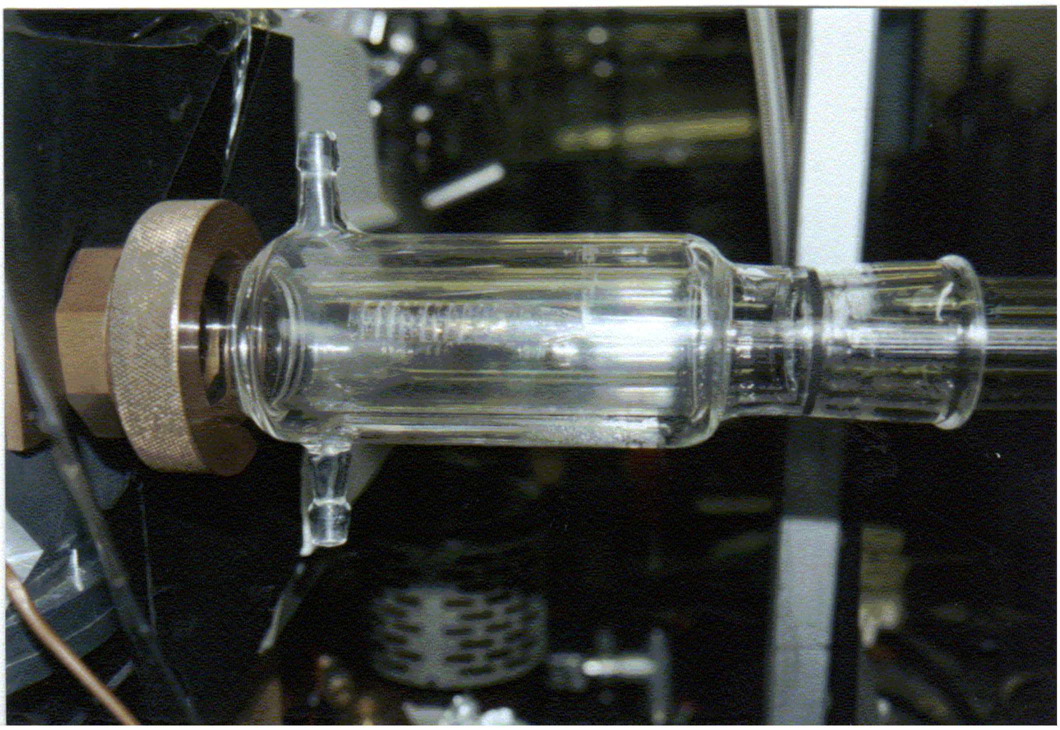

Figure 4.16 RF water jacket with a satin quartz furnace, without windings, being used as the sample holder.

4.8 Computational Calculations.

Within this work computational calculations were conducted using ADF[10], Gaussian 98W,[11] and Gaussian 03W[12] and are detailed when presented.

References.

1. S. Cradock and A. J. Hinchcliffe, *Matrix Isolation*, 1st Edn., Cambridge University Press, 1975.
2. D. G. Avery and R. Witty, *Proc. Phys. Soc.*, 1947, **59**, 1016.
3. M. Moskovits and G. A. Ozin, eds., *Cryochemistry*, Wiley-Interscience, New York, 1976.
4. I. R. Dunkin, *Matrix isolation techniques a practical approach*, Oxford University Press, Oxford, 1998.
5. O. M. Wilkin and N. A. Young, *J. Synch. Rad.*, 1999, **6**, 204.
6. A. C. Thompson, D. Vaughan, D. T. Attwood, E. M. Gullikson, M. R. Howells, J. B. Kortright, A. L. Robinson, J. H. Underwood, K. J. Kim, J. Kirz, I. Lindau, P. Pianetta, H. Winick, G. P. Williams and J. H. Scofield, *Center for X-ray Optics and Advanced Light Source X-ray Data Booklet*, 2nd Edn., Lawrence Berkeley National Laboratory, University of California, Berkeley, California, USA, 2001.
7. N. Binsted, PAXAS, Program for the analysis of X-ray absorption spectra, 1988.
8. P. Ellis, PhD, University of Sydney, 1995.
9. P. Ellis, EXSPLINE, A Program for EXAFS Background Subtraction., CCLRC, Daresbury Laboratory, U.K., 2000.
10. ADF 2003.01, Theoretical Chemistry, Vrije Universiteit, Amsterdam, The Netherlands, 2003.
11. M. J. Frisch, G. W. Trucks, H. B. Schlegel, G. E. Scuseria, M. A. Robb, J. R. Cheeseman, V. G. Zakrzewski, J. J. A. Montgomery, R. E. Stratmann, J. C. Burant, S. Dapprich, J. M. Millam, A. D. Daniels, K. N. K. M. C. Strain, O. Farkas, J. Tomasi, V. Barone, M. Cossi, R. Cammi, B. Mennucci, C. Pomelli, C. Adamo, S. Clifford, J. Ochterski, G. A. Petersson, P. Y. Ayala, Q. Cui, K. Morokuma, D. K. Malick, A. D. Rabuck, K. Raghavachari, J. B. Foresman, J. Cioslowski, J. V. Ortiz, B. B. Stefanov, G. Liu, A. Liashenko, P. Piskorz, I. Komaromi, R. Gomperts, R. L. Martin, D. J. Fox, T. Keith, M. A. Al-Laham, C. Y. Peng, A. Nanayakkara, C. Gonzalez, M. Challacombe, P. M. W. Gill, B. Johnson, W. Chen, M. W. Wong, J. L. Andres, C. Gonzalez, M. Head-Gordon, E. S. Replogle and J. A. Pople, Gaussian 98 Revision A.3, Pittsburgh, 1998.

12. M. J. Frisch, G. W. Trucks, H. B. Schlengel, G. E. Scuseria, M. A. Robb, J. R. Cheeseman, V. G. Zakrzewski, J. J. A. Montgomery, R. E. Stratmann, J. C. Burant, S. Dapprich, J. M. Millam, A. D. Daniels, K. N. Kudin, M. C. Strain, O. Farkas, J. Tomasi, V. Barone, M. Cossi, R. Cammi, B. Mennucci, C. Pomelli, C. Adamo, S. Clifford, J. Ochterski, G. A. Petersson, P. Y. Ayala, Q. Cui, K. Morokuma, D. K. Malick, A. D. Rabuck, K. Raghavachari, J. B. Foresman, J. Cioslowski, J. V. Ortiz, A. G. Baboul, B. B. Stefanov, G. Liu, A. Liashenko, P. Piskorz, I. Komaromi, R. Gomperts, R. L. Martin, D. J. Fox, T. Keith, M. A. Al-Laham, C. Y. Peng, A. Nanayakkara, M. Challacombe, P. M. W. Gill, B. Johnson, W. Chen, M. W. Wong, J. L. Andres, C. Gonzalez, M. Head-Gordon, E. S. Repplogle and J. A. Pople, Gaussian 03, Pittsburgh, 2003.

Chapter 5

First Row Transition Metal Halides

5.1 Introduction.

Molecular transition metal halides have long been of interest to chemists from both computational and experimental backgrounds, even though these molecules are high temperature vapour phase species only generated in the gas phase well above 1000 K. Under these conditions many of the vibrational and rotational levels are populated and so their shape and geometries have often been difficult to assign.[1] Past attempts at assigning the spectra of such molecules have often been hampered by complex vapour compositions which lead to unsuccessful assignment of bands present.[2, 3]

The transition metal chlorides have been extensively studied due to their naturally occurring chlorine isotopes making their assignment much easier. This is not present in fluorine and so assignment of these compounds becomes markedly more difficult with the absence of metal isotopic data.

From work conducted on transition metal chlorides, until recently,[4, 5] there was a consensus that all the first row transition metal dichlorides, as well as $CaCl_2$ and $ZnCl_2$, are linear.[3] For transition metal fluorides on the other hand only MnF_2 to ZnF_2 are linear and CaF_2 is bent. But due to the lack of isotopes for ScF_2 and VF_2 no determination from their spectra can be made.[2, 3] This leaves titanium, with its five naturally stable isotopes, as the key element in understanding the geometric and electronic structures of the first row transition metal dihalides.

5.1.1 History of Titanium and Vanadium.

Within this next chapter a series of experiments which were carried out on selected first row transition metal fluorides will be detailed. Firstly a brief introduction about titanium and vanadium metals will be given with a specific look at the fluorides of these metals. This will then be expanded with a detailed literature review of first row transition metal halides with particular interest with titanium and vanadium. The results achieved will then be detailed and any conclusion that can be drawn from this work and any further work that may be required.

5.1.1.1 Titanium.

Titanium was first discovered in 1791 by a pastor called William Gregor in Cornwall, England.[6] Gregor discovered a black mineral called ilmenite, $FeTiO_3$, in a stream close to his parish. Subsequent investigation of the mineral showed it would only dissolve in concentrated sulfuric acid. He further investigated the mineral and developed reactions which would form the basis of the production of TiO_2 for the next 200 years.[6] Four years after this discovery German chemist Martin Heinrich Klaproth also discovered titanium in an ore called rutile, TiO_2, and subsequently named the element after the Titans from Greek mythology.[6]

Titanium compromises 0.63% (6320 ppm) of the earth's crust and is the ninth most abundant of all elements on earth. Titanium naturally occurs in the minerals anatase (TiO_2), brookite (TiO_2), ilmenite ($FeTiO_3$), perovskite ($CaTiO_3$), rutile (TiO_2), titanite ($CaTiSiO_5$), and it also occurs with many iron ores.[6, 7] The most important of these minerals is ilmenite, which is extracted in Canada, the USA, Australia, Scandinavia, and Malaysia, and rutile, which is extracted mainly in Australia. Preparation of titanium metal in the early history of the element difficult due to the high reactivity of the element with oxygen and so it was only possible to isolate it in the absence of air. In 1932 Wilhelm Kroll produced titanium by reducing $TiCl_4$ with calcium, but the expense of this procedure meant that commercial use of titanium was not favourable.[7]

These factors meant that titanium was not used very often until the development of the aircraft. The use of titanium expanded with the use of aircraft due to titanium's properties. Titanium has low density, half that of steel, and when this is combined with its mechanical strength, which is even higher when in an alloy, titanium has one of the highest strength to weight ratios of any engineering metal; it is easy to see why its use in gas-turbine engines rapidly increased.[7] This new demand for titanium led to the development of new methods of extracting the metal, a variation of the Kroll method is still in use in the isolation of titanium metal today. Ilmenite or rutile are heated with chlorine and carbon to around 1100 K, this produced $TiCl_4$, $FeCl_3$ and CO. $TiCl_4$ is fractionally distilled from $FeCl_3$ and then reduced using magnesium in a sealed furnace under argon at around 1100 K. This produces titanium metal and $MgCl_2$ which is removed leaving titanium which is further treated and cast into ingots.[7]

5.1.1.1.1 Titanium Halides.

Titanium along with zirconium and hafnium, the other group 4 metals, all have a tendency to exhibit their highest oxidation state, +4. All of the tetrahalides of titanium are easily prepared and have a gradation in their colour,[8-12] this relates to the charge transfer band moving steadily to lower energies and thus absorbing more in the visible spectrum as the halide becomes more easily oxidized, i.e. from F^- to I^-. TiI_4 is a dark brown compound, $TiBr_4$ is a orange compound. On the other hand $TiCl_4$ is a colourless liquid and TiF_4 is a white powder.[8] All of the gas phase structures of the tetrahalides are thought to be monomeric tetrahedral structures.[6] As a solid TiF_4 is different to the other tetrahalides as it forms a polymer consisting of corner sharing TiF_6 octahedra,[13] whilst the other tetrahalides remain tetrahedral and are essentially molecular. All of the tetrahalides and especially the chloride and bromide behave as Lewis acids, they are all hygroscopic compounds with the chloride and bromide being most vulnerable to it. $TiCl_4$ will readily hydrolyse even reacting with moist air, while TiF_4 is less susceptible to hydrolysis.

The trihalides of titanium are also common. $TiCl_3$ is the most abundant halide of titanium and is used as a catalyst for the production of polyolefins. There are several crystal forms of $TiCl_3$, the β form is produced by the reduction of $TiCl_4$ by aluminium alkyls in inert solvents. This can be converted to the α form at 500 K to 600 K. There are also two other forms that are known, but these and the α form have layer lattices containing $TiCl_6$ groups, whereas β-$TiCl_3$ is fibrous with single chains of $TiCl_6$

octahedral edge sharing. The β form of $TiCl_3$ is the $TiCl_3$ which is used in the polymerisation of propene.

Oxidations states of titanium below +3 are very rare. This is due to the highly reactive nature of these compounds. $TiCl_2$ is a black solid but there has been little study of this compound due to its high reactivity, and even less work has been conducted on TiF_2 due to its highly reactive nature.

5.1.1.2 Vanadium.

Vanadium was discovered in 1801 by Andrés Manuel del Río in a sample of Mexican ore, now called vanadinite.[6] He found that the salts exhibited a wide range of colours and they all turned red when heated. Even with these discoveries various scientists of the time told him that he had discovered impure chromium and so he ceased his investigations. In 1831 Nils Gabriel Sefström rediscovered vanadium in a new ore which also contained iron and later that year Friedrich Wöhler confirmed del Río's earlier work.[14] Sefström choose a name beginning with V as it had not been assigned to any element yet and called it vanadium after Vanadis the Scandinavian goddess of fertility and beauty because of the variety of colours it produced.[6] The first time the metal was isolated in a reasonable pure form was by Henry Enfield Roscoe in 1867 who reduced vanadium trichloride with hydrogen.[6]

Vanadium is a relatively common element; it is contained in the lithosphere (0.02%) in more than sixty different minerals, although few of these minerals are usable for the isolation of pure vanadium.[6, 7] Vanadinite is a mineral with the formula $Pb_5(VO_4)_3Cl$, which forms the basis for the modern industrial use of vanadium.[7] Over 80% of vanadium produced is used as ferrovanadium in steel and other alloys.[6, 7] As with titanium the most common oxidation state of vanadium is the highest, +5. Vanadium usually occurs as an oxide in this high oxidation state and only one halide in this oxidation state is known to occur, VF_5. This compound is known to have a trigonal bipyramidal structure in the gas phase with some distortions.[15]

5.1.1.2.1 Vanadium Halides.

VCl_4 is a brown oil that is violently hydrolysed by water;[6, 7, 16, 17] its magnetic and spectral properties confirm that this compound is tetrahedral in nature.[18] The only other tetrahalides that has been definitively isolated is VF_4; this is a lime green powder that readily decomposes to VF_3.[6, 7] The most common use of VCl_4 is for the preparation of VCl_3, VCl_2 and various other organo-vanadium compounds.[19] All of the vanadium trihalides can be produced easily,[6] VI_3 and VBr_3 are both stable compounds but lose a halide rapidly upon heating, VI_3 is prepared in the form of brown crystals and is hygroscopic while VBr_3 has brown hygroscopic crystals.[20] VCl_3 is a purple compound[19] and along with VI_3 and VBr_3 adopts a structure very similar to BI_3, hexagonally close packed chloride framework with vanadium atoms occupying the octahedral holes. VF_3 on the other hand is a grey/green powder[21] that forms a structure more closely related to ReO_3, which is a prototypical structure.[17] The lowest known halides of vanadium are the dihalides. VCl_2, the most common, has a polymeric structure and is a powerful reducing species,[22, 23] VI_2 and VBr_2 are structurally and chemically similar to the chloride, VI_2 has red/violet crystals[24] while VBr_2 has orange/brown crystals.[25] VF_2 on the other hand forms blue hygroscopic crystals, although it is highly unstable.

5.2 Literature Review.

In this section a brief review of titanium and vanadium halides is given with specific reference to TiF_2 and VF_2 and why these molecules were studied. A major problem encountered when working with metal fluorides is that fluorine has only one isotope and so it is difficult to identify how many fluorine atoms are present. If the metal has no isotope either, unambiguous identification can be very difficult. Often chlorine is used due to its two isotopes which can help in assignments. For this reason the use of chlorine in a MX_2 compound is common. Work done on VCl_2 and $CrCl_2$ by Hargittai,[26] with electron diffraction studies showed the bond angles to be 110°, but due to the disproportionation and/or oligomers in the gas phase the results are in doubt. Other work showed that $FeCl_2$, $CoCl_2$ and $NiCl_2$ have bond angles of 161°, 157° and 161° respectively,[27] these can effectively be considered as linear, due to the insensitivity of the sine function near linearity.[28] Work by Bridgeman and Bridgeman[29] and by Jensen[30] have suggested that $CrCl_2$ may be a non-linear molecule due to Renner-Teller symmetry breaking, meaning that if $CrCl_2$ is bent it is probable that CrF_2 will also undergo Renner-Teller distortion and be a bent molecule. If this is the case a bent CrF_2 along with CaF_2 being bent then leaves ScF_2, TiF_2 and VF_2 as molecules which as yet are unassigned and investigation of these molecules for evidence of Renner-Teller symmetry breaking could lead to important results for the understanding of first row transition metal halides.

5.2.1 Theoretical/Calculations.

The first row transition metal dihalides constitute a class of small and apparently simple molecule but ones which cause much controversy.[31] The partially occupied 3d subshell on the metal gives rise to low lying states representing a challenge to theoretical and experimental scientists. Many of these simple molecules form high temperature molecules which are generated in the gas phase well above 1000 K.[32-41] Under such conditions many of the vibrational and rotational levels are populated making their spectra very difficult to assign and so many mistakes have been made in interrupting the spectra of these molecules.

Early computational studies of these molecules assumed an ionic structure of these compounds, $X^-M^{2+}X^-$, which results in the standard order of 3d orbital levels, $\delta < \pi < \sigma$. The method used to study these molecules, Ligand Field Theory (LFT), does not take strong orbital interaction nor specific electron correlation into account, except if unusual parameter values are used. More recently various types of quantum chemical calculations of some of the dihalides have indicated that this simple LFT model is not well suited for these compounds and the actual ground states may not correspond to the standard order of LFT d-orbital energy levels.[42, 43]

Some early computational calculations by Bridgeman[44, 45] using DFT provided new assignments of various transition metal dihalides and are shown in Table 5.1. Within this work he finds that the previous assignment of $NiCl_2$ to a $^3\Pi_g$ ground state,[33, 34, 46-50] is incorrect and he reassigns it to a $^3\Sigma_g^-$ ground state.[44] When $CuCl_2$ was investigated he found that the previous assignment of the ground state to a $^2\Sigma_g^+$ was incorrect but another previous assignment to a $^2\Pi_g$ ground state is correct.[44] Work conducted upon $FeCl_2$ agrees with the previous assignment of the ground state as $^5\Delta_g$.[32, 33, 45-47, 49] The calculations performed on $CoCl_2$ confirm the previous assignment of the ground state to $^4\Sigma_g^-$ but disagree with the assignment made by Hougen *et al.*,[34] DeKock and Gruen,[33] and by Smith to $^4\Phi_g$.[47]

Metal	**Electronic Ground State – Previous LFT Assignments.**	**Electronic Ground State**
$NiCl_2$	$^3\Pi_g$ [33, 34, 46-50]	$^3\Sigma_g^-$ [44]
$CuCl_2$	$^2\Sigma_g^+$ [32, 34, 44, 46, 47, 51]	$^2\Pi_g$ [43, 44, 52, 53]
$FeCl_2$	$^5\Delta_g$ [32, 33, 45-47, 49]	$^5\Delta_g$
$CoCl_2$	$^4\Sigma_g^-$ [34, 45, 50, 54, 55] $^4\Phi_g$, [33, 47, 56]	$^4\Sigma_g^-$

Table 5.1 Electronic Ground-State assignments of selected first row transition metal dihalides from LFT and DFT approaches.[44, 45]

Wang and Schwarz[57] also conducted a DFT study after this work by Bridgeman[44, 45] on transition metal difluorides and dichlorides of manganese to zinc. Within this study they looked at the electronic assignment of the transition metal dihalides and conducted calculations to determine the stretching frequencies, bond angles and bond lengths.

Metal	**Electronic Ground State – Previous LFT and Experimental Assignments.**	**Alternative Assignments - LFT and Experimental Assignments.**	**Electronic Ground State – Proposed DFT Assignment By Wang and Schwarz**[57]	**Experimental Agreement**
Ca (d^0)	$(\delta^0)\ {}^1\Sigma_g^{+}$[57]		$(\delta^0)\ {}^1\Sigma_g^{+}$	
Sc (d^1)	$(\delta^1)\ {}^2\Delta_g$[57]	${}^2\Pi_g$, ${}^2\Sigma_g^{+}$[57]	$(\delta^1)\ {}^2\Sigma_g^{+}$	
Ti (d^2)	$(\delta^2)\ {}^3\Sigma_g^{-}$[57-59]	${}^3\Delta_g$, ${}^3\Phi_g$[57-59]	$(\delta^1\ \sigma^1)\ {}^3\Delta_g$	
V (d^3)	$(\delta^2\pi^1)\ {}^4\Pi_g$[57, 59]	${}^4\Delta_g$, ${}^4\Sigma_g^{-}$[57, 59]	$(\delta^2\ \sigma^1)\ {}^4\Sigma_g^{-}$	
Cr (d^4)	$(\delta^2\pi^2)\ {}^5\Sigma_g^{+}$[32, 46, 47]	${}^5\Pi_g$[30, 60]	$(\delta^2\pi^1\ \sigma^1)\ {}^5\Pi_g$	
Mn (d^5)	$(\delta^2\pi^2\sigma^1)\ {}^6\Sigma_g^{+}$[33, 49]		$(\delta^2\pi^2\sigma^1)\ {}^6\Sigma_g^{+}$	
Fe (d^6)	$(\delta^3\pi^2\sigma^1)\ {}^5\Delta_g$[32, 33, 45-47, 49]	${}^5\Pi_g$[45], ${}^5\Sigma_g^{+}$[45]	$(\delta^{3-\eta}\pi^2\sigma^{1+\eta})\ {}^5\Delta_g$	
Co (d^7)	$(\delta^4\pi^2\sigma^1)\ {}^4\Sigma_g^{-}$[34, 45, 50, 54, 55]	${}^4\Phi_g$,[33, 47, 56] ${}^4\Delta_g$[45]	$(\delta^{4-\eta}\pi^2\sigma^{1+\eta})\ {}^4\Sigma_g^{-}$	
Ni (d^8)	$(\delta^4\pi^3\sigma^1)\ {}^3\Pi_g$[33, 34, 46-50]	${}^3\Delta_g$,[46] ${}^3\Sigma_g^{-}$[44]	$(\delta^4\pi^2\sigma^2)\ {}^3\Sigma_g^{-}$	${}^3\Sigma_g^{-}$[37, 61-65]
Cu (d^9)	$(\delta^4\pi^4\sigma^1)\ {}^2\Sigma_g^{+}$[32, 34, 44, 46, 47, 51]	${}^2\Pi_g$[43, 44, 52, 53]	$(\delta^4\pi^3\sigma^2)\ {}^2\Pi_g$	${}^2\Pi_g$[36, 65-70]
Zn (d^{10})	$(\delta^4\pi^4\sigma^2)\ {}^1\Sigma_g^{+}$		$(\delta^4\pi^4\sigma^2)\ {}^1\Sigma_g^{+}$	

Table 5.2 Electronic Ground-State assignments of first row transition metal dihalides from LFT and DFT approaches.[57]

From this study they concluded that all of the first row transition metal dihalides were linear but with soft, low energy, large amplitude vibrations. The difluorides of calcium to chromium were quasi-linear with large amplitude vibrations over a linear geometry saddle point. This leads to imaginary harmonic frequencies for the bending mode of the linear molecules. A comparison of the results obtained by Wang and Schwarz and previous LFT calculations are given in Table 5.2.

This reordering of the orbital energy levels is related to the fact that ligand induced metal 3d-4s hybridization lowers the σ level and metal dπ - ligand π interaction (ligand π donation) raises the dπ level. The d/s hybridization of the metal shifts charge from the axial z^2 lobes of the dσ orbital into its equatorial (x^2-y^2) ring, this causes the metal dσ - ligand σ Pauli-repulsion to reduce significantly. Another point discovered by Wang and Schwarz was that with iron and cobalt when some orbitals became occupied the energy level of these orbitals increased. In some systems an empty dσ orbital would lie lower in energy than an occupied dδ orbital, while the occupied dσ orbital would lie above the empty dδ level. This can be explained using Janak's theorem,[71] the lowest total energy of a system is obtained for those fractional occupation numbers, where the two respective orbitals become energetically degenerate.

Wang and Schwarz also calculated stretching frequencies for the first row transition metal halides, Table 5.3. From this the υ_{asym} of TiF_2 was calculated to be at 744 cm^{-1}, for the linear (saddle point) geometry, but they also calculated a frequency of 722 cm^{-1} for the bent ground state structure, while VF_2 had a υ_{asym} of 773 cm^{-1}. Table 5.3 shows some of the calculated bond angles of the transition metals. One of the problems encountered with calculations of bond angles is related to the fact that as the sine function comes close to 155^{o} the accuracy significantly drops off to such a point that 155^{o} and above can effectively be considered linear.[28]

Other calculations using a multi-reference configuration interaction method (icMRCI) found TiF_2 to be linear, but the near degeneracy of the ground and first excited state ($^3\Sigma_g^-$, $^3\Delta_g$) meant that the ground state could not be determined.[58] They determined the

υ_{asym} to be 705 cm^{-1} for the $^3\Sigma_g^-$ state and 695 cm^{-1} for the $^3\Delta_g$ state. In this work comments were made about the better agreement between the calculated and the experimental vibrational data for $TiCl_2$ than was achieved for TiF_2.

Molecule	υ_{sym}	υ_{asym}	υ_{bend}
CaF_2	492	581	(imaginary)
ScF_2	584	700	(imaginary)
TiF_2	614	744 (705,695)	(imaginary)
VF_2	630	773	(very small)
CrF_2	584	700	(imaginary)
MnF_2	598	739	123
FeF_2	623	770	143
CoF_2	627	803	123
NiF_2	632	817	145
CuF_2	597	762	157
ZnF_2	608	72	179

Table 5.3 Calculated harmonic vibrational frequencies υ_{sym}, υ_{asym}, υ_{bend} (in cm^{-1}) of first row transition metal halides,[57] other calculations in parenthesis.[72]

When these results are compared to Wang and Schwarz's previous work it shows that calculations have yet to find an agreement on the frequency at which TiF_2 will appear in the IR spectrum with a difference of 60 cm^{-1} between the MRCI and DFT approaches, this is likely due to the low lying electronic states of these molecules making the calculations extremely challenging. The bond lengths and bond angles of other transition metal dihalides are discussed more extensively in an overview of all the metal halides.[3] Also a comprehensive review of the topic was written by Drake and Rosenblatt.[73]

The ground state of TiF and TiCl has caused various assignments over the years. Initially Dieber and Kay assigned the ground state of TiF to be a $^4\Sigma^-$,[74] this assignment was questioned by Shenyavskaya and Dubov who subsequently reassigned the ground state to a $^2\Delta$.[75] This was again questioned by Ram *et al.* who then assigned the ground state to a $^4\Phi$ using high resolution laser FT emission spectroscopy.[76] A similar story was followed for TiCl with the intial assignment of a $^4\Sigma^-$ [74, 77-80] being questioned and then reassigned $^2\Delta$[81] and finally to $^4\Phi$.[82] The υ_{Ti-F} mode of TiF has been observed at about 650 cm^{-1} with calculated harmonic values of around 640 cm^{-1} for the $^4\Phi$ ground state.[83]

Molecule	Bond angle/^{0}	Bond Lengths (pm)
CaF_2	148.6 (142.1±1)[84, 85]	200
$CaCl_2$	180	245.2 (248.3)[86]
ScF_2	112.4	186.7
$ScCl_2$	128.5	229.7
TiF_2	132.9 (130 ± 5)[87]	180.7
$TiCl_2$	150.2	223.2

VF_2	180	176.3
VCl_2	180	218.3 (217.2)[86]
CrF_2	136.0	177.2 (179.6 ± 8)[40, 88]
$CrCl_2$	143.2 (109.8)[86]	217.3 (220.7)[86]
MnF_2	180	177.9 (181.2 ± 6)[40, 88]
$MnCl_2$	180	216.4 (218.4 ± 1)[35, 89, 90]
FeF_2	180	173.8 (177.0 ± 4)[40, 88]
$FeCl_2$	180	210.9 (212.8 ± 1)[35, 89, 90]
CoF_2	180	170.5 (175.6 ± 4)[40, 88]
$CoCl_2$	180	206.9 (209.0 ± 1)[35, 89, 90]
NiF_2	180	169.1 (173.0 ± 4)[40, 88]
$NiCl_2$	180	203.8 (205.6, 205.3)[35, 37, 89, 90]
CuF_2	180	171.1 (171.3)[86]
$CuCl_2$	180	205.5 (203.6)[65]
ZnF_2	180	172.4 (174.2 ± 8)[40, 88]
$ZnCl_2$	180	207.8 (207.2)[86]

Table 5.4 Calculated bond angles and lengths of first row transition metal dihalides with nonlinear potential energy minima,[57] values in brackets are some experimental values.

Aside from the calculations by Wang and Schwarz,[57] few calculations have been conducted upon VF_2, one study by Vogel and Weber[59] predicted the ground state of VF_2 to be the same $^4\Sigma_g^-$ state that Wang and Schwarz predicted.[57] The majority of computational work performed on vanadium fluorides concentrated on VF_3 and more recently has concentrated on the Jahn-Teller distortion of VF_3, but this is not in the scope of the current work and so will only be discussed briefly.

Early computational work on VF_3 involved using simple valence state energy and hybridization models to predict that VF_3 along with ScF_3, TiF_3, and CrF_3 is pyramidal.[72, 91-94] This work was continued by Yates and Pitzer[95] who used *ab initio* restricted Hartree-Fock calculations on MF_3 (M = Sc to Ni). They determined that VF_3 has a non-degenerate ground state and that the molecule would have a trigonal planar structure. Perhaps most importantly this study determined that molecular VF_3 would present some Jahn-Teller distortion. The Jahn-Teller distortion occurs due to a very low lying excited electronic state of $^3E''$ symmetry which is above the $^3A'_2$ ground state by 4060 cm^{-1}. This value could be reduced significantly by an electron correlation effect and a Jahn-Teller distortion of a $^3E'$ state D_{3h} structure could lower its energy sufficiently to make it the ground state. This work resulted in Solomonik *et al.*[96] conducting a detailed study of the two low lying states using coupled-cluster singles and doubles (CCSD) methods. From this study they assigned peaks observed in a matrix due to VF_3, discussed later, at 733.2 cm^{-1} and 731.8 cm^{-1} are not due to a matrix effect as Bukhmarina *et al.* suggested but in fact is related to a Jahn-Teller distortion.[97] They came to this conclusion based on evidence shown from spectra of MnF_3, which has a large Jahn-Teller distortion, which has its band split by 46 cm^{-1} [95, 98, 99] they postulate that a splitting of 1.4 cm^{-1} for VF_3 is possible as VF_3 only has a slight Jahn-Teller distortion.

The literature of VF is limited to two experimental papers and a few computational studies. Work conducted by Jones and Krishnamurty observed an emission spectrum of VF in the 3.4 eV – 3.6 eV range and determined its ground state to be $^5\Pi$.[100] Ram *et al.* also investigated VF using emission spectrum in the 3400 cm^{-1} – 17,000 cm^{-1} range and determined its ground state to be $^5\Delta$.[101] Averyanov and Khait conducted a theoretical studies of VF.[102] They used *ab initio* calculations of the low lying states of VF and proposed a $^5\Delta$ ground state with the $^5\Pi$ state found to be 1700 cm^{-1} higher. A further computational study by Koukounas *et al.* using *ab initio* calculations determined that the ground state of VF is $^5\Pi$ with the $^5\Delta$ state found to be 700 cm^{-1} – 900 cm^{-1} higher.

5.2.2 IR Data.

With the use of group theory the Γ_{str} can be predicted to see what would be expected for the various titanium halides, and is presented in Table 5.5 and are is given in more detail Appendix 1.

	Γ_{str}	**IR Active**
TiF	Σ^+	Σ^+
TiF_2 C_{2v} $D_{\infty h}$	 $A_1 + B_2$ $\Sigma_g^+ + \Sigma_u^+$	 $A_1 + B_2$ Σ_u^+
TiF_3	$A_1' + E'$	E'
TiF_4	$A_1 + T_2$	T_2

Table 5.5 Table showing the Γ_{str} for the titanium halides in likely geometries.

5.2.2.1 Titanium Fluorides in a Matrix.

A key early piece of matrix isolation IR work on titanium fluorides was conducted by Hastie *et al.* in 1969.[87] They superheated TiF_3, in the presence of titanium metal, in a graphite double Knudsen cell assembly, in the hope of forming TiF_2. The TiF_3/Ti mixtures indicated a bond angle of about 130° for TiF_2.[87] The results obtained from this work are shown in Figure 5.01.

They assigned a peak at 792.8 cm^{-1} as the υ_3 asymmetric stretch for TiF_3, this was the most intense peak in the IR spectra, the spectra also showed the titanium isotope pattern, 5 peaks in a 1:1:9:1:1 ratio. The next largest peak present in the spectra, 740.6 cm^{-1}, they assigned to the υ_3 asymmetric stretch for TiF_2, from the isotope pattern of this peak the bond angle of 130° was calculated. This work was however proved to be unreliable by Beattie *et al.* in 1989.[103] They plotted a graph using simple valence force field (SVFF) force constant (f_r-f_{rr}) from the υ_3 values for MF_2 versus those of MCl_2, Figure 5.02. The straight line is a fit to the data used for chromium, manganese, iron, cobalt, nickel and zinc and the data point for titanium is taken from Hastie *et al.*.[87]

Due to the fact that most other elements fit the line extremely well it was likely that the results obtained by Hastie *et al.* were to be wrong, likely owing to the complexity of the titanium fluoride vapour phase system and high volatility of TiF_4. The closer a point is to the line to closer to linearity it will be.

From this work the TiF_3 band at 790 cm^{-1} was reassigned to TiF_4, based on gas phase[104] and matrix experiments[103] which involved the evaporation of TiF_4. This subsequently led to the bands at 740 cm^{-1}, originally assigned to TiF_2, being almost certainly due to TiF_3. Thus the reported bond angle of 130° is likely to be the 120° angle of trigonal planar TiF_3 instead. Further analysis of the titanium isotope pattern confirms this.[103] Further work on TiF_2 is limited to ESR reports from the late 1970s. Work conducted by Ault with TiF_4 and NH_3 also confirms the presence of TiF_4 at 790 cm^{-1}.[105]

2652 HASTIE, HAUGE, AND MARGRAVE

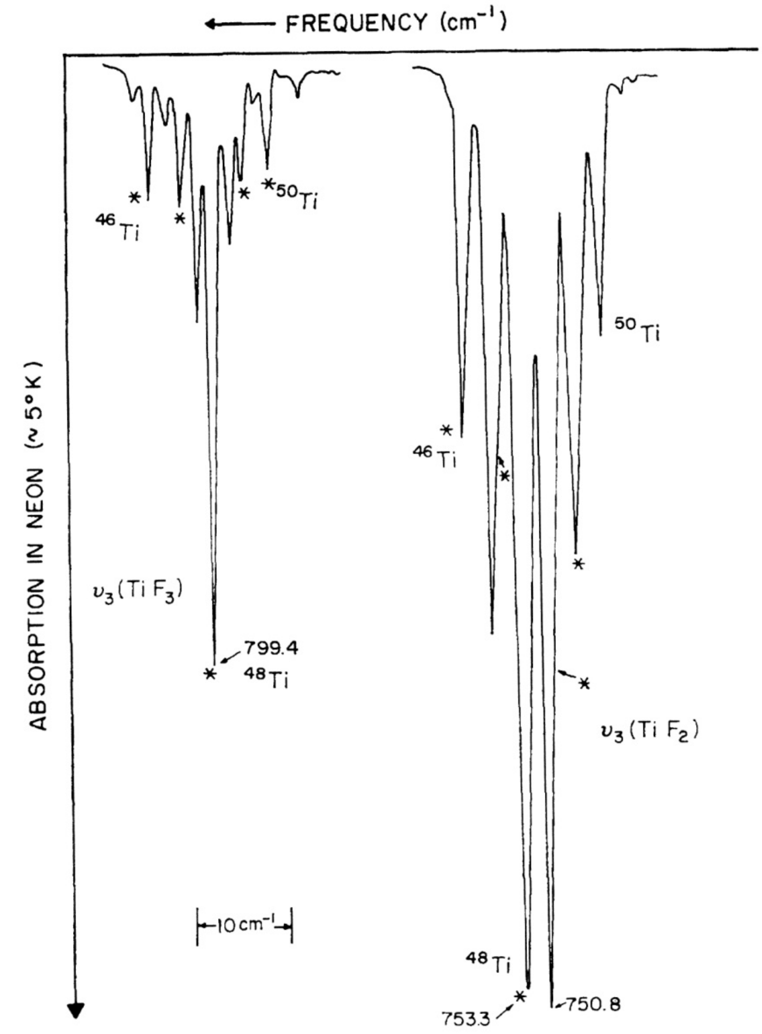

FIG. 4. Infrared absorption spectra of TiF_3 and TiF_2 matrix isolated in solid neon. The TiF_2 was produced by passing TiF_3 vapor from a relatively cool Knudsen cell ($T=630°C$) into a hotter cell ($T=1020°C$) containing solid Ti metal. The equilibrated vapor from the hot cell then passed to the cold surface as a molecular beam for matrix trapping.

Figure 5.01 IR spectra showing the assignment of TiF_3 and TiF_2 made by Hastie *et al.*.[87]

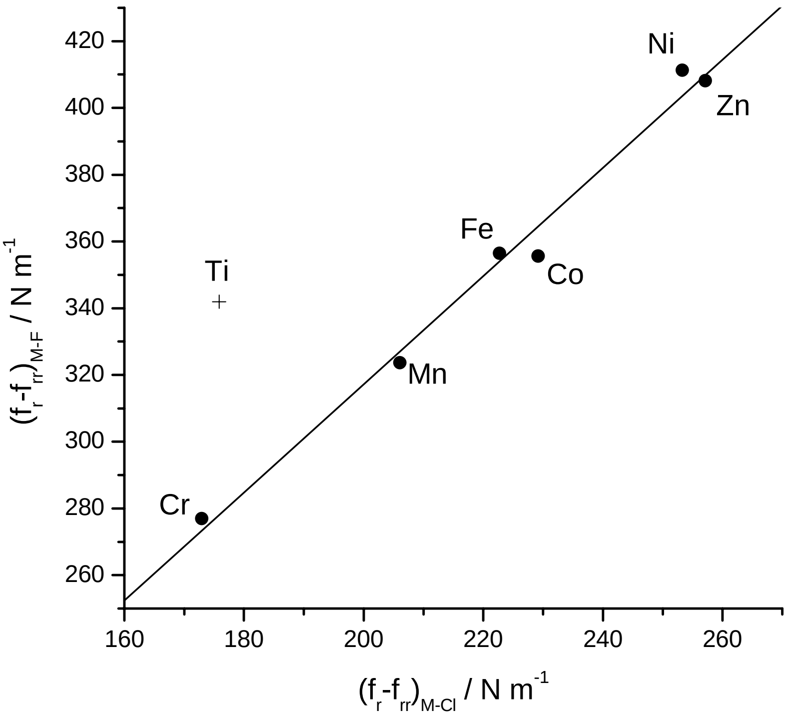

Figure 5.02 Plot of SVFF force constant (f_r-f_{rr}) from the ν_3 values for MF_2 versus those of MCl_2.[2, 3, 57]

5.2.3 ESR Studies on TiF_3 and TiF_2.

De Vore and Weltner[106] conducted work upon TiF_2 and also TiF_3 using ESR, the data which was reported for TiF_2 was consistent with a bent triplet structure; however, the signals were weak and broad with no observable titanium or fluorine hyperfine couplings.[106] The ESR spectra obtained for TiF_3 by DeVore and Weltner shows it to be in a D_{3h} field. The small values for the fluorine hyperfine splitting spectra of TiF_3 compared to the atomic fluorine values A_{iso} = 47 910 MHz and A_{dip} = 1515 MHz[107] indicates very little spin density on the fluorine ligands. Therefore the electron is located in a non bonding orbital on the titanium. This leads to the consideration that the titanium is essentially Ti^{3+}.

5.2.4 Conclusion from the Literature.

From the literature the band of TiF_4 has clearly been identified at 790 cm^{-1}, while TiF_3 has been suggested to be present at 740 cm^{-1}.[104] While TiF_2 has yet to be identified experimentally, calculations have given an insight into its possible location in an IR spectrum. Calculations have been performed upon TiF_2 but due to the near degeneracy of the ground state and the low lying state a definitive answer has yet to be agreed upon. The two stretching frequencies for TiF_2 were proposed, 705 cm^{-1} for the $^3\sum_g^-$ state and 695 cm^{-1} for the $^3\Delta_g$ state.[72] The work by Beattie *et al.*, shown in Figure 5.02, can also be used to indicate a possible location for the stretching frequency of TiF_2. This predicts the band to be around 670 cm^{-1}. Calculations performed upon TiF have suggested a $^4\Phi$ ground state and the $\upsilon_{Ti\text{-}F}$ mode of TiF has been observed at about 650 cm^{-1}.[83]

5.3 Experimental Results.

5.3.1 Introduction.

From the work conducted in these experiments with fluorine certain peaks are consistently present within the spectrum while others appear with specific conditions all of which shall be assigned here and not mentioned again. Firstly impurities present in the purchased gas mixture include SiF_4 present at 1029 cm^{-1}, and CF_4 at 1274 cm^{-1} and 1260 cm^{-1}.[108] With the use of fluorine, HF will likely always be present at 3965 cm^{-1}, 3916 cm^{-1}, and 3910 cm^{-1},[109] a spectrum of 1% F_2/Ar is shown in Appendix 3.1. Previous experiments conducted within this research group have also shown the mobility of fluorine atoms when a matrix containing fluorine is photolysed, these experiments showed the formation of KrF_2 after photolysis.[110] This means that any matrix containing oxygen and fluorine can result in various forms of oxygen fluorides being present.[110] These can include O_2F_2 at 624 cm^{-1} and 613 cm^{-1},[111, 112] O_2F at 593 cm^{-1} and 1500 cm^{-1},[113, 114] OF_2 at 926 cm^{-1}, 915 cm^{-1}, and 821 cm^{-1} [112, 114] which are usually present after photolysis.[110] If any H_2O is present within the matrix a characteristic band at 1620 cm^{-1} and 1595 cm^{-1} will always be present,[115] but when fluorine is also present with H_2O then it is likely that FOH can be present at 1005 cm^{-1}. CO_2 is often present within a matrix isolation spectrum at 662 cm^{-1}, and also the Q branch of atmospheric CO_2 appears at 667 cm^{-1}. CO_2 is often present within the experiments and is likely due to it being present within the heated filament and even after degassing it is still often observed. This presence of CO_2 along with fluorine also leaves the possibility of peaks at 770 cm^{-1} and 1023 cm^{-1} being present, related to F_2CO (υ_6) and FCO (υ_3) respectively.[111] FCO will also have bands in the $\upsilon_{Ti\text{-}F}$ region at 626 cm^{-1} while F_2CO will have a band at 764 cm^{-1}.[116] With the presence of F_2 and CO_2 could also leave the possibility of a CO_2...HF complex present at around 3871 cm^{-1}, 2354 cm^{-1}, 656 cm^{-1}, and 313 cm^{-1}.[117] Some of these impurities, most notably H_2O and CO_2 can also be present from out gassing of the chamber walls.

Initially a titanium wire was bought specifically for the purpose of these experiments; this wire is often used in titanium sublimation pumps as a filament. This wire was a pure titanium wire with a 0.5 mm diameter and was initially used in the first attempts at these reactions. It was found after numerous attempts that this wire was not suitable for the experiments conducted here. This was due to that fact that it was found that insufficient titanium was evaporated before the temperature in the titanium wire became too high and the wire melted. This meant that another solution was required.

The first solution tried was to use a tantalum support with titanium foil wrapped around it. This did not prove to be very successful due to the fact that as any heat was applied to the titanium foil the foil would no longer keep in the position it was placed and would simply fall off the tantalum support and so no titanium would be evaporated. The next step was to try and hold the titanium foil in place by winding it in with the tantalum support in the hope that it would not be possible for the titanium to fall out. This also failed due to the fact that only the part of the titanium that was wound in with the tantalum would stay in place; all other parts of the foil simply came loose and hung too far away from the tantalum to promote any evaporation.

The final technique attempted was the use of tantalum wire as a support and titanium wire wrapped around it. This proved to work well with the wire staying close to the tantalum so significant heat transfer could occur. A slight improvement was made on this design by also incorporating the titanium wire within the tantalum support as well as wrapped around the exterior of the support. This involved wrapping 3 titanium wires together and then using this in place of one of the tantalum supports previously used. This meant that the support wire was now made up of two tantalum and one titanium wire. This new support wire then had extra titanium wire wrapped around as before for the sublimation. This was done in the hope that it would support the evaporation of more titanium without putting excessive current and voltage through the support and thus melting it. These two techniques were successful and were thus used in the following experiments involving all of the transition metal halide experiments.

5.3.2 Titanium Results.

The main aim of this work was to isolate TiF_2, with the hope of using the isotope pattern of titanium to determine the bond angle, and then subsequently attempt to conduct UV/Vis spectroscopy to determine which electronic transition could be assigned. As previously stated the isolation and characterisation of TiF_2 would be extremely useful in analysis of the trends seen for first row transition metal fluorides.

The first step taken towards this was to isolate titanium atoms in an argon matrix and take UV/Vis spectra to determine the conditions required to sublime titanium. This was done with UV/Vis spectroscopy as titanium atoms are IR inactive and their electronic transition have previously been assigned and so comparison would allow easy assignment.[118] From the outset this work encountered difficulties relating to the thermal load placed on the window by the heated filament. The temperatures required to sublime titanium, a vapour pressure of 10^{-3} Torr requires a temperature of 1848 K, led to the heating of the window by a few degrees and meant that isolation of the gas was disrupted and gave poor spectra. This meant that the first series of experiments involving titanium in argon were unsuccessful but the next set of reactions with a 10% F_2/Ar mixture were attempted to see if the results would be any different. These experiments again failed and so a solution to this problem was required.

After numerous attempts the problem was solved by simply using a pure copper disc with a 5mm hole drilled through the centre, shown in Figure 4.13; the disc was placed between the filament and the window on the very edge of the chamber. The main aim of the copper disc was to act as a heat sink and reduce the thermal load placed on the deposition window by the heated wire. While this would reduce the heat transfer from the wire to the window it would also reduce the metal vapour transfer to the chamber, but it was decided that this was a necessary compromise to take in order to isolate atoms in the matrix.

To make sure that new experimental set up was working the first series of experiments conducted involved the use of oxygen instead of fluorine as TiO_x compounds are known and are very stable and was attempted to check that the technique would work with something that was easy to isolate.[119] E.g. TiO_2 is a very common compound found in nature and used in various compounds from paint to sunscreen to food colouring.

5.3.2.1 Ti in O_2/Ar.

5.3.2.1 Ti in 10% O_2/Ar.

In these series of experiments it was expected that TiO_2 and possibly TiO would be isolated. TiO_2 has previously been assigned to bands at 917.1 cm^{-1} and 946.9 cm^{-1},[120] and TiO has previously been assigned to a band at 997 cm^{-1}.[119] In these experiments the asymmetric stretching frequency (υ_3) for TiO_2 was observed as can be seen from Figure 5.03. The symmetric stretching frequency (υ_1) at 946 cm^{-1} was also present which shows the formation of TiO_2 in these experiments and thus shows that the experimental set up is working to a satisfactory level and the use of the copper disc had prevented the heating of the spectroscopic window. There was no sign of the formation of TiO in this short series of experiments, which would produce a peak around the 997 cm^{-1} as shown by Weltner and McLeod.[121]

Now that the new technique had proved that it worked effectively for titanium in O_2/Ar, the emphasis could switch to the main target of the work, the isolation and spectroscopic characterisation of TiF_2 and the determination of its bond angle.

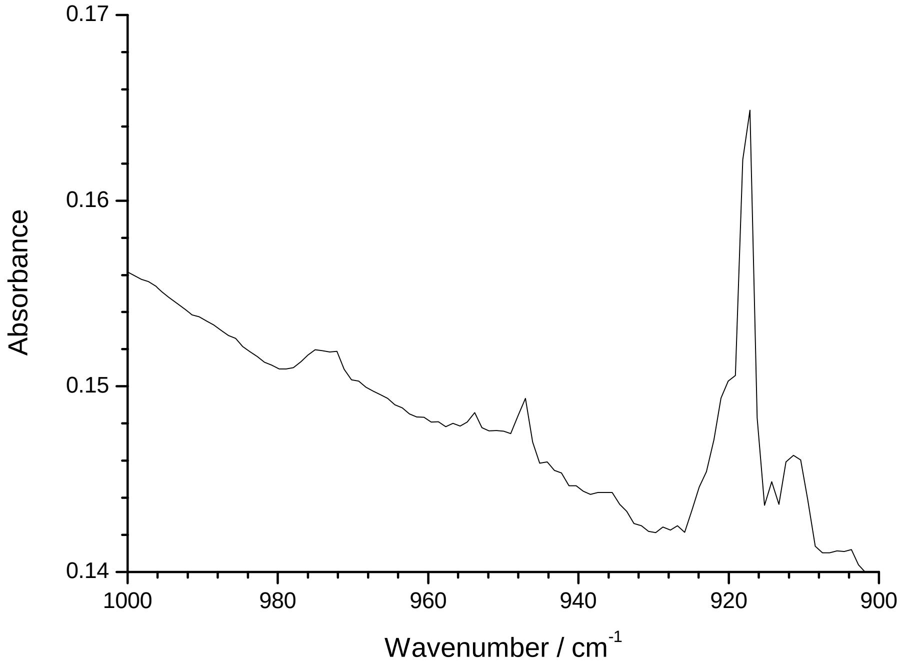

Figure 5.03 IR spectrum of titanium isolated in 1% O_2/Ar.

5.3.2.2 Ti in F_2/Ar.

5.3.2.2.1 Ti in 10% F_2/Ar.

From the literature, TiF_4 produces a peak at 792 cm^{-1} and TiF_3 is likely due to a peak previously observed at 740 cm^{-1} in the IR spectrum.[103, 105] From the literature review above, TiF_2 has never been isolated in a matrix aside from Hastie *et al.*[87] whose claims have since been shown to probably be incorrect.[103] DFT calculations by Wang and Schwarz predicted the υ_{sym} to be at 614 cm^{-1} and the υ_{asym} to be at 744 cm^{-1},[57] if Figure 5.02 is considered the expected frequencies can be calculated, by knowing the frequency which $TiCl_2$ is observed, and is likely to be around 670 cm^{-1}. This could prove to be a problem due to the predominance of the atmospheric CO_2 Q-branch at 667 cm^{-1} and matrix isolated CO_2 at 662 cm^{-1}. TiF would be expected to be around 640 cm^{-1} for the $^4\Phi$ ground state.[83]

From the experiments conducted, shown in Figure 5.04, a peak is produced at 792 cm^{-1} which previously has been assigned to TiF_4,[104] there is also a peak present at 738 cm^{-1} which could possibly show the formation of TiF_3, although this is a tentative assignment. There does not appear to be much of anything around either the 640 cm^{-1} or 670 cm^{-1} areas aside from CO_2 related peaks, indicating no TiF or TiF_2 is forming in the areas predicted previously. Due to the high level of fluorine in the gas mixture and the clear formation of TiF_4 and possibly TiF_3, showing the experiment works, the fluorine concentration in the gas was reduced to try and limit the formation of the larger TiF_x molecules.

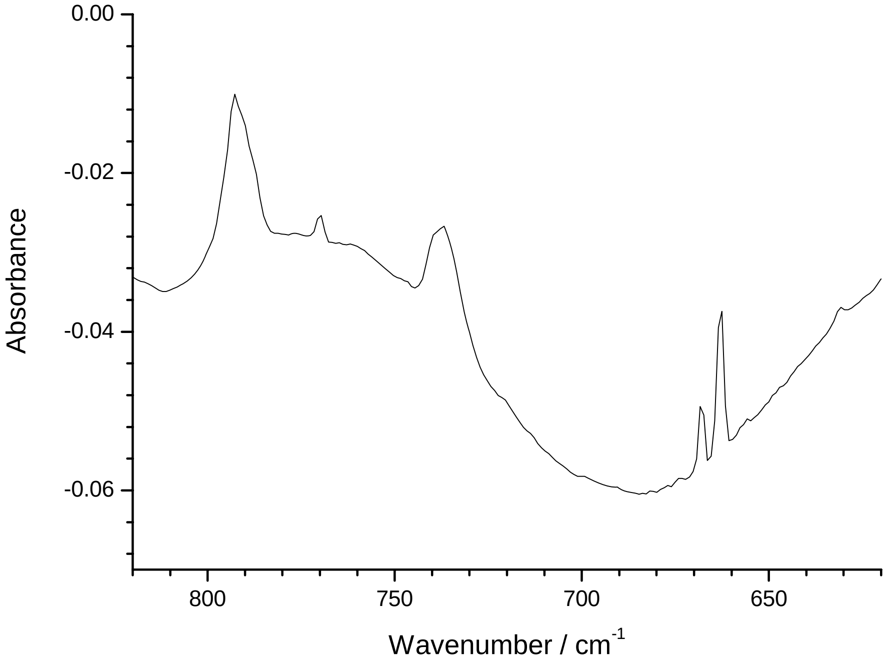

Figure 5.04 IR spectrum of titanium isolated in 10% F_2/Ar.

5.3.2.2.2 Ti in 0.63% F_2/Ar.

As seen with the 10% F_2/Ar experiments bands are present at 792 cm^{-1} and 740 cm^{-1}, due to TiF_4 and possibly TiF_3, Figure 5.05, when titanium was isolated in the 0.63% F_2/Ar matrix. As expected, with the lower concentration the formation of new peaks around 675 cm^{-1} and 635 cm^{-1} begin to appear. These peaks appear to show the formation of lower titanium fluorides, possibly TiF_2 and TiF. The assignment of TiF to the peak present at 635 cm^{-1} seem reasonable with previous observation of this molecule at 640 cm^{-1}, with the allowance of matrix shift. This means that the two peaks present in between these two are likely TiF_2 and TiF_3. If this is the case the TiF_2 peak at 675 cm^{-1} is in very good agreement with the prediction from Figure 5.02 of 670 cm^{-1}. The peaks at 675 cm^{-1} and 740 cm^{-1} always appear as doublets which is likely due to site effects, the peaks at 740 cm^{-1} and 743 cm^{-1}, often appear in different ratios, but when broadband photolysis is applied to the matrix the 740 cm^{-1} peak always grows more than the 743 cm^{-1} peak, while the TiF_4 peak at 792 cm^{-1} always increases the most of all bands when photolysis is carried out. This is most likely due to the photolytic breaking F-F bonds and the fluorine radicals combining with TiF_3, TiF_2, and TiF to form TiF_4.

Early in these series of experiments it appeared that there was a correlation between the 635 cm^{-1} peak and the peaks at 673 cm^{-1} and 678 cm^{-1}. With further experiments the 635 cm^{-1} peak and the 678 cm^{-1} peak show very similar patterns under photolysis and annealing, shown in Figure 5.06.

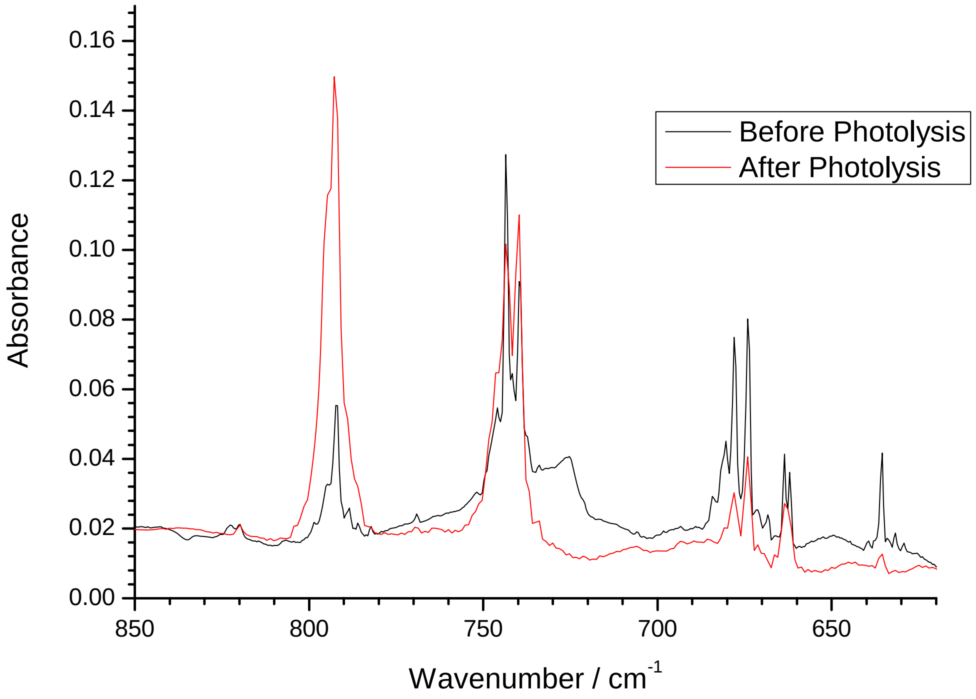

Figure 5.05 IR spectra of titanium isolated in 0.63% F_2/Ar, with the effect of broadband photolysis.

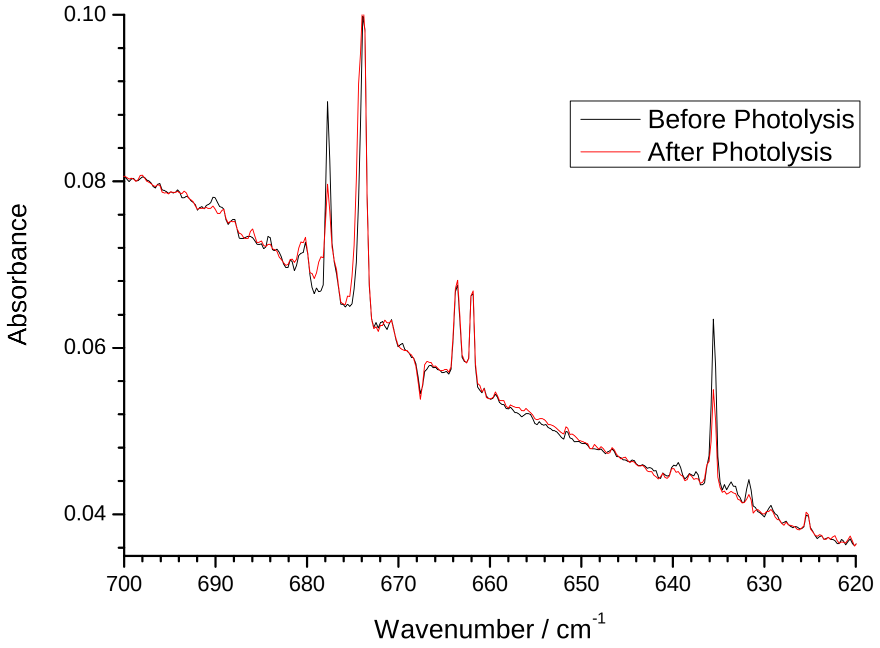

Figure 5.06 IR spectra of titanium isolated in 0.63% F_2/Ar, with the effect of broadband photolysis.

When the matrix is annealed the TiF_4 peak at 792 cm^{-1} always increases in intensity the most, followed by the 740 cm^{-1} peak, the peak present at 675 cm^{-1} nearly always reduces in intensity along with the peak at 635 cm^{-1}. In all of these experiments there is a broad peak around the 725 cm^{-1} area (only present on high resolution spectra), but in later experiments when the temperature of the wire was reduced this was not present, so was likely due to a titanium aggregate species isolated in the matrix.

5.3.2.2.3 Ti in 0.16% F_2/Ar.

The concentration of fluorine was reduced to try and limit the amount of fluorine that could react with titanium and thus favour the formation of the low TiF_x compounds even more than in previous experiments, with the hope of possibly forming more of the peaks assigned to TiF_2 and TiF. One initial interesting point noticeable from the spectra is that the ratio of the peaks at 678 cm^{-1} and 673 cm^{-1} change in certain spectra. In the majority of the 0.63% F_2/Ar experiments the 673 cm^{-1} band was always the predominant peak, but in some of the 0.16% F_2/Ar experiments this ratio appears to have been switched, the 678 cm^{-1} band is the larger one.

Up to this point it appeared that the peaks at 635 cm^{-1} and 673 cm^{-1} were related, however in one experiment carried out after photolysis both the bands at 673 cm^{-1} and 677 cm^{-1} increased in intensity while the 635 cm^{-1} band decreased, but there was also a peak at around 680 cm^{-1} which decreased in intensity. This pattern was not noticed previously due to the 677 cm^{-1} band obscuring the 680 cm^{-1} peak. One problem encountered when trying to assess if this pattern occurred in all the work conducted is the fact that the 680 cm^{-1} peak is often not noticeable in the spectra, either by being obscured by the background noise or simply being in the tail of the 677 cm^{-1} peak, so it is not possible to see if this pattern is followed in other experiments conducted. But this observation does rule out the possibility that the 635 cm^{-1} band is from the same species as the 677 cm^{-1}, 673 cm^{-1}, and 680 cm^{-1} bands.

The expected formation of more of the lower TiF_x compounds was again seen in this series of experiments, Figure 5.07, with the formation of significant amounts of TiF at 635 cm^{-1}. When the matrix was subjected to annealing and photolysis the formation of TiF_4 was still favoured the most with its related peak increasing by the largest factor.

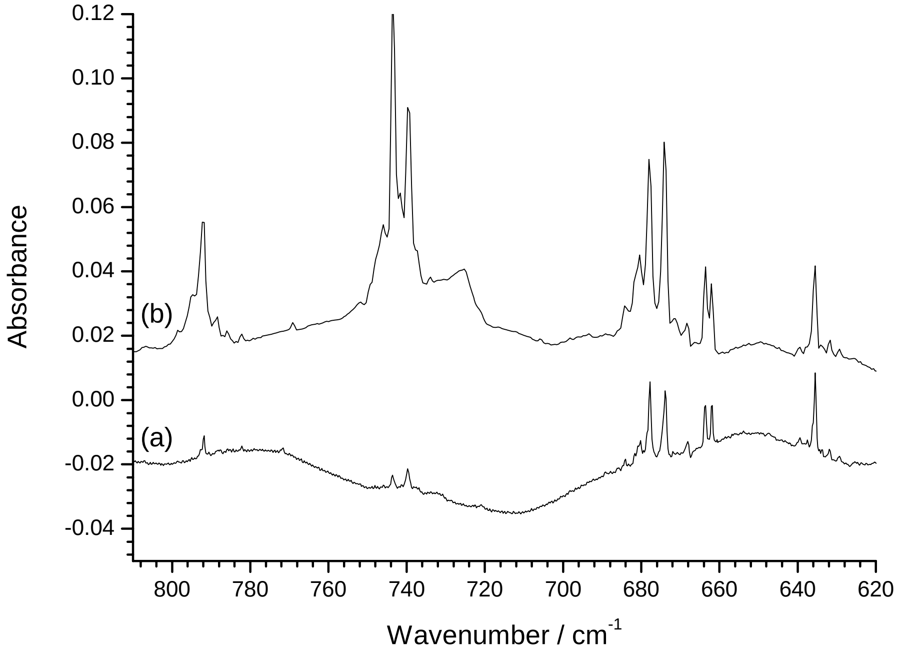

Figure 5.07 IR spectra comparison of different F_2/Ar concentrations, (a) Deposition of titanium in 0.16% F_2/Ar, (b) Deposition of titanium in 0.63% F_2/Ar.

An interesting point noticeable from these experiments is that at lower temperatures TiF_4 appears to be the most favoured TiF_x as it is always the largest at these low temperatures (1.3 V, 40 A furnace setting). But as the temperature increases, with limiting amounts of fluorine, the formation of the lower TiF_x compounds appear to be more favoured. This is likely due to the large amounts of titanium present in comparison to fluorine and so at the higher temperatures the lower TiF_x compounds form due to insufficient fluorine for the formation of larger TiF_x compounds. The results from some experiments have also shown the possibility that TiF_4 and the TiF_3 compounds form on the titanium filament when it is cooling down in the presence of fluorine, and that when the filament is re-heated they vaporise from the filament, thus disguising the amount of the larger TiF_x compounds that are actually forming in the vapour phase and within the matrix.

5.3.2.2.4 Ti in 0.3% and 0.2% F_2/Ar.

The next series of experiments, 0.3% and 0.2% F_2/Ar, were carried out to try and find the perfect spectra for peaks assigned to TiF_2 so that analysis of the isotope splitting would be easier. With this concentration of fluorine the peaks assigned to TiF_3 were the most prominent out of all the peaks present, possibly due to the ratio of titanium atoms to fluorine atoms being the correct ratio for the preferred formation of TiF_3 over TiF_4. But once again upon annealing TiF_4 grows the most showing that it is likely the most stable out of the 4 compounds made and the most favoured energetically.

5.3.2.2.5 Ti in 2% F_2/Ar.

In this experiment the same pattern was observed as with previous experiments, dominance of TiF_3 and TiF_4 in the initially deposition due to the large amount of fluorine present and upon broadband photolysis and subsequent annealing the same pattern of convergence to TiF_4 is once again observed.

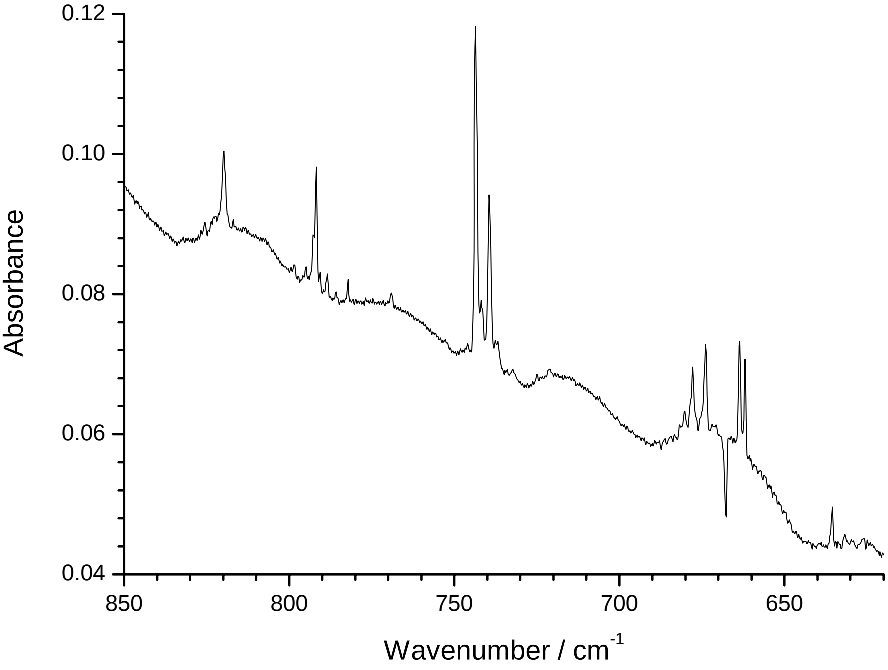

Figure 5.08 IR spectrum showing titanium isolated in 0.3% F_2/Ar.

5.3.2.3 Ti in N_2 and H_2O in Ar.

This experiment was carried out to see if the TiF_2 and TiF_3 peaks assigned were due to any leaks or impurities in the gas resulting in air getting into the system and reacting with the titanium atoms. As nitrogen, oxygen and water are the most likely compounds that the titanium could react with, eliminating nitrogen and water would show that the peaks assigned to TiF_2 and TiF_3 were reasonable. Previously in section 5.3.2.1 oxygen has been shown to produce peaks not that are not related to the peaks assigned to TiF_3 and TiF_2. From the experiments carried out no peaks were observed in the υ_{Ti-F} area of interest, except a peak at 767 cm^{-1} which is never seen when fluorine and titanium are present and is likely due to TiN_2 as previously this was reported to be present at 766.2 cm^{-1} by Chertihin and Andrews.[122] This shows that the peaks produced in this work are solely compounds made up of titanium and fluorine and that no Ti-N compounds are present along with no titanium interactions with water. Figure 5.09 shows the area of the spectrum of interest for nitrogen.

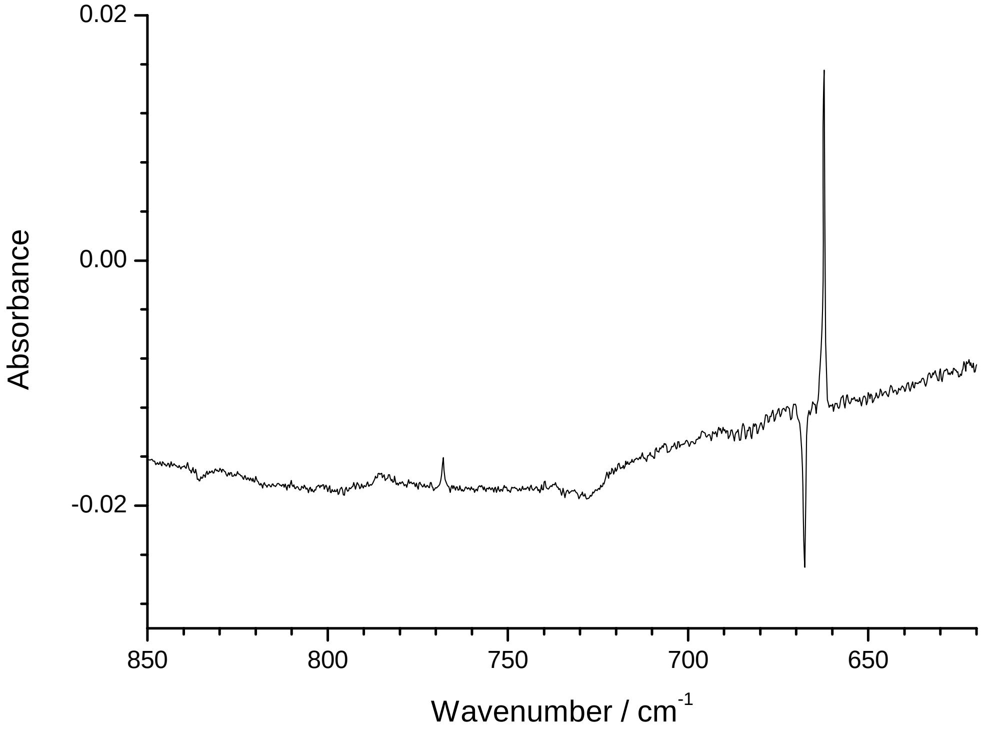

Figure 5.09 IR spectrum showing titanium isolated in 2% N_2/Ar.

5.3.2.4 Assignment of TiF_4 and TiF_3.

5.3.2.4.1 TiF_4 in Ar.

In order to identify the exact position of the TiF_4 band it was decided to use solid TiF_4 in a furnace evaporation configuration, described in section 4.8.2. The spectrum obtained is shown in Figure 5.10, it shows TiF_4 was isolated and its position does indeed correspond with what the assignment of TiF_4 from the literature,[104, 105] showing all previous assignments of TiF_4 in this work to be correct.

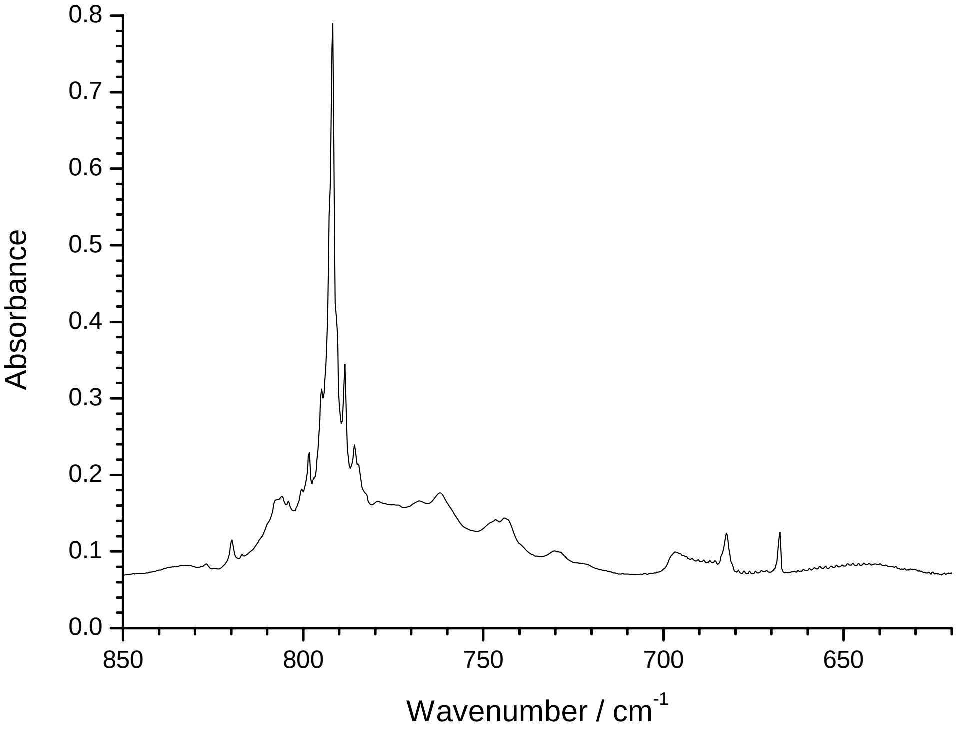

Figure 5.10 IR spectrum of TiF_4 isolated in an argon matrix.

5.3.2.4.2 TiF_3 in Ar.

Initially the exact same experimental set up was used for the TiF_3 series of experiments as was used for the TiF_4 experiments but this was met with limited success. All that was isolated within these experiments was a peak at 784 cm^{-1}, due to TiF_4. This failure to isolate TiF_3 led to new methods being tried to isolate TiF_3. The first of these involved placing TiF_3 inside titanium foil and then heating the new titanium ‘envelope’, the wire used on the furnace was also changed from platinum to tantalum due to tantalum having a much lower vapour pressure and higher melting point allowing the TiF_3 to be heated more. But like before this also failed to help in isolating TiF_3 and again solely isolated TiF_4.

5.3.2.4.3 Mass Spectrometry Work with TiF_3.

Due to the unsuccessful attempt to isolate TiF_3 in argon using matrix isolation with IR, it was decided that the use of mass spectroscopy would allow the determination of the conditions required. Initially TiF_4 was used to test the set up used as the conditions for this were already known.

The MS work on TiF_4 provided another confirmation that the peak shown to be TiF_4 in the IR series of experiments is indeed TiF_4 and not some thermal decomposition of TiF_4. When TiF_3 was tried it showed that the conditions required to isolate TiF_3 were indeed too extreme for the equipment being used and so TiF_3 was never being produced in the previous experiments only TiF_4 was produced as indicated by the IR spectra.

5.3.2.5 UV/Vis Spectroscopy.

The first experiment conducted on the UV instrument was the isolation of TiF_4 in argon. This was done initially so that the bands related to TiF_4 could be ignored in future spectra, as the previous work on the IR had showed TiF_4 would likely be the most abundant TiF_x present. Even though TiF_4 is a white compound it was thought that some charge transfer bands may be present within the spectrometer range. This work however proved to be unproductive; no significant bands were observed aside from a very broad feature at the limit of the spectrometer around the 50,000 cm^{-1} area. So the next step was to try and conduct our previous experiments and see if any peaks could be observed from any other of the species we produced which are coloured.[6, 7]

From previous work done by Gruen and Carstens[118] the spectrum of titanium atoms in a argon matrix was known, so the first part of this work was to reproduce these results. The spectra in Figure 5.11 are essentially identical to those produced by Gruen and Carstens and can be assigned to titanium atoms,[118] these experiments did however achieve a slightly improvement in resolution in the 40,000 cm^{-1} area. Now that these experiments had shown that no Ti_2 was present the next step was to do the same experiment but with a fluorine component to the gas which would produce TiF_x species and hopefully produce charge transfer bands and/or d-d transitions.

From all of the experiments conducted involving 10%, 5%, 1%, 0.2% and 0.1% F_2/Ar gas mixtures no significant bands were produced, aside from the atomic titanium bands when the lower concentration mixtures were used. It was determined that this was likely due to the extremely weak nature of the bands.

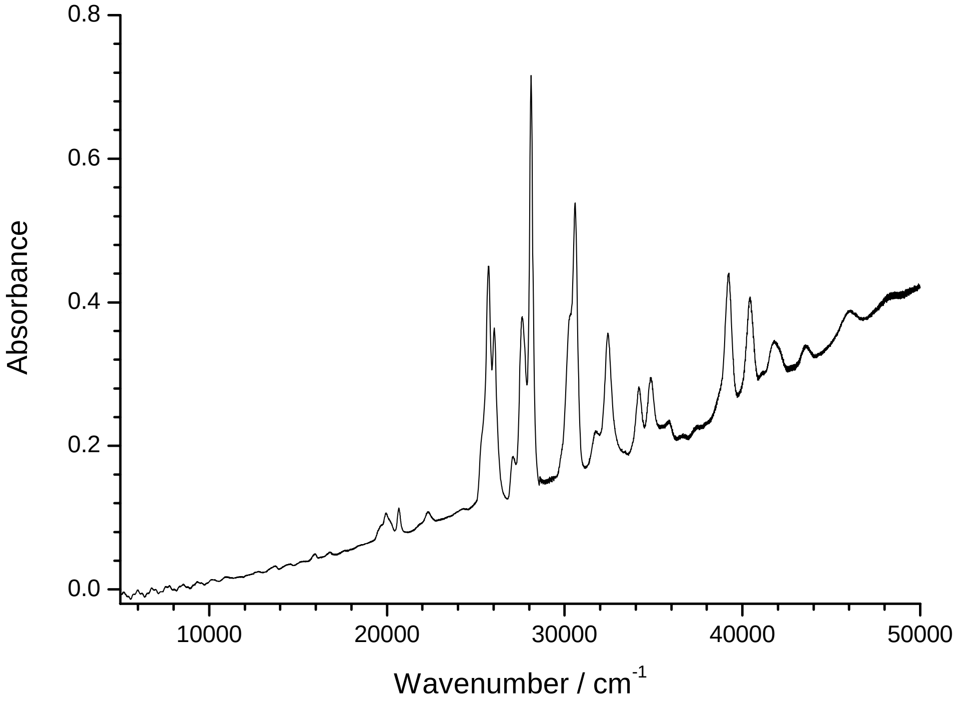

Figure 5.11 UV/Vis spectrum of titanium isolated in argon after 60 minutes.

5.3.2.6 Computational Work.

The final step in this series of experiments was to use the titanium isotope patterns on the peaks produced using high resolution spectra to determine if the assignment of TiF_x compounds was correct. This involved the use of the SOTONVIB program to determine if the molecules assigned to these peaks fit their splitting pattern which would also allow the calculation of the bond angle of TiF_2, although the CO_2 band along with the site effects present will complicate things. Some difficulties encountered with this investigations is the close proximity of the CO_2 bands and the site effects present on the peaks assigned to TiF_2; one thing which should be noted is that when the bond angle gets closer to linearity the nature of the sine function makes determination of bond angles above 155° difficult.

Spectral patterns were initially plotted for the bond angles of 110°, 120°,130°... up to 180°. These were then all plotted onto a graph and compared to the actual spectrum, Figure 5.12, and the relevant calculations tabulated in Table 5.6. Figure 5.12 shows that the peaks assigned to TiF_2 are indeed due to two sites and that the molecule is very close linear, 165°. Figure 5.13 shows a further break down of these two sites to show even more clearly the isotope splitting and how these results correlate to a bond angle of 165°.

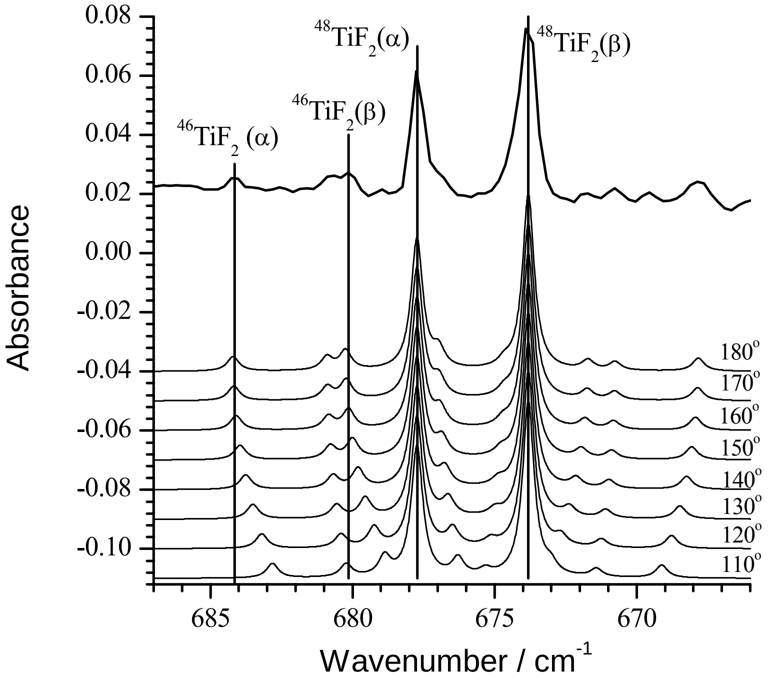

Figure 5.12 SVFF calculated spectra at different angles for TiF_2.

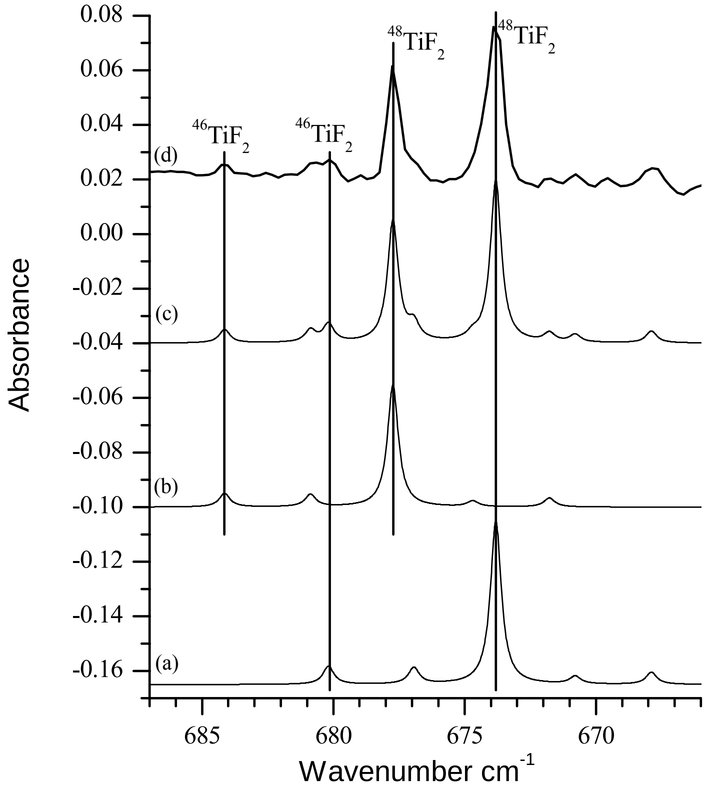

Figure 5.13 Calculated TiF_2 spectral pattern vs. experimental TiF_2 pattern from 0.2 % F_2/Ar, d) IR spectrum of TiF_2 from matrix isolation experiments, c) SVFF calculated spectrum for TiF_2 with a 165^o bond angle, b) α site only, a) β site only.

	Site A	**Calculated 180°**	**Calculated 170°**	**Calculated 166°**	**Calculated 165°**	**Calculated 162°**	**Calculated 160°**	**Calculated 155°**
$^{46}\mathrm{TiF}_2$	684.15	684.20	684.18	684.15	684.14	684.12	684.09	684.03
$^{47}\mathrm{TiF}_2$	680.74	680.90	680.89	680.88	680.87	680.86	680.85	680.82
$^{48}\mathrm{TiF}_2$	677.73*	677.73	677.73	677.73	677.73	677.73	677.73	677.73
$^{49}\mathrm{TiF}_2$	¥	674.66	674.68	674.69	674.69	674.71	674.72	674.74
$^{50}\mathrm{TiF}_2$	671.81	671.71	671.74	671.77	671.77	671.80	671.82	671.87
f_r-f_{rr} / N m^{-1}		286.67	287.64	288.57	288.85	289.86	290.55	292.74
	Site B	**Calculated 180°**	**Calculated 170°**	**Calculated 166°**	**Calculated 165°**	**Calculated 162°**	**Calculated 160°**	**Calculated 155°**
$^{46}\mathrm{TiF}_2$	680.14	680.25	680.22	680.19	680.19	680.16	680.14	680.07
$^{47}\mathrm{TiF}_2$	¥	676.96	676.95	676.94	676.93	676.92	676.91	676.88
$^{48}\mathrm{TiF}_2$	673.81*	673.81	673.81	673.81	673.81	673.81	673.81	673.81
$^{49}\mathrm{TiF}_2$	670.78	670.76	670.77	670.79	670.79	670.80	670.81	670.84
$^{50}\mathrm{TiF}_2$	¶	667.83	667.85	667.88	667.89	667.91	667.93	667.99
f_r-f_{rr} / N m^{-1}		283.37	284.32	285.24	285.52	286.47	287.20	289.36

Table 5.6 Calculated vibrational data for the υ_3 mode of TiF_2. * vibrational data used for SVFF calculation, ¥ obscured by other TiF_2 bands, ¶ obscured by CO_2 band.

SOTONVIB was also used to calculate the splitting pattern for TiF, Figure 5.14. As can be seen the calculated splitting pattern fits perfectly for TiF and is thus clearly the correct assignment. Table 5.7 gives the data in tabulated form.

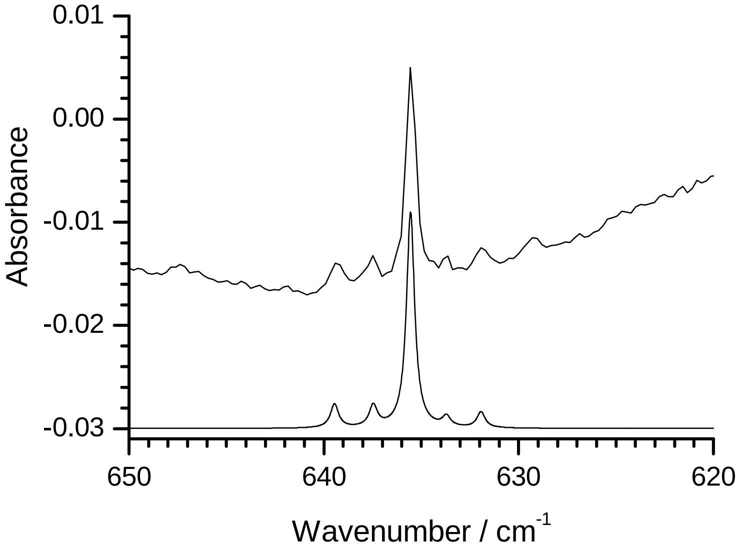

Figure 5.14 Calculated TiF spectral pattern vs. experimental TiF pattern from 0.2% F_2/Ar.

A isotope pattern was observed for TiF_3 but it was difficult to fit the pattern to the calculated splitting pattern obtained. This pattern is shown in Appendix 3.2.

	Observed	**SVFF Calculated**
^{46}TiF	639.41	639.45
^{47}TiF	637.42	637.46
^{48}TiF	635.55*	635.55
^{49}TiF	633.71	633.71
^{50}TiF	632.13	631.93
f_r-f_{rr} / N m^{-1}		320.71

Table 5.7 Observed and calculated data for TiF, * vibrational data used in SVFF calculation.

5.3.2.7 Discussion.

From the combination of IR spectra and computational calculations the results obtained clearly indicate that TiF_4, TiF_3, TiF_2, and TiF have all been formed. Further work conducted on various pure gas mixture, including, oxygen, water and argon showed that no peaks were present in the area of interest without the presence of both fluorine and titanium. From the work conducted by Beattie *et al.*,[103, 104] and Ault[105] TiF_4 can be clearly assigned to the peak at 792 cm^{-1}. The peak present at 740 cm^{-1} can be assigned to TiF_3, and from the calculations performed the peak at 675 cm^{-1} can be definitively assigned to TiF_2. Similarly the peak at 635 cm^{-1} can be assigned to TiF due to the evidence presented by the computational work. So this work is the first evidence of the formation TiF_2 and TiF within a matrix environment and the first calculation of the bond angle of approximately 165^{o}, or effectively linear showing that it is likely that all of the first row transition metal fluorides are in fact linear within a matrix and that only CaF_2 is a bent molecule. Figure 5.15 shows how these results obtained fit with the previous assignment of TiF_2 by Hastie *et al.*[87] and other transition metals. This graph shows that the results obtained within these experiments correlates with the other transition metal difluorides much more than the previous assignment by Hastie *et al.*[87] and so confirms the conclusions.

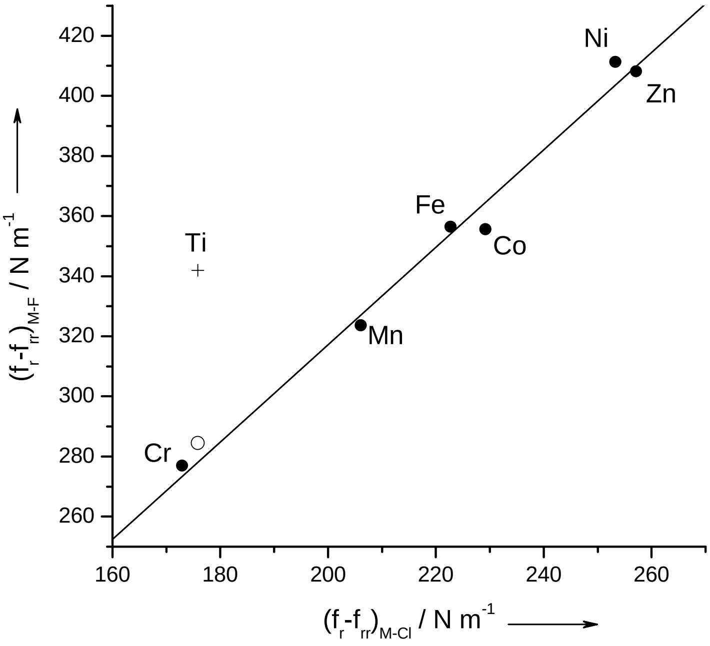

Figure 5.15 The Plot of SVFF force constant (f_r-f_{rr}) from the ν_3 values for MF_2 versus those of MCl_2. Assuming linearity; it moves further away from the line if the molecule is bent, the ○ represents the results from this work.[2, 3, 57]

5.3.3 Vanadium Fluorides in a Matrix.

As stated earlier work with vanadium and fluorine is extremely challenging due to the fact that neither posses isotopes and thus assignment of any vanadium fluorides is very difficult. Early work in 1963 by Cavell and Clark[123] studied many of the physical properties of VF_5 in the gas phase. This work on the IR spectra[124] of VF_5 by Cavell and Clark proved to be inconclusive and so further work was conducted in 1966 by Claassen and Selig[125] who observed a cluster of peaks at 800 cm^{-1}. They assigned this to two stretching motions, with one centred at a Q branch at 784 cm^{-1} and the other at 810 cm^{-1}, with the peak in the middle resulting from a superposition of the branches of the two peaks based on a D_{3h} symmetry.

From the previous gas phase work conducted on VF_5 it was suggested that VF_5 would also have the D_{3h} symmetry from gas phase data in a matrix. However, work conducted by Brisdon *et al.*[126] has shown that the symmetry taken in the gas phase is not necessary what is formed in a matrix environment, as $MoCl_5$ forms D_{3h} in the gas phase but takes C_{4v} symmetry in a matrix. The first reported study of VF_5 in a matrix was conducted by Blinova *et al.*, they managed to isolate VF_5 in solid argon, neon, krypton, and xenon. [127, 128] They concluded, based on D_{3h} symmetry, that peaks present at 806 cm^{-1}, with a shoulder at 804.6 cm^{-1}, were due to the υ_5 (E') of VF_5 and a peak at 774 cm^{-1}, with a shoulder at 772 cm^{-1}, was due to υ_3 (A_2''). In this paper Blinova *et al.* also assigned peaks at 730 cm^{-1} to υ_3 (E') of VF_3,[128] based on D_{3h} symmetry, and surprisingly peak at 733.4 cm^{-1} to υ_3 (B_1) of VF_2, based on C_{2v} symmetry. Although they also claimed to have isolated aggregate complexes of VF_4, they did not isolate the VF_4 molecule although they determined its structure to be T_d. Within this work and previous work by Claassen and Selig[129] both have shown that a peak present at 798 cm^{-1}, due to the υ_4 (E) of VOF_3, can cause considerable problems and can complicate the VF_5 spectrum due to its close proximity to the peak υ_5 (E') of VF_5 around 800 cm^{-1}. Work by Hope upon VF_5 also found it to have stretching frequencies at 802.0 cm^{-1} and 771.0 cm^{-1} and from this assign VF_5 to a D_{3h} symmetry.[130]

Data on transition metal trifluorides is limited, with most work carried out on CrF_3. The earliest matrix isolation work on VF_3 was conducted by Hastie *et al.* in 1969.[131] But due to the correction[103] of Hastie *et al.*[87] assignment of TiF_3, Bukhmarina *et al.*[97] also looked at the Hastie *et al.*[131] assignment of VF_3 and VF_2. Hastie *et al.* initially determined that VF_2 had a υ_3 antisymmetric stretch at 733.2 cm^{-1} in an argon matrix and they estimated the bond angle to be 150°. As a result of these conclusions work by Blinova *et al.*[127] also assigned the peak at 733 cm^{-1} to VF_2 in work they conducted on VF_5. Bukhmarina *et al.*[97] then started to look at the assignment of the peak at 733.2 cm^{-1} to see if this was VF_3 instead of VF_2. With use of mass spectroscopy data along with IR results they showed that the peak at 733.2 cm^{-1}, with a shoulder at 731.8 cm^{-1}, was as a result of VF_3 and not VF_2 as Hastie *et al.* had assigned it. Thus leaving VF_2 unassigned within a matrix environment, very little work has also been conducted on VF_4.

Within the literature no experiments have been carried out upon VF within a matrix environment and the only work conducted upon this molecule are computational calculations and emission spectroscopy stated above.[57] From the work conducted by Koukounas *et al.* an estimation of the stretching frequency for VF ranges from 636 cm^{-1} to 650 cm^{-1} for the $^5\Pi$ ground state, depending upon which basis sets were used.[83]

5.3.4. Conclusions from Literature.

From the work conducted by Blinova *et al.* VF_5 has two stretching bands present at 805 cm^{-1} and 773 cm^{-1},[128] these assignments are agreed with by Hope.[130] VF_3 has a band present at 733 cm^{-1} as previously shown by Bukhmarina *et al.*.[97] The other vanadium fluorides have not been isolated successfully in a matrix environment, computational calculations predict that VF should have a stretching frequency between 650 cm^{-1} and 636 cm^{-1}.[83] VF_2 and VF_4 have little computational work conducted upon them, Wang and Schwarz predicted VF_2 to linear and have stretching frequencies at 630 cm^{-1} (υ_{sym})and 773 cm^{-1} (υ_{asym}), but due to the success of the use of Figure 5.02 seen with titanium this was again used for vanadium. This method, as can be seen from Figure 5.16, predicts a value of 707 cm^{-1} for the stretching frequency of VF_2.

5.3.5 Vanadium Isolated in F_2/Ar.

The main aim of this work was to see if it was possible to isolate and characterise VF_2 and VF due to the success attained with titanium. VF_5 and VF_3 have previously been isolated in a matrix environment by Blinova *et al.*,[128] and Hope,[130] and as stated previously VF_3 has been the most comprehensively computationally studied compound out of the vanadium fluorides due to its Jahn-Teller distortion.

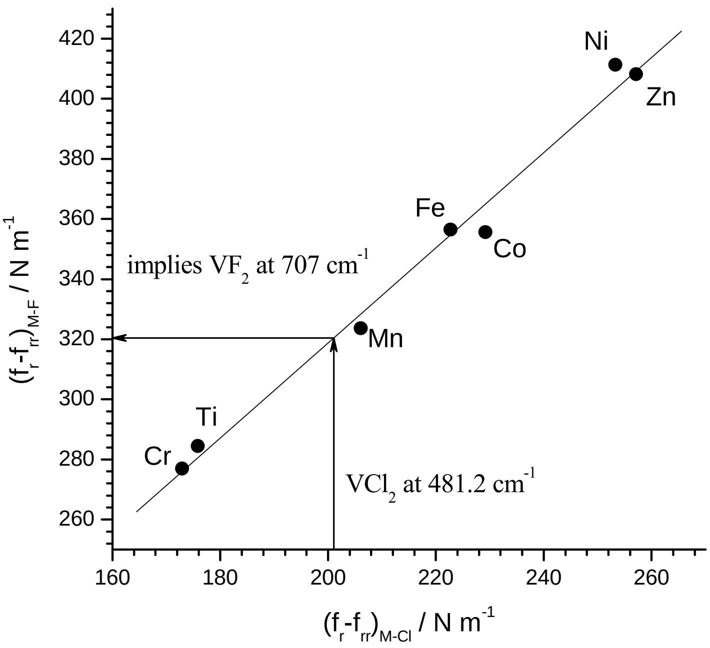

Figure 5.16 Plot of SVFF force constant (f_r-f_{rr}) from the ν_3 values for MF_2 versus those of MCl_2.[2, 3, 57]

With the use of group theory the Γ_{str} can be predicted to see what would be expected for the various vanadium halides, and is presented in Table 5.8 and are is given in more detail Appendix 1.

	Γ_{str}	IR Active
VF	Σ^+	Σ^+
VF_2		
C_{2v}	$A_1 + B_2$	$A_1 + B_2$
$D_{\infty h}$	$\Sigma_g^+ + \Sigma_u^+$	Σ_u^+
VF_3	$A_1' + E'$	E'
VF_4	$A_1 + T_2$	T_2
VF_5	$2A_1' + E' + A_2''$	$E' + A_2''$

Table 5.8 Table showing the Γ_{str} for the vanadium halides in likely geometries.

5.3.5.1 V in Ar.

The first part of the work concentrated on determining the optimum conditions for thermal evaporation of the vanadium wire. As vanadium has a slightly lower vapour pressure than titanium the voltage going through the wire would likely need to be slightly higher.[132]

To determine the optimum conditions the first series of experiments performed involved isolating vanadium in argon and studying the results with UV/Vis spectrometry. This work had previously been done by De Vore[133] and Ford[134] who both had isolated and assigned peaks of the UV spectrum of vanadium. Figure 5.17 shows vanadium isolated in argon at 12 K, this spectrum shows essentially the same spectra as that observed by De Vore[133] and Ford[134] but with a much higher resolution. This also showed that little, if any, dimers were formed within the experimental procedure, as dimers appear below 20,000 cm^{-1} in the spectrum.[134] A large number of peaks are produced above 35,000 cm^{-1} are due to a $^4F_{3/2}$ ground state with a large number of spin-allowed transitions. The three main peaks within the UV/Vis spectrum are assigned as a $^4D_{1/2} \leftarrow {}^4F_{3/2}$ at 33,750 cm^{-1}, the largest peak at 31,810 cm^{-1} is assigned to a $^2P_{3/2} \leftarrow {}^4F_{3/2}$ transition and the final large peak at 26,790 cm^{-1} to a $^4F_{3/2} \leftarrow {}^4F_{3/2}$ transition.[134]

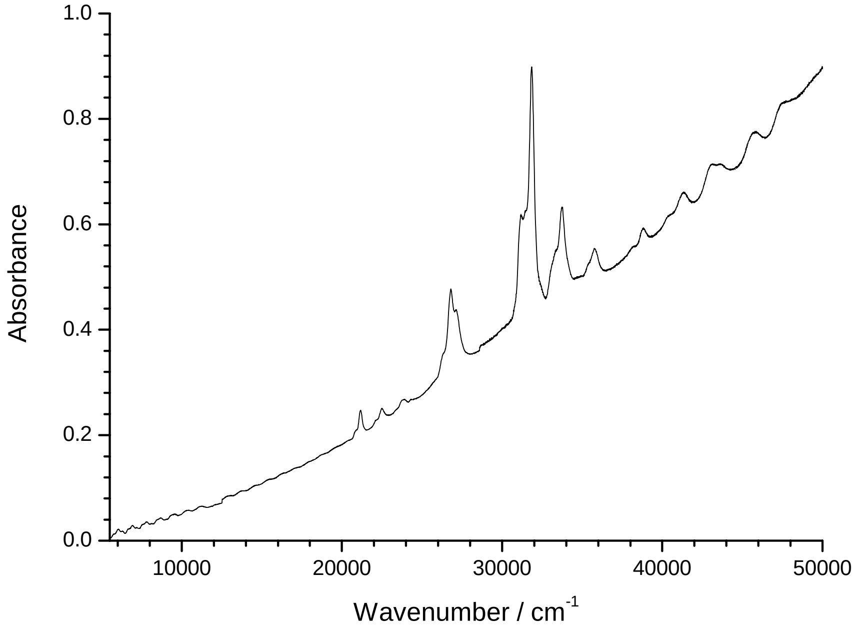

Figure 5.17 UV/Vis spectrum of vanadium isolated in argon after 60 minutes.

5.3.5.2 V in 10%, 1%, 0.18% and 0.055% F_2/ Ar.

Once the conditions for the vaporisation of vanadium were known the next series of experiments involved the isolation of vanadium within a matrix gas containing 10 % F_2/Ar. This was the first experiment in which vanadium and fluorine were combined together. If previous results with titanium are considered it would be expected that only the most stable higher vanadium fluorides should be isolated, meaning that VF_5 and VF_3, VF_4 should also be present although this has not been seen in previous experiments within the literature.[97, 128] From the literature VF_5 should be present around 805 cm^{-1} and 773 cm^{-1}, while VF_3 should be around 733 cm^{-1}.[128]

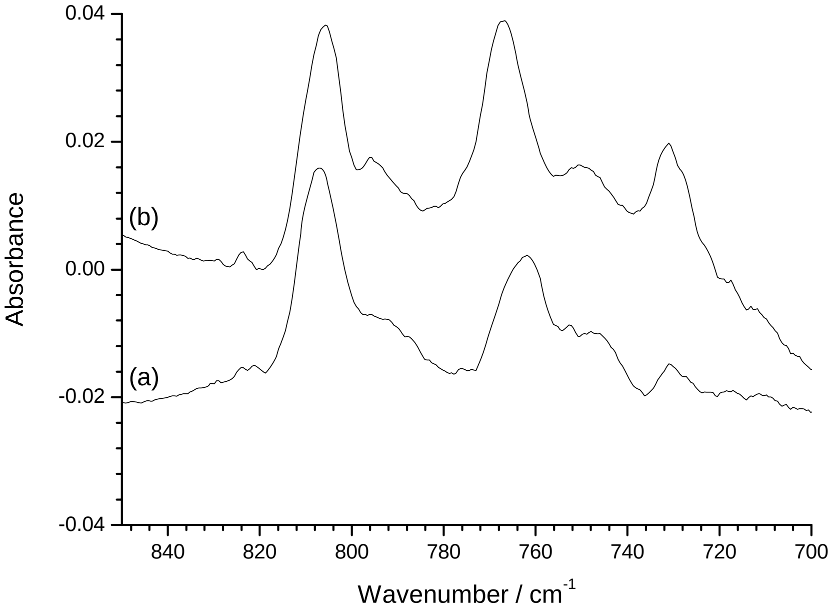

Figure 5.18 IR spectra showing vanadium isolated in 10% F_2/Ar, (a) after annealing conducted, (b) before annealing.

As can be seen from Figure 5.18(b) peaks are present at 805.6 cm^{-1}, 767.1 cm^{-1}, and 731.1 cm^{-1}, there is the presence of smaller peaks at 795.6 cm^{-1} and 750.4 cm^{-1}. From the literature these peaks at 805.6 cm^{-1} and 767.1 cm^{-1} can be assigned to VF_5, and that at 731.1 cm^{-1} to VF_3.[128] Within the literature site effects have often been observed with experiments conducted upon these molecules,[128] however there is also the possibility that these peaks could be due to VOF_3.[135] This was however found not to be the case as the peaks obtained do not correlate with the observed bands for VOF_3, shown in Appendix 3.3.[135] Selig and Claassen observed bands at 1057.8 cm^{-1}, 806.0 cm^{-1}, and 721.5 cm^{-1} for VOF_3 and within this work these bands were not observed and so the peaks present at 795.6 cm^{-1} and 750.4 cm^{-1} are assigned to site effects.[128] When the matrix was subjected to broadband photolysis all of the bands present increased slightly but no new bands appears in the $\nu_{V\text{-}F}$ region. When the matrix was annealed to 20 K the bands at 731.1 cm^{-1} and the band at 767.1 cm^{-1} decreased slightly and the band due to VF_5 at 767.1 cm^{-1} appears to shift a small amount to 761.6 cm^{-1}, but again no new bands appear lower in the spectrum. This shift in only one of the bands due to VF_5 could imply that another band is present underneath the asymmetric stretch of VF_5, Figure 5.18(a).

Due to only the higher vanadium fluorides being present with a 10% F_2/Ar gas mixture, as expected, the concentration was reduced to 1% F_2/Ar as this would limit the amount of fluorine around the vanadium atoms and favour the formation of lower vanadium fluorides. As can be seen from Figure 5.19, VF_5 and VF_3 have been isolated but no signs of any lower VF_x compounds forming. The bands previously assigned to VF_5 have shifted to 804.5 cm^{-1} and 771.2 cm^{-1} and the peak assigned to VF_3 moved to 733.2 cm^{-1}. There also appears to be splitting of the peak due to VF_3, this can again be assigned to Jahn-Teller distortion as previously seen.[97, 130, 136] A similar pattern was observed when photolysis and annealing was carried out as was witnessed in the 10% F_2/Ar gas mixture. Upon photolysis all bands increase by a small amount and upon subsequent annealing the band at 804.9 cm^{-1} increases further and the band at 771cm^{-1} increased slightly and shifts again but the band at 733.2 cm^{-1} decreases in size. This shows VF_5 increasing in the matrix upon annealing and photolysis while VF_3 is decreasing, likely due to free fluorine atoms reacting with VF_3 to form VF_5, and the shift in the asymmetric stretch of VF_5 could indicate the presence of another band underneath the VF_5 band.

The fluorine concentration was reduced further to 0.18% F_2/Ar to restrict the amount of fluorine around the vanadium atoms even more. As can be seen from Figure 5.20, this again failed to produce any lower VF_n and only produced VF_5 and VF_3, peaks at 803.7 cm^{-1}, 795.9 cm^{-1}, 773.5 cm^{-1}, and 732.7 cm^{-1}. The annealing and photolysis behaviour is the same as was achieved for the previous higher concentration experiments.

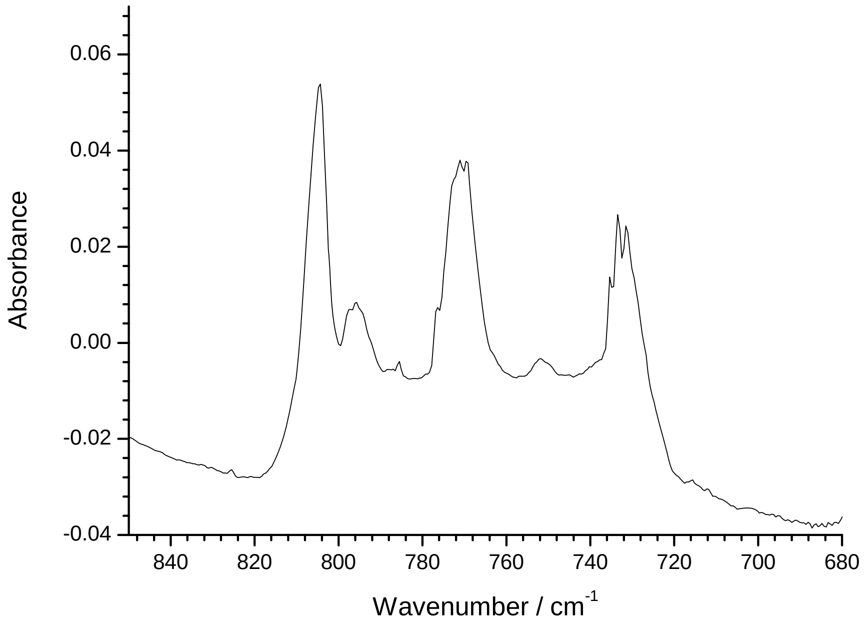

Figure 5.19 IR spectrum of vanadium isolated in 1% F_2/Ar.

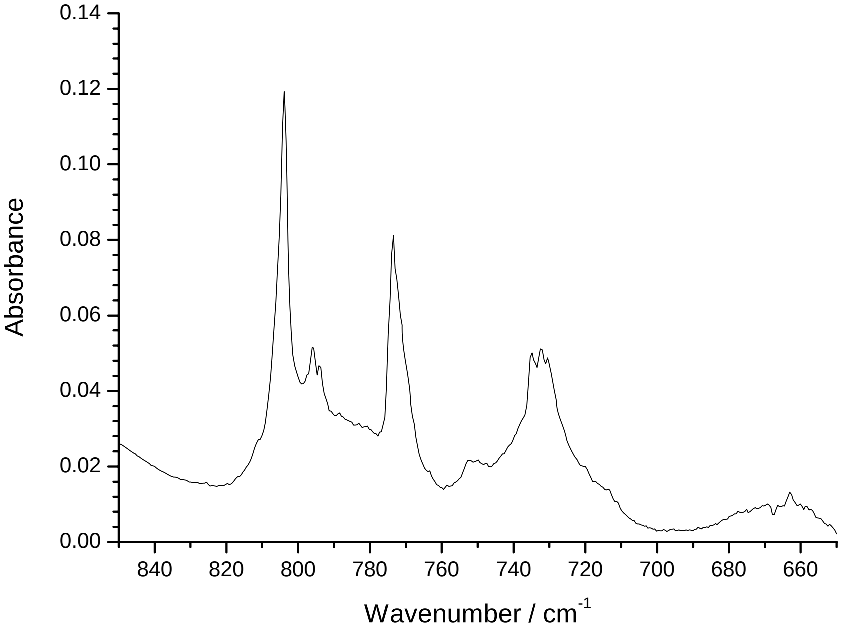

Figure 5.20 IR spectrum of vanadium isolated in 0.18% F_2/Ar.

5.3.5.3 New Methods of Vanadium Evaporation.

Due to the unsuccessful attempts to isolate VF_2 with the technique that worked with titanium, various new techniques were tried to try and isolate the less stable vanadium fluorides. The main idea behind these techniques was to prevent the fluorine from reacting with the hot filament as it was believed that this was occurring as previously seen in experiments with titanium. From the work with titanium it was shown that if fluorine reacted with the hot filament a layer of the most stable titanium fluoride was formed and so this was likely happening with vanadium too. This led to new experimental methods being developed to try and reduce the amount of fluorine reaching the filament and thus prevent this reaction from happening.

5.3.5.3.1 V in a F_2 and Ar 'Sandwich' Method.

The first such technique employed a 'sandwich' like structure of the matrix. This involved isolating a layer of vanadium atoms in argon and then a layer of F_2/Ar followed by a further layer of vanadium in argon. This prevented the fluorine reacting with the hot filament as the fluorine source was never open when the filament was turned on, Figure 5.21. To promote reaction within the matrix photolysis was conducted to release free fluorine within the fluorine layer and then mixing of the layers was attempted through annealing. The idea behind this technique was to prevent the vanadium atoms reacting with the fluorine in the gas phase and on the filament and try to make the reaction occur within the matrix to see if the results would be any different. Although numerous attempts were made with this technique, by altering the layer thickness and the temperature of annealing, this experiment failed to provide any results which showed the formation of any of the vanadium fluorides, even including the more stable VF_5 and VF_3. The probable reason that these experiments failed was due to the thickness of the layers. The thicker the layer the less likely it is that annealing would allow the vanadium atoms and fluorine to react together. A possible solution would be to increase the frequency of switching between the two flows, this was not possible with the apparatus used within these experiments.

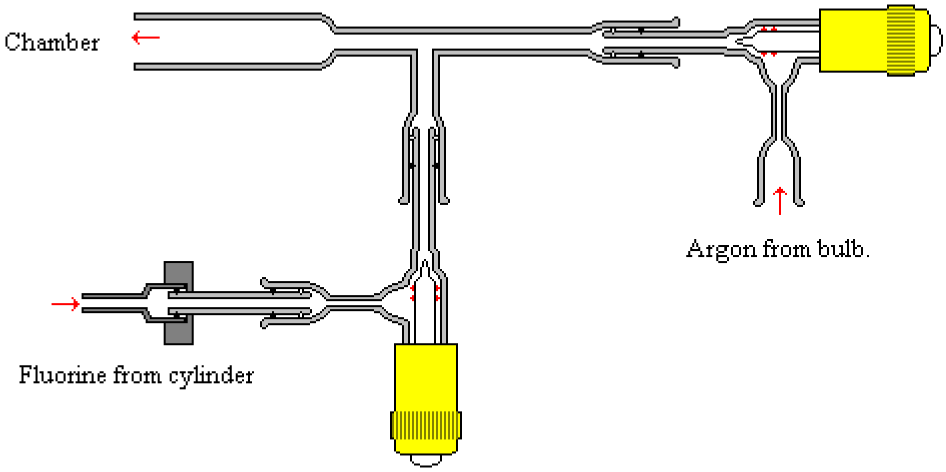

Figure 5.21 Diagram of the experimental set up used for the 'sandwich' technique.

5.3.5.3.2 V with Protective Ar and F_2/Ar.

The next experiment technique tried a different approach to prevent fluorine reacting with the filament by limiting the amount of fluorine that could actually reach the heated filament but still having both the filament on and the fluorine flowing at the same time. This was achieved by having a 'protective' argon atmosphere around the vanadium wire. This was achieved by passing argon over the filament and having a small amount reaching the chamber through the copper disc and then heating the filament and opening the fluorine thus preventing the fluorine from reaching the heated filament and only reacting with vanadium atoms which have been vaporised and passed through the copper disc, see Figure 4.13. The copper disc was the most important part of these experiments as it not only acted as a heat shield, like before, but also acted as a throttle or barrier for the creation of the protective atmosphere. It was hoped that this protective atmosphere would only allow a gas phase reaction to occur and thus allow the formation of lower vanadium fluorides. One possible issue with the use of this technique was the possibility that vanadium could form divanadium and further confuse the spectra and make it even less likely to form lower VF_x, or that the vanadium would react with impurities in the argon.

Using this technique, Figure 5.22, numerous new peaks were produced at 822.7 cm^{-1}, 792.8 cm^{-1}, 768.7 cm^{-1}, and at 710.8 cm^{-1}. The peaks due to VF_5 and VF_3 are removed from the spectra and only a peak at 768.7 cm^{-1} was present in the areas that VF_5 and VF_3 would be expected. By altering the concentration of the fluorine little change was observed with the peaks. Various different concentrations were used including, 10%, 2% and 0.22%, but these concentrations would not be the exact concentrations seen within the matrix due to dilution occurring due to the 'protective' argon environment used around the vanadium filament bleeding into the chamber. The peak at 768.7 cm^{-1} is the only peak present with this method that was close to a previous assignment of VF_5 or VF_3. But previously upon annealing the peak at 770.0 cm^{-1} was shown to shift down by a few wavenumber. This pattern was previously rationalized by the possible presence of VF_4 underneath the peak and with the presence of this peak at 768.7 cm^{-1} now without any of the other VF_5 or VF_3 peaks could possibly show the formation of VF_4 within this series of experiments and the previous attempts. Figure 5.16 had predicted a value of 707.0 cm^{-1} for the position of VF_2, due to this and the previous accuracy of this method the peak present at 710.8 cm^{-1} is tentatively assigned to VF_2. This leaves the peak at 822.7 cm^{-1} which is often observed within the spectra, with both titanium and vanadium, and so cannot be assigned to a vanadium fluoride and is thus rationalised as a fluorine complex, like OF_2, the other peak seen with OF_2 at 926.0 cm^{-1} also present.[112, 114]

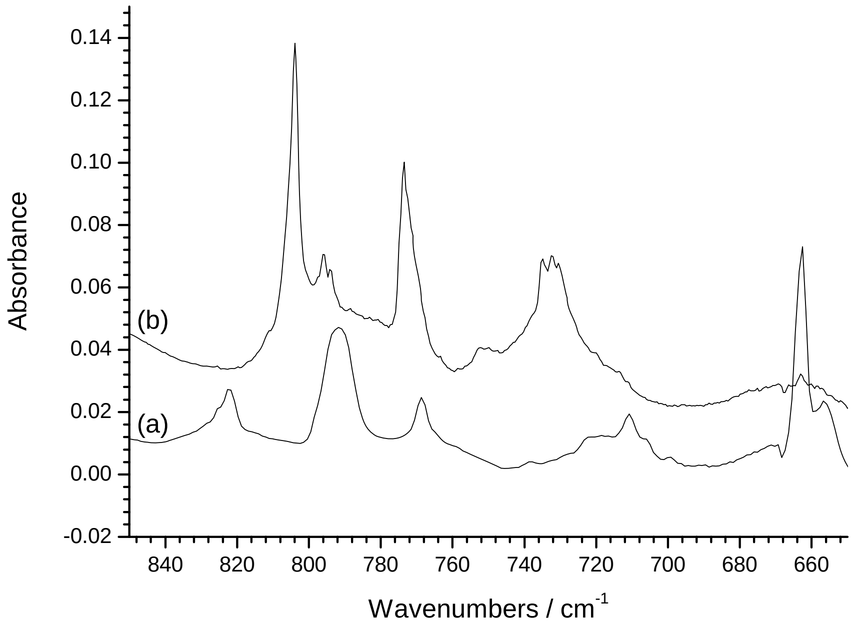

Figure 5.22 IR spectra comparing the different results achieved with the two techniques used for the isolation of vanadium in F_2/Ar matrices, (a) protective argon environment 2% F_2/Ar, (b) normal deposition 0.18% F_2/Ar.

5.3.5.4 Discussion.

From the initial results obtained using the standard procedure it is clear that VF_5 and VF_3 are the most stable compounds producible within a matrix for vanadium under these conditions. The peaks at 805.0 cm^{-1} and 776.0 cm^{-1} due to VF_5 consistently increased upon photolysis and upon annealing, likely due to excess fluorine combining with VF_3 within the matrix. This is supported by the fact that VF_3 decreases upon photolysis and annealing. An interesting fact that occurs upon photolysis and annealing is that the peak at 766.0 cm^{-1} also shifts slightly. This could be due to this peak obscuring a peak due to VF_4 which should be around this area. Unfortunately with the use of this technique this could not be proven as the VF_5 peak was always the most dominant and always obscured any possible peaks close by.

If the VF_3 peak is examined more closely it appears that there are two sites present for this molecule, although there is no change in the ratio of the peaks upon either photolysis or annealing. These two peaks for VF_3 have been observed previously by Bukhmarina *et al.*[97] and were assigned to matrix effects, but Solomonik *et al.*[136] suggest that this effect is in fact due to a weak Jahn-Teller distortion of the VF_3 molecule, based upon observations of MnF_3[137-139] and computational calculations. The peaks observed at 795.0 cm^{-1} and 750.0 cm^{-1} are also due to site effects of VF_5 as previously seen by Blinova *et al.*.[128]

When the 'protective' argon technique was used a new large peak was produced at 792.8 cm^{-1} this peak had previously not been seen in any of the spectra of past experiments, a further peak at 710.8 cm^{-1} was also produced using this technique, although the intensity of this peak was much less. There was also a small peak present at 768.7 cm^{-1} which would be the peak that caused the shift in the VF_5 peaks in the previous experiments possibly indicating this is VF_4. The peak at 710.8 cm^{-1} is assigned to VF_2 on the basis of the predicted position of VF_2 from Figure 5.16. The peaks present at 792.8 cm^{-1} and 768.7 cm^{-1} are assigned to VF_4 which could undergo Fermi resonance, as previously observed with VCl_4 by Beattie *et al.*.[140] There is also the possibility that VF_4 could undergo Jahn-Teller distortions as previously reported in calculations by Solomonik and Pogrebnaya.[141] These assignments also shows that when this protective atmosphere is used only even vanadium fluorides are formed, VF_4 and VF_2, while when the normal conditions are used only odd vanadium fluorides form, VF_5 and VF_3, leaving an unanswered question as to why this would occur.

Fermi resonance is a process which occurs if the fundamental and an overtone, or combination, are at a very similar energy and their vibrational wave functions have the same symmetry. This then pushes the two bands apart from where they would be expected and it also involves mixing of the intensities of the two transitions.[142]

5.3.6 Conclusion.

From this work conducted upon first row transition metal fluorides it is clear that TiF_2 is a linear molecule, which agrees with the prediction made by Beattie *et al.*.[103] This result means that there was then no evidence for the non linearity of any first row transition metal dihalides within a matrix environment.

From this work the stretching frequencies of all of the titanium fluorides can now be assigned. TiF_4 can be clearly assigned to the peak at 792.0 cm^{-1}, TiF_3 can be assigned to the peak at 740.0 cm^{-1}, and from computational calculations the peak present at 675.0 cm^{-1} can be definitively assigned to TiF_2. Similarly the peak at 635.0 cm^{-1} can be definitively assigned to TiF due to the evidence presented by the computational work conducted.

The work with vanadium was less successful than the work conducted upon titanium and it appears that it is much more difficult to isolate lower vanadium fluorides than observed with other transition metals using this technique of thermal evaporation. VF_5 and VF_3 were successfully isolated in agreement with previous work,[97, 125, 128, 130] and it appears as if VF_3 is also slightly Jahn-Teller distorted.[136]

When vanadium was isolated in F_2/Ar matrices with the use of a ‘protective’ argon atmosphere around the filament new bands were produced which can be tentatively assigned to VF_4 and VF_2. The assignment of a peak produced at 710.8 cm^{-1} to VF_2 is based on the use of Figure 5.16 which predicted a value of 707.0 cm^{-1} based upon the other first row transition metal halides. The assignment of VF_4 to peaks at 792.8 cm^{-1} and 768.7 cm^{-1} is based on previous observation of Fermi resonance on VCl_4 by Beattie *et al.*.[140] They observed two bands at 501.6 cm^{-1} and 474.5 cm^{-1} due to the υ_3 and a $\upsilon_1 + \upsilon_4$ combination of VCl_4. There is also the possibility that VF_4 could undergo Jahn-Teller distortions as previously reported in calculations by Solomonik and Pogrebnaya,[141] which would allow a second possible route for VF_4 to produce two bands. These peaks were only ever present when the protective atmosphere was used and so the assignment is tentative.

5.3.7 CrF_2 and $CrCl_2$ Investigations.

Recent work by Hargittai *et al.*,[4, 5] published after the work conducted upon TiF_2 described above was published,[143] has suggested that CrF_2 and $CrCl_2$ are both bent and not linear as previous work has suggested.[144-146] Previously computational work on $CrCl_2$ by Bridgeman and Bridgeman[29] suggested that the electronic structure of $CrCl_2$, $\delta_g < \pi_g < \sigma_g$, derived from crystal field theory is incorrect and that $\delta_g < \sigma_g < \pi_g$ is more probable as also predicted by Wang *et al.*[57] shown earlier, Figure 5.24.

Figure 5.24 shows that the metal 3d orbitals transform as $\sigma_g + \pi_g + \delta_g$. There are no low lying ligand orbitals of δ symmetry and so the d_δ orbitals are non-bonding. The d_π functions interact with the chlorine based π_g combination to give rise to the anti-bonding $2\pi_g$ orbitals. The d_σ orbital suffers two perturbations: an anti-bonding interaction with the chlorine σ_g combination and a stabilization due to the interaction with the 4s dominated $8\sigma_g$ orbital. They also suggested that ligand induced 3d-4s hybridization from the partially filled 3d sub-shell on chromium lowers the energy of the σ_g orbital and the strong π donating properties of the halide ligands tends to increase the energy of the π_g orbital.[29]

From this work Bridgeman and Bridgeman[29] assigned the ground state to a linear $^5\Pi_g$ $(\delta_g^2\sigma_g^1\pi_g^1)$. This was different from the previously assigned ground state of $^5\Sigma_g^+$ $(\delta_g^2\sigma_g^0\pi_g^2)$,[32, 46, 47, 147] Wang *et al.*[57] have also predicted this ground state, $^5\Pi_g$, in calculations they have performed. Within this work Bridgeman and Bridgeman also suggested that the calculated linear $^5\Pi_g$ ground state correlates closely with the experimental data, but they also noted that there is a flat potential energy surface in these calculation.

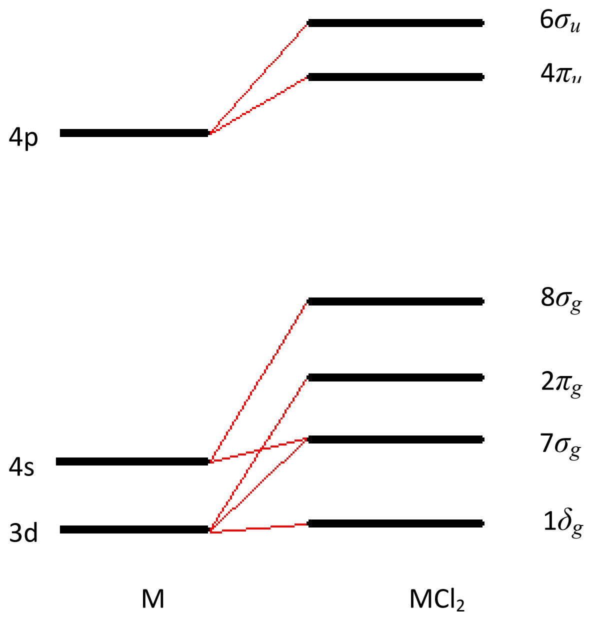

Figure 5.24 Chromium valence orbitals and the effect of interaction with chlorine orbitals in linear $CrCl_2$.[29]

Previous electron diffraction studies on $CrCl_2$ by Hargittai *et al.*[148] appear to indicate that the geometry of $CrCl_2$ is linear along with the fact that the absence of symmetric stretching bands in IR studies also appear to indicate linearity.[144-146] Another electron diffraction study by Hargittai *et al.*[26] have suggested a bond angle of 110° even after allowance for shrinkage and for the presence of dimers. A computational study by Jensen[30] concluded that the $^5\Pi_g$ ground state splits into a $^5A_2$ and a $^5B_2$ when the $CrCl_2$ molecule bends, and that the $^5B_2$ state is the more stable, this bending is a result of a Renner-Teller distortion. But again this state is in a flat energy curve making determination of the exact energy minimum difficult. Jensen also noted that vibrational analysis of the bent configuration revealed larger isotopic shifts for the asymmetric stretch than has been observed in matrix isolation IR studies suggesting that $CrCl_2$ is linear when trapped within a matrix environment.[30]

The two papers by Hargittai *et al.*[4, 5] have re-analysed previously unpublished electron diffraction data originally collected in the 1980s. They used new high level computational calculations to re-examine the data and draw new conclusions. They determine that the $CrCl_2$ molecule under goes Renner-Teller symmetry breaking to form a bent molecule with a bond angle of $149^o \pm 10$ and an electronic ground state of $^5B_2$. A problem with this work, as stated by Hargittai,[4] is that electron diffraction gives a thermally averaged structure and so even if the molecule was truly linear it would still show a slightly bent structure in electron diffraction studies. The study that Hargittai *et al.*[5] conducted upon CrF_2 again states that this molecule undergoes Renner-Teller distortion and is thus bent with an electronic ground structure of $^5B_2$. They state that the molecule has multiple configurations which are very close to each other due to the molecule having a very shallow energy curve and an extreme of this is a bond angle of 110^o which is very close to the other configurations.

In the larger picture of the first row transition metal fluorides even if CrF_2 and $CrCl_2$ are bent due to Renner-Teller distortion, the TiF_2 data shown above proving that TiF_2 is linear is very significant in the understanding of bonding and the structure of the 3d dihalides, the data obtained for VF_2 also indicates that this is also probably linear.

5.3.8 Further Work.

Further work that is required with the first row transition metal fluorides includes work upon vanadium and the investigation of chromium. The work with vanadium conducted within this thesis proved to be very challenging, vanadium is much more difficult to sublime using our equipment than other transition metals dealt with. This, added to the lack of an isotope pattern, makes anything that actually is made extremely difficult to assign. A possible avenue for the future investigation with vanadium would be to attempt the ‘protective’ argon atmosphere experiments on a UV spectrometer to see if vanadium atoms are being produced with the method and thus allow the assignment of the bands produced to be done with more confidence than achieved in this work. Work with chromium within a matrix will likely be futile as previously stated by Jensen[30] who states that within a matrix $CrCl_2$ is likely linear, meaning any study of this molecule within a matrix will likely not settle the discussion.

A reinvestigation of previous work done by Ogden and Wyatt[146] upon $CrCl_2$ could also be re-examined to see if the isotope splitting pattern is consistent with a linear molecule, and a further investigation to try and isolate $CrCl_2$ and obtain both isotope patterns, which Ogden and Wyatt did not achieve. This all could confirm Jensen's assertion that $CrCl_2$ is likely linear in a matrix environment.[30]

References.

1. V. P. Spiridonov, A. G. Gershikov and V. S. Lyutsarev, *J. Mol. Struct.*, 1990, **221**, 57.
2. I. R. Beattie, *Angew. Chem. Int. Ed.*, 1999, **38**, 3295.
3. M. Hargittai, *Chem. Rev.*, 2000, **100**, 2233.
4. B. Vest, X. Varga, M. Hargittai, A. Hermann and P. Schwerdtfeger, *Chem. Eur. J.*, 2008, **14**, 5130.
5. B. Vest, P. Schwerdtfeger, M. Kolonits and M. Hargittai, *Chem. Phys. Lett.*, 2009, **468**, 143.
6. N. N. Greenwood and A. Earnshaw, *Chemistry of the Elements*, 2nd Edn., Butterworth Heinmann, Oxford, 1997.
7. F. A. Cotton and G. Wilkinson, *Advanced Inorganic Chemistry*, 5th Edn., Wiley-Interscope, Toronto, 1988.
8. O. Ruff and W. Plato, *Ber.*, 1904, **37**, 673.
9. W. Biltz and K. Keep, *Z. anorg. Chem.*, 1927, **162**, 32.
10. W. Biltz, A. Sapper and E. Wünneber, *Z. anorg. Chem.*, 1932, **203**, 277.
11. P. A. Bond and E. C. Crone, *J. Am. Chem. Soc.*, 1934, **56**, 2028.
12. J. M. Blocher and I. E. Campbell, *J. Am. Chem. Soc.*, 1947, **69**, 2100.
13. H. Bialowons, M. Müller and B. G. Müller, *Z. anorg. allg. Chem.*, 1995, **621**, 1227.
14. N. G. Sefström, *Ann. Phys.*, 1831, **1**, 43.
15. K. Hedberg, K. Hagen, M. Gilbert and L. Hedberg, *Inorg. Chem.*, 1982, **21**, 2690.
16. O. Ruff and L. Friedrich, *Z. anorg. Chem.*, 1914, **89**, 279.
17. N. V. Sidgwick, *Chemical Elements and their Compounds*, Oxford University Press, Oxford 1950.
18. W. N. Lipscomb and A. G. Whittaker, *J. Am. Chem. Soc.*, 1945, **67**, 2019.
19. J. Meyer and R. Backa, *Z. anorg. Chem.*, 1924, **135**, 177.
20. J. Locke and G. H. Edwards, *J. Am. Chem.*, 1898, **20**, 594.
21. O. Ruff and H. Lickfett, *Ber.*, 1911, **44**, 2539.
22. J. B. Conant and A. W. Sloan, *J. Am. Chem. Soc.*, 1923, **48**, 2466.
23. J. B. Conant and H. B. Cutter, *J. Am. Chem. Soc.*, 1926, **48**, 1016.
24. A. Morette, *C. R. Acad. Sci.*, 1938, **207**, 1218.

25. F. Ephraim and E. Ammann, *Helv. Chem. Acta*, 1933, **16**, 1273.
26. M. Hargittai, O. V. Dorofeeva and J. Tremmel, *Inorg. Chem.*, 1985, **24**, 3963.
27. D. W. Green, D. P. McDermott and A. Bergman, *J. Mol. Spectrosc.*, 1983, **98**, 111.
28. I. R. Beattie, P. J. Jones and N. A. Young, *Chem. Phys. Lett.*, 1991, **177**, 579.
29. A. J. Bridgeman and C. H. Bridgeman, *Chem. Phys. Lett.*, 1997, **272**, 173.
30. V. R. Jensen, *Mol. Phys.*, 1997, **91**, 131.
31. M. Hargittai, *Coord. Chem. Rev.*, 1988, **91**, 35.
32. C. W. DeKock and D. M. Gruen, *J. Chem. Phys.*, 1966, **44**, 4387.
33. C. W. DeKock and D. M. Gruen, *J. Chem. Phys.*, 1968, **49**, 4521.
34. J. T. Hougen, G. E. Leroi and T. C. James, *J. Chem. Phys.*, 1961, **34**, 1670.
35. M. Hargittai, N. Y. Subbotina and M. Kolonits, *J. Chem. Phys.*, 1991, **94**, 7278.
36. A. J. Ross, R. Bacis, A. J. Bouvier, S. Churassy, J.-C. Coste, P. Crozet and I. Russier, *J. Mol. Spectrosc*, 1993, **158**, 27.
37. S. H. Ashworth, F. J. Grieman and J. M. Brown, *J. Chem. Phys.*, 1996, **104**, 48.
38. F. Dienstbach, F. P. Emmenegger and C. W. Schlapfer, *Helv. Chim. Acta*, 1977, **60**, 2460.
39. A. G. Gershikov, N. Y. Subbotine, G. V. Girichev, E. Z. Zasorin, V. P. Spiridonov and A. A. Ivanov, *Zh. Strukt. Khim.*, 1986, **27**, 36.
40. A. G. Gershikov, N. Y. Subbotina, G. V. Girichev, E. Z. Zasorin, V. P. Spiridonov and A. A. Ivanov, *Zh. Strukt. Khim.*, 1987, **28**, 56.
41. A. G. Gershikov, N. Y. Subbotina, G. V. Girichev, E. Z. Zasorin, V. P. Spiridonov and A. A. Ivanov, *Zh. Strukt. Khim.*, 1988, **29**, 139.
42. B. O. Roos, K. Andersson, M. P. Fulscher, P.-A. Malmqvist, L. Sorrano-Andres, K. Pierloot and M. Merchan, *Adv. Chem. Phys.*, 1996, **93**, 219.
43. R. J. Deeth, *J. Chem. Soc., Dalton Trans.*, 1993, 1061.
44. A. J. Bridgeman, *J. Chem. Soc., Dalton Trans.*, 1996, **13**, 2601.
45. A. J. Bridgeman, *J. Chem. Soc., Dalton Trans.*, 1997, **24**, 4765.
46. A. B. P. Lever and Hollebon.Br, *Inorg. Chem.*, 1972, **11**, 2183.
47. D. W. Smith, *Inorg. Chim. Acta.*, 1971, **5**, 231.
48. E. P. F. Lee, A. W. Potts, M. Doran, I. H. Hillier, J. J. Delaney, R. W. Hawksworth and M. F. Guest, *J. Chem. Soc., Farad. Trans. II*, 1980, **76**, 506.
49. A. W. Potts, D. Law and E. P. F. Lee, *J. Chem. Soc. Faraday Trans. II*, 1981, **77**, 797.

50. J. Berkowitz, D. G. Streets and A. Garritz, *J. Chem. Phys.*, 1979, **70**, 1305.
51. P. Kasai, E. B. Whipple and W. Weltner, *J. Chem. Phys.*, 1966, **44**, 2581.
52. C. W. Bauschlicher and B. O. Roos, *J. Chem. Phys.*, 1989, **91**, 4785.
53. F. Rogemond, H. Chermette and D. R. Salahub, *Chem. Phys. Lett.*, 1994, **219**, 228.
54. J. T. Hougen, G. E. Leroi and T. C. James, *J. Chem. Phys.*, 1961, **34**, 1670.
55. A. B. P. Lever and B. R. Hollebone, *Inorg. Chem.*, 1972, **11**, 2183.
56. D. M. Gruen, *Prog. Inorg. Chem.*, 1971, **14**, 119.
57. S. G. Wang and W. H. E. Schwarz, *J. Chem. Phys.*, 1998, **109**, 7252.
58. M. Vogel and W. Wenzel, *Chem. Phys. Lett.*, 2005, **413**, 42.
59. M. Vogel and W. Weber, *J. Chem. Phys.*, 2006, **125**, 034106.
60. B. O. Roos, K. Andersson, M. P. Fulscher, P. A. Malmqvist, L. SerranoAndres, K. Pierloot and M. Merchan, in *Advances In Chemical Physics, Vol Xciii*, Editon edn., 1996, vol. 93, pp. 219-331.
61. S. H. Ashworth, F. J. Grieman, J. M. Brown, P. J. Jones and I. R. Beattie, *J. Am. Chem. Soc.*, 1993, **115**, 2978.
62. S. H. Ashworth, F. J. Grieman and J. M. Brown, *Chem. Phys. Lett.*, 1990, **175**, 660.
63. F. J. Grieman, S. H. Ashworth, J. M. Brown and I. R. Beattie, *J. Chem. Phys.*, 1990, **92**, 6365.
64. L. R. Zink, J. M. Brown, T. R. Gilson and I. R. Beattie, *Chem. Phys. Lett.*, 1988, **146**, 501.
65. M. P. Barnes, R. T. Carter, N. M. Lakin and J. M. Brown, *J. Chem. Soc., Farad. Trans.*, 1993, **89**, 3205.
66. T. Tokuda, N. Fujii, S. Yoshida, K. Shimizu and I. Tanaka, *Chem. Phys. Lett.*, 1990, **174**, 385.
67. A. J. Bouvier, R. Bacis, J. Bonnet, S. Churassy, P. Crozet, B. Erba, J. B. Koffend, J. Lamarre, M. Lamrini, D. Pigache and A. J. Ross, *Chem. Phys. Lett.*, 1991, **184**, 133.
68. H. P. Yang, Y. Qin, Q. N. Yuan, X. B. Xie, Q. Zhuang and C. H. Chuang, *Chem. Phys. Lett.*, 1992, **191**, 130.
69. T. Tokuda and N. Fujii, *J. Phys. Chem.*, 1992, **96**, 6504.
70. P. Crozet, A. J. Ross, R. Bacis, M. P. Barnes and J. M. Barnes, *J. Mol. Spectrosc.*, 1995, **43**, 172.

71. J. F. Janak, *Phys. Rev. B.*, 1978, **18**, 7165.
72. O. P. Charkin and M. E. Dyatkina, *Zh. Strukt. Khim* 1964, **5**, 921.
73. M. C. Drake and G. M. Rosenblatt, *J. Electrochem. Soc.*, 1979, **126**, 1387.
74. R. L. Diebner and J. G. Kay, *J. Chem. Phys.*, 1969, **51**, 3547.
75. E. A. Shenyavskaya and V. M. Dubov, *J. Mol. Spectrosc.*, 1985, **113**, 85.
76. R. S. Ram, J. R. D. Peers, Y. Teng, A. G. Adams, A. Muntianu, P. F. Bernath and S. P. Davis, *J. Mol. Spectrosc*, 1997, **184**, 186.
77. K. R. More and A. H. Parker, *Phys. Rev.*, 1937, **52**, 1150.
78. V. R. Rao, *Ind. J. Phys.*, 1949, **23**, 535.
79. E. A. Shenyavskaya, Y. Y. Kuzyakov and V. M. Tatevskii, *Opt. Spectrpsc.*, 1962, **12**, 197.
80. A. Chatalic, P. Deschamps and G. Pannetier, *C. R. Acad. Sci. Paris*, 1970, **270**, 146.
81. K. P. Lanini, PhD Thesis, University of Michigan, 1972.
82. R. S. Ram and P. F. Bernath, *J. Mol. Spectrosc.*, 1997, **186**, 113.
83. C. Koukounas, S. Kardahakis and A. Mavridis, *J. Chem. Phys.*, 2004, **120**, 11500.
84. F. Ramondo, V. Rossi and L. Bencivenni, *Mol. Phys.*, 1988, **64**, 513.
85. F. Ramondo, L. Bencivenni, S. N. Cesaro and K. Hilpert, *J. Mol. Struct.*, 1989, **192**, 83.
86. K. Kuchitsu, *Structure Data of Free Polyatomic Molecules*, Springer-Verlag, Berlin, 1992.
87. J. W. Hastie, R. H. Hauge and J. L. Margrave, *J. Chem. Phys.*, 1969, **51**, 2648.
88. V. P. Spiridonov, A. G. Gershikov and V. S. Lyutsarev, *J. Mol. Struct.*, 1990, **221**, 79.
89. D. R. Salahub and M. C. Zerner, *The Challenge of d and f Electrons*, ACS, Washington DC, 1989.
90. A. Ricca and C. W. Bauschlicher, *Theor. Chim. Acta*, 1995, **92**, 123.
91. O. P. Charkin and M. E. Dyatkina, *Zh. Strukt. Khim.*, 1964, **5**, 924.
92. O. P. Charkin, *Zh. Strukt. Khim.*, 1969, **10**, 754.
93. O. P. Charkin, *Zh. Neorgan. Khim.*, 1973, **18**, 2307.
94. O. P. Charkin, *Zh. Strukt. Khim.*, 1973, **18**, 289.
95. J. H. Yates and R. M. Pitzer, *J. Chem. Phys.*, 1979, **70**, 4049.
96. V. G. Solomonik, J. E. Boggs and J. F. Stanton, *J. Chem. Phys.*, 1998, **103**, 838.

97. V. N. Bukhmarina, A. Y. Gerasimov and Y. B. Predtechenskii, *Vib. Spectrosc.*, 1992, **4**, 91.

98. S. B. Osin, D. I. Davlyatshin, V. F. Shevelkov and V. N. Mitkin, *Zh. Fiz. Khim.*, 1995, **69**, 876.

99. V. N. Bukhmarina and Y. B. Predtechenskii, *Opt. Spektrosk.*, 1996, **80**, 762.

100. W. E. Jones and G. Krishnamurty, *J. Phys. B.*, 1980, **13**, 3375.

101. R. S. Ram, P. F. Bernath and S. P. Davis, *J. Chem. Phys.*, 2002, **116**, 7305.

102. A. S. Aveyanov and Y. G. Khait, *Opt. Spectrosc*, 1990, **67**, 829.

103. I. R. Beattie, P. J. Jones and N. A. Young, *Angew. Chem. Int. Ed. Engl.*, 1989, **28**, 313.

104. I. R. Beattie and P. J. Jones, *J. Chem. Phys.*, 1989, **90**, 5209.

105. B. S. Ault, *J. Phys. Chem. A*, 1998, **102**, 7245.

106. T. C. De Vore and W. Weltner, *J. Am. Chem. Soc.*, 1977, **99**, 4700.

107. B. A. Goodmad and J. B. Raynor, *Adv. Inorg. Chem. Radiochem.*, 1970, **13**, 156.

108. K. Mierzwicki, Z. Mielke, M. Saldyka, S. Coussan and P. Roubin, *Phys. Chem. Chem. Phys.*, 2008, **10**, 1292.

109. L. Andrews and G. L. Johnson, *J. Chem. Phys.*, 1983, **79**, 3670.

110. J. F. Rooms, A. V. Wilson, I. Harvey, A. J. Bridgeman and N. A. Young, *Phys. Chem. Chem. Phys.*, 2008, **10**, 4594.

111. M. E. Jacox, *J. Mol. Spectrosc.*, 1980, **84**, 74.

112. R. Spartley, J. J. Turner and G. C. Pimentel, *J. Chem. Phys.*, 1966, **44**, 2063.

113. D. J. Gardiner, N. J. Lawrence and J. J. Turner, *J. Chem. Soc. A*, 1971, 400.

114. J. S. Ogden and J. J. Turner, *J. Chem. Soc. A*, 1967, 1483.

115. H. E. Hallam, *Vibrational Specroscopy of Trapped Species*, Wiley, London, 1973.

116. D. Milligan, M. Jacox, J. J. Comeford, D. Mann and A. Bass, *J. Chem. Phys.*, 1965, **42**, 3187.

117. L. Andrews and G. L. Johnson, *J. Chem. Phys.*, 1982, **76**, 2875.

118. D. M. Gruen and D. H. W. Carstens, *J. Chem. Phys.*, 1971, **54**, 5206.

119. N. S. McIntyre, K. A. Thompson and W. Weltner, JR., *J. Phys. Chem.*, 1971, **75**, 3243.

120. G. V. Chertihin and L. Andrews, *J. Phys. Chem.*, 1995, **99**, 6356.

121. W. Weltner, JR. and D. McLeod, JR., *J. Phys. Chem.*, 1965, **69**, 3488.

122. G. V. Chertihin and L. Andrews, *J. Phys. Chem.*, 1994, **98**, 5891.

123. R. G. Cavell and H. C. Clark, *J. Chem. Soc.*, 1963, 4261.

124. R. G. Cavell and H. C. Clark, *Inorg. Chem.*, 1964, **3**, 1789.

125. H. H. Claassen and H. Selig, *J. Chem. Phys.*, 1966, **44**, 4039.

126. A. K. Brisdon, J. T. Graham, E. G. Hope, D. M. Jenkins, W. Levason and J. S. Ogden, *J. Chem. Soc., Dalton Trans.*, 1990, **5**, 1529.

127. O. V. Blinova, Y. B. Predtechenskii and L. D. Shcherba, *Khim. Fiz.*, 1982, **11**, 1562.

128. O. V. Blinova, D. D. Moldavskii and Y. B. Predtechenskii, *Khim. Fiz.*, 1983, **10**, 1363.

129. H. Selig and H. H. Claassen, *J. Chem. Phys.*, 1966, **44**, 1404.

130. E. G. Hope, *J. Chem. Soc., Dalton Trans.*, 1990, **3**, 723.

131. J. W. Hastie, R. H. Hauge and J. L. Margrave, *Chem. Comm.*, 1969, **24**, 1452.

132. M. Moskovits and G. A. Ozin, eds., *Cryochemistry*, Wiley-Interscience, New York, 1976.

133. T. De Vore, *J. Chem. Phys.*, 1975, **62**, 520.

134. T. Ford, H. Huber, W. E. Klotzbücher, E. P. Kündig, M. Moskovits and G. A. Ozin, *J. Chem. Phys.*, 1977, **66**, 524.

135. H. Selig and H. H. Claassen, *J. Chem. Phys.*, 1966, **44**, 1404.

136. V. G. Solomonik, J. E. Boggs and J. F. Stanton, *J. Phys. Chem. A*, 1999, **103**, 838.

137. V. G. Solomonik, V. V. Sliznev and N. B. Balabanov, *Z. Phys. Chem.*, 1997, **200**, 77.

138. V. G. Solomonik, V. V. Sliznev and N. B. Balabanov, *Zh. Neorg. Khim.*, 1998, **43**, 1172.

139. M. Hargittai, B. Réffy, M. Kolonits, C. J. Marsden and J. L. Heully, *J. Am. Chem. Soc.*, 1997, **119**, 9042.

140. I. R. Beattie, P. J. Jones, A. D. Willson and N. A. Young, *High Temp. Sci.*, 1990, **29**, 53.

141. V. G. Solomonik and T. P. Pogrebnaya, *Russ. J. Inorg. Chem.*, 2001, **46**, 1851.

142. J. M. Hollas, *High Resolution Spectroscopy*, Butterworth & Co, London, 1982.

143. A. V. Wilson, A. J. Roberts and N. A. Young, *Andew. Chem. Int. Ed.*, 2008, **47**, 1774.

144. M. E. Jacox and D. E. Milligan, *J. Chem. Phys.*, 1969, **51**, 4143.

145. J. W. Hastie, R. Hauge and J. L. Margrave, *High Temp. Sci.*, 1971, **3**, 257.

146. J. S. Ogden and R. S. Wyatt, *J. Chem. Soc., Dalton Trans.*, 1987, 859.

147. S. Smith and I. H. Hillier, *J. Chem. Soc. Chem. Commun.*, 1989, 539.

148. M. Hargittai, O. V. Dorofeeva and J. Tremmel, Ref. 108(b) in Ref. 31.

Chapter 6.

Second Row Transition Metal Halides.

6.1 Introduction.

The main aim of this work was to try and isolate palladium fluorides with a previously proven technique. Then, if successful, continue to try and isolate the more interesting palladium chlorides, particularly $PdCl_2$. $PdCl_2$ is of interest as it is often calculated to be a bent molecule while most other second row transition metal dichlorides are linear.[1]

6.1.1 History of Palladium.

Palladium occurs in the ores cooperite (Pt, Pd, Ni)S and polarite (Pd(Bi, Pb)), and occurs at 0.015 ppm in the lithosphere.[2] The main areas of the world in which palladium is mined and refined include South Africa, former Soviet Union countries, especially Russia, and the USA, current annual production of palladium is around 200 tonnes.[3]

Palladium was discovered in 1803 by William Hyde Wollaston who was investigating a platinum ore from South America.[2] He dissolved this platinum ore in aqua regia (nitric acid and hydrochloric acid mixed in a 1:3 ratio)[4] then neutralised the solution with sodium hydroxide. Platinum was then extracted through filtration of the ammonium chloroplatinate $(NH_4)_2PtCl_6$. To the remaining solution $Hg(CN)_2$ was then added and the formation of $Pd(CN)_2$ occurred which was subsequently heated to give the palladium metal. The compound was named after an asteroid called Pallas which was discovered a few years prior to this work. Pallas was named after the Greek goddess of wisdom.

Palladium and platinum are the most closely resembled elements in the periodic table.[2] Both of these elements are commonly only divalent and tetravalent. In the case of palladium the tetravalent state is much less stable than the divalent while in platinum they are about the same.[5] Palladium also has a remarkable ability to absorb hydrogen, more than any other metal in the group.[2] The electronic structure of palladium is also interesting; the atomic number of 46 is similar to that of an inert gas, 2.8.18.18, like those of nickel and platinum.[2] In nickel the outer 18-electron group breaks down, as one or perhaps two of its electrons going into the higher quantum group to give the configuration of 16.2 ($3s^2$ $3p^6$ $3d^8$ $4s^2$), in platinum the structure is 16.2 ($5s^2$ $5p^6$ $5d^9$ $6s^1$). The elements of the second transitional series often tend to have fewer electrons in their outmost group than those of the first and third, for example cobalt – 15.2 ($3s^2$ $3p^6$ $3d^7$ $4s^2$), rhodium 16.1 ($4s^2$ $4p^6$ $4d^8$ $5s^1$), iridium 15.2 ($5s^2$ $5p^6$ $5d^7$ $6s^2$), and this effect is shown in a very marked way by palladium. Spectroscopic data and the absence of a magnetic moment[6] indicate that in the isolated atom all the 18 electrons are in the fourth quantum group ($4s^2$ $4p^6$ $4d^{10}$ $5s^0$). From this we should expect that palladium will not act as a transition metal at all and should resemble an inert gas instead. But due to the fact that elemental palladium is a solid with the conductivity and other properties of a metal shows that this electronic group of 18 electrons breaks down and loses some of its electrons as soon as the atoms come together.[6]

Some early uses of palladium were in the form of palladium chloride which was used as a treatment for tuberculosis, but the side effect meant that this use was later replaced by more effective drugs.[7] Currently palladium is used in the manufacture of electronic components, but the largest single use of palladium is in the manufacture of catalytic convertors in motor vehicles, which accounts for approximately 65% of the yearly use of palladium.[8] Palladium is used in electronics to make multilayer ceramic capacitors in which it is used as an electrode.[8] Another use of palladium is in the production of hydrogen gas. This is due to the fact that as palladium is heated, hydrogen can easily diffuse through it and so palladium is often used with membrane reactors to produce hydrogen. Palladium may also be used in future for the storage of hydrogen due to the fact that palladium hydride can store up to 900 times its own volume of hydrogen within its crystal lattice in a reversible process, which with the possible future use of hydrogen as a power source could be exploited for hydrogen storage.[2, 4] Palladium was also used as an electrode in an early experiment with cold fusion due to its ability to store hydrogen, and thus deuterium.[9]

6.2 Palladium.

6.2.1 Literature Review.

The halides of palladium are known but are few in number. PdF_4 in the solid state is a red compound which is very similar in its properties to PtF_4.[4, 5] Although this is not the most stable palladium fluoride as the $Pd^{II}[Pd^{IV}F_6]$ compound is the most stable and as can be seen although this was classified as a Pd^{III} compound it is in fact a combination of Pd^{II} and Pd^{IV}, interestingly the trihalides of palladium are extremely rare.[10] All of the palladium dihalides are known, PdF_2 is a pale violet compound which is easily hydrolysed and is also paramagnetic.[5] This is due to the $t_{2g}^6 e_g^2$ configuration of Pd^{II} which is due to its octahedral coordination in the rutile structure.[4]

$PdCl_2$ can be present as both α and β forms, with the α form being the more common. The structure of the α form was first reported by Wells in 1938 as infinitely long chains of coplanar $PdCl_{4/2}$ units.[11] It took almost 30 years after this to discover another form of $PdCl_2$, the β form was reported by Schäfer *et al.* in 1967.[12] Schäfer *et al.* also reported that by heating β-$PdCl_2$ the α form can be obtained. The β form was reported to be isotypic with Pt_6Cl_{12} and so contained Pd_6Cl_{12} clusters and is reddish-black,[4] while the α is a dark red compound which forms a chain structure with square planar geometry, it is a hygroscopic compound that is often used in aqueous solution to study Pd^{II} coordination chemistry. The structure of Pd_6Cl_{12} was reported to be similar but not identical to that of Pt_6Cl_{12}. The Pd_6Cl_{12} molecule has a cubic shape and with an average

Pd-Cl bond length of 2.310 Å, which corresponds to that observed for the average Pd-Cl bond length in α-$PdCl_2$. Considering the structure of α-$PdCl_2$ being reported as an infinitely long chain comprised of square planar molecules and that each face of the cube is comprised of square planar molecules, this is not totally unexpected.[10] The average bond length of 2.43 Å from the crystal structure of a number of known palladium compounds compared with the reported bond length of 2.310 Å for Pd_6Cl_{12}, and this indicates a strong palladium chloride bond. The intramolecular Pd-Pd distances of 3.283 and 3.329 Å are longer than those observed in palladium metal (2.750 Å) indicating that a Pd-Pd bond is not present. Belli Dell' Amico *et al.*[13] also state that palladium chloride is a useful precursor for several catalytic processes. Other palladium complexes are also used in catalytic processes, for example, palladium (II) acetate catalyses the oxidation of methane to methyl trifluoroacetate, $CF_3CO_2CH_3$ in trifluoroacetic anhydride with hydrogen peroxide.[14] One of the most important examples of this catalytic behaviour is in the Suzuki reaction. It is widely used to synthesize alkane polymers, styrenes (vinyl benzene), and substituted biphenyls, several reviews using this process have been conducted.[15-17] The paper by Belli Dell' Amico reported that Thiele had also reported the structure of solvated Pd_6Cl_{12} and the results obtained were in agreement with those of Belli Dell' Amico.[13] Figure 6.01 shows the structure of the β-form of $PdCl_2$. $PdBr_2$ on the other hand is a red-black compound and PdI_2 is a black coloured compound, both of these compounds are insoluble in water.

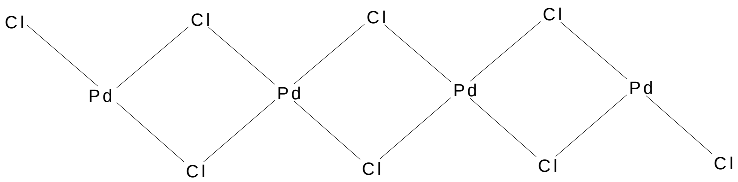

Figure 6.01 Structure of α-$PdCl_2$.[12]

There is very little literature on palladium halides outside of solid state chemistry, and literature on palladium halides in a matrix environment is even more limited. The only reported spectroscopic data for palladium halides was conducted up on $PdCl_2$ by Martin.[18] He isolated $PdCl_2$ vapour in solid argon and the IR spectrum was obtained, from this the structure was assigned to a O_h symmetry, which was a distorted cube of Pd_6Cl_{12}. The spectrum is shown but the exact band positions are not listed. However from the figure showing the IR spectrum the frequency appears to be approximately 330 cm^{-1}. There appears to be no information about PdF_2 within a matrix. A thesis conducted by Dr. E. L. Dixon investigated $PdCl_2$ but only managed to form the polymer cluster of $PdCl_2$ and failed in isolating molecular $PdCl_2$ despite significant effort.[19]

Palladium fluorides have been studied in solid state in various forms the one interesting point that comes from work on palladium is that the +3 oxidation state is very rare. The composition of PdF_3 has been reported by Thiele and Woditsch[20] to be a combination of Pd^{II} and Pd^{IV}, which was previously suspected from the magnetic measurements performed by Bartlett and Rao.[21] A palladium complex with a +5 oxidation state was claimed by Chen *et al.*.[22] This complex a $Pd(SiX_3)_6$ unit ($X = CH_3$) was initially claimed to be a Pd^{VI} complex but later it was agreed that it actually contained Pd^{II} with theoretical calculation performed to make a definitive assignment.[23-25] Timakov *et al.* claimed to have isolated PdF_6 in 1982 based upon a single band in the IR spectrum at 711 cm^{-1},[26] this assignment has however been called into doubt by computational calculations.[24, 27] Riedel and Kaupp say that 'an early report of the gas=pahse preparation of PdF_6 relied almost exclusively on a single IR band, and it appears unlikely that PdF_6 has been obtained under the conditions indicated'.[27]

A computational study of PdF_6 was conducted by Aullón and Alvarez.[24] They studied $Pd^{VI}R$ (R= SiH_3, NH_2, OH, Cl, and F) with the aim of understanding the bonding and electronic stability. Within this work they determined that PdF_6 was the most stable out of the compounds studied and as expected it would be paramagnetic due to its t_{2g}^4 configuration low spin state and also it has second-order Jahn-Teller distortion involving its π orbitals which acts to compress the axial bonds. They also conducted a vibrational analysis of PdF_6 in an distorted D_{2d} symmetry and found that a band at 585 cm^{-1} would be produced corresponding to the B_2 asymmetric stretch, which corresponds to the A_{2u} in ideal O_h symmetry. Within this work calculations were also performed on PdF_4, however only limited information was provided on this work. They calculated that PdF_4 was most stable in a pseudoplanar geometry (D_{2d} symmetry with a F-Pd-F bond angle of 167°) with a triplet ground state. They again conducted a vibrational analysis of PdF_4 and calculated PdF_4 should produce bands at 592 cm^{-1} and 157 cm^{-1}, which they note would overlap with the calculated bands for PdF_6 making determination with the use of IR more difficult.

Metal	**Electronic Ground State**	**Bond Angle**
YF_2 (d^1)	$^2A_1$	121.7
ZrF_2 (d^2)	$^3\Delta_g$	180
NbF_2 (d^3)	$^4\Sigma_g^-$	180
MoF_2 (d^4)	$^5B_2$	140.1
TcF_2 (d^5)	$^6\Sigma^+$	180
RuF_2 (d^6)	$^5\Delta_g$	180
RhF_2 (d^7)	$^4\Sigma_g$	180
PdF_2 (d^8)	$^3\Pi_g$	180

Table 6.1 Table showing the electronic ground state of second row transition metal difluorides.[1]

One of the very few studies of palladium difluorides was including in a computational study of the second row transition metal hydride, fluorides and chlorides by Siegbahn.[1] Within this work he calculated that PdF_2 was in a $^3\Pi_g$ state with a bond length of 1.94 Å. He also calculated that the compound would be linear, Table 6.1.

From this work only YF_2 and MoF_2 were found to be non-linear amongst the second row transition metal difluorides. MoF_2 is the more interesting case as it lies in between linear molecules, the reason Siegbahn[1] postulated that this molecule is bent and that in this molecule there will be only one empty 4d orbital. If this molecule was linear ligand field theory suggests that this empty orbital will be a $4d_\pi$ orbital since the $4d_\sigma$ orbital can efficiently mix together through sd hybridization. Ligand field theory also suggests that any interaction between an empty $4d_\pi$ orbital and the ligands will be maximised for a bent structure. YF_2 on the other hand only has one occupied 4d orbital and this will be a s/d hybrid pointing away from the ligands. This hybrid can point away from the ligands equally well in a bent structure as it can in a linear structure and thus the bent structure is preferred since the covalency is more optimal for this structure, however he notes this preference is quite small.[1]

As can be seen from Table 6.2 calculations performed by Cheng *et al.*[28] show the electronic configuration of the ground state for PdF is calculated to be $^2\Sigma^+$ ($6\sigma^1\ 3\pi^4\ \delta^4$). To assign this configuration Cheng *et al.* also determined the orbital energy levels. They found that the bonding orbitals are mainly composed of palladium 5s and 4d orbitals with some 2p from the fluorine. The metal σ orbital undergoes sd_σ hybridization and interacts with the p_σ orbital to form bonding, nonbonding, and antibonding orbitals. For the transition metals studied the σ orbital is largely from the 5s orbital. The metal $4d_\pi$ orbitals interact with the p_π orbitals to give bonding and antibonding orbitals, the metal $4d_\delta$ orbitals are nonbonding because there are no corresponding d orbitals in fluorine. Although the expected order of stability would be σ bond > π bond > σ and δ nonbonding > π antibonding > σ antibonding. This order is not what is always seen and is often much more complicated due to the fact that d-d exchange energy is larger than the energy separation between different orbitals and mixing of the metal s^2d^n and s^1d^{n+1} asymptotes. This is also further complicated by the fact that these compounds often involve ionic and covalent character in their bonding.

Metal	**Electronic Ground State**	**Vibrational Frequency (cm^{-1}) experimental values in parenthesis.**
YF (d^2)	$(6\sigma^2)\ ^1\Sigma^+$	612 (631)[29]
ZrF (d^3)	$(6\sigma^2\ \delta^1)\ ^2\Delta$	663 (620)[30]
NbF (d^4)	$(6\sigma^1\ 3\pi^1\ \delta^2)\ ^5\Pi$	619
MoF (d^5)	$(6\sigma^1\ 3\pi^2\ \delta^2)\ ^6\Sigma^+$	597
TcF (d^6)	$(6\sigma^1\ 3\pi^2\ \delta^2 7\sigma^1)\ ^7\Sigma^+$	533
RuF (d^7)	$(6\sigma^2\ 3\pi^2\ \delta^2 7\sigma^1)\ ^6\Sigma^+$	563
RhF (d^8)	$(6\sigma^1\ 3\pi^4\ \delta^3)\ ^3\Delta$	520 (575)[31]
PdF (d^9)	$(6\sigma^1\ 3\pi^4\ \delta^4)\ ^2\Sigma^+$	631 (541)
AgF (d^{10})	$(6\sigma^2\ 3\pi^4\ \delta^4)\ ^1\Sigma^+$	485 (513)[29] (515)[32]
CdF ($d^{10}s^1$)	$(6\sigma^2\ 3\pi^4\ \delta^4 7\sigma^1)\ ^2\Sigma^+$	475

Table 6.2 Table showing the electronic configuration of second row transition metal monofluorides.[28]

Another study on second row transition metal monofluorides was conducted by Siegbahn.[33] His study was very similar to Cheng *et al.*[28] and produced similar results for the electronic ground state with only one difference, he calculated that RuF has a ground state of $^4\Phi$ instead of $^6\Sigma^+$. He states that even though the $^6\Sigma^+$ is lower in energy than the $^4\Phi$ in his calculations there is a very large correlation effect favouring the $^4\Phi$ state and in a higher level calculation this will be the lower state. Within this work he also comments on the effect of the lone pair present on the fluorine and its affect on the bonding within the molecules. The interaction between the ligand lone pair and the transition metals has both attractive and repulsive components. The repulsion is a result of interaction between the lone pairs and the metal 4d electrons, and thus increases across the period as the number of electrons increases. The attractive component is similar to this as it relates to the interaction between the lone pairs and the unoccupied 4d orbitals, i.e. donation of electrons. Previously,[34] it has been shown that if a single electron is present within the 4d orbitals this attraction is totally removed. This interaction also means that in some cases, e.g. NbF and NbH, the transition metal will, if possible, opt for an unoccupied $4d_\pi$ orbital rather than the $4d_\delta$ so that the lone pair attractive interaction can occur.

6.2.2 Results.

The aim of this work was initially to try and isolate PdF_2 and determine the bond angle of this molecule from palladium's isotope pattern to see if the computational calculations are correct. Very little work has been conducted on palladium fluorides within a matrix environment so little was known about the position of even the most stable palladium fluorides.

Due to the reactive nature of palladium atoms and due to some difficulties that arose with the experiments, a comprehensive review of possible contaminants that could react with palladium was conducted and are given here. If oxygen was present in the matrix the formation of $(O_2)Pd(O_2)$ would be indicated by bands at 504.0 cm^{-1} and 1111.5 cm^{-1}, along with PdO_2 at 1023.5 cm^{-1} and 504.0 cm^{-1}, $Pd(O_2)$ at 1023.8 cm^{-1} and 427.3

cm^{-1}.[35-37] If nitrogen was present the formation of $Pd(N_2)_3$ would be likely which produces a peak at 2241.4 cm^{-1},[38] PdN_2 at 2214.0 cm^{-1} and 377.8 cm^{-1}, $Pd(N_2)_2$ at 2234.0 cm^{-1} and 339.0 cm^{-1}.[39] The formation of PdCO is also a possibility and would produce a peak at 472.1 cm^{-1}, along with a peak at 2044.2 cm^{-1}, there would also be a small peak at 615.7 cm^{-1} 14 times smaller than the peak present at 472.1 cm^{-1}.[40-43] A spectrum showing all bands produced when palladium and fluorine are isolated together is shown in Appendix 3.4, 3.5, and 3.6. Appendix 3.7 also shows the result of isolating palladium in argon during UV experiments, a problem encountered within the UV experiments was a leak on the system which allowed nitrogen to enter to chamber and thus react with the palladium atoms, although this still showed the sublimation of palladium atoms as the experiment was designed to do.

With the use of group theory the Γ_{str} can be predicted to see what would be expected for the various palladium halides, and is presented in Table 6.3 and is given in more detail in Appendix 1.

	Γ_{str}	**IR Active**
PdF	Σ^+	Σ^+
PdF_2	$\Sigma_g^+ + \Sigma_u^+$	Σ_u^+
PdF_3	$2\,A_1 + B_1$	$2\,A_1 + B_1$
PdF_4		
D_{2d}	$A_1 + B_2 + E$	$B_2 + E$
C_{4v}	$2\,A_1 + B_1 + B_2$	$2\,A_1 + B_1 + B_2$
D_{4h}	$A_{1g} + B_{1g} + E_u$	E_u
PdF_5	$2\,A_1 + B_1 + E$	$2\,A_1 + E$
PdF_6	$A_{1g} + E_g + T_{1u}$	T_{1u}

Table 6.3 Table showing the Γ_{str} for palladium halides in selected geometries.

6.2.2.1 Computational Studies.

6.2.2.1.1 DFT Study of PdF_x.

The majority of this computational study was conducted by Dr A. J. Bridgeman and T. Nguyen, University of Sydney. They used the ADF program with TZP basis sets, and they also included spin-orbit coupling which removes any Jahn-Teller effects. The main areas of interest for the study were the vibrational band positions of all the palladium fluorides and their relative stability which would help explain the assignments based on the photolysis and annealing behaviour. These calculations used spin-orbit coupling as they failed to reproduce the results obtained by Aullón and Alvarez,[24] despite efforts to do so and only saw very slight distortions. Further calculations were also performed within this group using Gaussian 03, with B3LYP and LanL2DZ basis set. These results agreed with the results obtained by Aullón and Alvarez,[24] but with a slightly smaller distortion present on PdF_4. Calculations conducted upon PdF_6 using Gaussian 03 failed to converge for an unknown reason.

From the study by A. J. Bridgeman and T. Nguyen it was determined that PdF_2, PdF_4, and PdF_6 were the most stable of the fluorides and the other less stable fluorides would disproportionate to form these fluorides, Table 6.4. PdF_5 will spontaneously disproportionate to form PdF_6 and PdF_4 (when there are two molecules present) and PdF will disproportionate into palladium and PdF_2. PdF_3 is more stable than PdF_5 but a small amount of energy will make it disproportionate to form PdF_4 and PdF_2. While this might be unlikely to occur in a matrix environment it does give important information about the relative stabilities of the palladium fluorides. A detailed description of the computational calculations is given in Appendix 2.

As can be seen in Table 6.5, all of the calculations conducted predict that PdF_4 will have the highest stretching frequency out of the palladium fluorides and the majority of the palladium fluorides, with the exception of PdF, will be very close together. This is due to the fact that all of the palladium fluorides will have very similar stretches due to their structures.

	Pd + (n/2)F_2	**PdF_{n-1} + (n/2)F_2**	**$2PdF_n \leftrightarrow PdF_m + PdF_o$**
PdF	-220.06	-220.06	-19.58 ($2PdF \rightarrow PdF_2 + Pd$)
PdF_2	-459.69	-239.64	71.90 ($2PdF_2 \rightarrow PdF_4 + Pd$)
PdF_3	-627.43	-167.74	26.02 ($2PdF_3 \rightarrow PdF_4 + PdF_2$)
PdF_4	-769.15	-141.72	158.86 ($2PdF_4 \rightarrow PdF_6 + PdF_2$)
PdF_5	-830.90	-61.75	-27.10 ($2PdF_5 \rightarrow PdF_6 + PdF_4$)
PdF_6	-919.75	-88.85	

Table 6.4 Tabulated values for the computational calculations of reaction enthalpies in kJ mol^{-1}, performed using ADF with TZP basis sets.

	Bridgeman and Nguyen	Aullón and Alvarez[24]	This group
PdF	533.88 (40.65)		
PdF_2	633.46 (146.16)		
PdF_3	661.78 (117.27) 556.30 (39.67)		
PdF_4	663.48 (163.26)	592 157	617.63 (35.54) 592.70 (4.68)
PdF_5	648.31 (79.09) 632.75 (15.46)		
PdF_6	649.50 (176.85)	585 (100) 530 (8)	

Table 6.5 Tabulated values for the computational calculations of stretching frequencies, performed using ADF with TZP basis sets, and Gaussian 03 using B3LYP, given in parenthesis are the relative intensities of the stretches, all values are in cm^{-1}.

6.2.2.2 Pd in 2% F_2/Ar.

When palladium was isolated in 2% F_2/Ar, as can be seen from Figure 6.02(a), peaks were produced at 534.6 cm^{-1}, a large sharp peak at 540.9 cm^{-1}, a broader peak at 617.0 cm^{-1} with a much smaller peak close by at 625.8 cm^{-1}, and a broad peak at 692.8 cm^{-1}, CO_2 is also present at 662.0 cm^{-1}. When this matrix was photolysed using broadband photolysis, Figure 6.02(b), the peaks at 692.8 cm^{-1} and 617.0 cm^{-1} both grow in size while the bands at 625.8 cm^{-1} and 534.6 cm^{-1} decreases in size. A peak also grows significantly at 656.0 cm^{-1} which was present upon deposition but barely above the background noise and easily missed. Upon subsequent annealing, Figure 6.02(c), the band at 617.0 cm^{-1} decreased and the band at 692.0 cm^{-1} increased, all of the other bands showed little change except the band at 534.6 cm^{-1} and 625.8 cm^{-1} which were totally removed upon photolysis. Upon close examination of the spectra some peaks are present which barely appear above the background noise, these include a peak at 631.0 cm^{-1}, which is not affected by either photolysis or annealing and a peak at 591.0 cm^{-1} which is not noticeable until photolysis is conducted and then grows further upon annealing. This peak at 591.0 cm^{-1} follows a similar pattern to the peak at 692.8 cm^{-1} in its photolysis and annealing behaviour, and the peaks at 534.6 cm^{-1} and 625.8 cm^{-1} also appear to follow a similar pattern.

From the computational calculations PdF_4 is always seen as the highest palladium fluoride and so is tentatively assigned to the peak present at 692.8 cm^{-1}, although if the work by Timakov *et al.* is correct this could easily be PdF_6 when matrix shift is taken into account, but as this work has been shown to be unlikely this peak will be assigned based on recent computational calculations. The peak present at 540.9 is assigned to PdF, based on the close agreement between this and the computational predictions of its position, 533.0 cm^{-1}. The other peaks present could be assigned to any of the other palladium fluorides and so the concentration of F_2/Ar was reduced to try and reduce the amount of higher palladium fluorides which could form and thus help with the assignment of the peaks present.

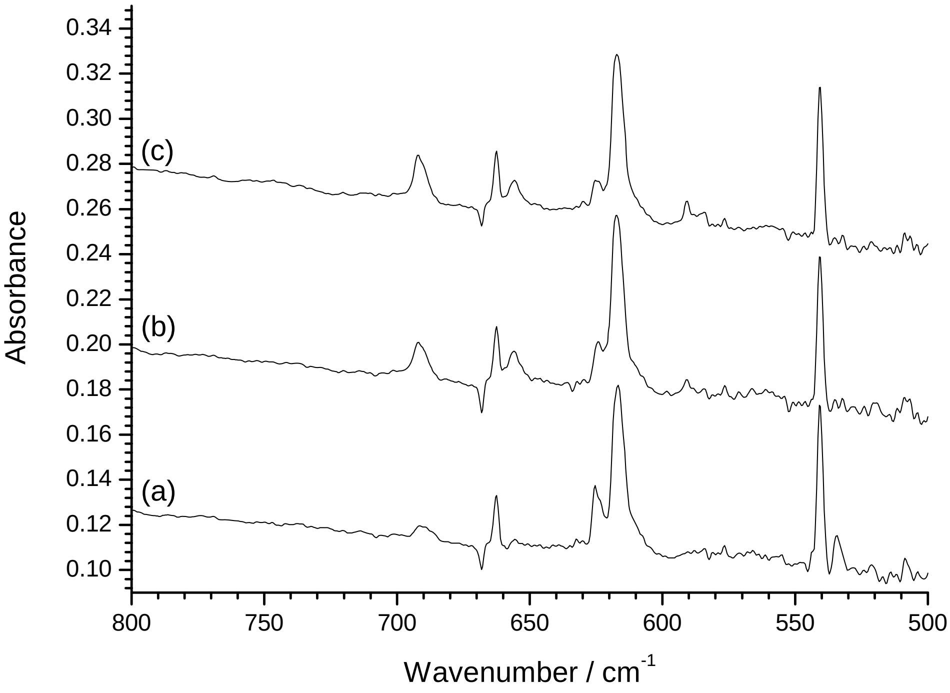

Figure 6.02 IR spectra of palladium isolated in 2% F_2/Ar, offset for clarity, (a) deposition of palladium, (b) after broadband photolysis, (c) after annealing to 20 K.

<u>6.2.2.3 Pd in 0.5% F_2/Ar.</u>

The reduction in the concentration of fluorine had the desired effects with all the peaks above the CO_2 band at 662.0 cm^{-1} only just noticeable upon deposition. This left only bands at 534.5 cm^{-1}, 541.0 cm^{-1}, 616.6 cm^{-1} and 625.0 cm^{-1} which were all much larger than previously seen, Figure 6.03. High resolution spectra collected within these experiments to try and see if the palladium isotope pattern was present and if this could help with the assignments to the correct palladium fluoride, Figure 6.04 gives a calculated example of a palladium isotope splitting pattern for square planar PdF_4, Appendix 3.8 and 3.9 show the high resolution spectra for the peaks at 590.9 cm^{-1} and 534.5 cm^{-1} as these peaks are too small to obtain an isotope pattern. Figure 6.05 and Figure 6.06(a) show the splitting patterns observed on the peaks present at 541.0 cm^{-1} and the peaks at 616.6 cm^{-1} and 625.0 cm^{-1}. The peak at 616.6 cm^{-1} on closer analysis appears to result from two palladium isotope patterns on top of one another, this could either be a site effect as seen for TiF_2, or as previously suggested by Aullón and Alvarez,[24] could be the result of two different palladium fluorides in the same area.

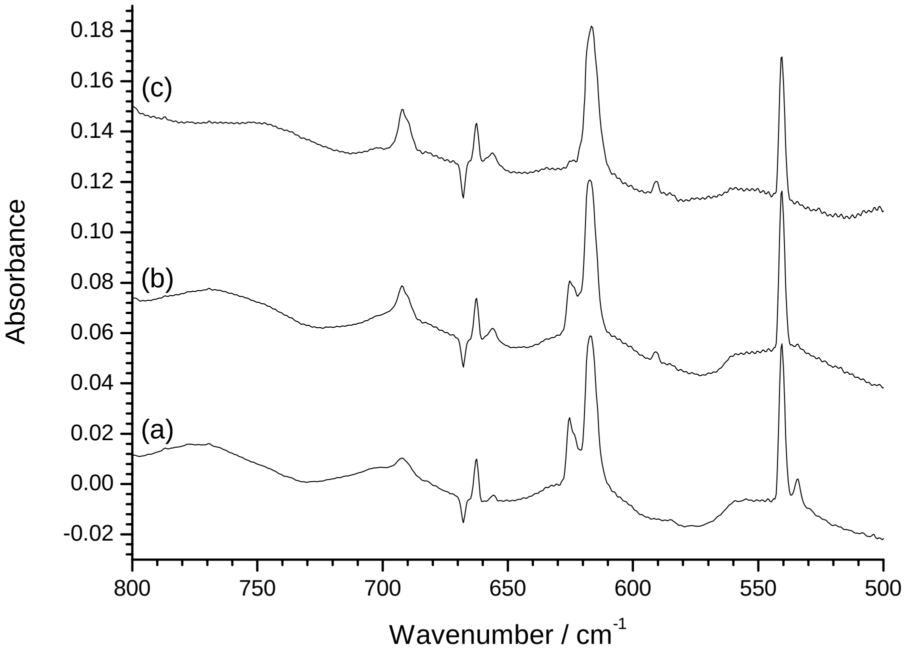

Figure 6.03 IR spectra of palladium isolated in 0.5% F_2/Ar, offset for clarity, (a) deposition of palladium, (b) after broadband photolysis, (c) after annealing to 25 K.

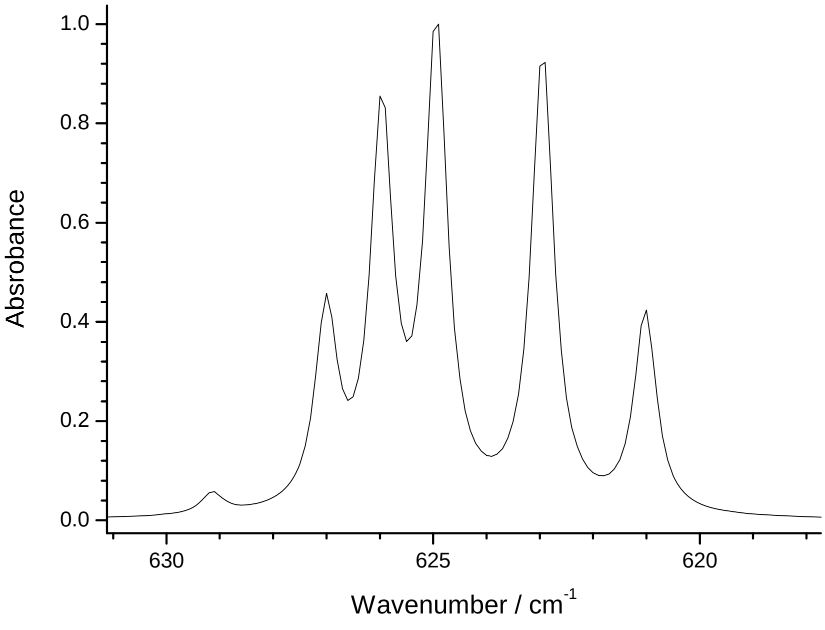

Figure 6.04 Calculation of the ideal palladium isotope splitting pattern.

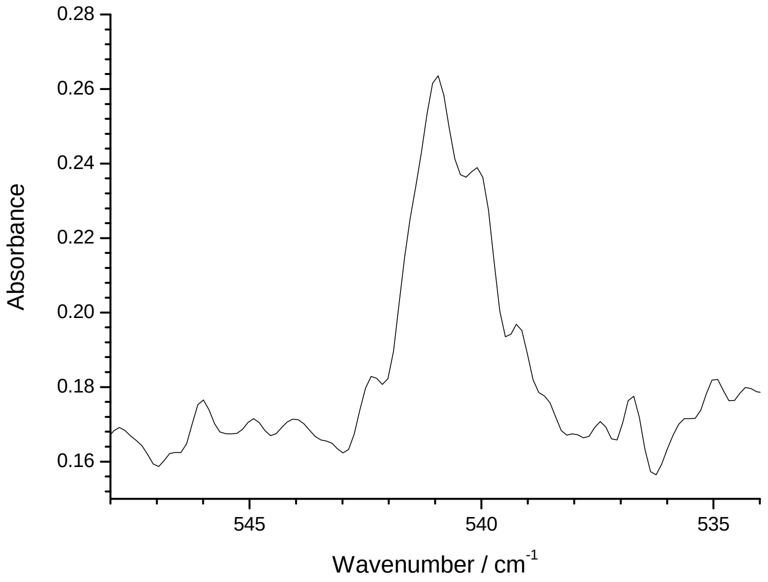

Figure 6.05 High resolution IR spectrum of palladium isolated in 0.5% F_2/Ar.

When the matrix was photolysed using broadband photolysis the peaks present around 625.0 cm^{-1} reduced significantly along with the peak at 534.5 cm^{-1}, Figure 6.03(b) and Figure 6.06(b), while the cluster at 616.6 cm^{-1} does not appear to change at all. The peak at 541.0 cm^{-1} does not change much with photolysis, Figure 6.03(b). The peaks previously seen at 655.0 cm^{-1} and 692.7 cm^{-1} in early experiments also begin to appear after photolysis. The peak at 692.7 cm^{-1} grows by the most significant amount and for the first time also shows a weak palladium isotope pattern which means the previous assignment to this as a palladium compound is correct, Figure 6.07. When the matrix was annealed the peaks at 625.0 cm^{-1} and 534.5 cm^{-1} are almost totally removed from the matrix, Figure 6.03(c) and Figure 6.06(c), while there also appears to be some change in the cluster of peaks at 616.6 cm^{-1}, with the growth of a shoulder at 614.6 cm^{-1}. The fact that two distinct palladium isotope patterns were present is shown and the tail of the palladium isotope pattern becomes more prominent at 612.9 cm^{-1}. The peak previously seen at 631.7 cm^{-1} is once again present before and after photolysis and again is not affected by either photolysis or annealing meaning it is unlikely to be a palladium fluoride compound. The peak which previously appeared to follow similar photolysis

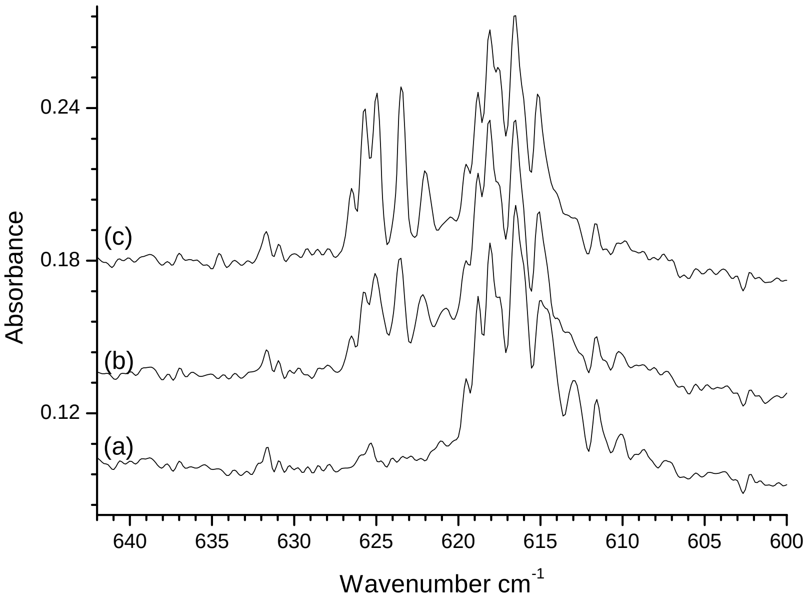

Figure 6.06 High resolution IR spectra of palladium isolated in 0.5% F_2/Ar, (a) after annealing, (b) after photolysis, (c) shows palladium on deposition isolated in 0.5% F_2/Ar.

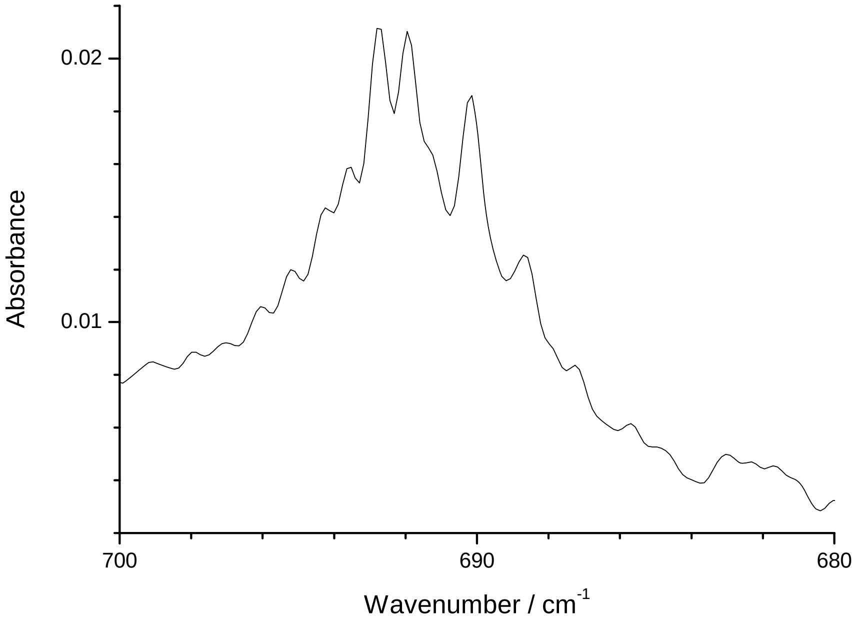

Figure 6.07 High resolution IR spectrum of palladium isolated in 0.5% F_2/Ar after photolysis and annealing.

and annealing pattern to the 692.7 cm^{-1} peak once again appears after photolysis at 590.9 cm^{-1} and again looks as though it could be from the same compound as seen at 692.7 cm^{-1}, and the peaks at 625.0 cm^{-1} appear to be from the same compound as the peak at 534.5 cm^{-1}.

From these results the peaks present at 692.7 cm^{-1}, 625.0 cm^{-1}, 616.6 cm^{-1}, and 541.0 cm^{-1} can be definitely assigned to compounds containing palladium, but assignment of these molecules past that is purely speculation currently and is solely based on computational calculations.

The previous assignment of the peak at 692.7 cm^{-1} to PdF_4 seems reasonable given the computational calculations suggesting its stability and the increase in its intensity seen when the matrix was photolysed and annealed, Figure 6.03 and Figure 6.06. This assignment will also mean that PdF_4 could be in a distorted geometry as the peak at 591.0 cm^{-1} appears to be from the same molecule from its photolysis and annealing behaviour, Figure 6.08 and Figure 6.09, although no isotope pattern could be observed on this band due to the background noise being too high, shown in Appendix 3.8. The assignment of PdF to the peak at 541.0 cm^{-1} also seems reasonable. The peaks present at 625.0 cm^{-1} and 616.6 cm^{-1} are still difficult to assign and are tentatively assigned to PdF_3 and PdF_2, respectively, based on their photolysis and annealing behaviour. This is due to the computational calculations suggesting that PdF_3 is barely stable and the reaction of the peak at 625.0 cm^{-1} to photolysis and annealing. The assignment of PdF_2 is related to the fact that this peak appears to be fairly consistent implying a stable compound as the computational calculations suggest. The assignment of the peaks at 625.0 cm^{-1} to PdF_3 is also backed up by the fact that this peak, like PdF_4, appears to have another peak associated with it at 534.5 cm^{-1}, Figure 6.08 and Figure 6.09, once again no isotope pattern could be observed on this band above the background noise, shown in Appendix 3.9. The peak present at 655.0 cm^{-1} has previously been assigned to a $HF...CO_2$ complex by Andrews and Johnson,[44] however in these experiments this peak does not correlate to the other peaks observed by Andrews and Johnson at 3870.9 cm^{-1}, 2839.5 cm^{-1}, 2354.4 cm^{-1}, and 2289.2 cm^{-1}, expanded spectrum shown in Appendix 3.4 and 3.5,[44] and does not occur in any other experiments involving F_2 as would be expected, it is thus tentatively assigned to a palladium fluoride. Unfortunately no isotope pattern could be obtained for this peak due to its extremely weak nature in lower concentration F_2/Ar experiments and its close proximity to the large CO_2 peak.

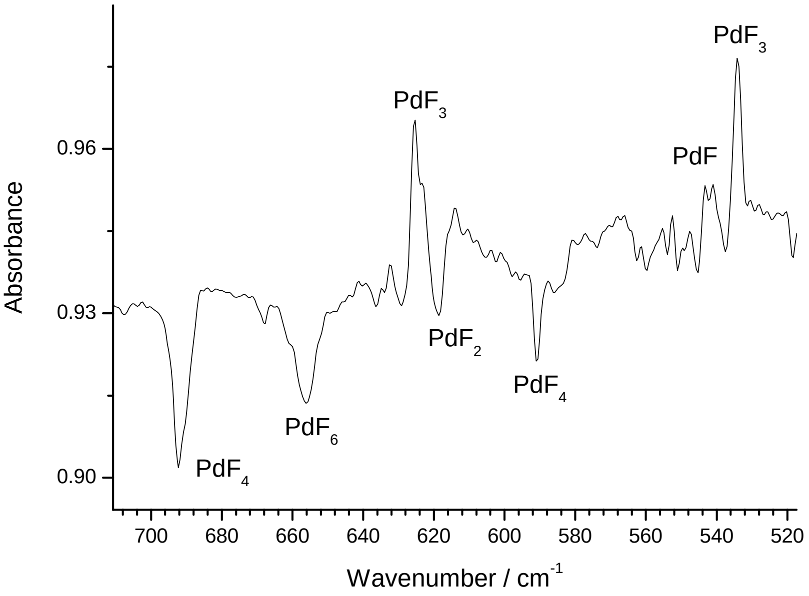

Figure 6.08 IR spectral subtraction for 2% F_2/Ar showing the change in peak intensity after photolysis and annealing.

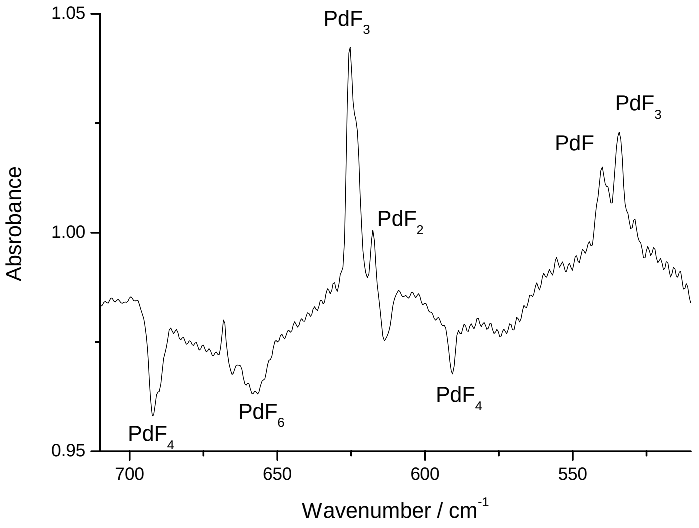

Figure 6.09 IR spectral subtraction for 0.5% F_2/Ar showing the change in peak intensity after photolysis and annealing.

6.2.2.4 Pd in 10% F_2/Ar.

Now that it had been shown that by reducing the concentration of fluorine the ratio of the palladium fluorides, like titanium before it, could be controlled the fluorine concentration was increased to 10% F_2/Ar to try and increase the presence of the higher palladium fluorides.

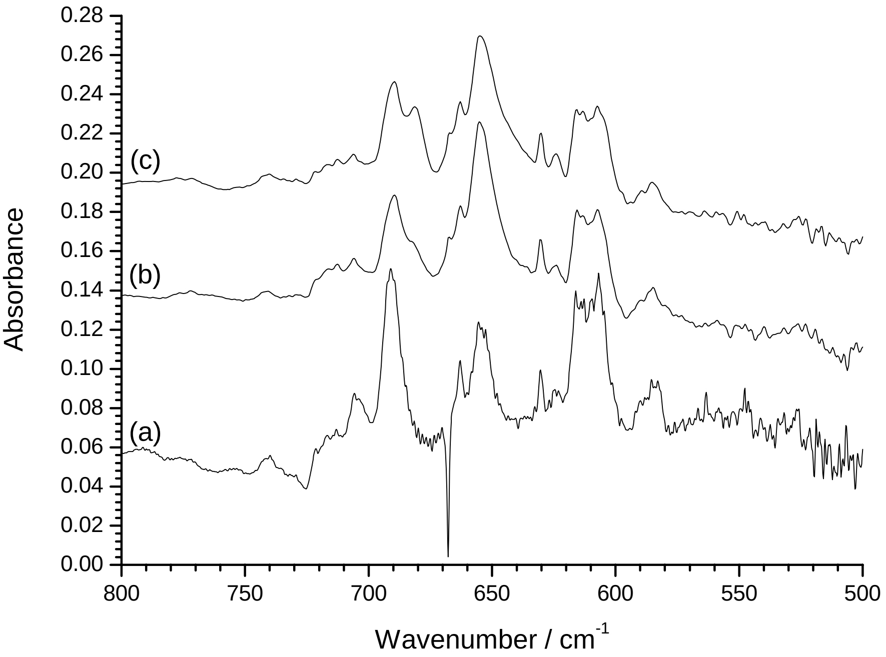

Figure 6.10 IR spectra of palladium isolated in 10% F_2/Ar, (a) shows palladium isolated in 10% F_2/Ar, (b) after photolysis, (c) after annealing.

Figure 6.10(a) shows the results obtained when palladium was deposited into 10% F_2/Ar. Peaks were present at 585.8 cm^{-1}, a cluster of peaks at 606.5 cm^{-1} to 616.5 cm^{-1}, 630.2 cm^{-1}, 654.5 cm^{-1}, 691.4 cm^{-1}, and 706.7 cm^{-1}. The peak at 691.4 cm^{-1} is larger than seen before meaning that this is likely correctly assigned to a larger palladium fluoride and thus PdF_4 is a reasonable assignment, and the peak previously shown at 585.8 cm^{-1} has increased in intensity upon deposition by a similar amount to the peak at 691.4 cm^{-1}, again implying these two peaks are linked. The peak previously seen at 541.0 cm^{-1} is now hardly noticeable above the background noise implying that the assignment of this peak to PdF is also reasonable. The peak previously seen at 657.0

cm^{-1} is now also much more intense than previously seen giving a good indication this assignment may also be correctly assigned to a larger palladium fluoride. Annealing was conducted on the matrix before any photolysis had taken place but no change was observed. When broadband photolysis was conducted the peak at 654.5 cm^{-1} increased while the peak at 691.4 cm^{-1} decreased, Figure 6.10(b). Subsequent annealing of the matrix to 25 K leads to a reduction in the peak at 654.5 cm^{-1} and a new shoulder appearing on the 691.4 cm^{-1} peak at around 681.5 cm^{-1}, Figure 6.10(c). The peaks previously suggested to be PdF_3, like PdF, within these spectra are very small and almost un-noticeable above the back ground. One of bands assigned to PdF_3 can be seen at 624.4 cm^{-1}, the other one is too small to be identified.

It was found within the experiments conducted with a 10% F_2/Ar matrix that if the tantalum/palladium filament was used for too long with small amounts of palladium present then tantalum would react with fluorine and sublimation of these compounds occurred resulting in the identification of TaF_5 in the spectra, Figure 6.11. This caused the analysis of the spectra to be much more difficult due to the close proximity of the TaF_5 and $(TaF_5)_3$ peaks and the palladium fluoride peaks, but once it was realised that tantalum was present within the matrix this was quickly resolved. The assignment of TaF_5 and $(TaF_5)_3$ within an argon matrix was conducted by Osin *et al.*[45] in 2001, comparison between these results and the ones obtained in Figure 6.09 show that tantalum was reacting with fluorine and then being sublimed and isolated in the matrix. Osin *et al.* assigned bands at 707.5 cm^{-1} and 658.1 cm^{-1} to TaF_5 and peaks at 751 cm^{-1}, 712.9 cm^{-1}, 696.7 cm^{-1}, 688.7 cm^{-1}, and 523 cm^{-1} to $(TaF_5)_3$.[45] The band at 523 cm^{-1} was always present and so was used to identify the production of $(TaF_5)_3$. With this information the re-examination of the 10% F_2/Ar spectra was conducted to try and see if previous assignments in the 10% F_2/Ar spectra could be revised, assignments made in the 2% F_2/Ar and 0.5% F_2/Ar gases would not be changed as tantalum has one stable isotope with 99.98% abundance and so would not account for the isotope patterns observed, the peaks present at 705.9 cm^{-1} and 655.4 cm^{-1} could be assigned to TaF_5.

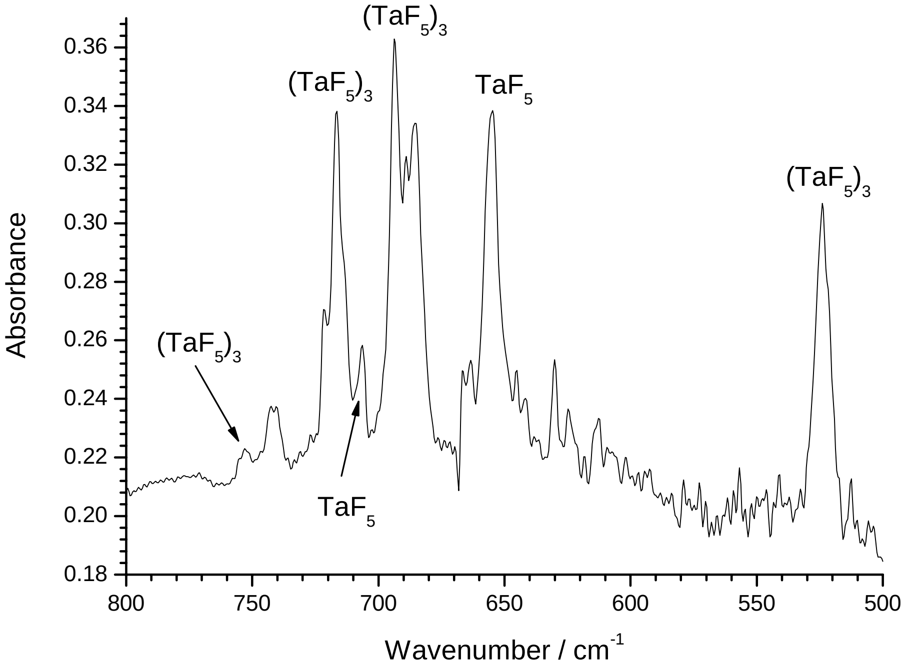

Figure 6.11 IR spectrum of tantalum and palladium isolated in 10% F_2/Ar.

Further investigations into the peaks using a N_2/Ar matrix produced no peaks in the area of interest corresponding with previous assignments suggesting that the peaks produced do not correspond to a palladium nitrogen complex, although some $Pd(N_2)_n$ compounds do occur at between 2210 cm^{-1} and 2250 cm^{-1}, they are extremely weak and their photolysis and annealing activity does not correspond to any peaks assigned to palladium fluorides.[36, 38, 46, 47]

6.2.2.5 SOTONVIB Calculations.

The next step was the use of the SOTONVIB program to try and assign the bands based on their splitting pattern, although it was already thought that this would prove futile. From the position calculated by ADF the peak present at 541 cm^{-1} is assigned to PdF. This seems reasonable given the fact that with higher concentrations of fluorine the peak is reduced until 10% F_2/Ar is used and then it is no longer present and its photolysis and annealing behaviour suggests that it reacts with fluorine to form higher palladium fluorides, and also based on the splitting pattern comparison shown in Figure 6.12.

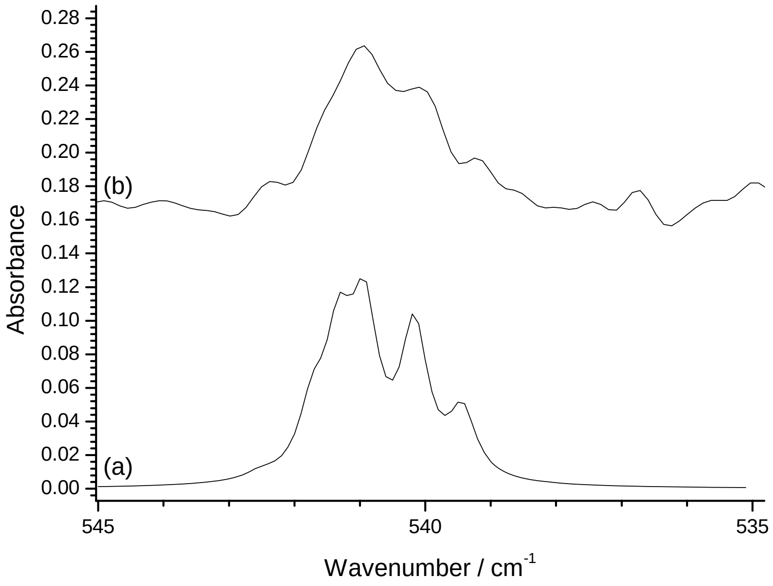

Figure 6.12 Calculated PdF spectral pattern vs. experimental PdF pattern from 0.5% F_2/Ar, (b) IR spectrum of PdF, (a) SVFF calculated spectrum for PdF.

When the computational calculations are compared for PdF_4 to previous calculations by Aullón and Alvarez[24] and calculations performed using Gaussian 03 within this group, there is a difference. The calculations using Gaussian 03 and by Aullón and Alvarez[24] indicate that the PdF_4 molecule is not in a square planar structure as the ADF calculations indicate, instead being in a distorted square planar structure (D_{2d} geometry) with bond angles of 167° and 90.7°, although this difference in structure cannot be distinguished by the use of the palladium isotope pattern, as shown in Figure 6.13, but this structure will give two bands in the spectrum whereas the square planar structure will only give one. This means that as the peak tentatively assigned to PdF_4 at 692.7 cm^{-1} is following this behaviour as the peak at 590.9 cm^{-1} appears linked, showing that if this assignment is correct PdF_4 is present in a distorted form within these experiments, although the extent of this distortion cannot be determined, Figure 6.13, isotope splitting on the peak at 590.9 was difficult to obtain and thus is shown in Appendix 3.8.

One major problem expected and shown with the palladium isotope splitting patterns and the results obtained shows that if the peak present at 692.7 cm^{-1} is adjusted for the increased energy then this peak and the peaks present at 625.0 cm^{-1} and 616.6 cm^{-1} cannot be distinguished from each other meaning that assignment of the peaks to palladium fluorides can only be done based upon their behaviour in the matrix and computational calculations meaning any assignment is purely speculative, Figure 6.14. This comparison involved deciding which was the most resolved peak, the ^{108}Pd peak was chosen, then subtracting the data from this peak. The peaks present assigned to PdF_4 and PdF_3 were then scaled to the peak assigned to PdF_2, as this was the most intense, resulting in Figure 6.14 which shows that the isotope pattern of these different molecules cannot be separated from one another.

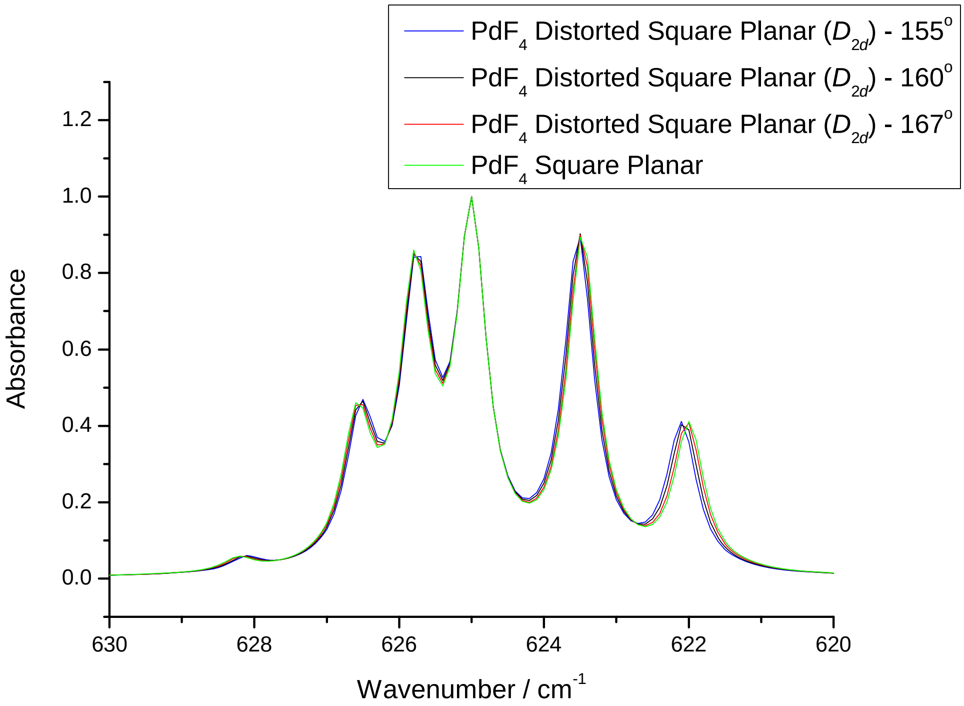

Figure 6.13 Computational comparison of PdF_4 in a square planar geometry and various distorted square planar geometry, ranging from 167^o to 155^o bond angles.

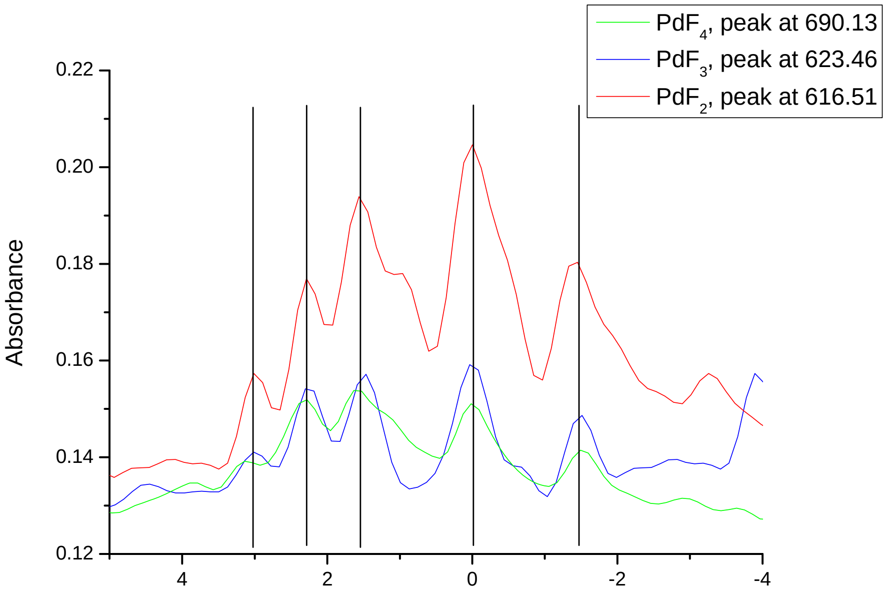

Figure 6.14 Comparison of the adjusted IR spectra and the splitting patterns of the peaks at 690.13 cm^{-1}, 623.46 cm^{-1} and 616.51 cm^{-1}.

Figure 6.15 also shows the SOTONVIB calculations for PdF_6, PdF_4, and PdF_2 if the ^{106}Pd peaks are all at the same energy showing that there is no difference between the isotope splitting observable due to all 3 having the same type of vibrations and thus the same isotope splitting patterns.

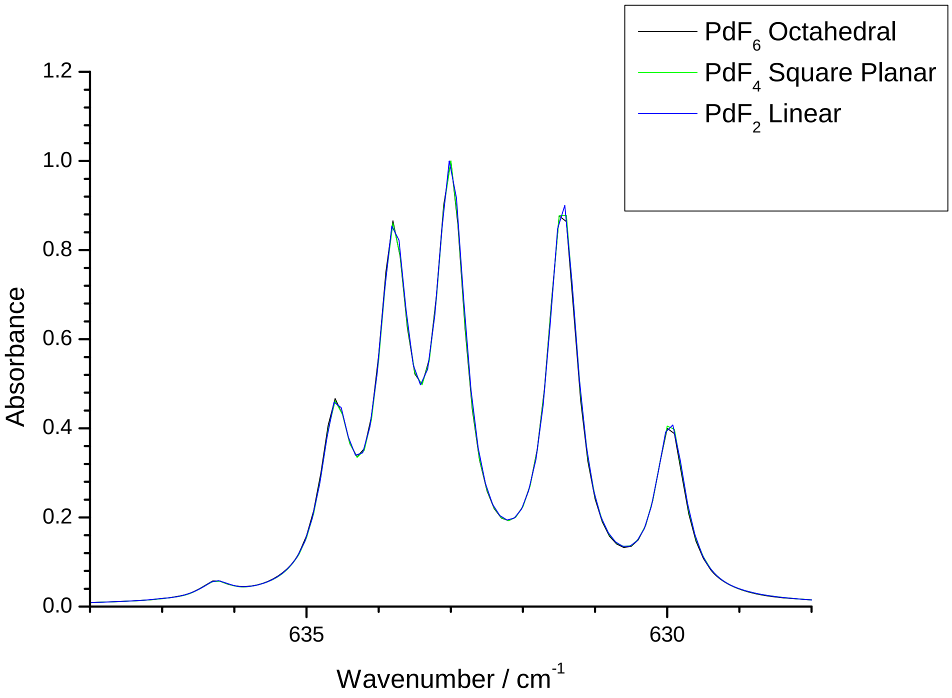

Figure 6.15 Comparison of the calculated splitting patterns of the peaks octahedral PdF_6, square planar PdF_4, and linear PdF_2.

6.2.3 Discussion.

Due to the fact that the isotope splitting patterns cannot be used diagnostically, other than to confirm the presence of palladium, the assignments of the palladium fluorides produced will be based upon the computational results obtained and the behaviour of the individual fluorides within the matrix. Table 6.6 shows the assignments in different F_2/Ar concentrations.

Possible Assignments	2% F_2/Ar	0.5% F_2/Ar	10% F_2/Ar
PdF	540.9	541.0	-
PdF_2	617.0	616.6	615.9
PdF_3	625.8 534.6	625.0 534.5	624.4 -
PdF_4	692.8 591.0	692.7 590.9	691.7 585.3
PdF_6	656.0	655.0	654.5

Table 6.6 Table showing the absorption bands of palladium halides within a argon matrix, values are in cm^{-1}.

Solely on the basis of the computational calculation the peak present at 541.0 cm^{-1} is assigned to PdF, Figure 6.12. This assignment is the only assignment in this work that can be given with a degree of certainty due to the difference observed and calculated for its splitting pattern. The behaviour of this molecule within a matrix, the intensity of this peak decreases as the fluorine concentration increases, would be expected from this fluoride.

The other assignments are now purely speculation based on computational calculations and rationalisation from matrix behaviour but cannot be given with any certainty. The peaks present at 692.7 cm^{-1} and 590.9 cm^{-1} are assigned to a distorted PdF_4. This is done on the basis that in all calculations PdF_4 is always highest in energy of all the palladium fluorides and so is assigned to the highest peak in our spectra, Table 6.4, and based upon the photolysis and annealing behaviour which show when the matrix is photolysed and annealed PdF_4 grows significantly. Previously Timakov *et al.*[26] assigned a peak at 711 cm^{-1} in the gas phase to PdF_6, and if matrix shift is taken into account the peak at 692.7 cm^{-1} could conceivably be due to PdF_6, however Riedel and

Kaupp[27] dispute these results and various calculations conducted since suggest that PdF_4 is higher in energy than PdF_6 and so this assignment is disregarded here. The peaks present at 625.0 cm^{-1} and 534.5 cm^{-1} are assigned to PdF_3. This assignment is based upon the computational calculations by Dr. A. J. Bridgeman and T. Nguyen. In these calculations PdF_3 is predicted to be stable, but with the addition of a very small energy PdF_3 will form PdF_4 and PdF_2 which is used to suggest that when the matrix is photolysed PdF_3 will react with fluorine to form PdF_4 readily, Figure 6.02 and Figure 6.04, and also that PdF_3 would produce two bands which are present in the IR spectrum, Figure 6.02, Figure 6.04, and Figure 6.08. Photolysis of the matrix results in the peaks at 625.0 cm^{-1} and 534.5 cm^{-1} decreasing in intensity, while the peaks assigned to PdF_4 increased in intensity, another reason the assignment of PdF_4 and PdF_3 seems reasonable. This leaves the peaks at 616.6 cm^{-1}, 618.0 cm^{-1}, and 655.0 cm^{-1} which will be assigned to two sites of PdF_2 and PdF_6 respectively. The peak present at 655.0 cm^{-1} is likely due to PdF_6, because the computational calculations suggest that PdF_6 is more stable than PdF_5 and that it will appear at a lower frequency than PdF_4. This assignment cannot be confirmed with isotope splitting and so can only be postulated based upon the photolysis and annealing behaviour which show PdF_6 forming and increasing as soon as the matrix is photolysed and annealed implying that fluorine is combining with the other palladium fluorides to form PdF_6, Figure 6.02, Figure 6.04, Figure 6.08, and Figure 6.09. The splitting patterns of PdF_4, PdF_3, and PdF_2 are compared to the computational calculations to show these assignments are reasonable in Figure 6.16, Figure 6.17, and Figure 6.18.

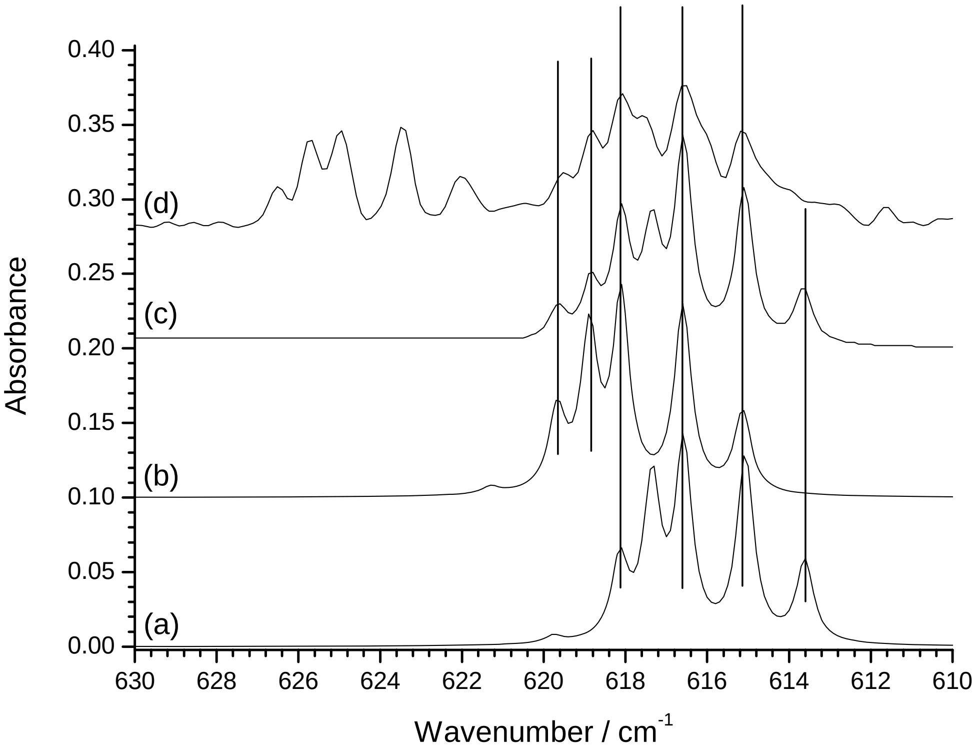

Figure 6.16 Calculated PdF_2 spectral pattern vs. experimental PdF_2 pattern from 0.5% F_2/Ar, (d) IR spectrum of PdF_2, (c) SVFF calculated spectrum for PdF_2, (b) α site only, (a) β site only.

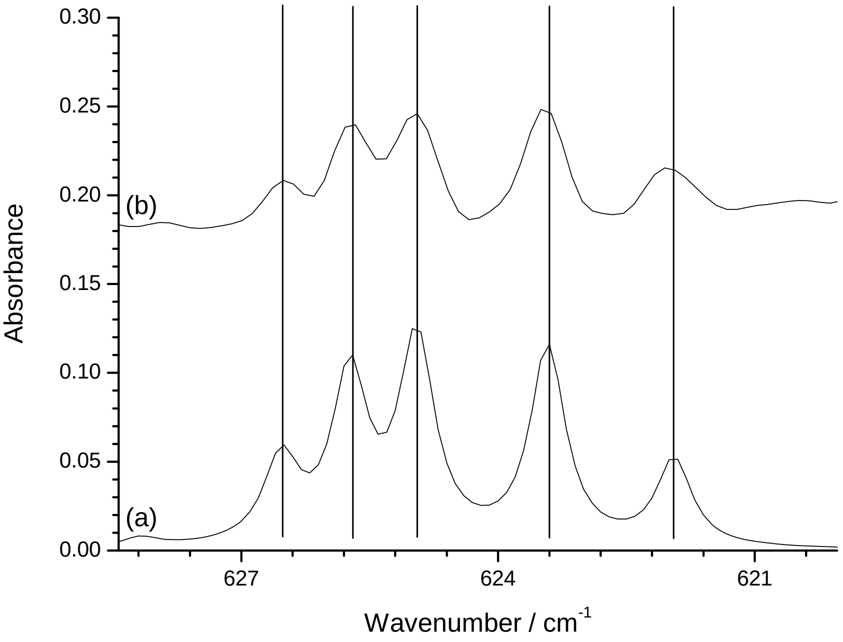

Figure 6.17 Calculated PdF_3 spectral pattern vs. experimental PdF_3 pattern from 0.5% F_2/Ar, (b) IR spectrum of PdF_3, (a) SVFF calculated spectrum for T-shaped PdF_3 (asymmetric stretch).

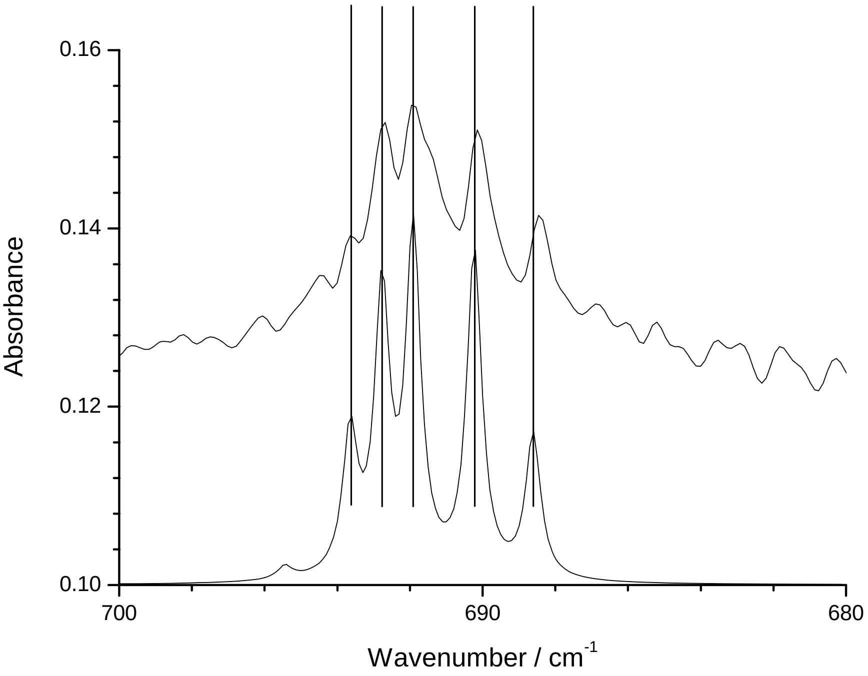

Figure 6.18 Calculated PdF_4 spectral pattern vs. experimental PdF_4 pattern from 0.5% F_2/Ar, (b) IR spectrum of PdF_4, (a) SVFF calculated spectrum for distorted square planar PdF_4 (167°).

6.2.4 Conclusion.

From the IR spectra there are 4 clear areas in which palladium fluorides are isolated, with one present at 616.6 cm^{-1} likely having multiple sites, there is also a further peak which is tentatively assigned to a further palladium fluoride. All of the peaks present within this work are extremely difficult to assign. This is because the structure of the palladium fluorides are all very similar and the splitting patterns produced as shown with the use of the SOTONVIB program, Figure 6.15 and from experimental Figure 6.14, cannot be separated from one another and by manipulation of the actual spectra it can be shown, Figure 6.11, that all of the splitting patterns are practically identical to one another and so separation and identification of these peaks is not possible.

Thus all assignments made in this work, with the exception of PdF, are purely speculative and based on computational calculations and experimental observations of the peaks within the matrix. The peaks produced can be tentatively assigned to PdF_6 at

656.0 cm^{-1}, PdF_4 at 692.0 cm^{-1} and 590.9 cm^{-1}, PdF_3 at 625.0 cm^{-1} and 534.5 cm^{-1}, PdF_2 at 616.6 cm^{-1}, and PdF at 541.0 cm^{-1}. These assignments are solely based on the computational calculations stating that PdF_6, PdF_4, and PdF_2 are stable while PdF_3 requires a small amount of energy to react to form PdF_4 and PdF_2. Thus the photolysis behaviour of the peak at 625.0 cm^{-1} and 534.5 cm^{-1} is rationalised as the reaction of PdF_3 with fluorine to form PdF_4. If the assignment of PdF_4 to peaks at 692.0 cm^{-1} and 590.9 cm^{-1} is correct it shows that this molecule is in a distorted square planar geometry, although it is not possible to determine how distorted this molecule.

6.2.5 Further work.

Due to the clear success in isolating palladium fluorides the next step would be to take this technique on and try to isolate palladium chlorides, this was the aim of this work but the equipment available could not be set up in the time constraints of this work to conduct the experiments. Further investigation of the palladium fluorides is also required to try and definitely identify the palladium fluorides.

References.

1. P. E. M. Siegbahn, *Theor. Chim. Acta*, 1994, **87**, 441.
2. N. V. Sidgwick, *Chemical Elements and their Compounds*, Oxford University Press, Oxford 1950.
3. F. A. Cotton and G. Wilkinson, *Advanced Inorganic Chemistry*, 5th Edn., Wiley-Interscope, Toronto, 1988.
4. N. N. Greenwood and A. Earnshaw, *Chemistry of the Elements*, 2nd Edn., Butterworth Heinmann, Oxford, 1997.
5. C. E. Housecroft, *Inorganic Chemisry*, Prentice Hall, Harlow, UK, 2000.
6. A. N. Guthrie and M. J. Copley, *Phys. Rev.*, 1931, **38**, 360.
7. C. E. Garret and K. Prasad, *Adv. Synth. Catal.*, 2004, **346**, 889.
8. J. Matthey, *The Platinum Metals Report*, London, 2009.
9. P. L. Hagelstein, M. C. H. McKubre, D. J. Nagel, T. A. Chubb and R. J. Hekman, *New Physical Effects in Metal Deuterides*, US Department of Energy, Washington, 2004.
10. J. D. Lee, *Concise Inorganic Chemistry*, Chapman & Hall, London, 1993.
11. A. F. Wells, *Z. Kristallgr.*, 1938, **100**, 189.
12. H. Schäfer, U. Weise, K. Rinke and K. Brendel, *Chem. Int. Ed. Engl.*, 1967, 253.
13. D. B. D. Amico, F. Calderazzo, F. Marchetti and S. Ramello, *Chem. Int. Ed. Engl.*, 1996, **35**, 1331.
14. L.-C. Kao, A. C. Hutson and A. Sen, *J. Am. Chem. Soc.*, 1991, **113**, 700.
15. A. Suzuki, *Pure Appl. Chem.*, 1991, **63**, 419.
16. N. Miyanura and A. Suzuki, *Chem. Rev.*, 1995, **95**, 2457.
17. A. Suzuki, *J. Organometallic Chem.*, 1999, **576**, 2457.
18. T. P. Martin, *J. Chem. Phys.*, 1978, **69**, 2036.
19. E. L. Dixon, PhD Thesis, The Univsersity Of Hull, 2004.
20. G. Thiele and P. Woditsch, *Chem. Int. Ed. Engl.*, 1969, **8**, 672.
21. N. Bartlett and P. R. Rao, *Proc. Chem. Soc.*, 1964, 393.
22. W. Chen, S. Shimada and M. Tanaka, *Science*, 2002, **295**, 308.
23. R. Crabtree, *Science*, 2002, **295**, 288.
24. G. Aullón and S. Alvarez, *Inorg. Chem.*, 2007, **46**, 2700.
25. E. C. Sherer, C. R. Kissinger, B. L. Kormos, J. D. Thompson and C. J. Cramer, *Angew. Chem. Int. Ed.*, 2002, **41**, 1953.

26. A. A. Timakov, V. N. Prusakov and Y. V. Drobyshevskii, *Russ. J. Inorg. Chem.*, 1982, **27**, 1704.
27. S. Riedel and M. Kaupp, *Coord. Chem. Rev.*, 2009, **253**, 606.
28. L. Cheng, M. Y. Wang, Z. J. Wu and Z. M. Su, *J. Comput. Chem.*, 2007, **28**, 2190.
29. K. P. Huber and G. Herzberg, *Molecular Spectra and Molecular Structure*, Van Nostrand Reinhold, New York, 1979.
30. D. L. Hildenbrand and K. H. Lau, *J. Chem. Phys.*, 1997, **107**, 6349
31. R. H. Li, R. H. Jensen, W. J. Balfour, S. A. Shepard and A. G. Adam, *J. Chem. Phys.*, 2004, **121**, 2591.
32. J. Hoeft, F. J. Lovas, E. Tiemann and T. Z. Torring, *Naturforsh*, 1970, **25a**, 35.
33. P. E. M. Siegbahn, *Theor. Chim. Acta.*, 1993, **86**, 219.
34. M. R. A. Blomberg, P. E. M. Siegbahn and M. Svensson, *J. Am. Chem. Soc.*, 1992, **114**, 6095.
35. H. Huber, W. E. Klotzbücher, G. A. Ozin and A. van der Voet, *Can. J. Chem.*, 1973, **51**, 2722
36. G. A. Ozin and W. E. Klotzbücher, *J. Am. Chem. Soc.*, 1975, **97**, 3965.
37. R. Yang, Y. Gong and M. Zhou, *Chem. Phys.*, 2007, **340**, 134.
38. H. Huber, E. P. Kündig, M. Moskovits and G. A. Ozin, *J. Am. Chem. Soc.*, 1973, **95**, 332.
39. W. E. Klotzbücher and G. A. Ozin, *J. Am. Chem. Soc.*, 1975, **97**, 2672.
40. B. Tremblay and L. Manceron, *Chem. Phys.*, 1999, **250**, 187.
41. J. H. Darling and J. Ogden, *J. Chem. Soc., Dalton Trans.*, 1973, 1079.
42. M. Filatov, *Chem. Phys. Lett.*, 2003, **373**, 131.
43. B. Y. Liang, M. F. Zhon and L. Andrews, *J. Phys. Chem. A*, 2000, **104**, 3905.
44. L. Andrews and G. L. Johnson, *J. Chem. Phys.*, 1982, **76**, 2875.
45. S. B. Osin, D. I. Davlyatshin and J. S. Ogden, *Russ. J. Phys. Chem.*, 2001, **75**, 1312.
46. H. Huber, W. E. Klotzbücher, G. A. Ozin and A. van der Voet, *Can. J. Chem.*, 1974, **51**, 2722.
47. G. A. Ozin and J. Garciaprieto, *J. Phys. Chem.*, 1988, **92**, 325.

Chapter 7.

Third Row Transition Metal Halides.

7.1 Introduction.

Group 12 elements are often considered as post transition metals due to the fact that the d electrons within these atoms are not involved in bonding within any of their known compounds. Isolation of a group 12 element in an oxidation state which would involve the d electrons would have significant consequences for the understanding and treatment of the periodic table. Previously only +2 oxidation states have been observed for group 12 elements meaning the outermost d orbitals are filled and do not participate in bonding. Oxidation states beyond this +2 oxidation state would mean that the 5d electron are becoming involved in bonding which means the group 12 elements would no longer be considered to be post-transition metals and would be reassigned to transition metals. This leads to the aim of this work to try and isolate a Hg^{IV} compound. A possible problem with this work, as previously seen with work involving fluorine, is the lack of fluorine isotope pattern means that identification of the complex is very difficult. There was a report of a Hg^{III} complex by Deming *et al.*[1] in 1976 but this has never been confirmed.

7.1.1 History of Mercury.

Within this chapter a series of experiments conducted by this research group will be detailed. Firstly a brief introduction about mercury and the history of mercury will be given and then a brief look at why a group 12 element in a +4 oxidation state would be so interesting, then finally a detailed literature review and the results obtained will be presented.

Mercury is an extremely rare element and is only present in the lithosphere at 0.02 ppm and has only one important ore, rhombohedral cinnabar (HgS).[2-4] Mercury has been known to have been used as early as 1500 BC by the ancient Chinese and Egyptians, confirmed by the presence of mercury in tombs dating back to these times. In China mercury compounds were thought to prolong life, heal bone fractures, and maintain good health. The Chinese emperor Qin Shi Huang died from drinking mercury and powered jade while trying to attain eternal life; he was also buried in a tomb that contained rivers of flowing mercury.[5] The ancient Greeks, Romans and Egyptians used mercury compounds in ointments and in cosmetics which often deformed the face. The first recorded use of mercury for chemistry was in the Mediterranean where it was used for extracting metals by amalgamation as early as 500 BC. Cinnabar was also often used as a pigment. Alchemists for over a thousand years, until 1500 AD, regarded mercury as the metal that was key to the transmutation of base metals to gold. They believed that varying the quality and quantity of sulfur contained within the mercury would allow the formation of different metals, the purest of which was gold.[6] The name mercury and symbol Hg comes from the Latin word hydragyrum which means water and liquid. The element was named after the Roman god Mercury known for speed and mobility.

The isolation of mercury is relatively straight forward; the simplest method consists of heating cinnabar in a fire of bush wood. The bush wood acts as a fuel and condenser and the metallic mercury collects in the ashes. Modern techniques use the same basic principle as this but with more advanced equipment. The ore is usually crushed and roasted at 870 K in a current of air. Other techniques used especially with rich ores involve roasting with scrap iron or quicklime. Blowing air through the sample quickly oxidises the iron which can be easily removed later. Further purification is achieved by distilling under a reduced pressure.[4] Eight thousand tonnes of mercury are produced each year mainly in China which accounts for two thirds of the world's production followed by Kyrgyzstan. The main uses of mercury currently are in the Castner-Kellner process for the manufacturing of chlorine and sodium hydroxide through the use of mercury as the cathode, and within some batteries, thermometers, diffusion pumps and electric relays.[4]

All of the Hg^{II} halides are known (HgF_2, $HgCl_2$, $HgBr_2$ and HgI_2) and all of the dimer Hg^{I} halides, Hg_2X_2, are also known. HgF_2 stands out from the rest of the dihalides due to the fact that its melting point and boiling point are much higher due to the compound's ionic character and its three dimensional structure, a 8.4 fluorite, Figure 7.01.[4] The other dihalides of mercury are covalent in nature and have low melting points and are soluble in most organic solvents. Their solubility in water decreases as the halide mass increases, HgI_2 being only slightly soluble.[7] The crystal structures of these compounds shows an interesting gradient of change. $HgCl_2$ is composed of linear Cl-Hg-Cl molecules, Hg-Cl distance 2.25 Å.[4] $HgBr_2$ and HgI_2 both have layered structures, however in the bromide the mercury may be regarded as a 6-coordinated with 6 bromides around each mercury atom and the Hg-Br bond distances are 2.48 Å and 3.23 Å. HgI_2 is the only coloured dihalide (red) and the mercury in this structure is 4-coordinate with a Hg-I bond distance of 2.78 Å.[2] When HgI_2 is heated above 400 K it converts to a structure very similar to $HgBr_2$ and shows a yellow colour. All three of these compounds in the gas phase exist as discrete linear molecules.[2]

7.1.2 Mercury in these Experiments.

The reason mercury is used in these experiments rather than the other group 12 elements is due to the fact that out of the group 12 elements mercury has been shown computationally,[8-11] partly due to the relativistic contraction and stabilization of the 6s orbital and to the relativistic expansion and destabilization of the 5d orbitals,[8-11] that an oxidation state beyond +2 would be most likely for mercury.

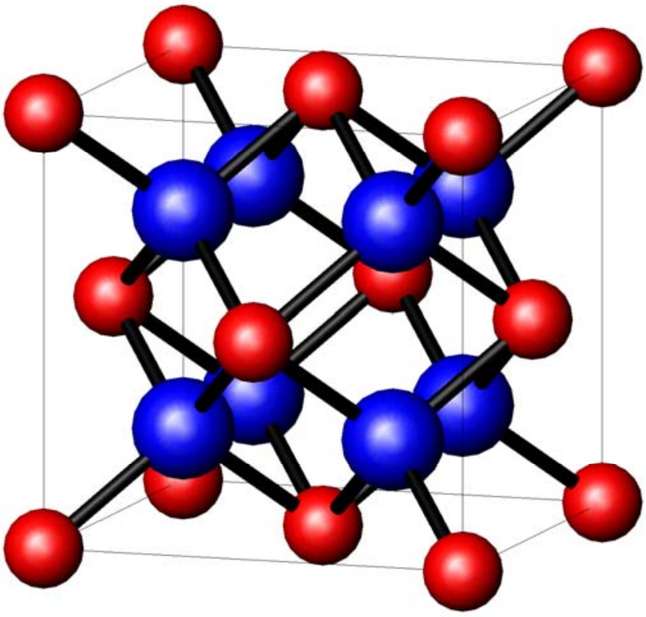

Figure 7.01 A representation of the **c**rystal structure of HgF_2 (8.4 fluorite).

If a graph of all known oxidation states of the transition metals is looked at, Figure 7.02, a regular increase of maximum group valence up to Mn^{VII}, Ru^{VIII}, and Os^{VIII}. But there is a less regular decrease throughout the last third of a given row. But the discovery of Cu^{IV} in Cs_2CuF_6[12] and Au^{V} in $CsAuF_6$[13] stimulated interest in the group 12 elements exhibiting oxidation states beyond +2.

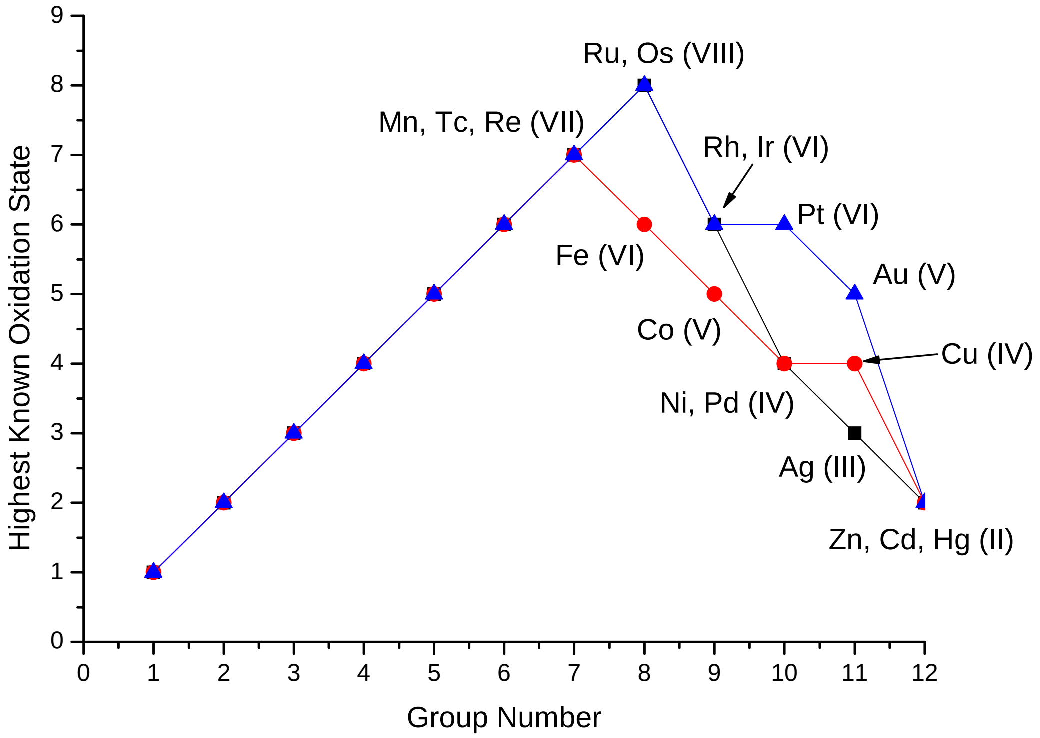

Figure 7.02 Highest known oxidation state for the elements of the first (red), second (black) and third row (blue) transition metals.[14]

Although matrix isolation as a technique has been used previously to synthesise numerous mercury containing species, such as HHgCl,[15, 16] $Hg(OH)_2$,[17] HHg(OH),[17, 18] HgH_2,[19-22] HHgMe,[23-25] $HHgSiH_3$,[26, 27] work conducted on mercury atoms and halides was limited to work conducted within a PhD thesis,[28] until a very recent report published after the conclusion of these studies.[29]

This led to this group beginning work with mercury and fluorine around 2005 with a post doctorial grant for Dr. J. F. Rooms. He conducted significant work with IR spectroscopy on krypton and oxygen and started work with HgF_2. He also conducted a small amount of work with UV/Vis spectroscopy upon HgF_2. When I joined the group in 2006 after an initial year studying computational chemistry with Dr. A. J. Bridgeman I continued the work upon HgF_2 in the IR and UV/Vis and also conducted experiments with atomic mercury in IR, UV/Vis, and EXAFS. All of the work conducted by Dr. J. F. Rooms will be detailed here so an understanding of the work I conducted can be attained.

7.2 Literature Review.

As stated above, little work had been conducted on mercury and halides within a matrix environment and much of the early work involved computational calculations predicting if a Hg^{IV} compound would be stable enough to isolate.

This stability of Hg^{IV} and in particular HgF_4 has been indicated from various computational works,[30-34] one of the first of these was conducted by M. Kaupp *et al.*.[35, 36] They used high level quasirelativistic pseudopotential QCISD (T) calculations to determine if HgF_4 was thermodynamically stable. One of the main conclusions of this paper is that HgF_4 may well be stable or only slightly endothermic with respect to the decomposition to HgF_2 and F_2. The best calculations that they performed including effects such as spin-orbit coupling, zero point vibrational energy corrections and basis set superposition errors calculated a reaction enthalpy for $HgF_4 \rightarrow HgF_2 + F_2$ (ΔH^o) of -0.1 kJmol^{-1}. The structure of HgF_4 was determined to be square planar (D_{4h}) with the use of Hartee-Fock (HF), MP2, and QCISD levels of theory.

Further work was then conducted by Liu *et al.*,[30] they performed similar calculations on the thermodynamic stability of HgF_4 and also concluded that it is stable. They calculated a decomposition energy between $HgF_4 \rightarrow HgF_2 + F_2$ of 19 kJ mol^{-1}. The methods they used, DFT and MP2-DPT, showed a relativistic stabilization of ~ 50 kJ mol^{-1} for this reaction resulting from the difference between the relativistic effects on HgF_2 (~ 130 kJ mol^{-1}) and HgF_4 (~ 88kJ mol^{-1}). This difference in relativistic effect on the stability of HgF_4 compared to HgF_2 is due to the fact that the relativistic destabilisation of the d-orbitals in HgF_4 and is partly compensated by the bonding stabilisation of the 5d orbitals in HgF_4.

They also investigated which effects altered the calculated stability of HgF_4 like Kaupp and others had done previously.[36-38] They found that nonrelativistic all electron HF yield a reaction energy of -333.7 kJ mol^{-1} for the decomposition of HgF_4. Including the relativistic effects by means of first order DPT on HF level leads to a reaction energy of -111.9 kJ mol^{-1}. They also determined that the cross-term between relativity and correlation reduces the reaction energy quite dramatically (97 kJ mol^{-1}) indicating that nonadditivity of relativity and correlation have to be taken into account to describe this reaction properly. Spin orbit coupling affects the stability of HgF_4 within the calculation by 10 kJ mol^{-1}, while ZPE corrections destabilise it by 7 kJ mol^{-1}. This means that both effects do not change qualitatively the prediction that HgF_4 is thermodynamically stable.

Work conducted by Kaupp *et al.*[33] in 2005 showed various precursor compounds to HgF_4 and their decomposition pathways to try and find an easier pathway of reaching the Hg^{IV} oxidation state. Within this work they also compared the relative stabilities of various Hg^{IV} compounds. They found that along with previous results the role of relativistic effects in the stabilising of HgF_4 against reductive elimination was found to arise mainly from a relativistic destabilisation of HgF_2, due to the relativistic contraction of the mercury 6s orbital. The corresponding loss of ionic bonding contributions on the Hg^{II} side and the resulting relative stability of Hg^{IV} thus depend on the presence of very electronegative ligands like fluorine. This would explain partly why $HgCl_4$ and HgH_4 are predicted to be strongly endothermic compounds.[30, 31, 32]

Out of the complexes studied by Kaupp *et al.*[33] none were found to be thermochemically stable as they were all found to exhibit at least one exothermic pathway for reductive elimination. This makes most of these system inferior to gas phase HgF_4, which eliminates fluorine endothermically.[30, 32, 35, 36] Despite this the author believed that due to the high sublimation energy of HgF_2 several of these complexes may provide a more favourable environment for Hg^{IV} than HgF_4 itself in the condensed phase. Calculations were also conducted by Dr. A. J. Bridgeman which are shown in Appendix 2.

7.3 Results - Hg and HgF_2 in F_2/Ar.

The large amount of computational evidence for the stability of HgF_4 and the assertion by Kaupp *et al.*[36] that matrix isolation would be a likely root for the identification of the Hg^{IV} compound led to work beginning within Dr N. A. Young's group with the set aim of isolating HgF_4. Aside from the advantages of matrix isolation already outline, one of the reason that matrix isolation is the best method for use with the reaction suggested by Kaupp *et al.*[36] is related to the properties of HgF_2. HgF_2 is very insoluble and therefore conventional solution reaction chemistry is not likely to be very successful. However, the use of gas phase, or pseudo gas phase, methods should overcome this problem.

The two main avenues of research would be the combination of mercury with varying concentrations of F_2/Ar and combination of HgF_2 with F_2/Ar. This would also involve various types of photolysis using mercury and Hg-Xe lamps, and xenon, krypton, and argon resonance lamps.

7.3.1 Early Mass Spectrometry Work.

The first series of experiments conducted within this research group involved the combination of HgF_2 with fluorine. The reason this specific reaction was chosen was due to suggestions by Kaupp *et al.*[36] that the use of HgF_2 could be a useful pathway to the isolation of HgF_4.

Once HgF_2 had been obtained commercially (three samples were purchased) it was decided to analyse the samples obtained using a mass spectrometer to determine what was released from the samples upon heating. Therefore in the first series of experiments HgF_2 was heated and the vapour directly above the sample was analysed using the mass spectrometry equipment described previously. All of the HgF_2 samples initially released $HgCl_2$ and HgFCl upon heating, but this could be removed by degassing the sample for a period of time. The amount of $HgCl_2$ released by the samples was found to be very dependent upon the batch used, with one sample releasing significantly more amounts than the other two. Once the degassing had been completed the vaporisation of HgF_2 was observed once the sample had been heated to 575 K, this was identified from its parent and daughter ions in the mass spectrometer. The other significant vapour species observed included mercury, HF and as the temperature was increased further oxygen was also observed. The presence of these species indicates that the thermal decomposition of HgF_2 is occurring and possibly any oxide formed is due to hydrolysis or reaction with the hot nickel sample holder.

When fluorine and HgF_2 were introduced into the chamber simultaneously analysis of the vapour showed no clear reaction occurring between the HgF_2 vapour and fluorine, even when the area when irradiated with a broadband Hg-Xe lamp. When mercury vapour was used along with fluorine no reaction was again observed even when photolysed. A consequence of these experiments is that upon heating the HgF_2 samples a complex vapour composition results meaning that care must be taken when interpreting any spectra.

7.3.2 Matrix Isolation IR Spectrometry.

The aim of these IR experiments was to try and trap HgF_2 or mercury atoms in a F_2/Ar matrix in order to prepare and then characterise HgF_4. Prior to the work commencing on mercury, experiments were conducted to confirm the production and mobility of fluorine atoms within the matrix. These experiments involved the use of krypton and a 10% F_2/Ar matrix.

Within these experiments no bands characteristic of KrF_2 were observed upon deposition. Upon photolysis however KrF_2 was observed at 579 cm^{-1},[39] and its intensity increased after further annealing to 22.5 K, Figure 7.03. Within these series of experiments peaks were also observed which have been assigned to O_2F_2 at 624 cm^{-1}, 613 cm^{-1},and 465 cm^{-1},[40] and O_2F at 585 cm^{-1},[40-42] when 10% F_2/Ar matrices contained oxygen. These experiments showed that under the conditions of these experiments fluorine atoms are being produced in the matrices and are mobile upon annealing.[43]

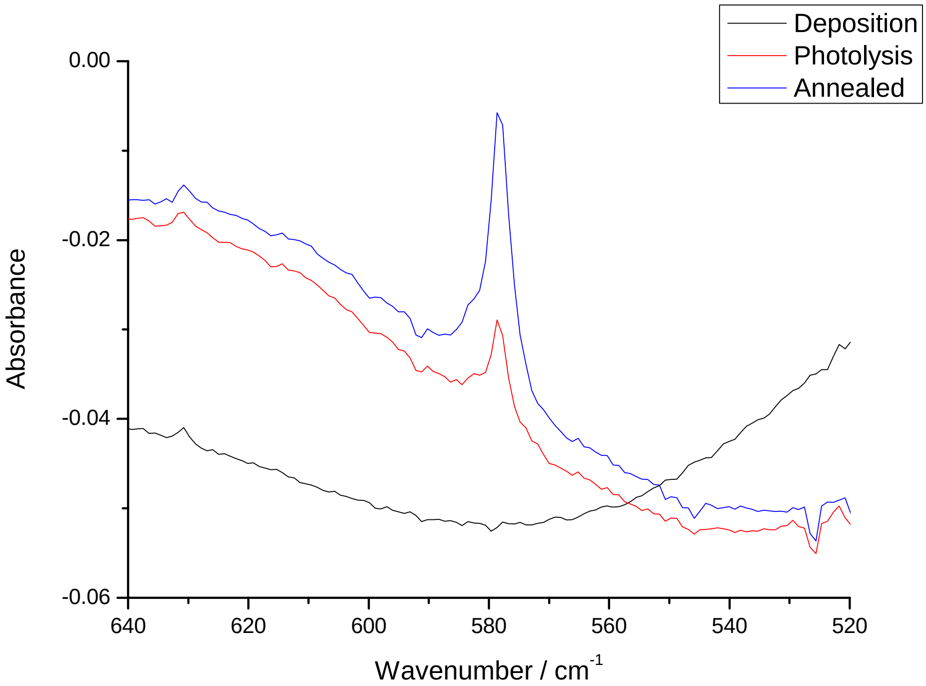

Figure 7.03 IR spectra of krypton isolated in a 10% F_2/Ar matrices, with the effects of photolysis and annealing.

Other important assignments determined from these experiments was the assignment of HF...H_2O,[44] O_2F_2 at 624 cm^{-1}, 613 cm^{-1}, and 465 cm^{-1},[40] O_2F at 585 cm^{-1} and 1500 cm^{-1},[40-42] FCO at 626 cm^{-1},[41,45] F_2CO at 764 cm^{-1},[45,46] FCO_2 at 975 cm^{-1}, 969 cm^{-1}, 957 cm^{-1}, 730 cm^{-1}, and 521 cm^{-1},[47] HHgOH at 2116.5 cm^{-1}, [18] and $Hg(OH)_2$ at 957.2 cm^{-1}, 946.1 cm^{-1}, and 606.9 cm^{-1} [17] all of which occur in the $\nu_{Hg\text{-}F}$ region which will make assignment of HgF_4 all the more difficult.

7.3.2.1 HgF_2 Vaporisation Experiments.

Previous experiments by Tevault *et al.*[48] have shown that HgF_2 should produce a peak in argon matrices around 645.9 cm^{-1}, they assigned this band to the asymmetric stretching mode, υ_3, of linear HgF_2. A recent investigation of mercury and F_2/Ar matrices by Andrews *et al.* assigned a band at 644.9 cm^{-1} to HgF_2.[29] This work produced a peak at 645.1 cm^{-1}, Figure 7.04(a), this was observed when HgF_2 was thoroughly degassed and was sublimed into an argon matrix, which is in agreement with the previous assignment of this as the asymmetric stretching mode, υ_3, of HgF_2.

The only other peak present within these spectra of interest is present at 620.6 cm^{-1}, this peak varies in intensity and was observed in most of the HgF_2/Ar experiments conducted. This peak could possibly be due to dimer or higher aggregates of HgF_2 but in the literature previously a band at 589 cm^{-1} in krypton matrices has been assigned to a dimer mode meaning that this is unlikely.[49,50] Tevault *et al.* have previously assigned a peak a few wavenumbers lower than HgF_2 to a HgF_2...Y complex (Y = N_2, CO, NO).[48] However the peak at 620.6 cm^{-1} is not due to $HgF_2.N_2$ or $HgF_2.CO$[48] and its intensity does not correlate with the bands within the spectra due to H_2O or CO_2 eliminating those possibilities. The difference of 20 cm^{-1} is likely too large to be explained by a HgF_2...Y complex, so this peak remains unassigned but is likely due to some impurity resulting from the vaporisation of HgF_2, as shown in the mass spectrometry experiments. Even after prolonged degassing of the sample there were always numerous bands present that can be assigned to species such as SiF_4, H_2O, CO_2, and small amounts of CO and HF.[44] The presence of HF within the spectra confirms the decomposition observed in the mass spectroscopy experiments when HgF_2 was heated in nickel Knudsen cells. The presence of mercury when HgF_2 was heated was also later confirmed by electronic absorption experiments.

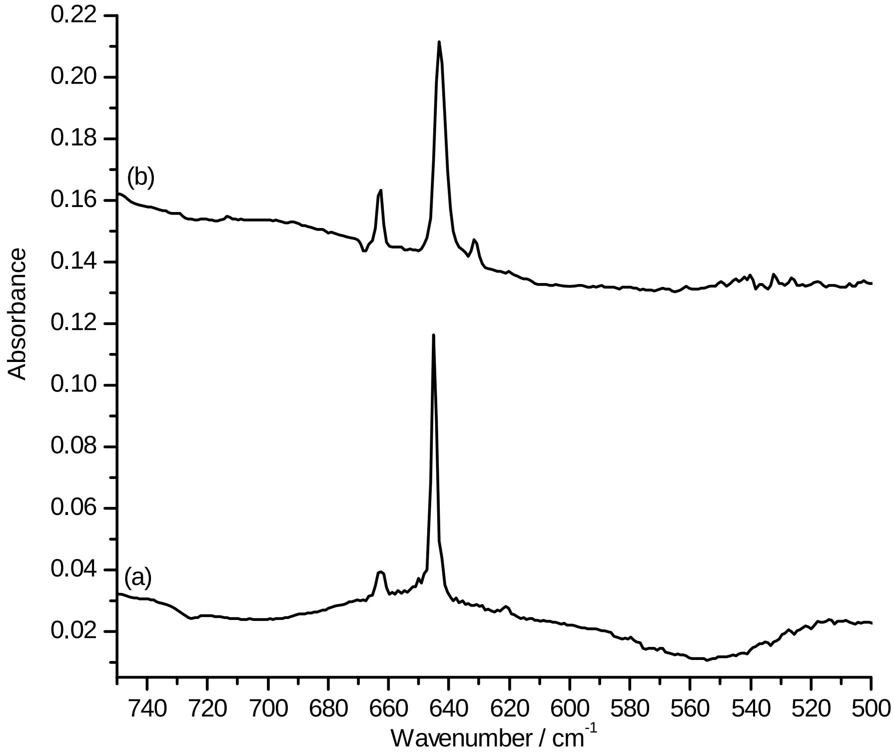

Figure 7.04 IR spectra of HgF_2 isolated in argon and 10% F_2/Ar, (a) HgF_2 in argon, (b) HgF_2 in 10% F_2/Ar.

When HgF_2 was isolated within a 10% F_2/Ar matrix the most intense band was at 643.1 cm^{-1}, Figure 7.04(b), with weaker bands present at 632.0 cm^{-1} and 620 cm^{-1}. Photolysis and annealing had no effect on these peaks. With the previous work by Kaupp *et al.*,[36] it was thought that a 10% F_2/Ar matrix would provide the idea conditions for the formation of HgF_4 as one fluorine molecule would be present around the HgF_2 molecule when photolysis and annealing was conducted, but no evidence for the formation of HgF_4 could be found in these experiments. The bands observed in these experiments can be assigned to HgF_2 at 643.1 cm^{-1}, red shifted by 2.8 cm^{-1} when compared to HgF_2 within a pure argon matrix. The peak at 632.0 cm^{-1} is not present within pure argon experiments but is always present within a F_2/Ar matrix, a simple assignment of this would be to a $HgF_2 \ldots F_2$ complex similar to those observed by Tevault *et al.*,[48] another assignment could be to a HgFCl complex like those observed within the mass spectrometry work, although this was previously reported at 592.0 cm^{-1} in krypton matrices.[51]

When higher concentrations of fluorine were used within these experiments, 20% and neat, it was found to produce very complicated spectra that were highly dependent upon minor variation in both the HgF_2 evaporation conditions and matrix gas flow rate. When 20% F_2/Ar concentration was used a peak at 633.0 cm^{-1} was present in addition to a band at 640.3 cm^{-1}. When neat fluorine was used a peak at 633.8 cm^{-1} was the most intense with a shoulder at 641.0 cm^{-1}, the relative ratio of these two peaks was found to be very dependent on the fluorine flow rate. When the flow rate was increased only one band at 642.0 cm^{-1} was observed in neat fluorine which was not affected by photolysis. These two different peaks appear likely to be a result of either site effects, poor isolation or products of the reaction between the components of the vapour above HgF_2 and fluorine, including its trace impurities at relatively high concentrations, shown in Figure 7.05.

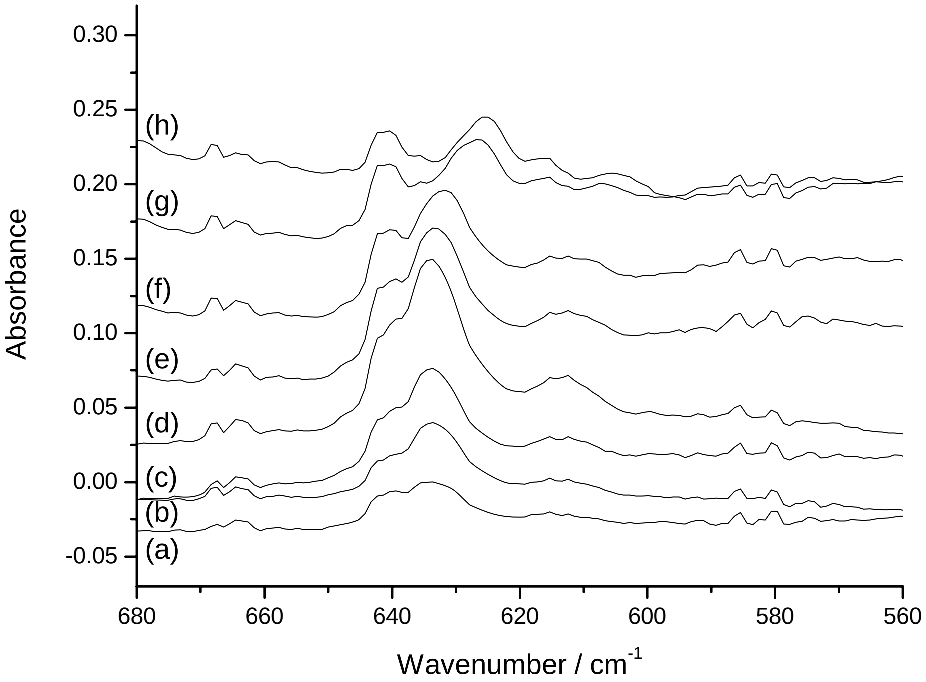

Figure 7.05 IR spectra showing HgF_2 isolated in 20% F_2/Ar and F_2 matrices. (a) deposition of HgF_2 into 20% F_2/Ar, (b)(c)(d) further deposition with broadband photolysis, (e) annealed to 20 K, (f) further annealing to 22.5 K, (g) further annealing to 25 K, (h) further annealing to 30 K

7.3.2.2 Mercury Vaporisation Experiments.

Due to the failure of the previous experiments to isolate HgF_4 with HgF_2 as a precursor, as suggested likely to be the best method by Kaupp *et al.*,[36] mercury atoms were the next method attempted as they have the advantage of producing much cleaner vapour systems than HgF_2, meaning the spectra should also have less impurities present. This method involved the isolation of mercury atoms within a F_2/Ar matrix, initially mercury was isolated within a 5% F_2/Ar matrix, upon deposition no bands were observed other than the often seen CO_2 peaks. However once this matrix was photolysed with broadband for 10 minutes a peak at 644.7 cm^{-1} grew rapidly, and changed little upon annealing the matrix to

25 K, except for peaks due to O_2F appearing at 584.7 cm^{-1}. On further annealing to 28 K peaks due to O_2F and O_2F_2 (625.7 cm^{-1} and 612.5 cm^{-1}) increased and when photolysed at 28 K they increased even more. When deposition of mercury was conducted with broadband photolysis the peak at 644.3 cm^{-1} was observed straight away. There was also a small peak at 631.4 cm^{-1} that was not present previously, this peak is in a similar position to the one observed when HgF_2 was isolated in a 10% F_2/Ar matrix. The ν_3 mode of HgF_2 was assigned to 645.1 cm^{-1} in a 10% F_2/Ar matrix thus the peaks at 644.7 cm^{-1} and 644.3 cm^{-1} can be assigned to this mode of HgF_2 within a 5% F_2/Ar matrix. In the $\nu_{F\text{-}F}$ region there was no evidence of the fluorine band at 892 cm^{-1} for either 2% or 5% F_2/Ar mixtures.[52, 53]

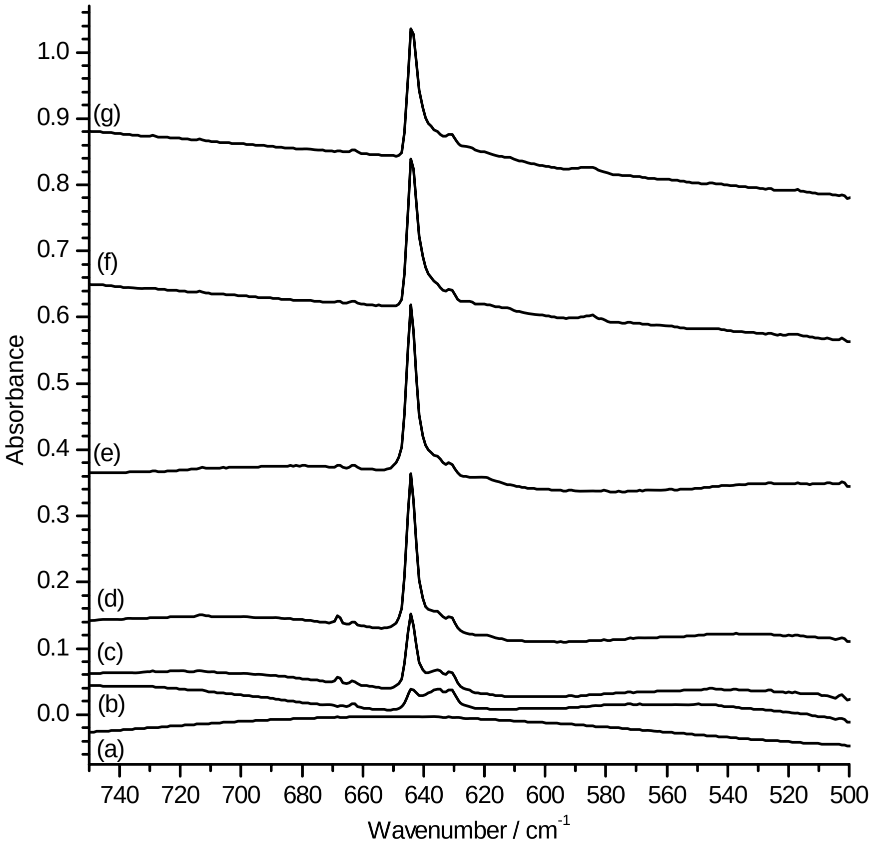

Figure 7.06 IR spectra of mercury isolated in 10% F_2/Ar, (a) 10% F_2/Ar after 60 minutes, (b) mercury and 10% F_2/Ar after 125 minutes, (c) after selective photolysis for 1 min (250-380 nm), (d) after 6 minutes of photolysis, (e) after 21 minutes of photolysis, (f) after annealing to 20 K, (g) after annealing to 24 K.

When the fluorine concentration was increased to 10% F_2/Ar peaks were observed upon deposition at 643.7 cm^{-1}, 635.4 cm^{-1}, and 631.2 cm^{-1}. When selective photolysis, 250 – 380 nm, was conducted the peak at 643.7 cm^{-1} increased dramatically after only 1 minute. Further photolysis increased the peak size even more and shifted it slightly to 644.3 cm^{-1}. The peaks at 635.4 cm^{-1} and 631.2 cm^{-1} did not change their intensity upon photolysis, Figure 7.06. When the matrix was annealed to 20 K the peak at 644.3 cm^{-1} reduced in intensity, broadened and shifted to 643.8 cm^{-1}. The peaks previously seen due to O_2F and O_2F_2 again appeared upon annealing of the matrix, O_2F was present at 585.2 cm^{-1} with a shoulder at 588.4 cm^{-1} while O_2F_2 was present at 625.3 cm^{-1} and 612.2 cm^{-1}. Further annealing to 24 K again reduced the intensity of the band at 643.8 cm^{-1} and increased the peak at 588.3 cm^{-1} on the tail of the O_2F peak. The band seen at 643.7 cm^{-1} before any photolysis or annealing can be assigned to the ν_3 mode of HgF_2 as a peak was observed at 645.1 cm^{-1} for HgF_2 in argon and 643.1 cm^{-1} for HgF_2 in 10% F_2/Ar previously. The peak present close to O_2F at 588.4 cm^{-1} can be assigned to a HgF_2 dimer due to its behaviour upon annealing and as a band at 589.0 cm^{-1} in krypton matrices has previously been assigned to $(HgF_2)_2$.[49, 51] This leaves the peaks seen on initially deposition at 635.4 cm^{-1} and 631.2 cm^{-1}, these are more difficult to assign but are likely due to impurities within the fluorine combining with mercury. Although it is unlikely that they are due to CF_4, which has a mode at 631.5 cm^{-1} in argon,[54] they could be due to a Hg...CF_4 complex.

When the spectrum is examined in the $\nu_{F\text{-}F}$ region no bands were observed upon initial deposition due to either fluorine or fluorine complexes. When the mercury is deposited as well small peaks are observed at 892.1 cm^{-1} and 877.7 cm^{-1} both of which are on top of a broad feature, Figure 7.07. The peak at 892.1 cm^{-1} is very close to a band previously seen by Andrews and Howard[53] within Raman studies of fluorine. They assigned this band to an impurity induced fluorine mode similar to that which has previously been observed for nitrogen by Andrews *et al.*.[55] The other peak present at 877.7 cm^{-1} has previously been assigned to a F_2...H_2O complex at 877.5cm^{-1},[52] this assignment however does not match the observation of these experiments. The peak at 877.7 cm^{-1} is only observed once mercury is present within the matrix and its intensity does not correlate to other H_2O bands present in the spectrum. When the matrix was photolysed there was no change in the 892.1 cm^{-1} band but the peak present at 877.7 cm^{-1} decreased, under these conditions the peaks previously assigned to HgF_2 grew rapidly. The previous work upon F_2...H_2O complex showed that the peak at 877.7 cm^{-1} was photo-bleached and was then accompanied by the formation of HOF...HF complexes,[52] none of which were observed within these experiments (3781 cm^{-1} and 3638 cm^{-1}). As the peak at 877.7 cm^{-1} is only present when mercury is present with fluorine the best tentative assignment would be to a very photo sensitive Hg...F_2 complex. When the matrix is annealed the only change is a slight increase in the band at 892.1 cm^{-1}.

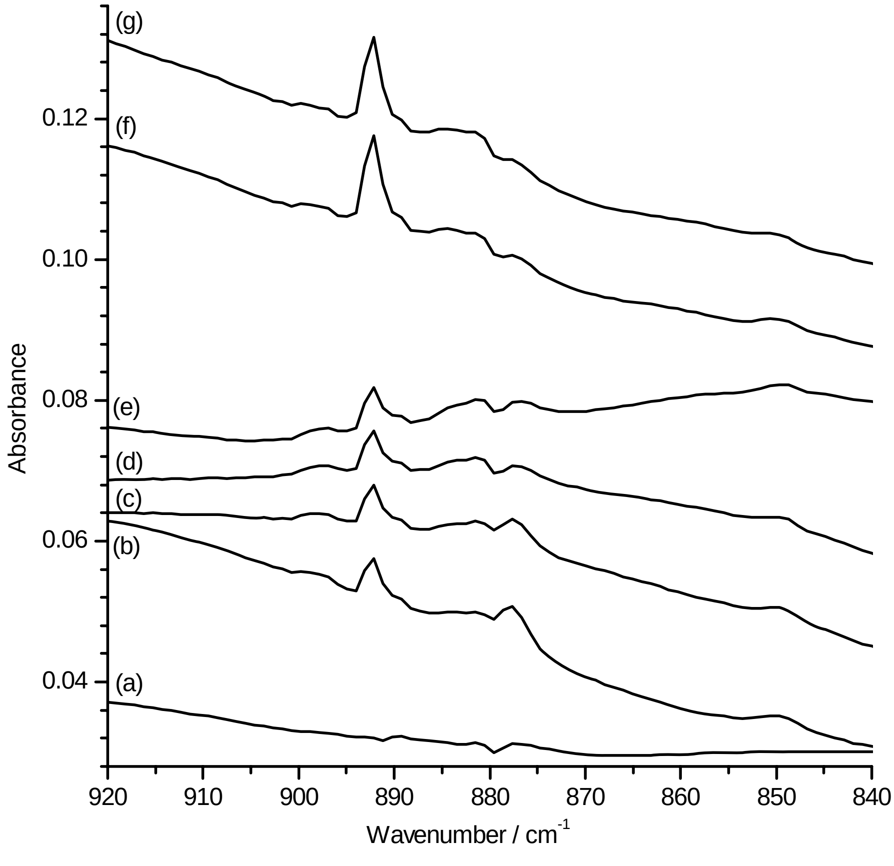

Figure 7.07 IR spectra of mercury isolated in 10% F_2/Ar, (a) 10% F_2/Ar after 60 minutes, (b) mercury and 10% F_2/Ar after 125 minutes, (c) after selective photolysis for 1 min (250-380 nm), (d) after 6 minutes photolysis, (e) after 21 minutes photolysis, (f) after annealing to 20 K, (g) after annealing to 24 K.

When the concentration was increased to 20% F_2/Ar as expected similar behaviour was observed once again. A broad feature was observed at 634.7 cm^{-1} and a shoulder was present at 640.8 cm^{-1}, neither of these bands were present when the gas was deposited on its own. Upon annealing the matrix to 20 K the peak present at 640.8 cm^{-1} increased and some small peaks began to grow at 622.8 cm^{-1}, 613.2 cm^{-1}, and 588.0 cm^{-1}. Upon photolysis the peak at 640.8 cm^{-1} increased and shifted slightly to 641.9 cm^{-1}, and the peak at 584.3 cm^{-1} also increased in intensity which corresponds with the appearance of a band at 1497 cm^{-1}confirming that this was due to O_2F.[40-42] The peak at 588.8 cm^{-1} decreased upon photolysis while the shoulder at 634.2 cm^{-1} did not appear to change but it is difficult to definitively say as it is in the tail of the large band at 641.9 cm^{-1}. When the matrix was annealed the largest peak at 641.9 cm^{-1} shifted back to 641.5 cm^{-1} and with further annealing to 641.0 cm^{-1}. The only other effect of annealing was the appearance of new bands at 624.6 cm^{-1} and 616.4 cm^{-1}, and the band at 584.0 cm^{-1} shifted to 588.0 cm^{-1}. When the $\nu_{F\text{-}F}$ region is looked at it was very similar to the previous 10% spectra. A peak present at 892.2 cm^{-1} is assigned to matrix isolated F_2,[52, 53] along with a shoulder present 889.2 cm^{-1} and a broad feature present at 881.6 cm^{-1}. When mercury was added a new peak emerged at 878.7 cm^{-1} and then with subsequent photolysis and annealing was removed. This is consistent with previous behaviour and the assignment of this to a Hg...F_2 complex.

When previous 10% F_2/Ar matrices are examined HgF_2 was assigned to a band at 643.7 cm^{-1}, so in a 20% F_2/Ar matrix it seems reasonable to assign the peak seen at 640.8 cm^{-1} to the asymmetric stretching mode of HgF_2. The weak peaks observed around 630 cm^{-1} are present when both HgF_2 and mercury are used with a 20% F_2/Ar matrix and thus could be due to mercury complexes in both cases. To try and eliminate O_2F_2 and O_2F from the picture an experiment was carried out using the 20% F_2/Ar gas in the absence of mercury and then oxygen was introduced into the chamber, Figure 7.08. No bands were initially observed due to either O_2F_2[40] or O_2F[40-42] but after broadband photolysis was conducted peaks appeared at 626.0 cm^{-1} and 612.1 cm^{-1} due to O_2F_2 and at 583.9 cm^{-1} due to O_2F. [40-42] When the matrix was then annealed to 25 K the O_2F_2 bands moved slightly to 624.7 cm^{-1} and 613.1 cm^{-1} and the O_2F band also moved to 587.8 cm^{-1}. This combined with the shift of a band present at 1497.7 cm^{-1} has previously been interpreted to be related to the dimerisation of the O_2F radical to O_4F_2.[56] Due to this the assignment of the bands after photolysis at 624.6 cm^{-1}, 616.4 cm^{-1}, and 466.0 cm^{-1} to O_2F_2 and the band at 584.3 cm^{-1} to O_2F and the band at 584.3 cm^{-1} to O_4F_2. The band observed at 588.0 cm^{-1} after annealing, but before photolysis is not due to O_2F but is more likely to be $(HgF_2)_2$ based on previous work by Loewenschuss *et al.*.[49, 51]

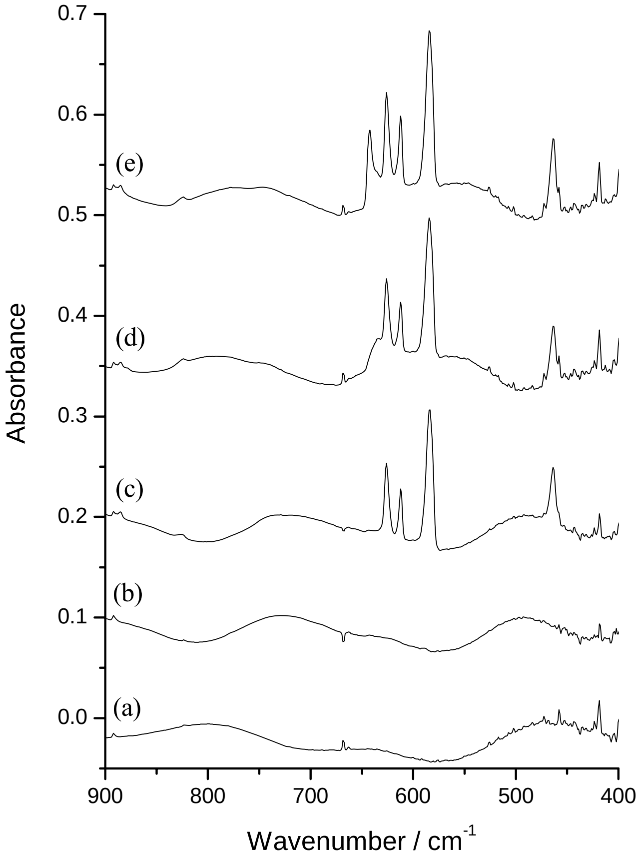

Figure 7.08 IR spectra of 20% F_2/Ar with O_2, (a) after 90 minutes deposition, (b) after annealing to 25 K, (c) after 20 minutes broad band photolysis, (d) after 60 minutes of mercury and 20% F_2/Ar, (e) after 25 minutes broadband photolysis.

These results show that the formation of HgF_4 does not happen under these conditions. The use of a 20% F_2/Ar matrix was thought to be the optimum conditions for the formation of HgF_4 from mercury as 2 fluorine molecules would be in the immediate environment of each mercury atom. The only peak within the spectra that remains unassigned is at 634.2 cm^{-1}, however this is formed on initial deposition and is not affected by photolysis or annealing and so is unlikely to be HgF_4.

Since the optimum coordination of fluorine molecules around mercury atoms does not produce HgF_4, 100% fluorine was used to see if this had any different affect. When mercury was deposited into 100% fluorine a peak was observed at 639.9 cm^{-1}, with shoulders present at 636.1 cm^{-1}, 630.5 cm^{-1}, and 614.8 cm^{-1}. There were also bands present at 892.6 cm^{-1} and 884.6 cm^{-1} higher in the spectrum. When the sample was photolysed with broadband radiation the only change was a slight increase in the peak at 588.3 cm^{-1}. Upon annealing peaks present at 639.9 cm^{-1}, 632.2 cm^{-1} and 625.9 cm^{-1} reduced in intensity and the band at 588.3 cm^{-1} increased. Previous assignment of HgF_2 to a peak at 639.5 cm^{-1} means it is reasonable to assign the peak at 639.9 cm^{-1} to HgF_2. HgF_2 was only observed in significant amounts upon deposition when using a neat fluorine matrix. The peak present at 588.3 cm^{-1} based on its reaction to photolysis and annealing is assigned to a HgF_2 dimer and it is also close to previous assignment of this dimer at 589.0 cm^{-1} in a krypton matrix.[49, 51]

7.3.2.3 Noble Gas Discharge Lamps.

Due to the previous work conducted on the matrices with Hg-Xe photolysis and the behaviour observed related to this photolysis further investigation of this photolysis behaviour was conducted using noble gas discharge lamps, the lamps used were argon, krypton and xenon. These experiments used exactly the same procedure as previously used with the use of vac-UV photolysis instead of a Hg-Xe lamp.

The experiments were carried out using a 10% F_2/Ar gas mixture. All three of the lamps produced identical results and so only the xenon discharge lamp will be discussed in any detail and only the $\nu_{Hg\text{-}F}$ and $\nu_{F\text{-}F}$ regions will be considered as the other areas of the spectrum followed the same patterns as previously detailed.

As can be seen from Figure 7.09 deposition produced the exact same results as were previously attained with a small peak around 644 cm^{-1} and other peaks at 635.5 cm^{-1} and 630 cm^{-1}. As soon as the xenon discharge lamp was applied the peak at 644 cm^{-1} increased in size dramatically in the same nature as observed in previous experiments with the Hg-Xe lamp. Upon annealing of the sample little changed apart from the appearance of a shoulder on the peak at 644 cm^{-1}. This behaviour was also observed for all of the discharge lamps used showing that the pre-cursor to the peak at 644 cm^{-1} is extremely photo sensitive to various wavelengths. The behaviour of the spectra in the $\nu_{F\text{-}F}$ region was again identical to previous experiments.

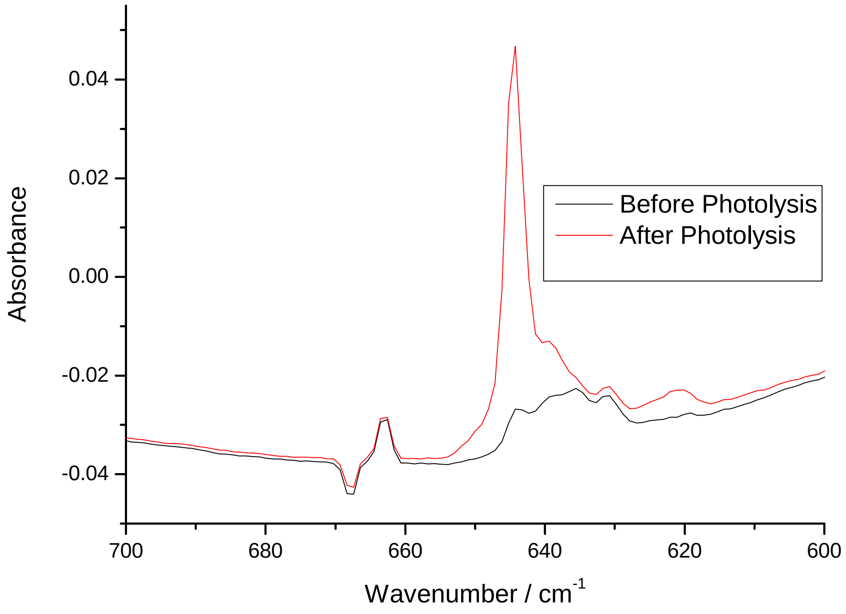

Figure 7.09 IR spectra showing mercury isolated in 10% F_2/Ar, with the effect xenon discharge lamp photolysis shown.

7.3.2.3 Conclusions From IR Experiments.

From the experiments conducted with krypton and oxygen it is clear that there are both fluorine and fluorine atoms present within the matrix and that they are mobile upon annealing. From the experiments conducted with mercury this again appears to be the case with mobile fluorine reacting with mercury to give HgF_2. HgF_2 is only formed upon deposition in significant amounts with a neat fluorine matrix, with lower concentrations of fluorine no HgF_2 is observed upon deposition or annealing until after photolysis. This behaviour could mean that mercury atoms are reacting with free fluorine atoms within the matrix or that a complex, Hg...F_2, is formed upon deposition and photolysis of this complex leads to the formation of HgF_2. It is not possible to determine exactly which is occurring without further investigation although it is likely that it is the Hg...F_2 complex. This is thought as the mechanism of formation of HgF_2 does not require annealing to form and since large amounts of HgF_2 are formed after only photolysis it implies a large proportion of the fluorine is already present around the mercury atoms without the need for annealing implying that the fluorine is already associated with the mercury atoms, as in the $Hg...F_2$ complex. This means that there is no reliable evidence for the formation of any higher oxidation states that Hg^{II}.

The only band found within the IR experiments that is left unassigned is a peak present at 631-634 cm^{-1}. This peak is only observed when both fluorine and mercury are present within the matrix, either from mercury atoms or HgF_2. It also has a greater intensity as the fluorine concentration is increased. This could mean that it can be assigned as HgF_4 but the lack of photolysis and annealing behaviour means a $HgF_2...F_2$ complex like those observed by Tevault *et al.*,[48] or to mercury interacting with an impurity in the gas such as CF_4 which has a bending mode at 631.5 cm^{-1},[54] is much more likely.

The use of Raman spectroscopy would have been diagnostic, and was attempted but the results obtained failed to show any bands likely to the sensitivity of the equipment. The reason Raman spectroscopy would have been useful is because if HgF_4 is square planar then it would have $\Gamma_{str} = A_{1g} + B_{1g} + E_u$, where the E_u would be IR active and the $A_{1g} + B_{1g}$ will be Raman active, while for linear HgF_2, $\Gamma_{str} = \Sigma_g^+ + \Sigma_u^+$, only Σ_u^+ IR active, while Σ_g^+ is Raman active meaning that HgF_4 would produce two bands in a Raman spectra while HgF_2 would only produce one.

7.3.3 Matrix Isolation UV/Vis Spectroscopy.

7.3.3.1 Background and Introduction.

The reason the UV/Vis spectroscopy could be extremely useful for the identification of HgF_4 is compared to the fact that other $5d^8$ compounds such as $PtBr_2$ and $AuCl_3$ are coloured, green and yellow/gold respectively, thus it would be expected that Hg^{IV} would also be coloured. Computational calculations performed by Dr. A. J. Bridgeman have predicted the transitions shown in Table 7.1 along with experimental values for $HgCl_2$ and $HgBr_2$, which give a comparison of where HgF_2 and HgF_4 would be expected.

Even though from the IR experiments there was no evidence for HgF_4 in an F_2/Ar matrices, it was decided to see if any signs of HgF_4 could be found with UV/Vis spectroscopy using both HgF_2 and Hg as mercury precursors. Previous computational calculations have suggested that HgF_2 and HgF_4 could have very similar stretching frequencies[30] and so any HgF_4 could have been obscured by the presence of HgF_2. There is no previous data for the electronic absorption spectra of HgF_2 within a matrix or in the gas phase. Whitehurst and King[57] estimated that the lowest energy transition should be around 7 eV (ca. 57,000 cm^{-1}). Calculations conducted within by Dr. A. J. Bridgeman have shown that a charge transfer band for HgF_2 should be present around 44,800 cm^{-1} due to a mercury 6s ← F_π transition. Laser studies by Whitehurst and King on the fluorescence of HgF_2 concluded that no single photon processes are observed unless a fluorine laser, 157 nm, is used.[57] When these results are compared to experimentally attained UV/Vis spectroscopic results for $HgCl_2$ and $HgBr_2$ it appears that these calculated and estimated values for HgF_2 may be rather low, but agree with the observations that suggest the absorption bands of HgF_2 lie beyond the range of the equipment that will be used in these experiments and so will be spectroscopically silent.

Molecule					
HgF_4	**d-d transistions,**	20,380 cm^{-1} $d_{x^2-y^2} \leftarrow d_{xy}$	20,860 cm^{-1} $d_{x^2-y^2} \leftarrow d_{xy,yz}$	46,980 cm^{-1} $d_{x^2-y^2} \leftarrow d_{z^2}$	
	Charge transfer transitions	24,570 cm^{-1} $d_{x^2-y^2} \leftarrow F\ 2p_{\pi}$	25,320 cm^{-1} $d_{x^2-y^2} \leftarrow F\ Hg_{\pi}$	28,110 cm^{-1} $d_{x^2-y^2} \leftarrow F\ Hg_{\pi}$	46,810 cm^{-1} $d_{x^2-y^2} \leftarrow F\ Hg_{\pi}$
HgF_2	**Charge transfer transitions**	44,800 cm^{-1} $6s \leftarrow F_{\pi}$	57,000 cm^{-1}		
$HgCl_2$	**Charge transfer transitions**	58,635 cm^{-1} 59,002 cm^{-1} 59,294 cm^{-1} 59,584 cm^{-1}			
$HgBr_2$	**Charge transfer transitions**	43,478 cm^{-1} 53,950 cm^{-1} 54,171 cm^{-1} 54,394 cm^{-1}			

Table 7.1 Tabulated computational calculations of the transitions of HgF_4 and HgF_2, also includes UV/Vis data for $HgCl_2$ and $HgBr_2$,[58, 59] (assignments of $HgCl_2$ and $HgBr_2$ are not made in the literature and are difficult to convert and so are not given).

7.3.3.2 Experimental Results.

The first experiment conducted on the UV/Vis spectrometer was the isolation of mercury vapour in argon so that the molecular transitions of mercury could be eliminated from the spectrum in future experiments. As can be seen from Figure 7.10 the sharp feature shown at 40,640 cm^{-1} is assigned to the $^3P_1 \leftarrow {}^1S_0$ transition of atomic mercury and the 48,530 cm^{-1} peak is assigned to the $G0_u^+ \leftarrow X0_g^+$ transition of dimercury.[60] The weak features at 44,530 cm^{-1} and 46,140 cm^{-1} are likely associated with other dimercury, higher oligomers, and other mercury bands.[60] Further experiments were conducted with mercury in an argon matrix to investigate the relationship between monomer and dimers. As the flow rate of the argon was increased the dimer ratio gradually reduced as a proportion of the monomer peak, this is likely due to the mercury within the matrix being more dispersed than at lower flow rates and so dimercury is formed less often. The monomer:dimer peak areas are different with the dimer peak being just over twice the area of the monomer, Figure 7.10(a), and using the previously determined 1:6 ratio of extinction coefficients[60] implies a dimer fraction of about 33.9%, in Figure 7.10(b) the dimer ratio is reduced to 20.8%, while in Figure 7.10(c) the ratio is slightly higher, 23.3%, due to the reduction in both monomer and dimer.

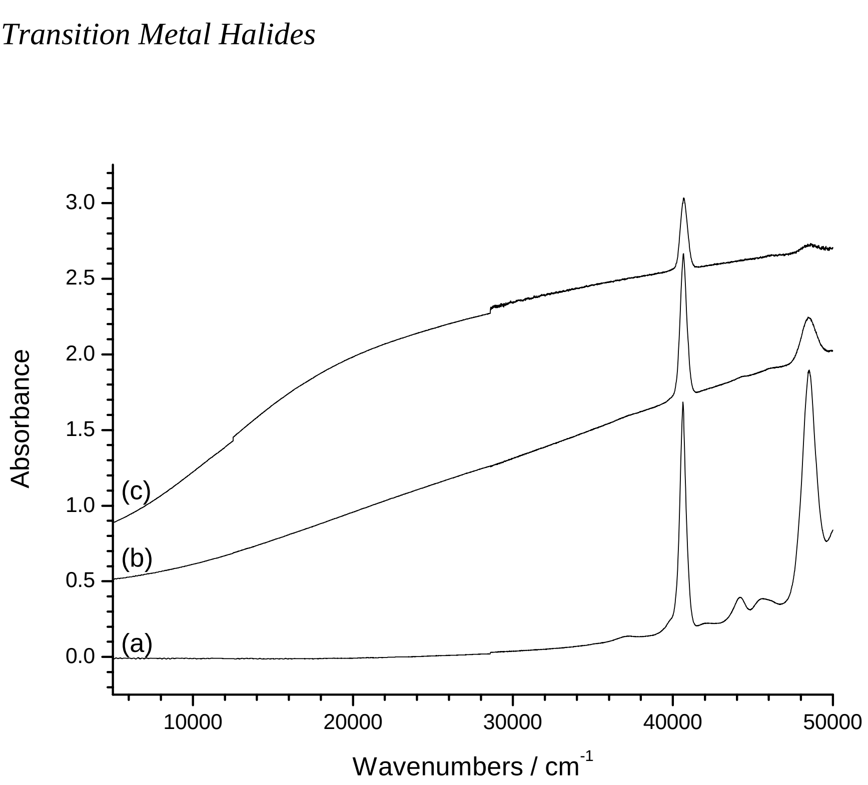

Figure 7.10 UV/Vis spectra showing mercury isolated in solid argon at varying flow rates, (a) pressure in chamber at 2 x 10^{-6} mbar, (b) at 6 x 10^{-5} mbar, (c) at 1 x 10^{-5} mbar.

7.3.3.2.1 HgF_2 Experiments.

With the assignment of bands produced within the UV/Vis spectrum by atomic mercury, HgF_2 was isolated in a pure argon matrix, Figure 7.11(a). The only bands that were observed in the spectra were assigned to mercury and dimercury.[60] However, there was evidence of the sublimation of HgF_2 on the apparatus after the experiments were concluded, showing that HgF_2 was present within the matrix. These results thus confirm the computational calculations that HgF_2 has bands that are beyond the range of the spectrometer used in these experiments. The presence of mercury within the matrix also once again confirms the previous mass spectrometry results which showed the decomposition of HgF_2 upon heating. The monomer:dimer peak areas are very similar, and using the previously determined 1:6 ratio of extinction coefficients[60] implies a dimer fraction of about 16%.

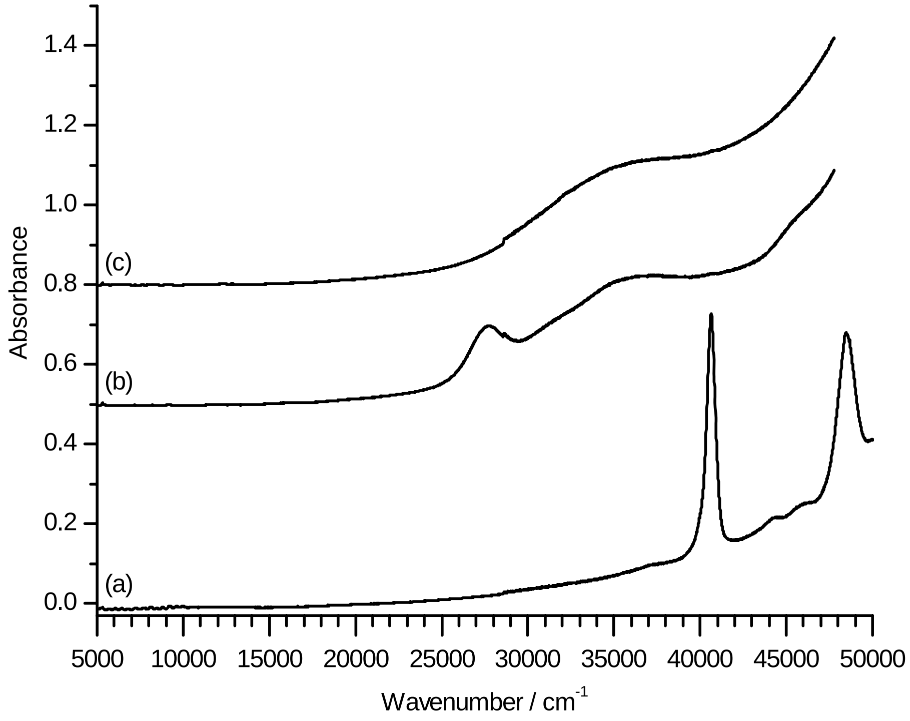

Figure 7.11 UV/Vis Spectra of HgF_2 isolated in 10% F_2/Ar, (a) HgF_2 in solid argon, (b) HgF_2 in 10% F_2/Ar, (c) after 5 minutes broadband photolysis.

When 10% F_2/Ar was introduced into these matrices, the intensity of the mercury peaks was reduced dramatically, Figure 7.11(b). When HgF_2 was isolated in a 10% F_2/Ar matrix a broad feature was observed at 35,200 cm^{-1}, Figure 7.11(b), and a new band at 27,770 cm^{-1} was also observed. After broadband photolysis the peak at 27,770 cm^{-1} was totally removed, Figure 7.11(c), leaving only the fluorine band at 35,200 cm^{-1}. From these results it appears that the mercury atoms released in the thermal decomposition of HgF_2 react with fluorine to form a new complex at 27,770 cm^{-1} and this is then subsequently photo-bleached to give a product that has no bands within the spectral range. The peak at 27,770 cm^{-1} cannot be HgF_2 as it is not present upon the deposition of HgF_2 in a pure argon matrix.

7.3.3.2.2 Hg Experiments.

The previous results obtained with the vaporisation of HgF_2 show that a complex is formed which can then be photo-bleached, however the mass spectrometry results showed that the thermal decomposition of HgF_2 leaves a variety of species and so it was decided to continue the investigation by skipping the thermal decomposition of HgF_2 step and just depositing mercury atoms straight into the matrix. Concentrated fluorine gases, 20% F_2/Ar, 10% F_2/Ar, and dilute fluorine gases, 2.2% F_2/Ar, were used, pure fluorine was also tried but it was found that the fluorine absorptions were too intense and would have masked any other peaks present within the matrix and so was no longer investigated.

The spectrum of 20% F_2/Ar is shown in Figure 7.12(a), and shows that the previous bands observed were not due to impurities in the fluorine as no change was observed within the matrix with either annealing or photolysis. Work by Crepin and Tramer[61] have shown the UV/Vis spectra of Hg/H_2O/Ar mixtures are very similar to Hg/Ar spectra and so once again care must be taken in analysis of results obtained. After deposition of mercury into a 20% F_2/Ar matrix two clear bands are observed at 27,500 cm^{-1}, 45,640 cm^{-1}, and a further peak present at 35,710 cm^{-1} which was on top of the broad fluorine feature, Figure 7.12(c). As soon as photolysis is conducted all three bands are photo-bleached to leave only the fluorine features within the spectrum, Figure 7.12(d). Annealing had no effect aside from increasing the base line, due to increased scattering. The lack of any difference between the spectra in Figure 7.12(a)(e)(f) suggest no evidence once again for the formation of HgF_4, despite the conditions being optimal. The bands produced at 27,500 cm^{-1}, 35,710 cm^{-1}, and 45,640 cm^{-1} cannot be assigned to any HgF_x species as no bands in the ν_{Hg-F} region of the IR spectra reduce upon photolysis.

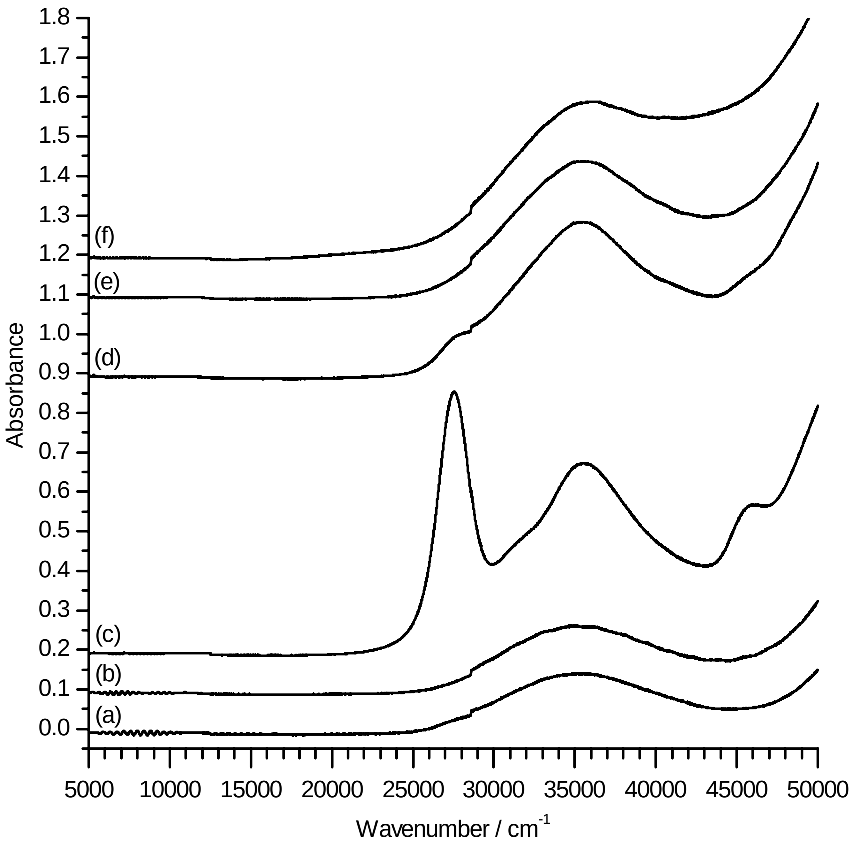

Figure 7.12 UV/Vis spectra of mercury isolated in 20% F_2/Ar, (a) 20% F_2/Ar for 60 minutes, (b) after 10 minutes broadband photolysis, (c) 20% F_2/Ar and mercury for 55 minutes, (d) 1 min broadband photolysis, (e) 5 minutes broadband photolysis, (f) after annealed to 24 K.

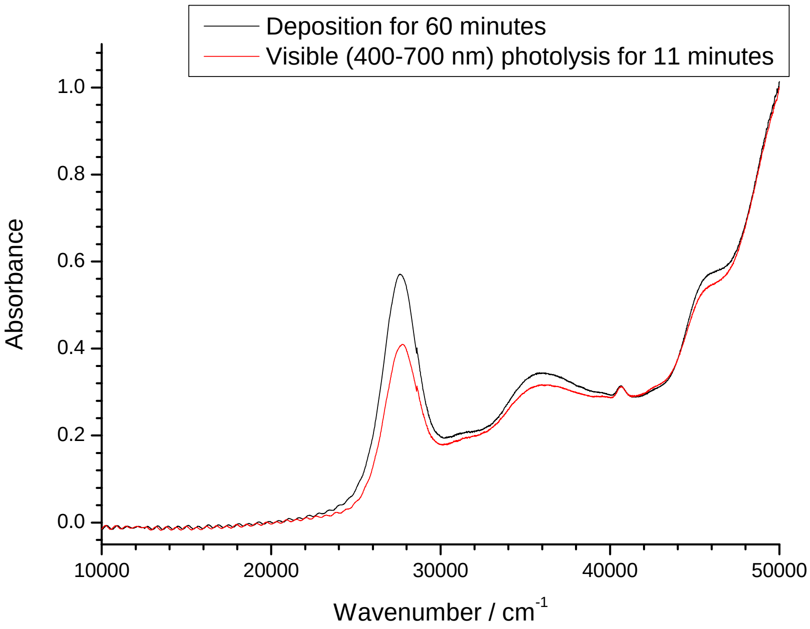

Figure 7.13 UV/Vis spectra of mercury isolated in 10% F_2/Ar, showing the effects of visible photolysis.

When the concentration of fluorine was reduced to 10% F_2/Ar the spectra were found to be practically identical to the ones observed previously for a 20% F_2/Ar matrix, with peaks present at 27,580 cm^{-1}, 36,100 cm^{-1}, and 45,680 cm^{-1}, and a weak peak is also present at 40,680 cm^{-1} likely due to unreacted mercury atoms. When selective photolysis is used, 400-700 nm transmission filter, there was a decrease in the three bands at 27,580 cm^{-1}, 36,100 cm^{-1}, and 45,680 cm^{-1}, as previously seen in a 20% F_2/Ar matrix, Figure 7.13. When the selective photolysis was continued with the use of Schott BG40 (700-320 nm), BG1 (2600–700 nm and 500-280 nm) and UG5 (2600-620 nm and 420-230 nm) filters used successively there was a significant decrease in all three of the bands, Figure 7.14 shows the effect of using the UG5 filter. A further development in the investigation into the ability to photo-bleach these peaks resulted in the use of a monochromator to selectively irradiate specific peaks. It was found that when the peak at 27,580 cm^{-1} was irradiated with 365 nm (27,400 cm^{-1}) radiation all three bands reduced in intensity the most. This is most probably due to the presence of a mercury emission line at 365 nm (27,400 cm^{-1}) whereas the 297 nm (33,700 cm^{-1}) and 254 nm (39,400 cm^{-1}) mercury lines are well removed from the 36,100 cm^{-1} band, Figure 7.15.

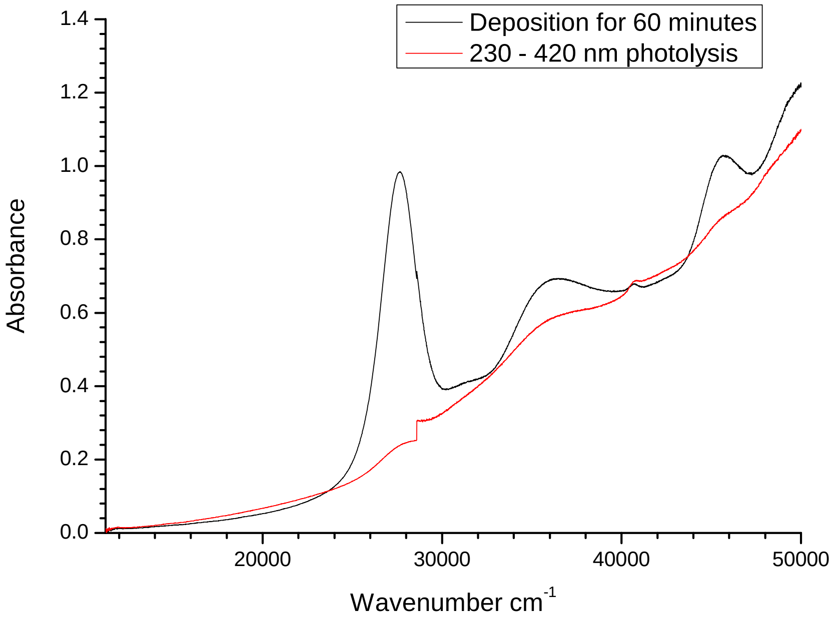

Figure 7.14 UV/Vis spectra of mercury isolated in 10% F_2/Ar, showing the effects of 230 – 420 nm photolysis.

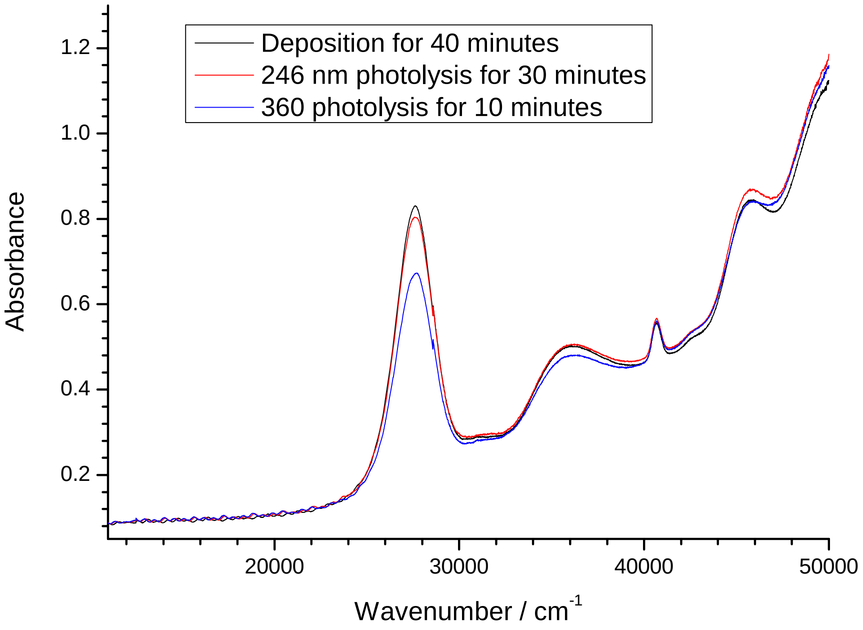

Figure 7.15 UV/Vis spectra of mercury isolated in 10% F_2/Ar, showing the effects of photolysis with a monochromator.

The concentration of fluorine was again reduced to 2.2% F_2/Ar to see what effect it would have on the bands previously observed. Upon deposition of mercury into 2.2% F_2/Ar, Figure 7.16(b), peaks were observed at 27,770 cm^{-1}, 36,850 cm^{-1}, and 45,350 cm^{-1}, and peaks due to atomic mercury were also much more intense than previously seen following the pattern from 20% to 10% F_2/Ar, Figure 7.16(b). A new band was observed in these experiments at 49,020 cm^{-1} which would not have been observed previously due to the fluorine tail in the UV being too intense. Upon annealing of the matrix to 24 K, Figure 7.16(c) no changes were observed. However, as soon as broadband photolysis was conducted the peaks at 27,770 cm^{-1}, 36,850 cm^{-1}, 45,350 cm^{-1}, and 49,020 cm^{-1} reduced in intensity dramatically, Figure 7.16(d), and after 5 minutes of photolysis they have been completely photo-bleached, Figure 7.16(e). After subsequent annealing to 27 K, Figure 7.16(f), the bands at 27,770 cm^{-1}, 36,850 cm^{-1}, and 45,350 cm^{-1} could be observed again and the mercury peaks were slightly reduced implying that excess fluorine in the matrix has reacted with the mercury atoms present. To confirm that these bands had the same photolytic behaviour as the previous peak photolysis was again conducted and they once again were photo-bleached away, Figure 7.16(g).

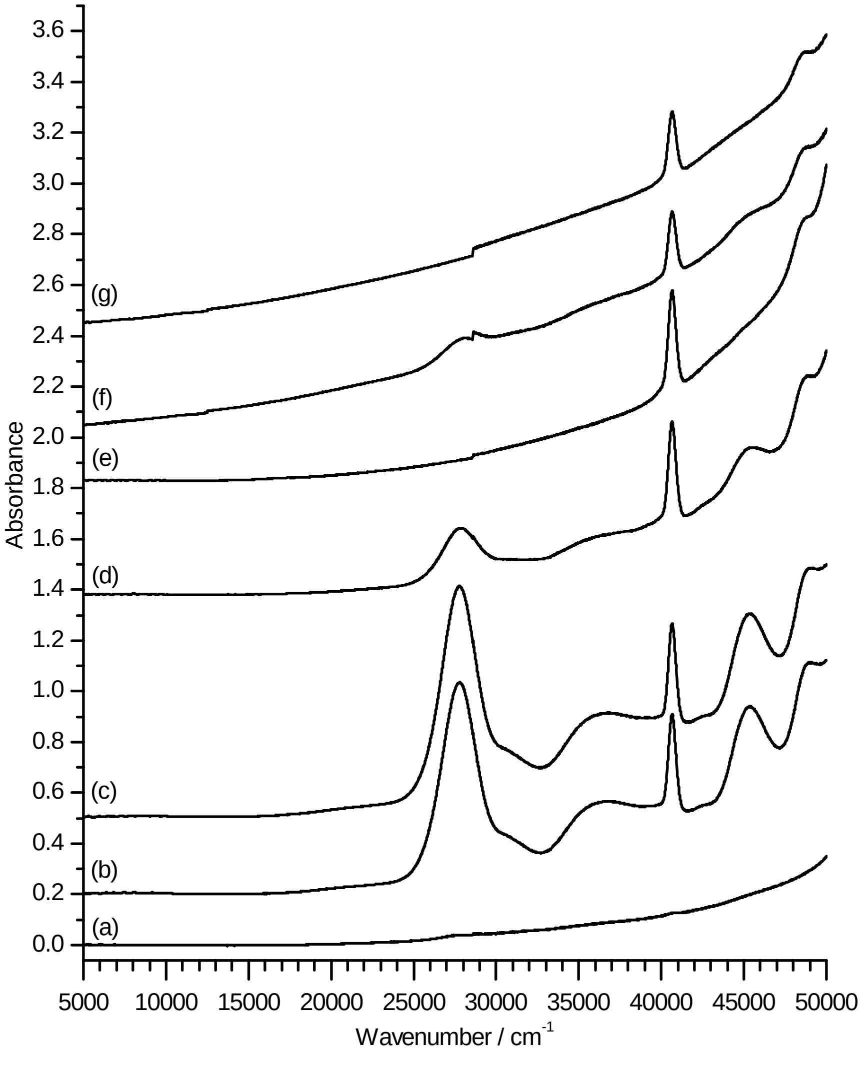

Figure 7.16 UV/Vis spectra of mercury isolated in 2.2% F_2/Ar, (a) 2.2% F_2/Ar for 50 minutes, (b) 2.2% F_2/Ar and mercury for 45 minutes, (c) after annealing to 24 K, (d) after 1 minute broadband photolysis, (e) after 5 minutes broadband photolysis, (f) after annealing to 27 K, (g) after broadband photolysis.

7.3.3.2.3 Summary.

From the UV/Vis results three distinct bands, four in dilute F_2/Ar matrices, are observed when mercury is isolated within a F_2/Ar matrix. These three bands are only observed when both mercury and fluorine are present within the matrix and therefore must arise from some type of mercury-fluorine interaction. Since the peaks are always of a similar relative intensity and have the same photolytic and annealing behaviour regardless of the matrix it is reasonable to assign these all to the same species. These bands are not related to any peaks present within the ν_{Hg-F} range of the IR spectrum as none of the bands reduce upon photolysis. As no bands are present after photolysis except those due to fluorine, the IR bands at 631-634 cm^{-1} cannot be due to HgF_4. A band present within the ν_{F-F} region of the IR spectrum at 877.8 cm^{-1} decreased upon photolysis in a 10% F_2/Ar matrix at the same time as the HgF_2 band grew in intensity. This means that the best assignment of the peaks observed within the UV/Vis spectra is due to a $(Hg...F_2)_n$ complex. This complex is formed upon the initial deposition of mercury into a F_2/Ar matrix and is then photolysed to HgF_2. This also shows that the photochemical process involved in the formation of HgF_2 involves the irradiation of a $Hg...F_2$ complex rather than irradiation of a fluorine molecule or atom, or the excitation of mercury. Table 7.2 tabulates the values obtained for HgF_2 and the $Hg...F_2$ complex in different F_2/Ar concentrations.

	20% F_2/Ar	**10% F_2/Ar**	**5% F_2/Ar**	**2.2% F_2/Ar**	**Ar**
HgF_2	640.8 cm^{-1} (640.3 cm^{-1})	643.7 cm^{-1} (643.1 cm^{-1})	644.7 cm^{-1}	-	(645.1 cm^{-1})
$Hg...F_2$	27500 cm^{-1}	27580 cm^{-1}	-	27770 cm^{-1}	-

Table 7.2 Tabulated values for the stretching frequency of HgF_2 from mercury isolated in various F_2/Ar concentrations, and the largest bands present in the UV/Vis data for $Hg...F_2$ complex, values in parenthesis are for the direct deposition of HgF_2 into the F_2/Ar matrix.

7.3.4 X-ray Absorption Spectroscopy.

The main aim of this section of work was to try and characterize the complex formed upon deposition of mercury into a F_2/Ar matrix. This would allow the determination if the complex is indeed Hg...F_2, as thought, or a result of fluorine atoms reacting with mercury. Subsequent photolysis of the matrix would also allow the determination of the Hg-F bond length in HgF_2, which has previously never been achieved for molecular HgF_2. Also it was hoped that this would show if any HgF_4 had been formed. The equipment used in these experiments was a FTIR-XAFS apparatus modified to operate on Station 9.3 of the SRS so that the matrix could be monitored at every stage of the experiment.

7.3.4.1 XANES Results.

When conducting X-ray absorption spectroscopy the observation of the mercury L_3 edge can be useful as the mercury L_3 edge XANES is sensitive to the oxidation state of the species being analyzed and the spectra for Hg^0 [62] and Hg^{II} [63, 64] are very distinctive. In a final attempt to observe if any HgF_4 is present the d^8 Hg^{IV} should be similar to those of Pt^{II} and Au^{III}, which have an intense white line at the edge due to 2p and 5d transitions.[65, 66]

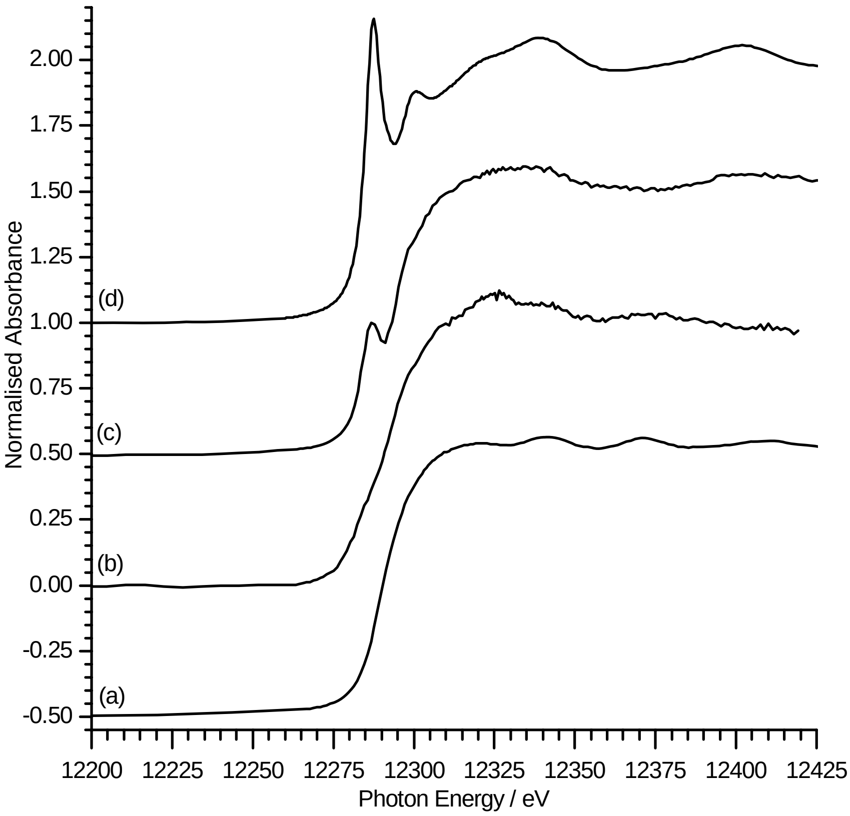

Figure 7.17 Mercury L_3-edge XANES spectra of mercury atoms in a) 100% argon, b) 10% F_2/Ar matrix at 14 K, c) after broadband photolysis, d) silver L_3-edge XANES spectrum of $HAuCl_4$ at 298 K, energy scale shifted by 364 eV.

When mercury atoms are isolated in an argon matrix, Figure 7.17(a), the edge, as expected, is mostly featureless which is consistent with atomic mercury being present, as previously shown by Filipponi *et al.*.[62] When mercury is isolated within a matrix containing 10% F_2/Ar, Figure 7.17(b), the XANES spectrum again shows an almost featureless edge indicating that mercury is still present as Hg^0. This therefore confirms that the peaks seen in the UV/Vis spectra when mercury is isolated in a F_2/Ar matrix cannot be due to either Hg^{II} or Hg^{IV}, and thus it must be due to some form of $Hg...F_2$ complex. The mercury L_3-edge XANES spectrum obtained once photolysis had been conducted is shown in Figure 7.17(c). There is clearly a very large change in the edge before and after photolysis with the appearance of a sharp peak on the edge, edge feature. Previous this has been shown to be due to a 2p-6s transition and is characteristic of both Hg_2^{II} and Hg^{II}. It becomes more resolved for Hg^{II} and in this case is more closely resembles Hg^{II}.[63, 64]

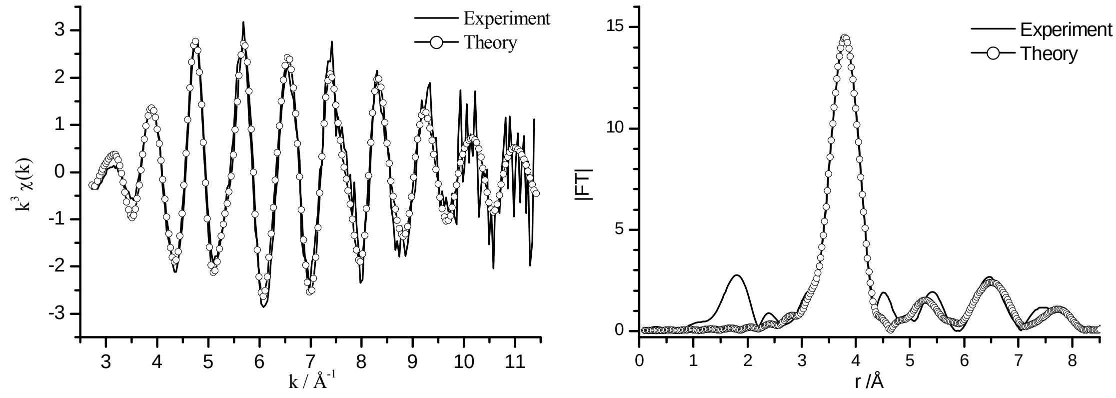

Figure 7.18 Mercury L_3-edge EXAFS (left) and FT (right) of mercury atoms in an argon matrix.

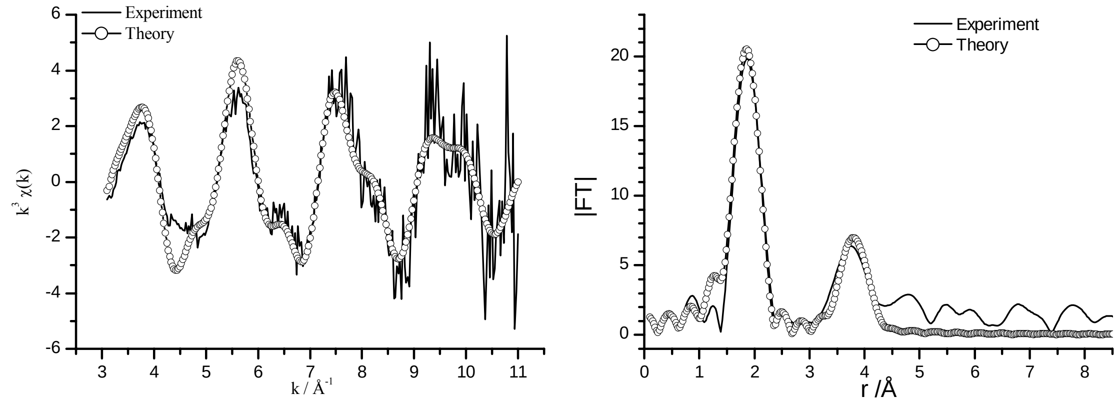

Figure 7.19 Mercury L_3-edge EXAFS (left) and FT (right) of mercury atoms in 10% F_2/Ar matrix after photolysis.

In Figure 7.17(d) a comparison is shown of what the Hg L_3-edge XANES spectrum of HgF_4 could look like in a XANES spectrum. A gold L_3-edge spectrum of $HAuCl_4$ (shifted by 364 eV) is given to show what a d^8 spectrum would look like, with its intense white line characteristic of a partially filled d-shell.[65, 66] The presence of an edge feature after photolysis, Figure 7.17(c), shows the formation of HgF_2, but as there is no evidence of an intense white line, which would indicate the formation of Hg^{IV}, this lack of Hg^{IV} is consistent with the other spectroscopic results. This data was collected simultaneously with IR data and thus comparison of the two proved the assignment of the band at 644 cm^{-1} to the υ_3 mode of HgF_2. When mercury was trapped in 100% fluorine the XANES spectrum obtained is essentially identical to that shown in Figure 7.17(c), showing the formation of HgF_2.

7.3.4.2 EXAFS Results.

When mercury was isolated in solid argon the data suggests that the mercury is isolated within a substitutional hole within an argon fcc lattice.[67] There was no evidence found for the presence of any Hg-Hg interaction around 3 Å, confirming evaporation of mercury at 298 K results in mainly monomer fractions. The Hg-Ar distances are slightly longer than expected for a perfect fcc lattice.[67] The value of 3.86 (4) Å for the first Hg-Ar shell is slightly larger than that for solid argon, 3.756 Å,[67] but significantly different from that of solid mercury (6 x 2.9916 Å, 6 x 3.4580 Å)[68] shown in Figure 7.18, indicating that some type of distortion is occurring. The analysis of the results obtained for EXAFS are given in Table 7.3.

It was hoped that the EXAFS results would allow the structural determination of the $Hg...F_2$ complex, but due to the extreme photo instability of this complex and the time required to obtain high quality results from EXAFS, 10 hours, this was not possible as HgF_2 was observed within the IR spectra within an hour of deposition. So detailed analysis of the complex was not possible.

When the FT is examined after photolysis, Figure 7.19, the first peak present is due to a Hg-F distance of 1.94(2) Å, this bond length compares to the Hg-F distance in solid state HgF_2 of 2.40 Å,[69] whilst Hg_2F_2 in solid state is 2.13 Å, with a Hg-Hg distance of 2.509 Å.[70] In computational studies of HgF_2[30, 36, 71, 72] the Hg-F bond length was found to shorten by 0.06 Å, from 2.1 Å to 1.95 Å, when relativistic effects are taken into account. When this value is compared to the EXAFS value of 1.94(2) Å there appears to be a close agreement between the theoretical and experimental values when relativistic effects are considered. This value also corresponds well with computational calculations performed within this research group of 1.956 Å compared with 1.914 Å obtained from the CCSD(T)/aug-cc-pVQZ level of theory by Andrews *et al.*,[29] although more recently values have been reported using B3LYP and CCSD(D) calculations of 1.934 Å and 1.922 Å, respectively.[34] As expected with a large atom like mercury relativistic effects need to be included to accurately predict the bond lengths of such molecules.

The second feature in the FT contains contributions from multiple scattering within the linear HgF_2 unit,[73] as well as from the argon atoms in the matrix. If the multiple scattering is ignored the best fit is to a Hg-Ar interaction at 3.87(5) Å with an occupation number of around 4, but with unrealistically small Debye-Waller factors. If the multiple scattering is included this results in an increase of the Hg-Ar distance slightly to 3.90(5) Å, but makes it harder to determine the Hg-Ar occupation number. If the Debye-Waller factor is kept similar to that of the first shell in the Hg/Ar data then it is between 3 and 4. Although there were weak bands from mercury atoms present within the 10% F_2/Ar UV/Vis spectra, Figure 7.13, it is thought that in addition to the HgF_2 multiple scattering, this feature in the FT mainly reflects an interaction between HgF_2 and the argon lattice with 3 or 4 argon atoms around the mercury, with the possibility of a small component from Hg...Ar.

	$R_{\text{Hg-Ar}}$/Å[b]	$2\sigma^2_{\text{Hg-Ar}}$/Å^2[c]	$N_{\text{Hg-Ar}}$	E_f/V[d]	R/%[e]
Hg/Ar	3.857(8)	0.0233(25)	9.25	-7.5(6)	40.1
	5.308(47)	0.0370(141)	4.6		
	6.541(28)	0.0377(78)	18.5		
	7.714[f]	0.0279(134)	9.25		
Hg/ 10% F_2/Ar after photolysis	1.936(9)	0.0089(16)	2	2.4(15)	50.9
	3.903(43)	0.0352(110)	4		

[a] Standard deviation in parentheses. [b] Estimated systematic errors in XAFS bond lengths are ± 1% for well-defined co-ordination shells. [c] $2\sigma^2$ is the Debye-Waller factor. [d] E_f is a single refined parameter to reflect differences in the theoretical and experimental Fermi levels. [e] $R = [\int|\chi^T - \chi^E|k^3\mathrm{d}k / \int|\chi^E|\,k^3\mathrm{d}k] \times 100\%$

Table 7.3 Refined mercury L_3-edge parameters[a] for mercury atoms in argon and 10% F_2/Ar matrices.

7.3.4.3 Summary.

The results obtained from the EXAFS experiments showed a bond length for the HgF_2 molecule of 1.94 (2) Å, which is the first time this has been determined for molecular HgF_2. When this value is compared to computational values,[30, 36, 71, 72] the agreement is very good when relativistic effects are taken into account. Relativistic effects within these computational calculations reduced the bond lengths from 2.1 Å to 1.95 Å. The results obtained with the XANES results also show that no Hg^{IV} is formed within these experiments confirming the IR and UV/Vis data.

7.3.5 Discussion.

From this work, IR, EXAFS, UV/Vis, and XANES, there is no convincing evidence for the formation of HgF_4 in argon. However, a new $Hg...(F_2)_n$ complex has been identified. As the proportion of mercury in the spectra of 10% F_2/Ar is very small, and the complex can be readily converted to HgF_2, the complex is most likely to be $Hg...F_2$. This route probably presents the cleanest way of making HgF_2 in matrices.

7.3.6 Conclusion.

This work shows that mobile fluorine within the matrix will react with mercury to form a $Hg...F_2$ complex, which can then be subsequently photolysed to form HgF_2. No evidence was found which shows the formation of any higher oxidation states than +2. It may seem to be a strange occurrence that when mercury and fluorine are placed together, except in neat concentrations, photolysis is required to form HgF_2, but it does have precedence. The need to activate mercury using photolysis from its $^1S_0$ ground state has previously been observed with the formation of HHgCl,[15, 16] $Hg(OH)_2$,[17] HHg(OH),[17, 18] HgH_2,[19, 21, 22] HHgMe,[24] and $HHgSiH_3$.[27] This is due to the relative unreactivity of the $^1S_0$ ground state of mercury compared to the ^3P and ^1P excited states which can be accessed by photolysis (^3P at 254 nm, ^1P at 179 nm). The EXAFS investigation of HgF_2 has shown a Hg-F bond length of 1.94 (2) Å for the first time, and when this is compared to computational calculations it shows that relativistic effects must be included to produce accurate results.

7.3.7 Recent Developments.

After the conclusion of this work a paper published by Wang *et al.*[29] described the characterisation of HgF_4 in a neon and argon matrix, this is the first experimental evidence for a Hg^{IV} complex, Figure 7.20 and Figure 7.21. They assigned a band in neon matrices at 703 cm^{-1} to HgF_4 and a band at 682 cm^{-1} in argon, which appeared after photolysis and annealing. With the assignment of HgF_4 to a band around 682 cm^{-1} in argon, the results previously produced within this research group were again looked at for the presence of this band. Unfortunately within the results described above there was no evidence of this band and so HgF_4 has definitively not been produced within this work.

Within the work by Wang *et al.*[29] HgF_4 has been assigned to a band at 703 cm^{-1} in neon on the basis of their computational calculations. These calculations are contradicted in the literature by Liu *et al.*[30] and our calculations which place the HgF_4 and HgF_2 IR vibrational band extremely close to one another. The assignment of the band at 682 cm^{-1} to HgF_4 in argon is rather sporting, Figure 7.21. When all of the results achieved within this group are looked at no band can be observed within argon matrices close to this value. The main difference observed between our experimental procedure and the one used by Wang *et al.*[29] is in the mercury evaporation rate. The mercury vapour pressure Wang *et al.*[29] used appears to be in the order of 10 times higher than the one used within these experiments, which leads to the higher probability of dimers being present within the matrix. The annealing times used in neon were also extended in comparison to the ones often used within this group.

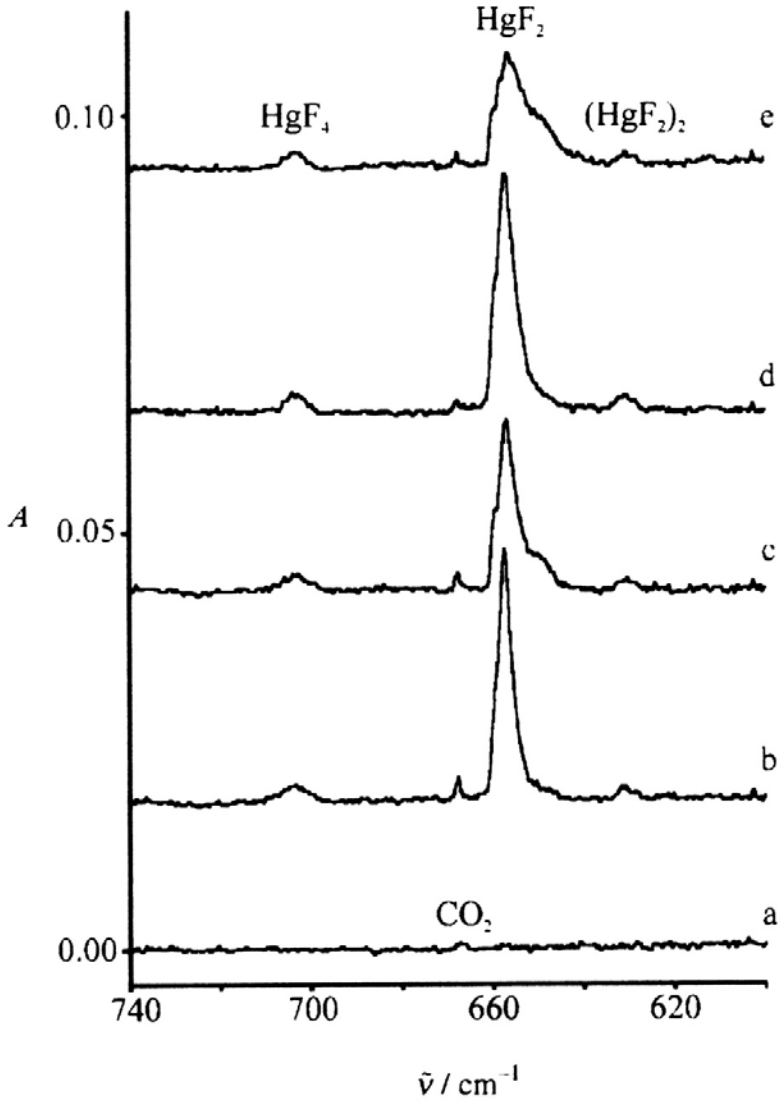

Figure 7.20 IR spectra of mercury isolated in F_2/Ne, a) mercury and 1% F_2 in solid neon at 4 k, b) after 240 – 380 nm irradiation for 15 minutes, c) after irradiation above 220 nm for 15 minutes using full arc, d) after annealing to 8 K, e) after annealing to 10 K, f) after annealing to 12 K.[29]

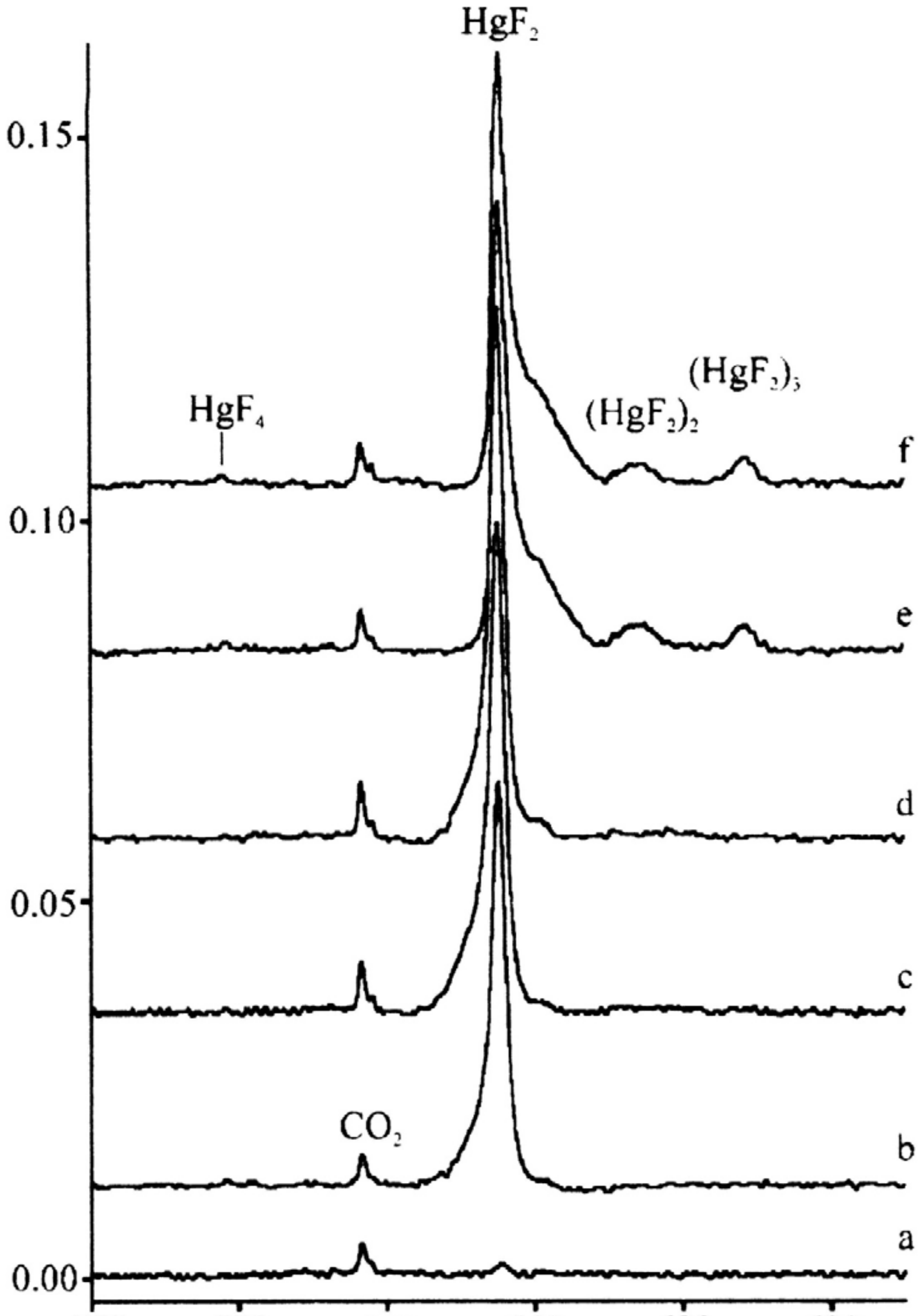

Figure 7.21 IR spectra of mercury isolated in F_2/Ar, a) mercury and 2% F_2 in solid argon at 4 k, b) after 240 – 380 nm irradiation for 15 minutes, c) after irradiation above 220 nm for 15 minutes using full arc, d) after annealing to 20 K, e) after annealing to 30 K, f) after annealing to 35 K.[29]

Due to the fact that within this work the band assigned to HgF_4 in argon by Wang *et al.*[29] cannot be found and their assignment could not be made without the neon results there is no real evidence for the formation of HgF_4 within argon matrices. This leaves the question of why is HgF_4 is apparently stable in neon matrices and not argon? It could be related to the fact the HgF_4 could oxidise the argon matrix but not the neon, but there is no evidence that fluorine can oxidise an argon matrix and so this is unlikely. It could also be related to the rigidity of the lattice making fluorine atoms mobile within the matrix. But annealing of the matrix should allow this mobility and so this is also unlikely. This just leaves the answer that they have probably not made HgF_4 in either a argon or neon matrix.

Further investigation of this band with the use of neon matrices could be the next step in the investigation of HgF_4, although this work can not currently be conducted with our equipment as the cryostats currently use are not able to reach the 4 K required for a neon matrix.

7.4 Results – Other Mercury Halides.

The use of other halogens to isolate a Hg^{IV} complex has previously been shown to be highly unlikely due to the increased instability of the mercury halide compounds with the exception of fluorine.[30-32] Wang *et al.*[29] also reported attempts to isolated $HgCl_4$, but only managed to isolate $HgCl_2$, showing the instability of Hg^{IV} complexes.

Since it was unlikely that the isolation of a Hg^{IV} compound would be obtained with the use of other halides the aim of this work was to see if the same behaviour could be observed with the other halides as seen with mercury and fluorine, the isolation of a photo-sensitive $Hg...F_2$ complex. The same experimental set up was used for these experiments except that the halides were contained in glass bulbs instead of the stainless steel cylinder which was used for fluorine. The work initially started using UV/Vis spectroscopy and then depending on the results obtained the possibility of some far-IR studies could be performed.

This work would be of significant importance to environmental chemists as reactions between mercury and the heavier halides are an area with a significant amount of interest.[74-79] Chlorine, for example, can be produced in the atmosphere near sea level as a result of waves breaking on the sea surface[75] or it can be produced from the photolysis of ozone and aqueous sea salt particles,[79] and so its reactions with mercury is an important process.

7.4.1 Literature Review.

Previously $HgCl_2$ and $HgBr_2$ have been extensively investigated so the υ_1, υ_2 and υ_3 modes of these molecules could be determined with the use of Raman,[80-88] IR,[49, 89-94] and UV/Vis spectroscopy,[58, 59, 95] this is mainly because these molecules are of interest in inorganic chemistry. This is related to the fact that these compounds are triatomic molecules with covalent bonds and have a symmetric linear configuration not only in the gaseous state but also in solution and molten state.[96] Due to this large amount of interest the stretching modes of these linear, $D_{\infty h}$, molecules has been assigned for gaseous,[85, 95] molten,[85] dissolved and matrix isolated[88, 97] samples by various spectroscopic methods. The assignments of the υ_1, υ_2 and υ_3 of $HgCl_2$, $HgBr_2$, and HgI_2 are all shown in Table 7.4, while the electronic assignments are shown in Table 7.1.

The electronic transitions of mercury halides have had extensive study over the years due to their possible use in lasers. Wieland spent 30 years studying these molecules in great detail,[98-102] and thoroughly classified all of the emission lines in $HgCl_2$, $HgBr_2$, and HgI_2. Work by Maya[103] upon $HgBr_2$ and HgI_2 gave UV/Vis bands for these molecules at 43,478 cm^{-1} and 51,282 cm^{-1} for $HgBr_2$ and 37,313 cm^{-1}, 44,444 cm^{-1}, and 50,000 cm^{-1} for HgI_2. Within this study he showed that photolysis of these compounds resulted in photo dissociation of the mercury halide bond and resulted in the formation of HgBr and HgI.

Molecule	**Phase**	**υ_3 (cm^{-1})**	**Experiment**	**υ_1 (cm^{-1})**	**Experiment**	**υ_2 (cm^{-1})**	**Experiment**
	Gas	413	IR Emission[93]	355	Raman[85]	71	UV[104]
				310	Raman[86]		
				365	UV[95, 104, 105]		
$HgCl_2$	Solid	368	IR[92]	330, 310	IR[92]		
		379	IR[106]	316, 310	Raman[106]		
		375	Raman[106]	313	Raman[107]		
		375	IR[91]	314	Raman[86]		
		373	IR[90]	313	Raman[108, 109]		
				319	Raman[110]		
	Gas	293	IR Emission[93]	220	Raman[85]	40	UV[104]
$HgBr_2$				229, 223	UV[95, 104, 105]		
	Solid	250	IR[92]	184	Raman[86]		
		299	IR[91]				
HgI_2	Gas	237	IR Emission[89]	155	Raman[85]	33	UV[104]
				156	UV[95, 104, 105]		

Table 7.4 Stretching frequencies of $HgCl_2$, $HgBr_2$, HgI_2.

Further investigation of this area by Whitehurst and King[111] used UV/Vis spectroscopy to study HgCl, HgBr and HgI after the photo dissociation of $HgCl_2$, $HgBr_2$ and HgI_2, respectively. For HgBr they assigned various peaks due to mercury and then a large peak was produced at 19,801 cm^{-1} due to HgBr itself based upon previous assignments.[102, 112]

	υ_3 (cm^{-1})	**υ_1 (cm^{-1})**	**Others unassigned bands observed**
$HgCl_2$	407 cm^{-1} (2.5) 403 cm^{-1} (3) 397.5 cm^{-1} (2.5)	358 cm^{-1}	107 cm^{-1} (8) 411.5 cm^{-1} (2.5)
$HgBr_2$	294 cm^{-1} (4.5)	225 cm^{-1} (6)	286 cm^{-1} (6) 261 cm^{-1} (10) 73 cm^{-1} (5)
HgI_2	237.5 cm^{-1} (3)	163 cm^{-1}	234.5 cm^{-1} (2) 229 cm^{-1} 220 cm^{-1} (20) 63 cm^{-1} (4)

Table 7.5 Table showing the absorption bands of mercury halides within a krypton matrix, values in parenthesis are band widths in cm^{-1}.[49, 88, 97]

The spectra for HgI this time contains I_2 and a transition is assigned to that at 29,411 cm^{-1}. There is one other major peak in the spectrum present at 22,727 cm^{-1} which was assigned to HgI based on previous observations.[98-102, 113] When HgCl was looked at a peak produced at 17,921 cm^{-1} was assigned to HgCl and other peaks present within the spectrum were assigned to mercury transitions.

Table 7.5 shows the absorption bands observed for the mercury halides within a matrix environment conducted by Loewenschuss *et al.*,[49, 88, 97] all again showing the need for the use of far-IR spectroscopy if a similar pattern is observed for the other halides as seen previously for HgF_2

For elimination purposes the assignments of the UV/Vis absorption bands of chlorine, bromine, and iodine will be given. Chlorine in its ground state produces one large transition in the UV/Vis spectrum at 30,303 cm^{-1} due to a C $^1\Pi_{1u} \leftarrow$ X $^1\Sigma_g^+$ transition.[114] Within this work Hubinger and Nee also assigned the transitions of bromine. They observed two main transitions at 23,809 cm^{-1} and 43,478 cm^{-1}, corresponding to transition to the C $^1\Pi_{1u}$ and the B $^3\Pi^+$, respectively.[114] Iodine has a band assigned to it present at 29,411 cm^{-1} by Whitehurst and King.[111]

7.4.2 Hg in Cl_2/Ar.

7.4.2.1 Hg in 10% Cl_2.

The first concentration of chlorine used was a 10% Cl_2/Ar gas mixture. Depositing 10% Cl_2/Ar on its own without mercury produced a peak around 30,000 cm^{-1}, and also produced a tail near the end of the spectrometer's range, around 45,000 cm^{-1} onwards, Figure 7.22.

This fits with the previous assignment of bands due to chlorine.[114] Mercury was also deposited on its own in argon to remove any mercury peaks from future assignments, Figure 7.10(c). The assignment of the mercury bands is shown in section 7.3.3.2.

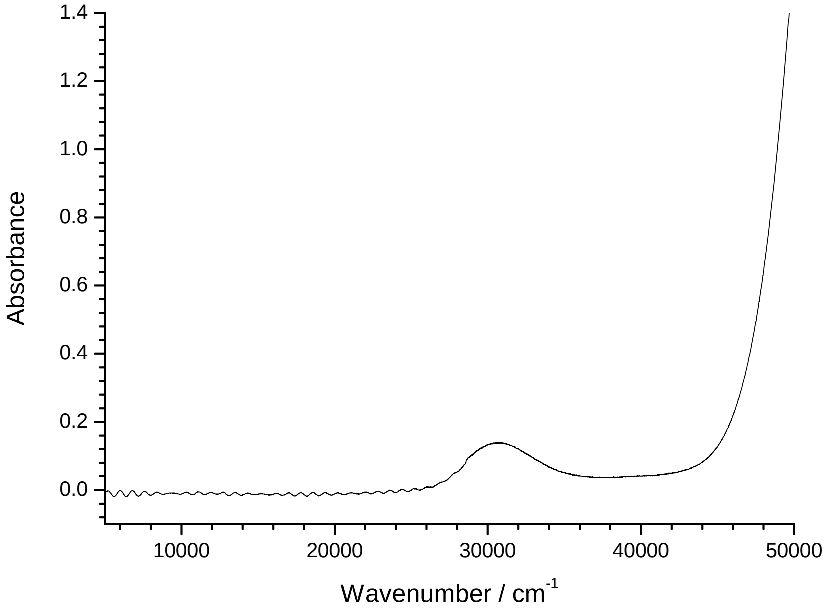

Figure 7.22 UV/Vis spectrum of 10% chlorine isolated in solid argon for 15 minutes.

As soon as mercury and chlorine are put together in a matrix new peaks are produced around 37,500 cm^{-1} and a selection of bands at 41,500 cm^{-1}, 42,200 cm^{-1}, and 43,000 cm^{-1}, Figure 7.23. With the high concentration of chlorine there also appears to be no mercury line at 40,640 cm^{-1}, indicating that all of the mercury has combined with the chlorine present. After selective photolysis, 200 – 470 nm, all of the peaks due to the new mercury chlorine complex reduce dramatically after only 10 minutes of photolysis, the peak due to chlorine at 30,000 cm^{-1} does not reduce aside from the part of the peak which was in the tail of the 37,500 cm^{-1} band. Subsequent annealing of the matrix to 20 K, 25 K and 30 K had no effect.

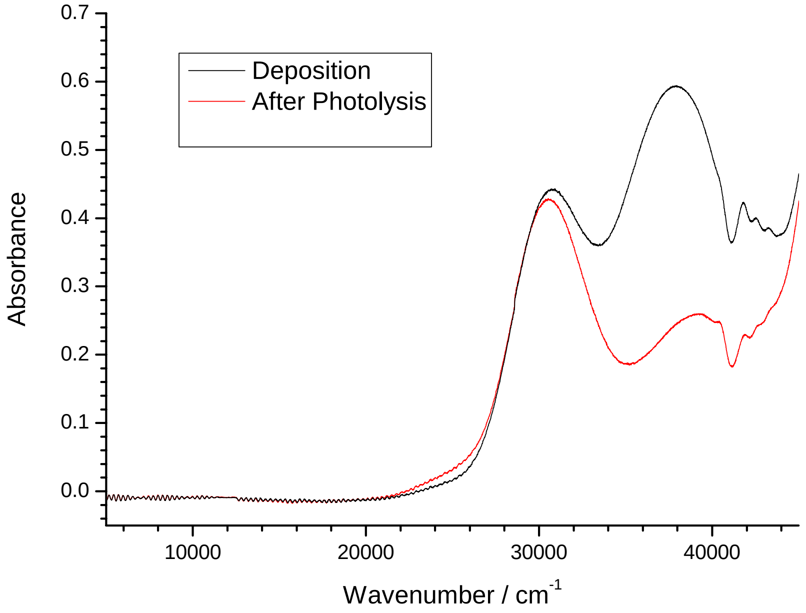

Figure 7.23 UV/Vis spectra of mercury isolated in 10% Cl_2/Ar, the effect of selective photolysis is also shown.

7.4.2.2 Hg in 2% Cl_2/Ar.

The concentration of chlorine was then reduced to a 2% Cl_2/Ar mixture to try and reduce the chlorine peaks and see if this allowed any other peaks to be observed as previously seen with fluorine, Figure 7.24. By reducing the concentration of Cl_2/Ar the peaks at 30,000 cm^{-1} relating to chlorine reduced, the peak at 40,500 cm^{-1}, $^3P_1 \leftarrow {}^1S_0$ transition of atomic mercury, shows that excess mercury is present in the matrix at the 2% Cl_2/Ar concentration, more significantly the tail at the end of the spectrometer reduced meaning that a new peak due to the dimercury $G0_u^+ \leftarrow X0_g^+$ transition is also produced. All of the peaks have been shifted by 400 cm^{-1} as a result of the reduction in concentration and the cluster of peaks between 42,000 cm^{-1} and 43,500 cm^{-1} are much more intense and defined and are unlikely to be due to any mercury transition,[60] and so are likely also associated with a mercury chlorine complex along with the peak around 37,000 cm^{-1}.

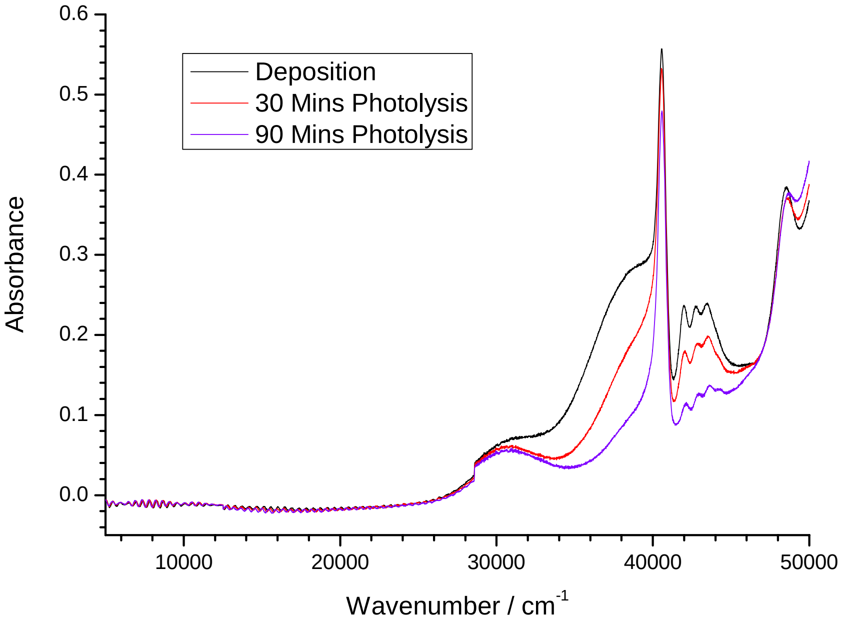

Figure 7.24 UV/Vis spectrum of mercury isolated in 2% Cl_2/Ar after 120 minutes, with the effects of continued photolysis also shown.

Upon selected, 230 - 470 nm, photolysis of the 2% chlorine matrix all of the peaks associated with the mercury chlorine complex reduce in intensity once again while the mercury and chlorine peaks change very little. Figure 7.24 shows the effect of continued 230 – 470 nm photolysis of the matrix for up to 90 minutes. The gradual photo-dissociation produced through photolysis is clear to see in Figure 7.24, over time more and more of the mercury chlorine complex is removed to leave only the peaks due to mercury and chlorine. Further annealing again had no effect other than losing the matrix. The peak at 37,000 cm^{-1} is assigned to the Hg...Cl_2 complex as there is no evidence of growth of a peak at 17,921 cm^{-1} relating to HgCl,[111] which implies that this peak cannot be due to $HgCl_2$.

7.4.2.3 Hg in Cl_2/Ar - IR Study.

Due to the results obtained when mercury is isolated in a Cl_2/Ar matrix within the UV/Vis experiments and the appearance of a similar set of results as that obtained when mercury was isolated in F_2/Ar it was decided that an IR study of this behaviour would allow for further identification of exactly what was happening within the matrix and if the photo dissociation of the complex leads to the formation of $HgCl_2$ as previously seen in the experiments with fluorine. $HgCl_2$ has previously been studied by Loewenschuss *et al.*[49] who assigned the vibrational spectra within a krypton matrix. They observed bands at 403 cm^{-1} and 397.5 cm^{-1} which would mean that a far-IR study of $HgCl_2$ would be required to provide the best results.

Despite numerous attempts at isolation of $HgCl_2$ and various other compounds that should be observable in the far-IR, these experiments failed to isolate anything meaning that further investigation in this area could not be continued for $HgCl_2$, $HgBr_2$, or HgI_2. Subsequent experiments with boric acid showed that the equipment was working but a significant amount of boric acid was required to observe a peak.[115]

7.4.3 Hg in Br_2/Ar.

Due to the unsuccessful investigation using the far-IR instrument the next step was to switch to bromine and try to isolate mercury within the a Br_2/Ar matrix. A problem found early in these experiments with concentrated bromine (10% and above) was that bromine produced a very intense band around 42,000 cm^{-1} in the spectrum masking anything else that might have been happening, Figure 7.25. This meant that no meaningful results could be obtained from 10% Br_2/Ar and so the concentration was reduced to 2% Br_2/Ar to see if this reduction in concentration would sufficiently reduce the bromine band.

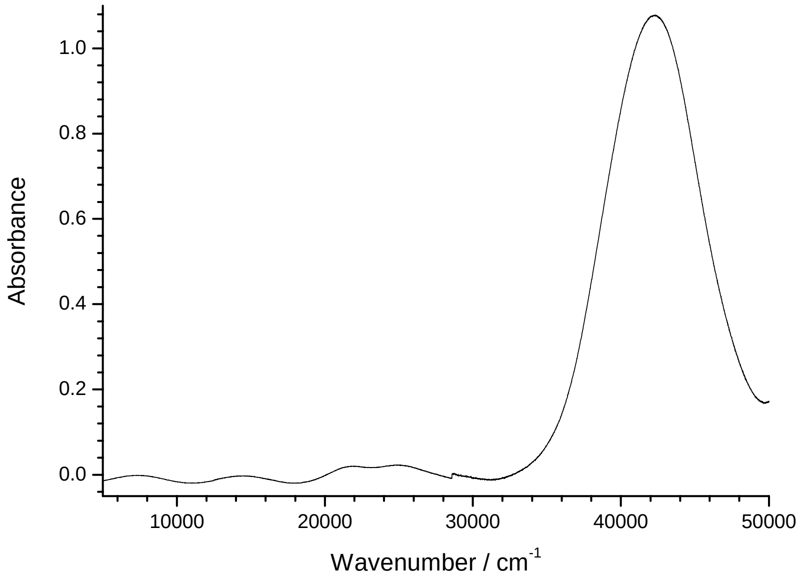

7.25 UV/Vis spectrum of mercury isolated in 10% Br_2/Ar for 5 minutes.

When 2% Br_2/Ar was isolated a broad band at 43,500 cm^{-1} was produced, Figure 7.26. There also appears to be two broad features at 23,800 cm^{-1} and 20,500 cm^{-1}, these bands correspond with the assignment of bromine from the literature.[114] When mercury was added to this matrix peaks due to mercury and dimercury are produced immediately, at 40,600 cm^{-1} and 47,890 cm^{-1} respectively.[60] There is also a new broad feature at 34,750 cm^{-1} which is likely due to a mercury bromine complex. When broadband photolysis was applied to the matrix, Figure 7.27(c), the broad feature at 34,750 cm^{-1} was photo-bleached after 15 minutes. This again follows the pattern of the other mercury halide complexes seen in both fluorine and chlorine and so an assignment of this band to a mercury bromine complex is reasonable and also removes the possibility of this peak being due to $HgBr_2$ due to that fact that no new peaks grow around 19,800 cm^{-1}, due to HgBr.[111]

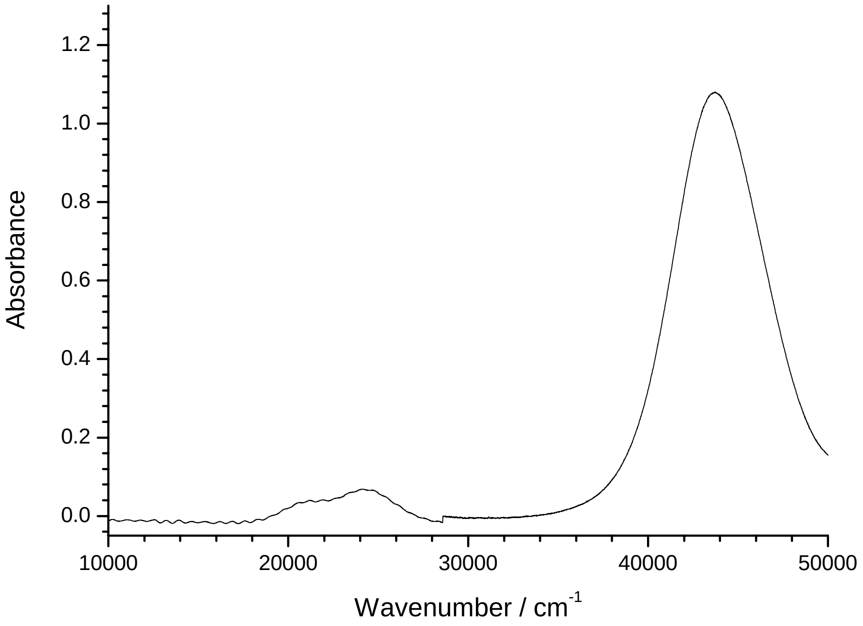

7.26 UV/Vis spectra mercury isolated in 2% Br_2/Ar.

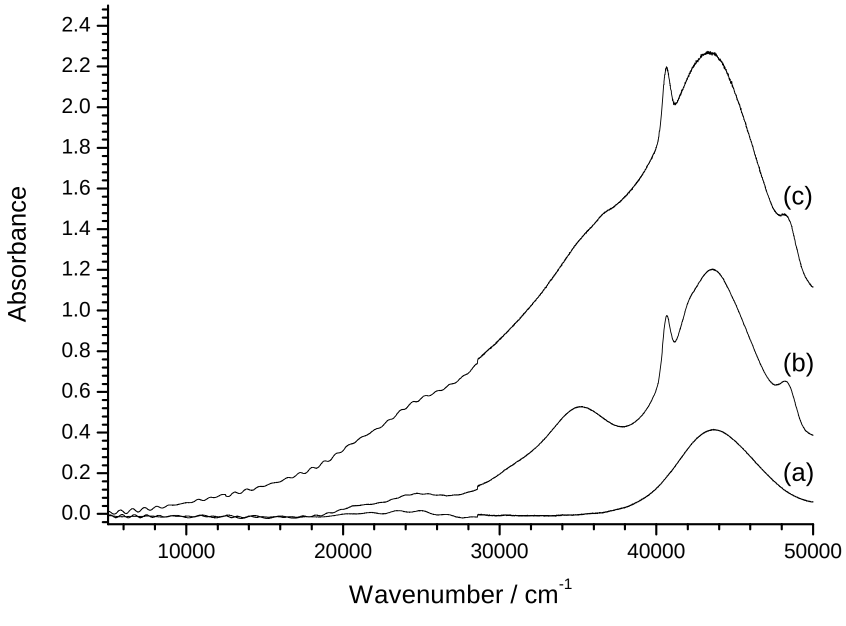

7.27 UV/Vis spectra mercury isolated in 2% Br_2/Ar, (a) 2% Br_2/Ar, (b) mercury isolated in 2% Br_2/Ar, (c) after broadband photolysis.

To see if the mercury halide complex was a phenomenon only observable in argon the next step was to isolate this species in a nitrogen matrix, Figure 7.28. These experiments used a 2% Br_2/N_2 matrix gas and produced bands at 44,550 cm^{-1}, 26,050 cm^{-1} and 21,500 cm^{-1} due to bromine and the mercury and dimercury peaks at 40,150 cm^{-1} and 47,750 cm^{-1} respectively. The broad peak seen previously at 34,250 cm^{-1} is also present in a similar intensity to previous results showing this band is almost certainly due to a mercury bromine complex and is observable in different matrix environments. Broadband photolysis of the matrix again photo-bleaches the complex, until after 15 minutes it is no longer seen any more. Annealing of the matrix had no effect in any of the experiments carried out here.

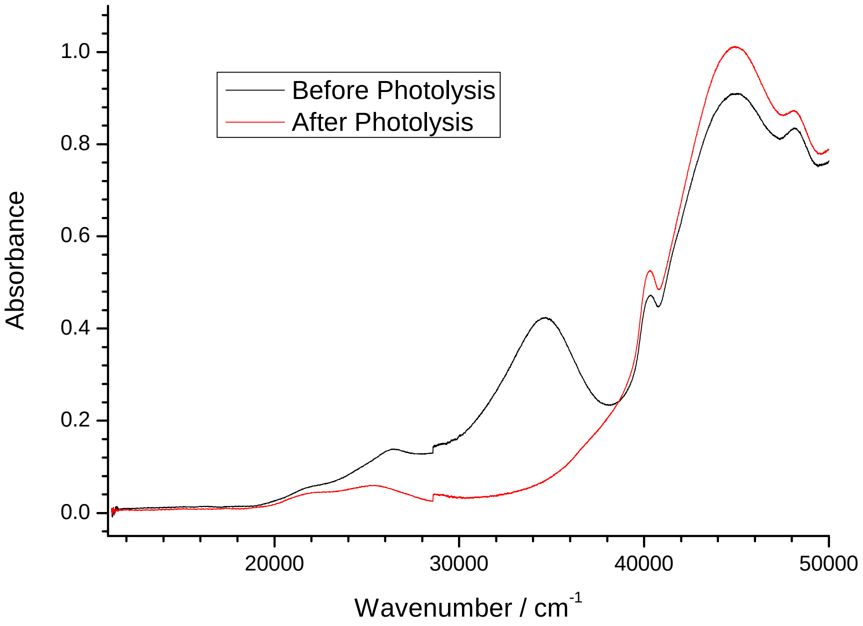

Figure 7.28 UV/Vis spectrum of mercury isolated in 2% Br_2/N_2, with the effect of broadband photolysis shown.

7.4.4 Hg in I_2/Ar.

The final step in this series of experiments was to isolate mercury in a matrix containing iodine and see if a similar complex could be formed. This posed more of a challenge than the previous halogen experiments as iodine is a solid and so transferring this into the matrix could pose problems. But as iodine has a vapour pressure of 0.305 torr at 298 K, it means that a bulb can actually contain approximately 0.3% iodine in half an atmosphere of argon without heating the iodine.[116] This was the starting point of these experiments, using a 0.3% iodine in argon gas mixture to see if any results could be attained without the need for more complex apparatus.

When iodine was isolated in argon numerous peaks were produced at 19,050 cm^{-1}, 34,600 cm^{-1}, 39,650 cm^{-1}, and 46,850 cm^{-1}. When mercury was deposited into the matrix, Figure 7.29, there is the usual appearance of the mercury and dimercury peaks and also significant growth of the peak at 34,600 cm^{-1} either indicating that this is not a iodine peak after all and was simply iodine reacting with residual mercury in the chamber, or that a new peak is in a very similar position to the iodine band in this area. HgI_2 has previously been assigned to a peak at 37,313 cm^{-1} meaning this peak could be either due to HgI_2 or $Hg...I_2$. Visible photolysis, 400 – 700 nm, of the matrix, Figure 7.29, produces a slight reduction in the peak at 34,600 cm^{-1} after 15 minutes, but when 200 – 470 nm photolysis is used for 15 minutes the band reduces significantly more than seen with visible light. Again annealing had no affect on any of the peaks. This shows that the initial peak was most likely produced from residual mercury within the chamber, and thus the peak at 34,600 cm^{-1} is due to a mercury iodine complex. This peak could also be assigned to HgI_2 due to its photolysis behaviour and previous assignment of HgI_2 to a peak at 37,313 cm^{-1}.[111] However this assignment was not made as when HgI_2 is photolysed it forms HgI which should produce a peak at 22,727 cm^{-1} which does not occur in these experiments and so this peak is assigned to $Hg...I_2$. The likely reason that the peak around 37,000 cm^{-1} does not appear to say a similar size during photolysis, as would be expected as the $Hg...I_2$ complex converts to HgI_2, is related to the weak nature of the HgI_2 transition at 37,313 cm^{1} meaning it is likely too weak to be observed.[111]

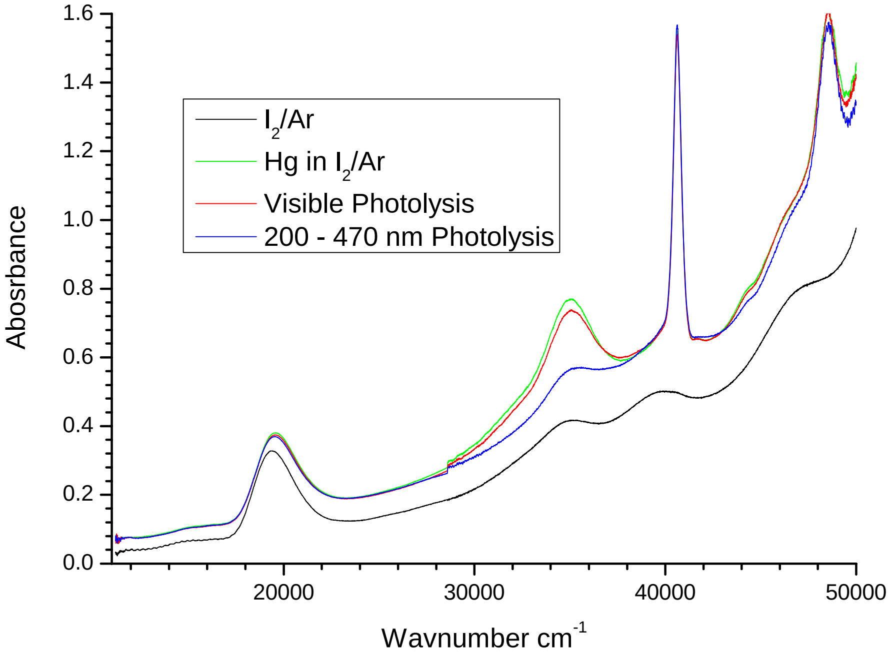

Figure 7.29 UV/Vis spectra of mercury isolated in I_2/Ar, also shows the effect of selective photolysis on the matrix.

7.4.5 Discussion.

From these experiments it appears as though all of the halides form a similar mercury halide complex which when photolysed likely converts to the relevant mercury dihalides. This is just a hypothesis as this route to produce the mercury dihalides has only been conclusively shown with HgF_2 but due to the similarity seen within UV/Vis spectra shown it is highly likely that all of the mercury dihalides follow this same pattern, Table 7.6 tabulates the most intense peaks observed for the $Hg...X_2$ complexes. The table clearly shows that the position clearly changes with a change in halogen and concentration, where data is available. An interesting point that should be considered relates to a simple experiment carried out in room conditions. Mercury was placed within a glass bulb and chlorine was introduced and left overnight. A layer of grey/white material was the formed on the surface of the mercury and with the dispersal of the mercury, eventually reacted with all of the mercury. This shows that chlorine will easily react with mercury to form a compound in room conditions, so this leaves the question of why it forms this Hg...Cl_2 complex in a matrix environment.

	20% X_2/Ar	**10% X_2/Ar**	**5% X_2/Ar**	**2%X_2/Ar**
Hg…F_2	27,500 cm^{-1}	27,580 cm^{-1}	-	27,770 cm^{-1}
Hg…Cl_2	-	37,500 cm^{-1}	-	38,390 cm^{-1}
Hg…Br_2	-	-	-	34,750 cm^{-1}
Hg…I_2	-	-	-	34,600 cm^{-1}

Table 7.6 Tabulated values for the UV/Vis data for Hg...X_2 complexes found in this study.

7.4.6 Conclusion.

The same pattern is observed for chlorine, bromine, and iodine as previously seen with fluorine. The formation of a mercury halide complex, which can then be photodissociated, is clearly apparent from the UV/Vis spectra and thus it is likely that this would then follow the same reaction process as the mercury fluorine complex and form the relevant mercury dihalide. Although the inability to analyse these reaction pathways using far-IR means this cannot be conclusively proven.

7.6 Further Work.

The main area of further work would be to further investigate the chlorine and bromine complexes with far-IR spectroscopy. This would allow the confirmation of the behaviour put forward here and confirm the formation of the mercury halides.

References.

1. R. L. Deming, A. L. Allred, A. R. Dahl, A. W. Herlinger and M. O. Kestner, *J. Am. Chem. Soc.*, 1976, **98**, 4132.
2. F. A. Cotton and G. Wilkinson, *Advanced Inorganic Chemistry*, 5th Edn., Wiley-Interscope, Toronto, 1988.
3. N. V. Sidgwick, *Chemical Elements and their Compounds*, Oxford University Press, Oxford 1950.
4. R. B. Heslop and K. Jones, *Inorganic Chemistry. A Guide To Advanced Study*, Elsevier Scientific Publishing Company, Amsterdam, 1976.
5. D. C. Curtis, *The History of China*, Greenwood Press Santa Barbara, 2001.
6. J. M. Stillman, *Story of Alchemy and Early Chemistry*, Kessinger Publishing, Whitefish, 2003.
7. A. E. Brodsky and J. M. Scherschewer, *Z. Elektrochem*, 1926, **32**, 3.
8. P. Pyykkö, *Chem. Rev.*, 1988, **88**, 563.
9. P. Pyykkö and J. P. Descluax, *Acc. Chem. Res.*, 1979, **12**, 276.
10. K. S. Pitzer, *Acc. Chem. Res.*, 1979, **12**, 271.
11. W. H. E. Schwarz, *Theoretical Models of Chemical Bonding, B.*, Springer, Berlin, 1990.
12. W. Harnischmacher and R. Hoppe, *Angew. Chem.*, 1973, **85**, 590.
13. K. Leary and N. Bartlett, *J. Chem. Soc., Chem. Commun.*, 1972, 903.
14. S. Riedel and M. Kaupp, *Coord. Chem. Rev.*, 2009, **253**, 606.
15. N. Legay-Sommaire and F. Legay, *Chem. Phys. Lett.*, 1999, **314**, 40.
16. V. A. Macrae, J. C. Green, T. M. Greene and A. J. Downs, *J. Phys. Chem. A*, 2004, **108**, 9500.
17. X. F. Wang and L. Andrews, *Inorg. Chem.*, 2005, **44**, 108.
18. V. A. Macrae, T. M. Greene and A. J. Downs, *Phys. Chem. Chem. Phys.*, 2004, **6**, 4586.
19. T. M. Greene, W. Brown, L. Andrews, A. J. Downs, G. V. Chertihin, N. Runeberg and P. Pyykkö, *J. Phys. Chem.*, 1995, **99**, 7925.
20. N. Legay-Sommaire and F. Legay, *J. Phys. Chem.*, 1995, **99**, 16945.
21. X. F. Wang and L. Andrews, *Inorg. Chem.*, 2004, **43**, 7146.

22. X. F. Wang and L. Andrews, *Phys. Chem. Chem. Phys.*, 2005, **7**, 750.
23. N. Legay-Sommaire and F. Legay, *Chem. Phys. Lett.*, 1994, **217**, 97.
24. T. M. Greene, L. Andrews and A. J. Downs, *J. Am. Chem. Soc.*, 1995, **117**, 8180.
25. N. Legay-Sommaire and F. Legay, *Chem. Phys.*, 1996, **211**, 367.
26. N. Legay-Sommaire and F. Legay, *J. Phys. Chem. A*, 1998, **102**, 8759.
27. V. A. Macrae, T. M. Greene and A. J. Downs, *J. Phys. Chem. A*, 2004, **108**, 1393.
28. K. R. Millington, PhD, The University of Southampton, U.K., 1987.
29. X. Wang, L. Andrews, S. Riedel and M. Kaupp, *Angew. Chem. Int. Ed.*, 2007, **46**, 8371.
30. W. J. Liu, R. Franke and M. Dolg, *Chem. Phys. Lett.*, 1999, **302**, 231.
31. P. Pyykkö, M. Straka and M. Patzschke, *Chem. Comm.*, 2002, 1728.
32. S. Riedel, M. Straka and M. Kaupp, *Phys. Chem. Chem. Phys.*, 2004, **6**, 1122.
33. S. Riedel, M. Straka and M. Kaupp, *Chem. Eur. J.*, 2005, **11**, 2743.
34. S. Riedel, M. Kaupp and P. Pyykkö, *Inorg. Chem.*, 2008, **47**, 3379.
35. M. Kaupp and H. G. von Schnering, *Angew. Chem. Int. Ed. Engl.*, 1993, **32**, 861.
36. M. Kaupp, M. Dolg, H. Stoll and H. G. von Schnering, *Inorg. Chem.*, 1994, **33**, 2122.
37. P. Schwerdtfeger, *J. Am. Chem. Soc.*, 1989, **111**, 7261.
38. P. Schwerdtfeger, M. Dolg, W. H. E. Schwarz, G. A. Bowmaker and P. D. W. Boyd, *J. Chem. Phys.*, 1989, **91**, 1762.
39. J. J. Turner and G. C. Pimentel, *Science*, 1963, **140**, 974.
40. M. E. Jacox, *J. Mol. Spectrosc.*, 1980, **84**, 74.
41. E. Y. Misochko, A. V. Akimov and C. A. Wight, *Chem. Phys. Lett.*, 1997, **274**, 23.
42. E. Y. Misochko, A. V. Akimov, I. U. Goldschleger and C. A. Wight, *J. Chem. Phys.*, 2002, **116**, 10307.
43. J. Feld, H. Kunttu and V. A. Aplarian, *J. Chem Phys.*, 1990, **93**, 3670.
44. L. Andrews and G. L. Johnson, *J. Chem. Phys.*, 1983, **79**, 3670.
45. M. E. Jacox, *J. Mol. Spectrosc.*, 1980, **80**, 257.
46. Y. Bouteiller, O. Abdelaoui, A. Schriver and L. Schriver-Mazzuoli, *J. Chem. Phys.*, 1995, **102**, 1731.

47. G. A. Argüello, H. Grothe, M. Kronberg, H. Willner and H.-G. Mack, *J. Phys. Chem.*, 1995, **99**, 17525.
48. D. Tevault, D. P. Strommen and K. Nakamoto, *J. Am. Chem. Soc.*, 1977, **99**, 2997.
49. A. Loewenschuss, A. Ron and O. Schnepp, *J. Chem. Phys.*, 1969, **50**, 2502.
50. A. Givan and A. Loewenschuss, *J. Chem. Phys.*, 1980, **72**, 3809.
51. A. Givan and A. Loewenschuss, *J. Chem. Phys.*, 1980, **72**, 3809.
52. T. C. McInnis and L. Andrews, *J. Phys. Chem.*, 1992, **96**, 2051.
53. W. F. Howard, JR. and L. Andrews, *J. Am. Chem. Soc.*, 1973, **95**, 3045.
54. K. Mierzwicki, Z. Mielke, M. Sałdyka, C. S and P. Roubin, *Phys. Chem. Chem. Phys.*, 2008, **10**, 1292.
55. C. A. Thompson, L. Andrews and R. D. Davy, *J. Phys. Chem.*, 1995, **99**, 7913.
56. A. Arkell, *J. Am. Chem. Soc.*, 1965, **87**, 4057.
57. C. Whitehurst and T. A. King, *J. Phys. D Appl. Phys.*, 1988, **21**, 385.
58. S. Bell, *J. Mol. Spec.*, 1967, **23**, 98.
59. S. Bell, R. D. McKenzie and J. B. Coon, *J. Mol. Spec.*, 1966, **20**, 217.
60. J. Helbing, M. Chergui and A. Haydar, *J. Chem. Phys.*, 2000, **113**, 3621.
61. C. Crepin and A. Tramer, *J. Chem. Phys.*, 1994, **100**, 5467.
62. A. Filipponi, L. Octtaviano and T. A. Tyson, *Phys. Rev. A*, 1993, **48**, 2098.
63. W. J. Jackson, A. Moen, B. K. Nicholson, D. G. Nicholson and K. A. Porter, *J. Chem. Soc., Dalton. Trans.*, 2000, 491.
64. F. E. Huggins, N. Yap, G. P. Huffman and C. L. Senior, *Fuel Proc. Technol.*, 2003, **82**, 167.
65. A. J. Bridgeman, G. Cavigliasso, N. Harris and N. A. Young, *Chem. Phys. Lett.*, 2002, **351**, 319.
66. A. L. Ankudinov, J. J. Rehr and S. R. Bare, *Chem. Phys. Lett.*, 2000, **316**, 495.
67. C. S. Barrett and L. Meyer, *J. Chem. Phys.*, 1964, **41**, 1078.
68. R. S. Amand and B. C. Giessen, *J. Less-Common Met.*, 1978, **58**, 161.
69. F. Ebert and H. Woitinek, *Z. anorg. allg. Chem.*, 1933, **210**, 269.
70. E. Schrötter and B. G. Müller, *Z. anorg. allg. Chem.*, 1992, **618**, 54.
71. M. Kaupp and H. G. von Schnering, *Inorg. Chem.*, 1994, **33**, 4179.
72. M. Kaupp and H. G. von Schnering, *Inorg. Chem.*, 1994, **33**, 4718.

73. A. van der Gaauw, O. M. Wilkin and N. A. Young, *J. Chem. Soc., Dalton Trans.*, 1999, 2405.
74. G. A. Impey, P. B. Shepson, D. R. Hastie, L. A. Barrie and K. G. Anlauf, *J. Geophys. Res-Atmos.*, 1997, **102**, 16005.
75. W. C. Keene, D. J. Jacob and S.-M. Fan, *Atmos. Environ.*, 1996, **30**, R1.
76. T. Kobayashi, *J. Jpn. Soc. Air. Poll.*, 1987, **22**, 230.
77. C.-J. Lin and S. O. Pehkonen, *J. Geophys. Res.*, 1998, **103**, 28093.
78. C.-J. Lin and S. O. Pehkonen, *Atmos. Environ.*, 1998, **33**, 2067.
79. K. W. Oum, M. J. Lakin, D. O. Dehaan, T. Brauers and B. J. Finlayson-Pitts, *Science*, 1998, **279**, 74.
80. P. Krishnamurti, *Indian. J. Phys.*, 1930, **5**, 113.
81. P. Krishnamutri, *Indian. J. Phys.*, 1931, **6**, 7.
82. H. J. Bernstein and W. H. Martin, *Trans. Roy. Soc. Canada.*, 1937, **31**, 95.
83. H. J. Bernstein and W. H. Martin, *Trans. Roy. Soc. Canada.*, 1938, **32**, 43.
84. H. Braune and G. Engelbrecht, *Z. Phys. Chem.*, 1931, **B11**, 409.
85. H. Braune and G. Englebracht, *Z. Phys. Chem.*, 1932, **B19**, 303.
86. K. V. K. Rao, *Indian Acad. Sci.*, 1941, **14A**, 521.
87. G. J. Janz and D. W. James, *J. Chem. Phys.*, 1963, **38**, 902.
88. A. Givan and A. Loewenschuss, *J. Chem. Phys.*, 1976, **64**, 1967.
89. W. Klemperer, *J. Chem. Phys.*, 1956, **25**, 1066.
90. F. A. Miller, G. C. Carlson, F. F. Bentley and W. H. Jones, *Spectro-Chim. Acta*, 1960, **16**, 135.
91. G. E. Coates and D. Ridley, *J. Chem. Soc.*, 1964, 166.
92. Y. Mikawa, R. J. Jacobson and J. W. Brash, *J. Chem. Phys.*, 1966, **45**, 4528.
93. W. Klemperer and L. Lindeman, *J. Chem. Phys.*, 1956, **25**, 397.
94. A. A. Malt'sev, G. K. Selivanov, V. I. Yampolsky and N. I. Zavalishin, *Nat. Phys. Sci.*, 1971, **231**, 157.
95. M. Wherli, *Helv. Phys. Acta.*, 1938, **11**, 339.
96. A. F. Wells, *Structural Inorganic Chemistry*, Oxford University Press, London, 1950.
97. A. Givan and A. Loewenschuss, *J. Chem. Phys.*, 1976, **65**, 1851.

98. K. Wieland, *Helv. Phys. Acta.*, 1929, **2**, 46.

99. K. Wieland, *Z. Phys.*, 1931, **76**, 801.

100. K. Wieland, *Z. Phys.*, 1932, **77**, 157.

101. K. Wieland, *Helv. Phys. Acta.*, 1941, **14**, 420.

102. K. Wieland, *Z. Elektrochem*, 1960, **64**, 761.

103. J. Maya, *J. Chem. Phys.*, 1977, **67**, 4976.

104. H. Sponer and E. Teller, *Rev. Mod. Phys.*, 1941, **13**, 75.

105. M. Wherli, *Helv. Phys. Acta.*, 1940, **13**, 153.

106. H. Boulet and J. P. Mathieu, *J. Chim. Phys.*, 1963, **60**, 442.

107. W. Bues, *Z. anorg. allem. Chem.*, 1955, **279**, 104.

108. P. Krishnamarti, *Indian. J. Phys.*, 1931, **5**, 113.

109. P. Krishnamatri, *Indian. J. Phys.*, 1931, **6**, 7.

110. M. L. Delvaulli, *Compt. Rend.*, 1938, **206**, 1965.

111. C. Whitehurst and T. A. King, *J. Phys. B. - At. Mol. Opt.*, 1987, **20**, 4035.

112. N. H. Cheung and T. A. Cool, *J. Quantum Spectrosc. Radiat. Transfer*, 1979, **21**, 397.

113. J. Tellinghuissen, P. C. Tellinghuissen, S. A. Davies, P. Berwanger and K. Viswanathan, *Appl. Phys. Lett.*, 1982, **41**, 789.

114. S. Hubinger and J. B. Nee, *J. Photoch. Photobio. A.*, 1994, **86**, 1.

115. J. S. Ogden and N. A. Young, *J. Chem. Soc., Dalton Trans.*, 1988, 1645.

116. A. N. Nesneyomov, *Vapour Pressure of the Chemical Elements*, Elsevier Publishing Company, London, 1963.

Appendix 1.

Titanium - Group Theory Tables.

TiF_4.

Assuming TiF_4 is tetrahedral, thus in the T_d group.

T_d	E	$8C_3$	$3C_2$	$6S_4$	$6\sigma_d$	Σ	Σ/h
Γ_{str}	4	1	0	0	2	(24)	
A_1	+4	+8	0	0	+12	24	1
A_2	+4	+8	0	0	-12	0	0
E	+8	-8	0	0	0	0	0
T_1	+12	0	0	0	-12	0	0
T_2	+12	0	0	0	+12	24	1

$\Gamma_{str} = A_1 + T_2$, only the T_2 IR active

TiF$_3$.

Assuming D_{3h} symmetry

D_{3h}	E	$2C_3$	$3C_2$	σ_h	$2S_3$	$3\sigma_v$	Σ	Σ/h
Γ_{str}	3	0	1	3	0	1	(12)	
A_1`	+3	0	+3	+3	0	+3	12	1
A_2`	+3	0	-3	+3	0	-3	0	0
E`	+6	0	0	+6	0	0	12	1
A_1``	+3	0	+3	-3	0	-3	0	0
A_2``	+3	0	-3	-3	0	+3	0	0
E``	+6	0	0	-6	0	0	0	0

$\Gamma_{str} = A_1' + E'$, only the E' IR active

TiF$_2$.

Assuming bent structure, will be C_{2v}

C_{2v}	E	C_2 (z)	$\sigma_v(xz)$	$\sigma_v(yz)$	Σ	Σ/h
Γ_{str}	2	0	0	2	(4)	
A_1	+2	0	0	+2	4	1
A_2	+2	0	0	-2	0	0
B_1	+2	0	0	-2	0	0
B_2	+2	0	0	+2	4	1

$\Gamma_{str} = A_1 + B_2$, both of which are active.

If linear;

Cannot use $D_{\infty h}$, so done for D_{2h}.

D_{2h}	**E**	C_2 **(z)**	C_2 **(y)**	C_2 **(x)**	**i**	$\sigma_{(xy)}$	$\sigma_{(xz)}$	$\sigma_{(yz)}$	Σ	Σ/h
Γ_{str}	+2	+2	0	0	0	0	+2	+2	(8)	
A_g	+2	+2	0	0	0	0	+2	+2	8	1
B_{1g}	+2	-2	0	0	0	0	-2	-2	0	0
B_{2g}	+2	-2	0	0	0	0	+2	-2	0	0
B_{3g}	+2	-2	0	0	0	0	-2	+2	0	0
A_u	+2	+2	0	0	0	0	-2	-2	0	0
B_{1u}	+2	+2	0	0	0	0	+2	+2	8	1
B_{2u}	+2	-2	0	0	0	0	-2	+2	0	0
B_{3u}	+2	-2	0	0	0	0	+2	-2	0	0

$\Gamma_{str} = A_g + B_{1u}$

This converts to $\Gamma_{str} = \Sigma_g^+ + \Sigma_u^+$, only Σ_u^+ IR active.

TiF

Cannot use $C_{\infty v}$, so done for C_{2v}.

C_{2v}	E	C_2 (z)	$\sigma_v(xz)$	$\sigma_v(yz)$	Σ	Σ/h
Γ_{str}	1	1	1	1	(4)	
A_1	+1	+1	+1	+1	4	1
A_2	+1	+1	-1	-1	0	0
B_1	+1	-1	+1	-1	0	0
B_2	+1	-1	-1	+1	0	0

Thus $\Gamma_{str} = A_1$

So in $C_{\infty v} = \Gamma_{str} = \Sigma^+$, which is IR active.

Vanadium - Group Theory.

VF_5.

Assuming D_{3h} symmetry.

D_{3h}	E	$2C_3$	$3C_2$	σ_h	$2S_3$	$3\sigma_v$	Σ	Σ/h
Γ_{str}	5	2	1	3	0	3	(12)	
A_1`	+5	+4	+3	+3	0	+9	24	2
A_2`	+5	+4	-3	+3	0	+9	0	0
E`	+10	-4	0	+6	0	0	12	1
A_1``	+5	+4	+3	-3	0	-9	0	0
A_2``	+5	+4	-3	-3	0	+9	12	1
E``	+10	-4	0	-6	0	0	0	0

$\Gamma_{str} = 2A_1' + E' + A_2''$, only the E' and A_2'' are IR active.

VF_4.

Refer to TiF_4

VF_3.

Refer to TiF_3.

VF_2.

Refer to TiF_2.

VF

Refer to TiF.

Palladium - Group Theory.

PdF_6.

Assuming octahedron

O_h	E	$8C_3$	$6C_2$	$6C_4$	$3C_2 (=C_4^2)$	i	$6S_4$	$8S_6$	$3\sigma_h$	$6\sigma_d$	Σ	Σ/h
Γ_{str}	6	0	0	2	2	0	0	0	4	2	(48)	
A_{1g}	+6	0	0	+12	+6	0	0	0	+12	+12	48	1
A_{2g}	+6	0	0	-12	+6	0	0	0	+12	+12	0	0
E_g	+12	0	0	0	+12	0	0	0	+24	0	48	1
T_{1g}	+18	0	0	+12	-6	0	0	0	-12	-12	0	0
T_{2g}	+18	0	0	-12	-6	0	0	0	-12	+12	0	0
A_{1u}	+6	0	0	+12	+6	0	0	0	-12	-12	0	0
A_{2u}	+6	0	0	-12	+6	0	0	0	-12	+12	0	0
E_u	+12	0	0	0	+12	0	0	0	-24	0	0	0
T_{1u}	+18	0	0	+12	-6	0	0	0	+12	+12	48	1
T_{2u}	+18	0	0	-12	-6	0	0	0	+12	-12	0	0

$\Gamma_{str} = A_{1g} + E_g + T_{1u}$. Only T_{1u} IR active.

PdF$_5$.

Assuming square based pyramid thus C_{4v}

C_{4v}	E	$2C_4$	C_2	$2\sigma_v$	$2\sigma_d$	Σ	Σ/h
Γ_{str}	5	1	1	3	1	(8)	
A_1	+5	+2	+1	+6	+2	16	2
A_2	+5	+2	+1	-6	-2	0	0
B_1	+5	-2	+1	+6	-2	8	1
B_2	+5	-2	+	-6	+1	0	0
E	+10	0	-2	0	0	8	1

$\Gamma_{str} = 2\ A_1 + B_1 + E$, both 2 A_1 and E IR active.

PdF$_4$.

If the structure is see-saw, will be C_{2v}.

C_{2v}	E	C_2 (z)	$\sigma_v(xz)$	$\sigma_v(yz)$	Σ	Σ/h
Γ_{str}	4	0	2	2	(4)	
A_1	+4	0	+2	+2	8	2
A_2	+4	0	-2	-2	0	0
B_1	+4	0	+2	-2	4	1
B_2	+4	0	-2	+2	4	1

$\Gamma_{str} = 2\ A_1 + B_1 + B_2$, all of which are IR active.

Assuming square planar structure thus D_{4h},

D_{4h}	E	$2C_4$	C_2	$2C_2$\`	$2C_2$\`	i	$2S_4$	σ_h	$2\sigma_v$	$2\sigma_d$	Σ	Σ/h
Γ_{str}	4	0	0	2	0	0	0	0	4	2	(16)	
A_{1g}	+4	0	0	+4	0	0	0	+4	+4	0	16	1
A_{2g}	+4	0	0	-4	0	0	0	+4	-4	0	0	0
B_{1g}	+4	0	0	+4	0	0	0	+4	+4	0	16	1
B_{2g}	+4	0	0	-4	0	0	0	+4	-4	0	0	0
E_g	8	0	0	0	0	0	0	-8	0	0	0	0
A_{1u}	+4	0	0	+4	0	0	0	-4	-4	0	0	0
A_{2u}	+4	0	0	-4	0	0	0	-4	+4	0	0	0
B_{1u}	+4	0	0	+4	0	0	0	-4	-4	0	0	0
B_{2u}	+4	0	0	-4	0	0	0	-4	+4	0	0	0
E_u	+8	0	0	0	0	0	0	+8	0	0	16	1

$\Gamma_{\mathrm{str}} = A_{1g} + B_{1g} + E_u$, only E_u IR active.

If D_{2d}

D_{2d}	E	$2S_4$	C_2	$2C_2$'	$2\sigma_d$	Σ	Σ/h
Γ_{str}	4	0	0	0	2	8	
A_1	+4	0	0	0	+4	8	1
A_2	+4	0	0	0	-4	0	0
B_1	+4	0	0	0	-4	0	0
B_2	+4	0	0	0	+4	8	1
E	+8	0	0	0	0	8	

$\Gamma_{str} = A_1 + B_2 + E$, only $B_2 + E$ IR active.

$\underline{PdF_3.}$

If structure t-shaped then C_{2v}

C_{2v}	E	$C_2 (z)$	$\sigma_v(xz)$	$\sigma_v(yz)$	Σ	Σ/h
Γ_{str}	3	1	3	1	(4)	
A_1	+3	+1	+3	+1	8	2
A_2	+3	+1	-3	-1	0	0
B_1	+3	-1	+3	-1	4	1
B_2	+3	-1	-3	+1	0	0

$\Gamma_{str} = 2\,A_1 + B_1$, both IR active.

$\underline{PdF_2.}$

Refer to TiF_2.

$\underline{PdF}$

Refer to TiF.

Appendix 2.

Computational Calculations for PdF_n.

Enthalpy of formations Pd + ½ F_2 -220.06 kJ mol^{-1}; PdF_1 + ½ F_2 -239.64 kJ mol^{-1}; PdF_2 + ½ F_2 -167.74 kJ mol^{-1}; PdF_3 + ½ F_2 -141.72 kJ mol^{-1}; PdF_4 + ½ F_2 -61.75 kJ mol^{-1}; PdF_5 + ½ F_2 -88.85 kJ mol^{-1}; Pd + F_2 -459.69 kJ mol^{-1}; Pd + 3/2 F_2 -627.43 kJ mol^{-1}; Pd + 2 F_2 -769.15 kJ mol^{-1}; Pd + 5/2 F_2 -830.90 kJ mol^{-1}; Pd + 3 F_2 – 919.75 kJ mol^{-1}. ADF calculated Pd-F bond lengths and angles, harmonic vibrational frequencies, IR intensities in km mol^{-1} () and Raman intensities in A^4 amu^{-1} [] for palladium fluorides. PdF: ($C_{\infty v}$); Pd-F, 1.9297 Å; 522.88 cm^{-1} (40.65). PdF_2: ($D_{\infty h}$); Pd-F, 1.865 Å, 1.886 Å; 661.78 cm^{-1} (117.27) [-], 560.89 cm^{-1} (0) [31.98], 176.09 cm^{-1} (16.37) [-]. PdF_3: (C_{2v}); Pd-F, 1.8949 Å, F-Pd-F, 167.96°, 96.02°; 633.46 cm^{-1} (146.16) [-], 597.985 cm^{-1} (0.86) [-], 565.30 cm^{-1} (39.6) [-], 171.97 cm^{-1} (13.65) [-], 170.84 cm^{-1} (11.36) [-], 156.34 cm^{-1} (2.32) [-]. PdF_4: (D_{4h}); Pd-F, 1.8664 Å, F-Pd-F, 90°; 663.48 cm^{-1} (81.63) [-], 585.56 cm^{-1} (0) [41.48], 523.72 cm^{-1} (0) [25.02], 232.85 cm^{-1} (6.52) [-], 226.18 cm^{-1} (11.99) [-]. PdF_5: (C_{4v}); Pd-F, 1.878 Å, 1.854 Å, F-Pd-F, 93.48°, 89.79°, 173.04°; 648.31 cm^{-1} (79.09) [-], 632.75 cm^{-1} (15.46) [-], 578.65 cm^{-1} (0.95) [-], 242.87 cm^{-1} (6.29) [-], 235.10 cm^{-1} (13.95) [-], 144.30 cm^{-1} (0.27) [-]. PdF_6: (D_{3h}); Pd-F, 1.8747 Å, F-Pd-F, **~90°**; 649.50 cm^{-1} (58.95) [-], 649.25 cm^{-1} (58.88) [-], 279.82 cm^{-1} (6.70) [-], 279.30 cm^{-1} (6.69) [-].

*note – Raman intensities were not calculated in these calculations.

Computational Calculations for HgF_n.

Computational calculations for HgF_4. ADF calculated enthalpies of formation: Hg + 2F -602 kJ mol^{-1}; Hg + F_2 -434 kJ mol^{-1}; HgF_2 + F -88 kJ mol^{-1}; HgF_2 + ½F_2 -4 kJ mol^{-1}; HgF_2 + 2F -317 kJ mol^{-1}; HgF_2 + F_2 -150 kJ mol^{-1}. ADF calculated ground terms, Hg-F bond lengths and angles, harmonic vibrational frequencies, IR intensities in km mol^{-1} () and Raman intensities in A^4 amu^{-1} [] for mercury fluorides. HgF: $^2\Sigma^+$ ($C_{\infty v}$); Hg-F, 2.104 Å; Σ^+, 395 cm^{-1} (27). HgF_2: $^1\Sigma_g^+$ ($D_{\infty h}$); Hg-F, 1.956 Å; Σ_g^+, 533 cm^{-1} (0) [22.5], Π_u, 163 cm^{-1} (26) [0], Σ_u^+, 623 cm^{-1} (97) [0]. HgF_3: $^2A_1$ (C_{2v}); Hg-F, 2.138, 1.965, 1.965 Å, F-Hg-F, 96.62 °, 96.62 °, 166.77 °; A_1 513 cm^{-1} (0.01), A_1 349 cm^{-1} (0.4), B_2 591 cm^{-1} (50),

A_1 154 cm^{-1} (14), B_1 66 cm^{-1} (3), B_2 140 cm^{-1} (6). HgF_4: $^1A_{1g}$ (D_{4h}); Hg-F, 1.947 Å; A_{1g} 526 cm^{-1} (0) [46], B_{1g} 517 cm^{-1} (0) [22], B_{2g} 202 cm^{-1} (0) [6], A_{2u} 217 cm^{-1} (2) [0], E_u 622 cm^{-1} (120) [0], E_u 196 cm^{-1} (32) [0].

Appendix 3.

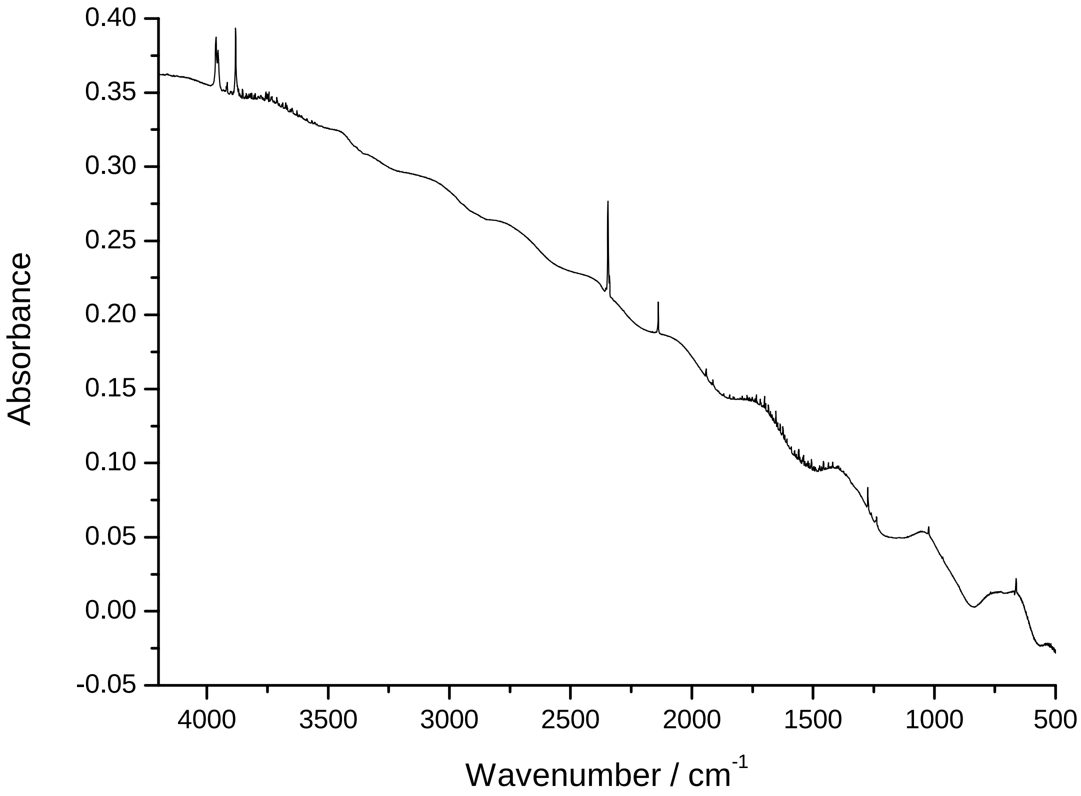

A3.1 IR spectrum of 1% F_2 isolated in argon.

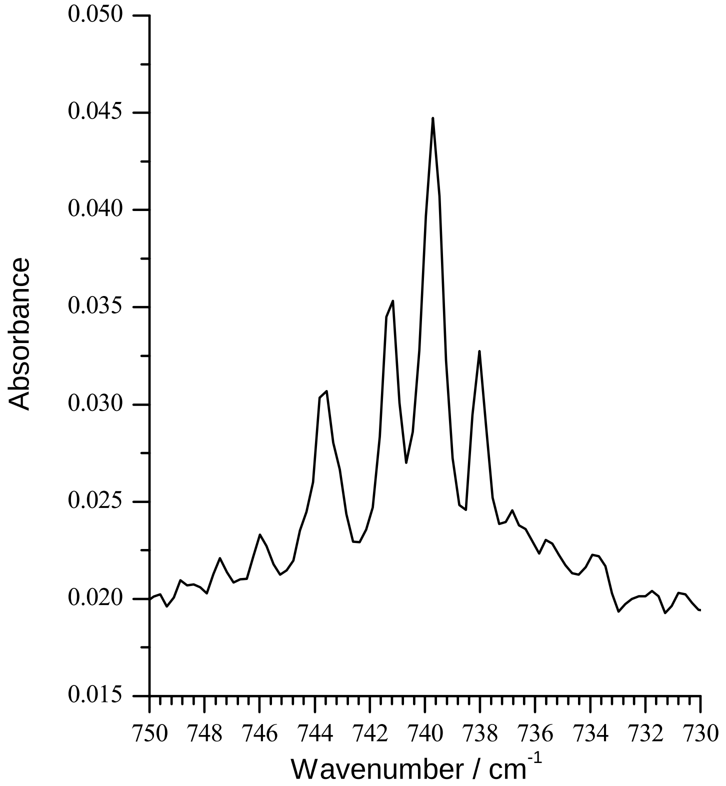

A3.2 IR spectrum showing the TiF_3 isotope splitting pattern.

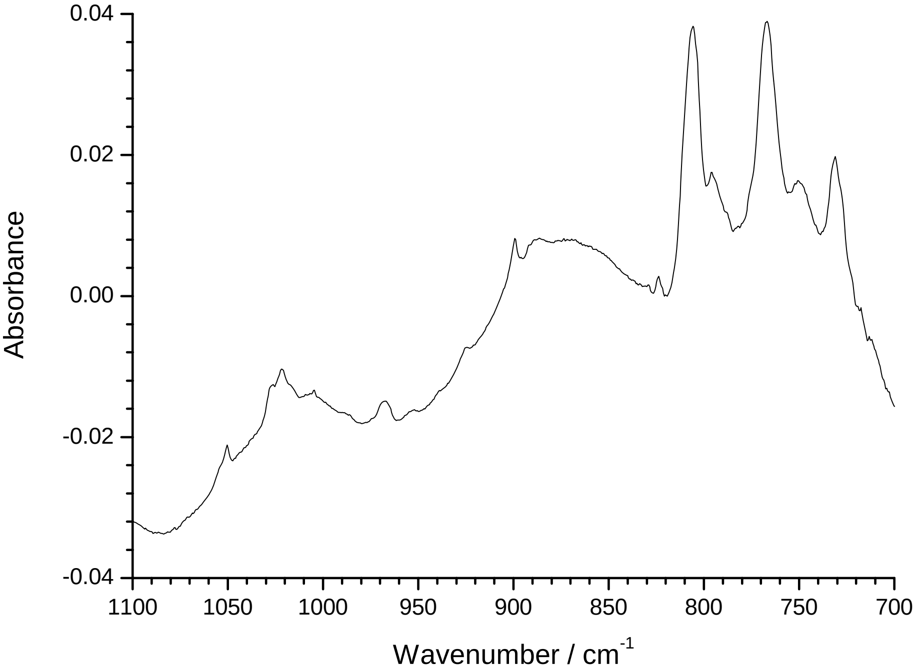

A3.3 IR spectrum showing the lack of bands indicative of VOF_3, present at 1057.8 cm^{-1}, 806.0 cm^{-1} and 721.5 cm^{-1}.

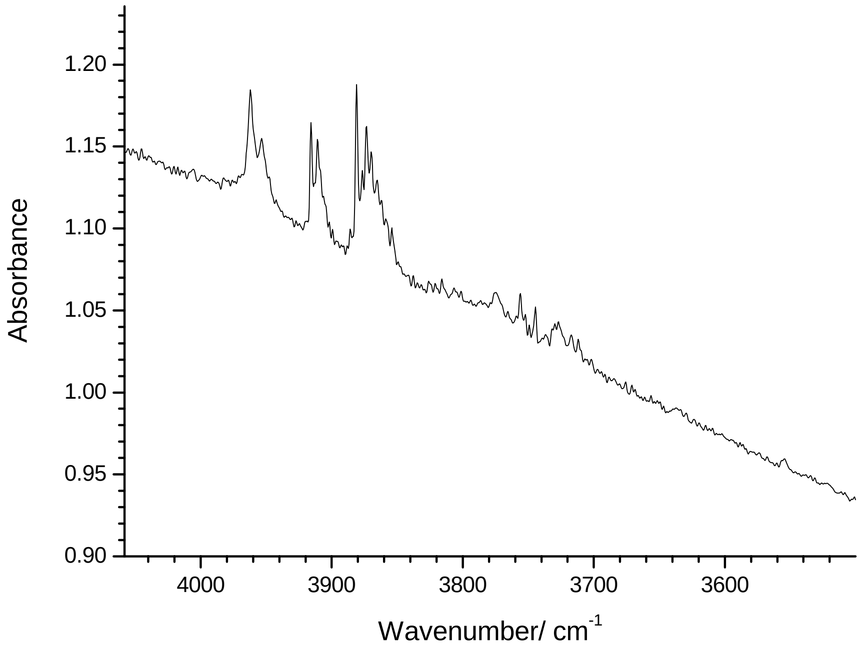

A3.4 IR spectra of palladium isolated in 2% F_2/Ar, between 4500 cm^{-1} and 3500 cm^{-1}.

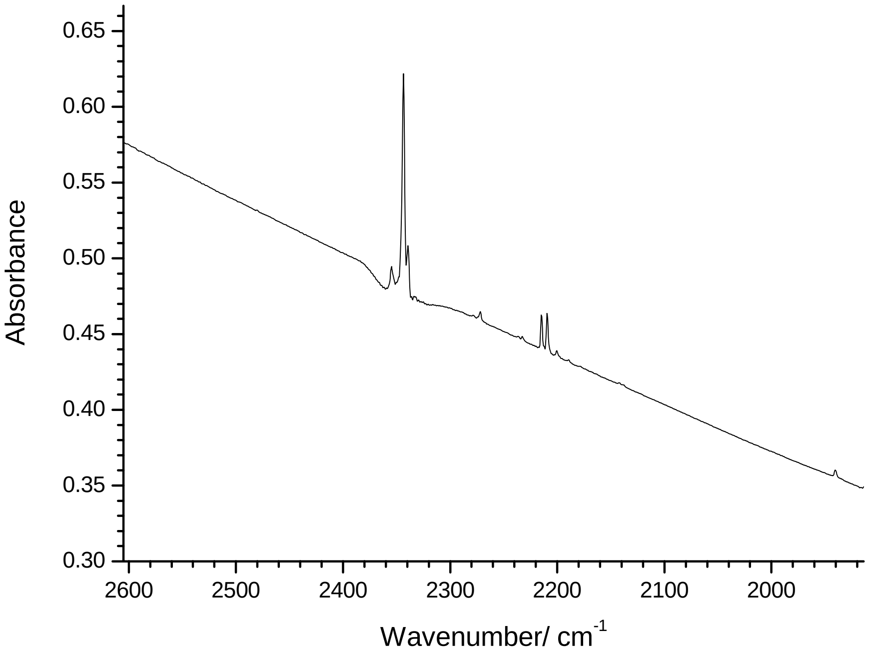

A3.5 IR spectra of palladium isolated in 2% F_2/Ar, between 2600 cm^{-1} and 1900 cm^{-1}.

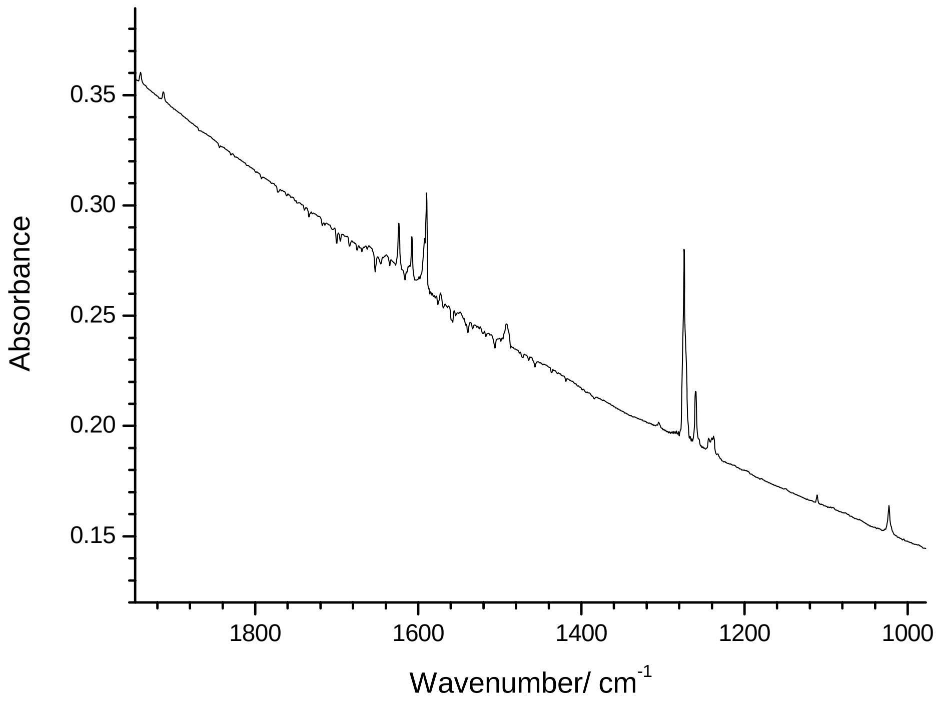

A3.6 IR spectra of palladium isolated in 2% F_2/Ar, between 1900 cm^{-1} and 1000 cm^{-1}.

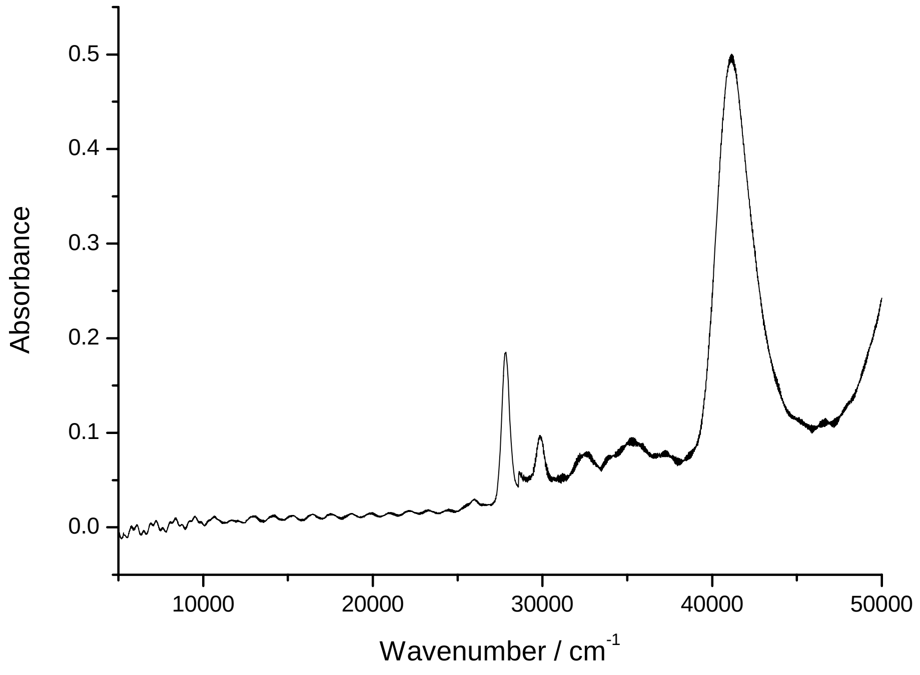

A3.7 UV spectrum of palladium isolated in argon, using normal deposition technique.

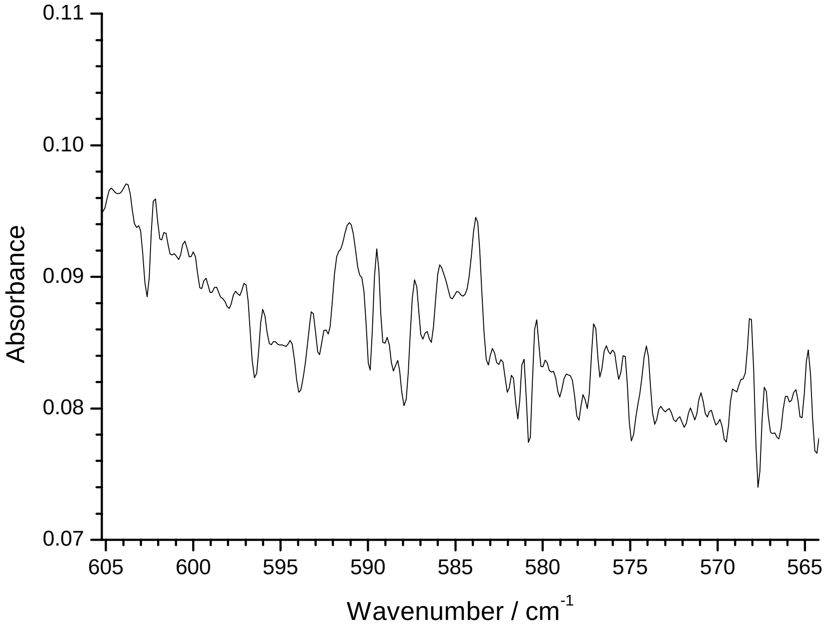

A3.8 IR spectrum of the peak seen at 590.9 cm^{-1}, showing the difficulty in obtaining an isotope pattern from this peak.

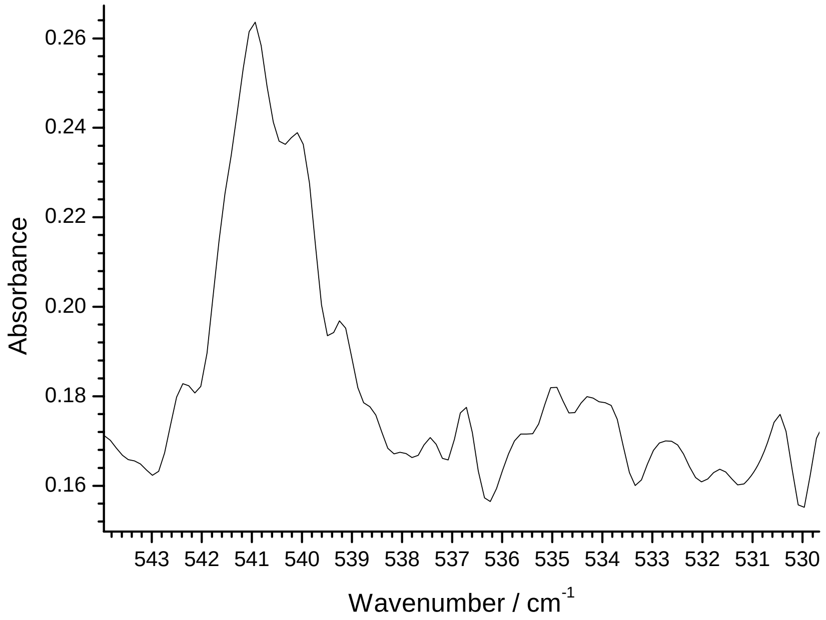

A3.9 IR spectrum of the peak seen at 534.5 cm^{-1}, showing the difficulty in obtaining an isotope pattern from this peak.

Bibliography.

- K. Nakamoto, *Infrared and Raman Spectra of Inorganic and Coordination Compound*s, Wiley, 1978.
- S. Cradock and A. J. Hinchcliffe, *Matrix Isolation*, Cambridge University Press, 1975.
- A. Vincent, *Molecular Symmetry and Group Theory*, Wiley, 2001.
- R. T. Conley, *Infrared Spectroscopy*, Boston, 1966.
- M. Moskovits and G. A. Ozin, *Cryochemsitry*, New York, 1976.
- J. M. Hollas, *Modern Spectroscopy*, Whiley, 1996.
- R. F. Barrow, D. A. Long, and D. J. Millen, *Molecular Spectroscopy: Volume 1*, The Chemical Society, 1973.
- R. B. Heslop and K. Jones, *Inorganic Chemistry. A Guide To Advanced Study*, ed. E. S. P. Company, Elsevier Scientific Publishing Company, 1976.
- F. A. Cotton and G. Wilkinson, *Advanced Inorganic Chemistry*,5th ed., Wiley-Interscope, 1988.
- N. N. Greenwood and A. Earnshaw, *Chemistry of the Elements*, 2nd ed., Butterworth Heinmann, Oxford, 1997.
- W. W. Porterfield, *Inorganic Chemistry: A Unified Approach*, Addison Wesley, London, 1984.
- N. V. Sidgwick, *Chemical Elements and their Compounds*, Oxford University Press, Oxford 1950.
- J. M. Hollas, *High Resolution Spectroscopy*, Butterworth & Co, London, 1982.
- H. E. Hallam, *Vibrational Spectroscopy of Trapped Species*, Wiley, London, 1973
- L. Andrews, M. Moskovits, *Chemistry and Physics of Matrix-Isolated Species*, North-Holland, Amsterdam, 1989.
- A. Arkharov, I. Marfenina, Ye. Mikulin, *Theory and Design of Cryogenic Systems*, Mir Publishers, Moscow, 1981.
- M. J. Almond, *Short-Lived Molecules*, Ellis Horwood, Chichester, 1990